Development of Laser Powder Bed Fusion Technique to Process NiTi with Retained Shape Memory Capabilities

By

Josiah Cherian Chekotu, M. Sc.

A thesis submitted in fulfilment of the requirements for the degree of

Doctor of Philosophy (PhD)

from

Dublin City University

School of Mechanical and Manufacturing Engineering

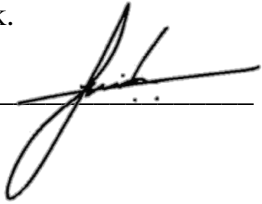Supervisors: Prof. Dermot Brabazon, Dublin City University

Dr. David Kinahan, Dublin City University

Co-supervisor: Prof. Russell Goodall, University of Sheffield

August 2023

Declaration

I hereby certify that this material, which I now submit for assessment on the programme of study leading to the award of PhD is entirely my own work, that I have exercised reasonable care to ensure that the work is original, and does not to the best of my knowledge breach any law of copyright, and has not been taken from the work of others save and to the extent that such work has been cited and acknowledged within the text of my work.

Signed: _____   ID No.: __18212182_____   Date: __29-Aug-2023___

Acknowledgements

Table of Contents

List of Figures

X

List of Tables

List of Publications

1. J.C. Chekotu, R. Groarke, K. O'Toole, D. Brabazon, Advances in selective laser melting of nitinol shape memory alloy part production, Mater. 12 (2019) 809. https://doi.org/10.3390/ma12050809

2. J.C. Chekotu, R. Goodall, D. Kinahan, D. Brabazon, Control of NiTi phase structure, solid-state transformation temperatures and enthalpies via control of L-PBF process parameters, Mater. Des. 218 (2022) 110715. https://doi.org/10.1016/j.matdes.2022.110715

3. J.C. Chekotu, D. Kinahan, R. Goodall, D. Brabazon, Influence of structural porosity and martensite evolution on mechanical characteristics of nitinol via in-silico finite element approach, Mater. 15 (2022) 5365. https://doi.org/10.3390/ma15155365

4. J.C. Chekotu, D. Brabazon, In silico finite element approach on mechanical behaviour in superelastic nitinol, Key Eng. Mater. 926 (2022) 213 – 219. https://doi.org/10.4028/p-mb5el0

5. J.C. Chekotu, G. Degli-Alessandrini, M.Z. Mughal, S. Chatterjee, R. Goodall, D. Kinahan, D. Brabazon, Control of mechanical characteristics and shape memory functionality in martensitic NiTi via L-PBF parameters and build orientation, J. Mater. Res. Technol. 25 (2023) 6407 – 6431. https://doi.org/10.1016/j.jmrt.2023.07.092

6. J.C. Chekotu, S. Kumar S, G. Degli-Alessandrini, M.Z. Mughal, R. Goodall, D. Kinahan, D. Brabazon, Formation of β-Ti phase during L-PBF processing of martensitic NiTi, Mater. Today Commun. 36 (2023) 106668. https://doi.org/10.1016/j.mtcomm.2023.106668

7. M.C.C. Monu, Y. Afkham, J.C. Chekotu, E.J. Ekoi, H. Gu, C. Teng, J. Ginn, J. Gaughran, D. Brabazon, Bi-directional scan pattern effects on residual stresses and distortion in as-built nitinol parts: A trend analysis simulation study, Integr. Mater. Manuf. Innov. 12 (2023) 52 – 69. https://doi.org/10.1007/s40192-023-00292-9

8. L.A. Khan, H. Ayub, J.C. Chekotu, K. Tamilselvam, C. Muilwijk, I.U. Ahad, D. Brabazon, Steady-state and transient mechanical response analysis of superelastic nitinol lattice structures prior to additive manufacturing: An in-silico study, J. Mater. Res. Technol. 25 (2023) 3258 – 3272. http://doi.org/ 10.1016/j.jmrt.2023.06.137

List of Oral Presentations

1. J.C. Chekotu, D. Brabazon, "**A Review of Nitinol Shape Memory Alloy Processed by Selective Laser Melting**," 22nd International Conference on Material Forming (ESAFORM 2019), May 2019, Vitoria-Gasteiz, Spain.

2. J.C. Chekotu, D. Brabazon, "**Metal AM for Processing Nitinol**," Additive Manufacturing Course Package, School of Mechanical & Manufacturing Engineering, Dublin City University, Nov 2019, Ireland.

3. J.C. Chekotu, B. Naab, A. Nyabadza, N. Sargiotti, G. Manning, "**Effect of Heat Treatment on Performance of NiTi Rods in Heat Pump Applications**," Industrial Training Project, Advanced Metallic Systems Centre for Doctoral Training, February 2020, Sheffield, UK.

4. J.C. Chekotu, D. Brabazon, "**Multiscale FEA of the Functional Properties of NiTi SMAs**," Mini Research Project Symposium, Advanced Metallic Systems Centre for Doctoral Training, May 2020, Virtual Event.

5. J.C. Chekotu, D. Brabazon, "**In Silico Finite Element Approach on Mechanical Behavior in Superelastic Nitinol**," 25th International Conference on Material Forming (ESAFORM 2022), April 2022, Braga, Portugal.

6. J.C. Chekotu, D. Brabazon, "**Control of Mechanical Properties and Functional Characteristics of NiTi via L-PBF Processing**," 152nd Annual Meeting and Exhibition (TMS 2023), March 2023, San Diego, California, USA.

List of Poster Presentations

R. Groarke, J.C. Chekotu, M.A. Obeidi, A. Mussatto, K. O'Toole, D. Brabazon, "**Additive Manufacturing of Nitinol Heat Exchanger**," I-Form Industry Partner Event, University College Dublin, Dublin, Ireland, December 2019.

J.C. Chekotu, R. Goodall, D. Kinahan, D. Brabazon, "**Multiscale Finite Element Analysis of Mechanical Behaviour of NiTi Shape Memory Alloys,**" International Student Conference in Metallic Materials (Virtual Event), University of Sheffield, UK, July 2020.

J.C. Chekotu, R. Goodall, D. Kinahan, D. Brabazon, "**Study of Variation of Mechanical Properties of NiTi SMAs via Finite Element Analysis**," I-Form Gathering (Virtual Event), Ireland, November 2020.

J.C. Chekotu, "**Development of Laser Powder Bed Fusion (L-PBF) Technique to Process Nitinol (NiTi) with Shape Memory Properties**," Faculty Research Day, Dublin City University, Ireland, April 2022.

Abstract

Josiah Cherian Chekotu

Development of Laser Powder Bed Fusion Technique to Process NiTi with Retained Shape Memory Capabilities

Nitinol (NiTi) alloys have a lot of potential applications in the medical, aerospace, and energy sectors, due to their superelasticity and shape memory effect (SME), low stiffness, good biocompatibility, and high corrosion resistance. However, their poor machinability has limited the ability to process NiTi, especially into complex shapes. Recently, the Laser Powder Bed Fusion (L-PBF) technique has been found effective to process complex shapes in metallic systems as well as providing a high degree of sustainability. The phase transformations which enable functional properties in NiTi are highly sensitive to the L-PBF processing conditions.

This thesis explores the functional and material behaviour of NiTi in the specific design space of L-PBF process parameters in the as-fabricated condition; and develop an understanding how the L-PBF process can be altered to attain tailored properties. Porosity is a common phenomenon and a major defect entity in L-PBF processed parts. A finite element model was used to correlate the macroscale effect of porosity and microscale effect of martensitic phase evolution with structural stiffness, dissipated energies, and damping properties. Experimental investigations were also performed following a systematic variation of L-PBF process parameters using different build orientations. The effect of these factors on porosity levels, phase transformations, transition enthalpies and thermal expansion characteristics were characterised and reported. The microhardness, impact and mechanical strength, and strain recovery of the L-PBF processed NiTi were investigated and presented alongside a full-field strain analysis. The detwinning mechanisms and local strain field effects were explored at submicron levels, which was then correlated with the SME capabilities of L-PBF samples. Several microstructural characterisation techniques were utilised to identify and elucidate the reported findings and present how the L-PBF parameters and build orientations control the SME of NiTi.

Chapter 1

Introduction

1.1 Background and Motivation

Shape memory is a unique property of certain metallic and polymeric materials by which they can recover their primary shape (programmed shape) after deformation (under temperature or stress conditions) when a thermal or mechanical force is applied. Nitinol (nickel-titanium alloy) or NiTi is the one of the most utilized intermetallic shape memory alloy (SMA) with other common alloys being CuZnAl and CuAlNi. Unlike other shape memory materials, NiTi has high ductility and mechanical strength, low stiffness, good corrosion resistance, and wear resistance. The inherent functional properties of NiTi are utilized in engineering applications such as smart structures, sensors/actuators, energy recovery systems, biomedical, and aerospace components [1–11]. In addition to these properties, NiTi is highly resistant to pulsatile flow fatigue caused by body kinematics. It also possesses low thrombogenicity and high biocompatibility, making it ideal to be used for medical applications as stents and implants. The material has low anisotropy and small grain size compared to other alloys [12–15]. The functional properties of NiTi are based on reversible solid-state diffusionless phase transformations. These include shape memory effect, pseudoplasticity (thermal behaviour), and pseudoelasticity (mechanical behaviour). Most applications of NiTi in the medical field rely on the superelastic property, whereas the shape memory effect is used in actuators and heat engine applications. These behaviours primarily depend on the transformation temperatures, which vary with the percentage composition of Ni and Ti. A higher content of Ti elevates the transformation temperatures resulting in shape memory effect, whereas a higher Ni content lowers the transformation temperatures, and the material exhibits superelastic properties [16,17].

NiTi alloys are difficult to fabricate and process because of the high spontaneity of titanium, and very low machinability. Conventional processing methods, including casting and powder metallurgy, pose several challenges in the processing of NiTi. These challenges can be summarized as follows [13,17–19].

- Achieving a uniform and homogeneous composition

- Producing complex geometries

- Low machinability (high elastic and abrasive nature of NiTi)

- Purchasing of high quality NiTi powders (free of oxides and inclusions)

- Provision of inert atmosphere (to avoid oxidation)

- Avoiding impurities (affects transformation temperatures and structural integrity at micro and macroscales)

- Avoiding flaws and undesired porosity (reduces load bearing capacity, initiates crack nucleation)

To tackle these challenges, the additive manufacturing (AM) technique innovated for metallic systems, was found to be effective in creating highly complex NiTi geometries. AM parameters can be used to control the material composition and properties of NiTi system. Compared to the conventional manufacturing techniques, AM provides integration of multi-component assembly into a single part, lightweight manufacturing, pre-designed porosity, processing of high temperature materials, and minimum material wastage. The process can achieve structures with high density and near net shape, requiring very little or no post-processing. Laser-based AM techniques are progressively being applied to produce NiTi parts (bulk and porous structures) [13]. For instance, processing NiTi for bone implants is much easier through AM techniques compared to the difficulty of machining such components with conventional processing methods. AM process parameters can be adjusted to create comparable properties to those of conventionally processed NiTi, including surface morphology and shape memory characteristics [20].

Among the various additive manufacturing techniques, Direct Energy Deposition (DED) and Laser Powder Bed Fusion (L-PBF) are the most utilized techniques [21]. In L-PBF process (also known as Selective Laser Melting, SLM), a computer aided design (CAD) model fully describing the build geometry along with the required design for additive manufacturing (DfAM) supports and struts, is input into the computer module initially. Then the 3D CAD model is sliced virtually to a layer-by-layer 2D format. Then the machine is setup with required build and process parameters. The printing process starts with spreading a thin layer (thickness < 100 µm) of NiTi powder on a substrate as illustrated in Figure 1.1. A high-power computer-controlled laser beam is then used to scan the powder bed following the model. The powder particles melt by absorbing the

energy from the laser beam, and solidify to form a cross-sectional layer of the input model slice. This cycle is repeated layer-by-layer with the help of a spreader/recoater blade and adjustable build platform, until the complete part is built [22].
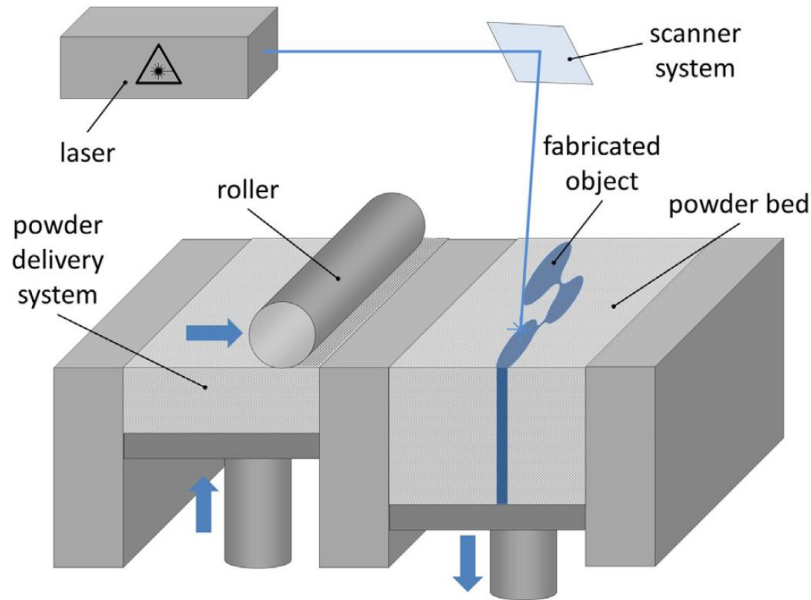
Figure 1.1 Schematic illustration of L-PBF processing [23].

In DED (also known as Laser Engineered Net Shape, LENS), a solid-state laser beam is focused on the building platform and used to melt the coaxially sprayed metal powder which solidifies in place [24], illustrated in Figure 1.2. Compared to conventional methods, both of these techniques have the potential to provide more gradual phase transformations in produced parts. Both DED and L-PBF can fabricate NiTi with complete shape memory recovery for about 6 % microscale and 3 % macroscale strains. The strains are stabilized at 4 % and 2 %, respectively after cycling [25,26]. However, the L-PBF process exhibits better processing of NiTi over the DED method [25,26]. A brief comparison between both methods is tabulated in Table 1.1.

The Laser Powder Bed Fusion (L-PBF) technique has been found effective in processing metallic alloys such as Ti64, stainless steels and Ni-base super alloys for specific applications [28–32]. However, L-PBF of NiTi is still in the early stages of development, due to the challenges faced in achieving a suitable microstructure for tailored phase transformations [33–37]. Over the past decade, the research work in this area has generally increased, but is still very sparse compared to other metallic systems.
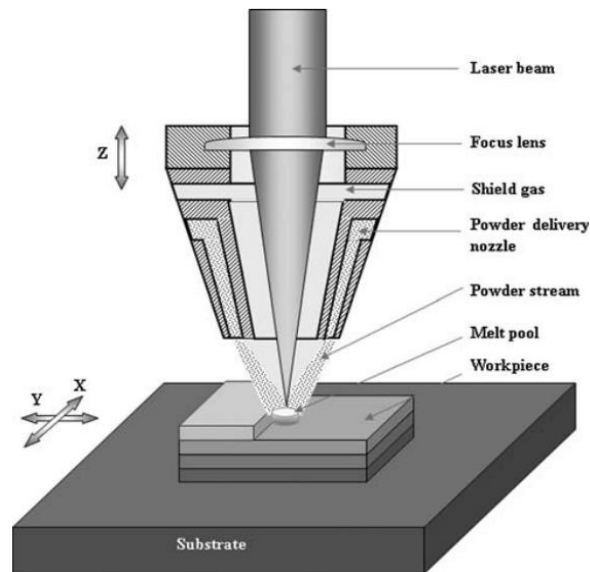
Figure 1.2 Schematic illustration of L-DED processing [27].

Table 1.1 Comparison between L-PBF and DED processing of NiTi.

L-PBF	DED
• Fabricates homogenous composition equivalent to the composition of the feedstock [25,26].	• Composition varies spatially and may differ from the powder feedstock composition [25].
• Exhibits high aspect columnar grains extending over multiple layers, due to orientation in the build direction (along largest thermal gradient) [26].	• Equiaxial grains are created with dimensions corresponding to the layer thickness (has smaller minor axis) [25].
• Strain accumulation is more uniform, as material microstructure is more homogeneous [26].	• Due to heterogeneity, strain accumulation varies. The stress-strain curve exhibits a strain-hardening like response once the critical stress was crossed [25].
• The stress-strain curve shows a plateau as per the response when critical stress is exceeded [26].	

5

For engineering applications such as in zero emission heat engines and heat pumps (refrigeration) with NiTi as the core, the material is required to operate in an environment of 70 °C to 100 °C. The cooling cycle during the operation will be between room temperature and freezing point of the working fluid (such as water). To meet this operational window, the NiTi structures need to have the correct phase transitions and microstructural properties, which can be controlled by controlling the L-PBF processing parameters. Therefore, a comprehensive investigation in this area can benefit the NiTi-based renewable energy applications and understanding of L-PBF design space for NiTi.

1.2 Thesis Aims and Objectives

The aim of this thesis was to explore the functional and material behaviour of as-fabricated NiTi in a specific L-PBF design space, attaining tailored properties while building in different build orientations. This aim was achieved through the following objectives:

1. Investigate the macroscale effect of porosity and microscale effect of martensitic phase evolution on structural and energy dissipation properties of NiTi.
2. Assess the influence of L-PBF process parameters on structural porosities, chemical composition, phase change temperatures, transition enthalpies, and thermal expansion characteristics of L-PBF processed NiTi.
3. Assess the mechanical responses and shape memory capabilities of L-PBF processed NiTi, along with microstructural effects of local strain fields at a submicron scale.
4. Investigation of microstructural features directly influencing SME capabilities of L-PBF processed NiTi.

1.3 Thesis Format and Outline

This thesis is presented as a collection of published research papers and submitted manuscripts with original contributions. The contribution of the candidate in the publications are as following:

Chapter	Publication Title	Status	Candidate contribution
2	Influence of Structural Porosity and Martensite Evolution on Mechanical Characteristics of Nitinol via In-Silico Finite Element Approach	Published, Materials, 2022	First author, corresponding author, project administration, conceptualisation, methodology, software, validation, formal analysis, data curation, writing - original draft, writing - review & editing
3	Control of NiTi Phase Structure, Solid-State Transformation Temperatures and Enthalpies via Control of L-PBF Process Parameters	Published, Materials & Design, 2022	First author, corresponding author, project administration, conceptualisation, methodology, validation, formal analysis, data curation, writing - original draft, writing - review & editing
4	Control of Mechanical Characteristics and Shape Memory Functionality in Martensitic NiTi via L-PBF Parameters and Build Orientation	Published, Journal of Materials Research & Technology, 2023	First author, corresponding author, project administration, conceptualisation, methodology, validation, formal analysis, data curation, writing - original draft, writing - review & editing
5	Formation of β-Ti Phase during L-PBF Processing of Martensitic NiTi	Published, Materials Today Communications, 2023	First author, corresponding author, project administration, conceptualisation, methodology, validation, formal analysis, data curation, writing - original draft, writing - review & editing

This thesis is comprised of six chapters, and has been arranged in a progressive manner. An infographic illustrating the thesis structure is presented in Figure 1.3.
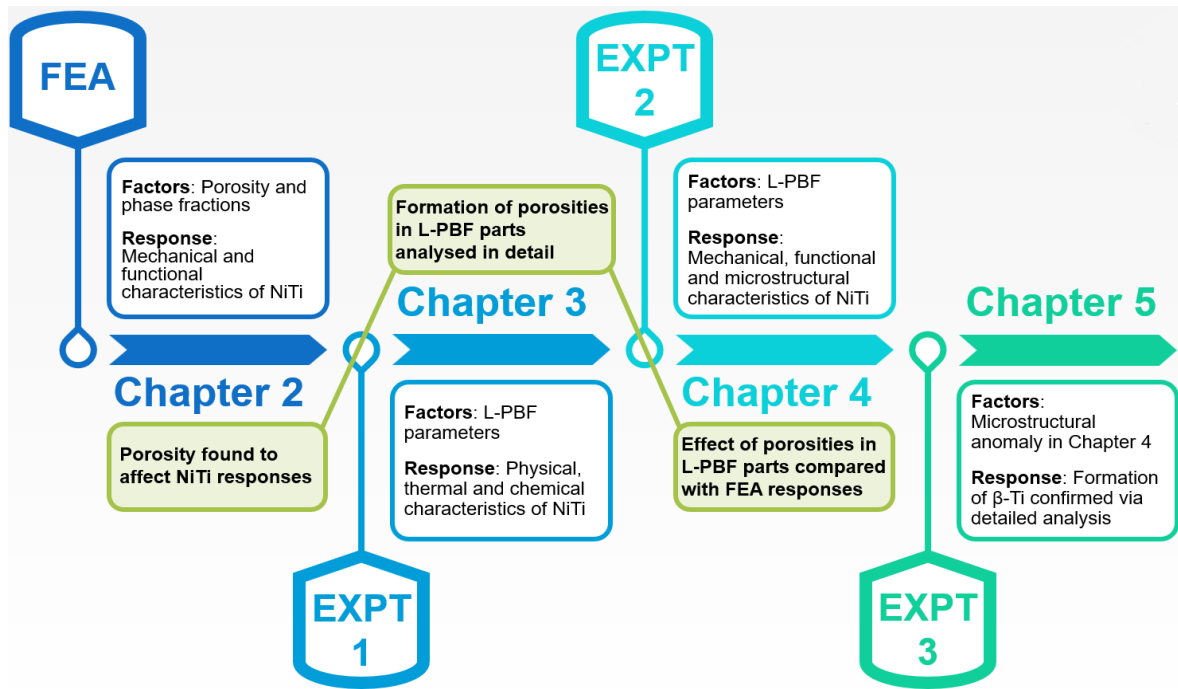
Figure 1.3 Infographic showing the connection between original works presented in the thesis; one finite element analysis (FEA) based study followed by three sets of experiments.

The following is a brief description of work performed and/or contents included in each chapter:

Chapter 1: This chapter introduces the thesis aims and objectives including the thesis structure, and explores several important subjects in relation to NiTi and L-PBF processing. It ends with summarising the state of the art and existing knowledge gaps.

Chapter 2: This chapter compiles a multiscale in-silico finite element (FE) model to simulate the mechanical behaviour of austenitic NiTi. The associated mechanical stress–strain curves indicate the amount of energy transfer during the phase transformations. Porosity being one of the major defects in L-PBF processed parts, the FE model was used to correlate the macroscale effect of porosity on mechanical responses. Stiffness is an important mechanical property influencing the structural integrity and maximum operational strain levels in heat pump applications. These can be classified as the structural stiffness and the material stiffness (Young's modulus). The structural stiffness is studied in the macroscale analysis, whereas a microscale analysis is performed to comprehend the material stiffness variation with respect to the phase volume fractions in the microstructure. In the case of shock absorption applications, the damping/self-

centring properties of the porous structures were analysed in terms of damping ratio and apparent stiffness calculated from the macroscale mechanical responses.

Chapter 3: In this chapter, NiTi fabricated using systematic variation of L-PBF parameters in two different build orientations, were analysed for relative density levels, transformation temperatures, compositional changes, phases present, and thermal expansion properties. The primary objective was to investigate significant correlations of selected laser parameters with the chemical, thermal and physical properties of the L-PBF processed NiTi. The porosity formations in the L-PBF processed samples were measured and studied, and their effect was further investigated in following chapters.

Chapter 4: This chapter investigates in detail how L-PBF processing controls the shape memory capabilities of martensitic NiTi SMAs. The effect of porosity on mechanical and functional properties were also analysed in the chapter, and compared with the FEA study in Chapter 2. The study presents a comprehensive response analysis (including correlations) of mechanical and functional properties for a specific L-PBF design space. The work also reports the effect of build orientations on these responses for similar process parameters, and how significant they are to control the intrinsic SME property of as-fabricated L-PBF NiTi. The local strain fields obtained via full-field analysis during controlled uniaxial compression, and the effect of build orientations on irrecoverability during SME recovery were also presented in detail. Further significant novelty lies in analysing the microstructural variations that occurred during SME functionality, specifically the detwinning mechanisms via submicron topology analysis. A significant number of correlations and results are presented both quantitatively and qualitatively, to provide insight into the design space, and to fill these knowledge gaps for building effective NiTi SMAs using L-PBF.

Chapter 5: In this chapter, a detailed investigation of tiny, hard protruding particles formed during L-PBF processing of horizontally printed samples were presented. These randomly distributed particles were found to directly affect the SME capabilities of L-PBF NiTi. To date, there have been several reports of Ti_2Ni precipitate formations in martensitic NiTi during L-PBF processing. However, the formation of hard $\beta - Ti$ phase protrusions, found and investigated in this study, has not previously been reported and was found to present novelty in terms of the resulting shape memory response as well as the phase structure resulting from the L-PBF processing of NiTi.

Chapter 6: This chapter summarises the significant findings of original research performed, and suggests future research directions in this area.

The following sections portray the NiTi system, and the advancements in the L-PBF processing of NiTi. The state-of-the-art is explored through various factors including process parameters, powder characteristics, and heat treatment conditions, and their effects on the microstructures, mechanical characteristics, and phase transformation properties of L-PBF processed NiTi samples. A later section also describes the various difficulties associated with producing retained shape memory properties, and several defects commonly observed in L-PBF fabricated components along with their causes.

1.4 Nitinol SMAs

1.4.1 Crystal Structures and Phases

There are three different functioning phases in NiTi. Martensite phase is a low temperature and low stress/stress-free phase which possess a low symmetry monoclinic structure (B19'), where B19 denotes an orthorhombic crystal and prime (') indicates an additional distortion from a shear strain. This phase is generally of a complex-twinned structure (Figure 1.4a), characterized by needle-like or hay-like crystals arrayed in a herringbone manner.

| (**a**) | (**b**) |

Figure 1.4 Crystal structure phases of NiTi showing (**a**) B19′ martensite, and (**b**) B2 austenite [17].

Austenite phase is a high temperature and high symmetry phase based on an ordered B2 body centred cubic crystal lattice structure (Figure 1.4b). The austenite phase is hard and stiff, while that of martensite is softer, more ductile, and has a lower yield stress. Thus, the shape recovery is associated with high actuation stresses resulting from a large change

in stiffness as NiTi transforms from a lower stiffness daughter phase (martensite) to a higher stiffness parent phase (austenite) [13,33,35,38,39].

At times, in some grades of NiTi, an intermediate phase called R-phase can show up due to a rhombohedral distortion of the B2 cubic structure [40]. This rhombohedral structure exhibits low transformation strain, and low temperature hysteresis (1 – 10 °C) [41,42]. The R-phase formation can be linked to any previous cold working or aging of Ni-rich alloys or may be due to alloying with an additional element like iron [17].

1.4.2 Functional Properties and Mechanical Characteristics

The phase transformations in NiTi are diffusionless shear (solid-state) transformations, which means the transition occurs through a coordinated motion of many atoms relative to their neighbours. A new crystal structure is formed from parent phase without any change in the composition [43].

The shape memory effect (SME) in NiTi is highly dependent on the composition of Ni and Ti. A higher Ti content elevates the phase transformation temperatures (TT), and vice versa. If the TTs are below room temperature, the material will be superelastic at room temperature. This type of NiTi SMA is referred as austenitic NiTi, as they have a fully austenitic structure at ambient temperature. On the other hand, when TTs are higher than room temperature, the material behaves as a classic shape memory material, and they are referred to martensitic NiTi, as they possess a fully martensitic matrix under ambient conditions [16,44].

In austenitic NiTi, the transformation is stress-induced, whereas in martensitic NiTi, the transformation is thermally induced [12,35,44–48]. Under purely martensitic phase, mechanical deformation in NiTi starts by detwinning the martensite (B19') twins. It requires a low yield stress to produce considerable strains under this phenomenon. As the material is loaded, the matrix gradually turns into a completely detwinned structure. Once the detwinning is fully saturated, further loading will elastically deform the material until the yield limit of detwinned state, ultimately at a sufficiently high stress resulting in plastic crystallographic slip. As long as the strain is not due to plastic slip phenomenon, for maximum shape recovery ideally the strain can be fully recovered via thermal excitation. The associated observable strain incorporates selection and formation of

martensite variants, detwinning, and slip. The strain can therefore be classified into recoverable and irrecoverable strains [45,49-52].

At room temperature, the martensitic NiTi (i.e., with shape memory) will be in twinned martensite phase – see point A in Figure 1.5b. When a deformation is applied, the crystal structure changes to a detwinned state (B) by reorienting and detwinning the lattice structure. The twin boundaries in martensite shift such that they orient in one preferential direction to better accommodate the load, referred to as "detwinning". This microstructural process enables NiTi to withstand high strain without any permanent deformations [41]. When this detwinned martensite (C) is heated to exceed the austenite start temperature (*As*), austenite begins to form (D), and once the temperature crosses the austenite finish temperature (*Af*), the austenite formation will be complete. This transformation from martensite into austenite, recovers the original programmed shape, and is also referred to as the "thermal memory effect" [13]. Figure 1.6 shows the typical strain-temperature and stress-strain curve of martensitic NiTi.

As mentioned earlier, for some grades of NiTi, the intermediate phase called the R-phase may form due to the presence of some precipitates. As the cubic austenite phase is cooled, one of the lattice diagonals elongates resulting at a reduced angle ($< 90°$). Hence, the name R-phase due to the rhombohedral structure it forms. If the material is cooled below the critical R-phase temperature (*Rs*), R-phase crystals may form. The resulting microstructure will contain both austenite and R-phase, and is referred as the pre-martensite phase [55]. When the material is further cooled down to the martensite start temperature (*Ms*), a martensite phase starts to form. The austenite (low strain phase) to martensite (high strain phase) transformation will be completed once it cools down below the martensite finish temperature (*Mf*). Conversely, when the austenite phase is sufficiently stressed, it changes to martensite. The Clausius–Clapeyron stress-temperature relationship for NiTi describes the activation process under stress of the forward transformation from austenite to martensite ($A \rightarrow M$), as well as the reverse transformation (martensite to austenite; $M \rightarrow A$). This relationship indicates that the activation temperatures (*Ms, Mf, As* and *Af*) increase linearly per unit stress [56–59]. At higher temperatures, martensite is unstable, and therefore, returns to the austenite phase on unloading. This large elastic response of reversing the deformation to original shape is called superelasticity.
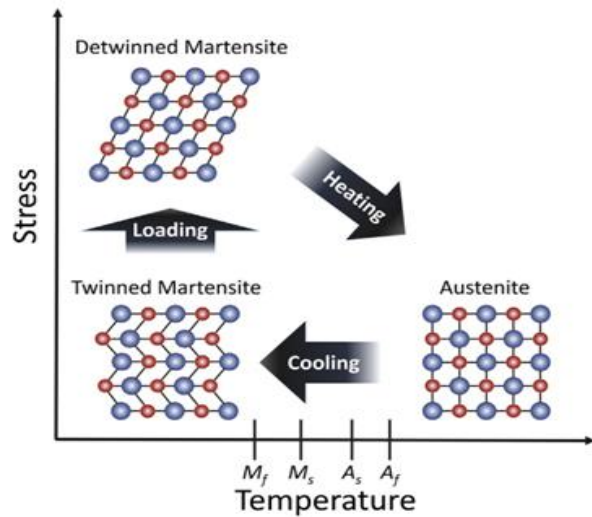
(**a**)
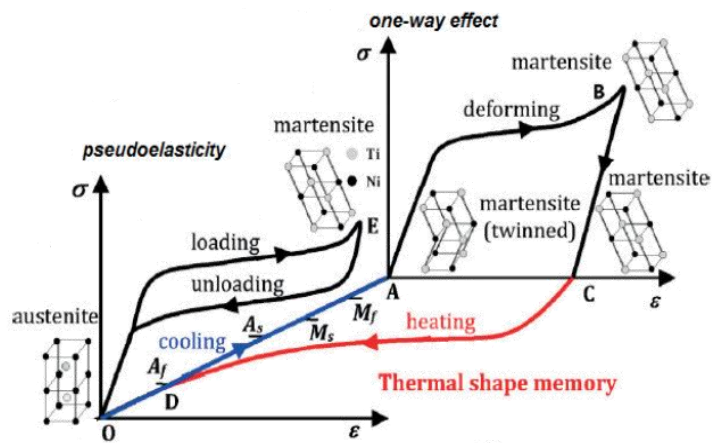
(**b**)

Figure 1.5 (a) Representation of phase transformation in shape memory NiTi [53], and **(b)** Stress-Strain-Temperature graph showing phase transformation in NiTi [54].
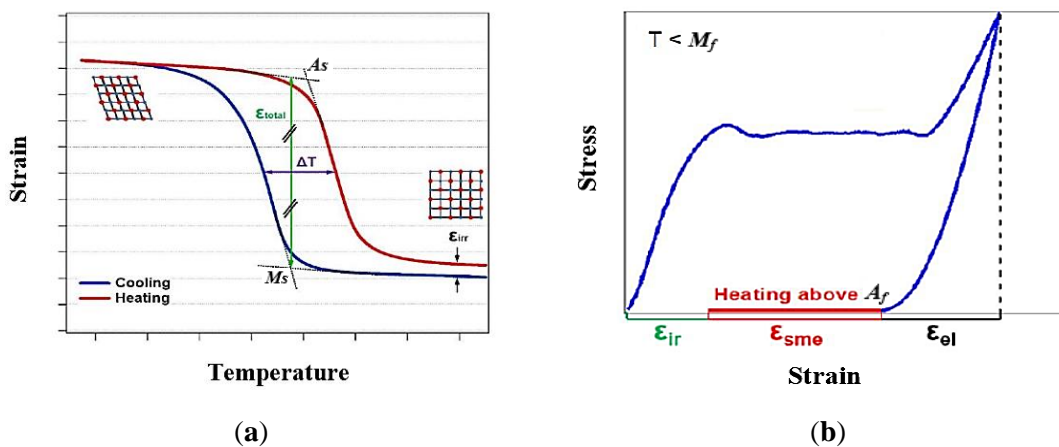
(**a**)   (**b**)

Figure 1.6 Repeatable cycling of NiTi are shown as **(a)** the thermal (strain-temperature) and **(b)** stress-strain cycles [17].

13

Superelasticity refers to the ability of the material to recover its original shape even after large deformations of 10 – 15 % strain [47,53]. At room temperature or operational temperature, a superelastic NiTi will be in austenite phase (*Af* below room temperature) as shown in Figure 1.5b. When stress is applied beyond the start of martensitic phase transformation, distortion of the crystal lattice occurs. This is associated with low hardening, and the lattice transforms completely into martensite. The crystalline phase of detwinned martensite occurs at lower temperatures and higher stresses, whereas the crystallization of austenite occurs at higher temperatures and lower stresses [57]. As seen in Figures 1.5b and 1.7, when the material is deformed at constant (room) temperature, initially it follows Hooke's law with the stiffness as that of the austenite phase. As the strain increases, a solid-state diffusionless phase transformation from austenite to martensite will occur, gradually forming a fully stress-induced martensite phase. When the strain is further increased, Hooke's law is again followed with the stiffness of the martensite phase. After reaching the maximum elastic strain limit, detwinning/yielding occurs creating a residual strain. If the material is unloaded within the elastic strain limit, martensite phase reverts to austenite. Both forward and reverse transformations are associated with latent heat release and absorption, respectively. Full-field measurement methods, such as Infra-Red Thermography (IRT) and Digital Image Correlation (DIC), can provide quantitative information about the temperature and strain, respectively, at each point on the surface [58,60].
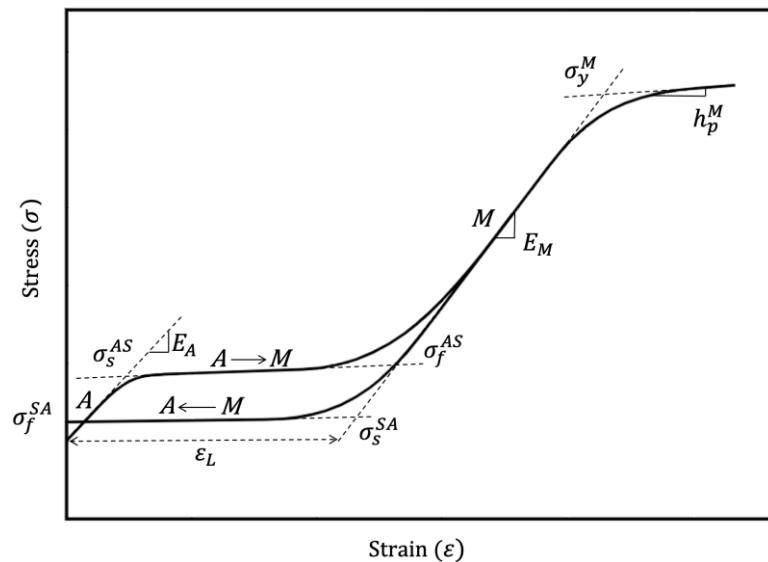
Figure 1.7 Schematic illustration showing the nomenclature used during phase transformations and mechanical loading. E_A—Young's modulus of austenite (*A*) phase; E_M—Young's modulus of martensite (*M*) phase; ε_L—maximum longitudinal strain; σ_s^{AS}—

stress to start martensitic transformation (austenite to single-variant martensite); σ_f^{AS}—stress at finish of martensitic transformation; σ_s^{SA}—stress to start reverse transformation (single-variant martensite to austenite); σ_f^{SA}—stress at finish of reverse transformation; σ_y^{M}—martensite yield stress; h_p^{M}—martensite hardening parameter [45].

The superelastic property is also accompanied with good damping curves, low stiffness, good corrosion resistance and good biocompatibility (TiO_2 prevents Ni leaching into the human body), enables NiTi to be used in stents, implants, spinal fusion cage, bone plates/screws and other medical applications [61–66]. During phase transformations, latent heat is absorbed or released during the shape deformation or recovery. The solid-state phase transformations between martensite and austenite involve absorption/release of latent heat in a significant quantity [14,67,68]. This high latent heat capacity of NiTi SMAs has been found to have good potential in energy harvesting through heat transfers. These applications will benefit from complex structures as the surface area is maximized for maximum energy absorption/release.

Compared to the tension mode, the deformation mechanism in the compression mode tends to create denser dislocations in both the martensite twins and the junction planes. Detwinning during compression is much sparser compared to that during tension [69]. This results in dramatic variations while transforming via detwinning; often articulated as plastic irrecoverable strains during compression. Recoverable strain generally increases with a rise in maximum applied strain, until the deformation crosses the yield limit. A significant amount of irrecoverable strain can indicate a large amount of actuating force taken up by the material. These variations are also associated with higher stress levels, compared to the same extent of strain in tension mode. Thus, plastic deformation cannot be ignored in compression of martensitic NiTi as it is necessary to determine the recoverable strain limits. It is also noted that the elastic modulus measured during compression is higher than in tension [70].

1.4.3 Kinematics of Phase Transformations

The mechanical response of NiTi can be divided into three regimes: elastic regime, phase transformation regime, and plastic regime. In the elastic regime, the deformation causes local atomic arrangements to be continuously varied (reversible), proportional to the change in applied stress, whereas the twinning and martensitic transformation can be considered as discontinuous and diffusionless reversible changes of local arrangement of

atoms propagating through the crystal as twin plane interfaces and habit planes when stress/temperature is varied. Habit planes are well-defined interfaces or contact plane between the martensite and austenite phases—these do not experience any distortion. Here, the discontinuous finite strains formed are fully recoverable under thermomechanical loads [71,72].

Plastic deformation proceeds either as movement of slip dislocations, or irreversible twinning. The material is permanently deformed without inducing any change to the crystal lattice. It must be noted that, slip dislocations and twinning occurs locally at moving lattice defects such as habit plane interfaces and twin interfaces [71]. Due to the requirement for compatibility of large finite strains of martensitic variants created by the transformation or twinning, plastic strains, irrecoverable lattice defects, and internal stresses can be introduced into the NiTi microstructure, specifically at elevated temperatures. Plasticity after forward martensitic transformation stabilises the martensite phase and hinders the reverse transformation [71,73].

It is often difficult to determine whether the martensitic transformation and plastic deformation propagate independently, or mutually coupled. The main concern is whether the strain compatibility is attainable only by transformation strains, and/or the plastic deformation plays a role in it. If this is the case, then the martensitic transformation and plasticity can be coupled intrinsically. In order to achieve compatibility during reverse phase transformation, martensite twinning and plastic slip in austenite often mechanise combined. The residual plastic strain in austenite supresses the twinning and the slip is facilitated. Consequently, depending on the residual strain levels, a stronger contribution of the plastic slip is expected to accommodate strain compatibility at the interfaces [71].

A more thorough understanding of martensitic transformation can be based on changes that happen in the crystal unit cell. During phase transformation, atoms are moved to their new locations (shuffling). Simultaneously, space is created to accommodate the resulting structure. Time dependency can be ignored since the transformation is diffusionless. The resulting structural change stretches the unit cell in certain directions while others are shortened. These directions do not lie on a cell edge; instead, they are irrational directions, resulting in different tension and compression levels [16]. If the transformation has no preferred direction, then the martensite opts for any of the different habit planes that exist and forms a series of crystallographically equivalent variants. This results in multiple-

variant martensite characterized by a twinned structure. In contrast, if there is a preferred direction, then all of the martensite crystals tend to opt for the most favourable habit plane. The product phase will then be called single-variant martensite, characterized by a detwinned structure. In addition to this, there is a possibility of conversion of each single-variant martensite into other different single-variants. This reorientation process is generally linked to non-proportional stress changes [72].

Since the austenite has a well-ordered BCC structure, only one variant will be present, while the martensite can form even 24 variants depending on the transformation history [74]. The martensite generally forms imaginary plates called correspondence variant pair (CVP) that denotes growth of two twin-related variants. The nucleation of each CVP begins with a shear stress in a direction parallel to the most favourable habit plane of each crystal. The 12 CVPs (24 variants) produce 12 distinct distortional strains, self-accommodating to the size and shape of its austenite parent phase cell [16,75]. Figure 1.8 shows the two distinct yield regions in a stress–strain curve of NiTi. The first yield region indicates the selection of preferred martensitic variants during phase transition, and the second yield region occurs after the detwinning event, which results in conventional slip causing plastic deformation.
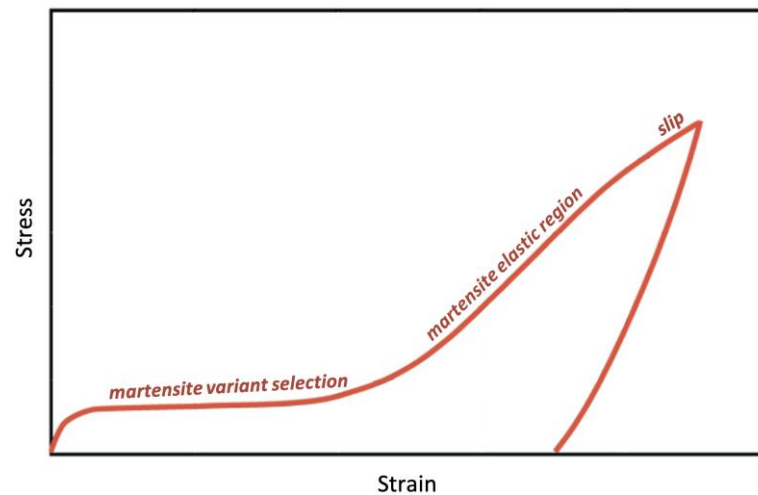
Figure 1.8 Stress–strain curve illustrating the various yield regions.

It is also commonly found that stresses to initiate the phase transformation decrease as the number of cycles are increased. This is due to the internal stresses related to plastic deformation during cycling that favour martensite formation [73]. Additionally, it is seen that if the stress direction is changed, martensite reorientation occurs, resulting in a slight change in load. Transformation usually results in a volume increase; hence, less stress is

required to produce the transformation in tension than in compression. This may cause asymmetry in stress–strain curves generated during tension and compression [76,77].

Numerical methods, including finite element analysis (FEA) methods, allow the analysis of complex problems, comprising intricate geometries, interactions, nonlinearities, and dynamic conditions. FEA models help the study of have been used to study the response of NiTi components, such as when printing stents and actuator springs [78]. Several works have been conducted to evaluate the post-implantation structural and functional response [79–81], and degradation and fatigue-related changes [82–84].

Mathematical models have provided a considerable insight into the complex mechanical behaviour of NiTi. Most of the models in the literature have not been able to simulate the following prevalent NiTi phenomena: cyclic instability of superelasticity; actuation instability; shape setting; two-way SME; and functional thermomechanical fatigue [71, 85]. Several constitutive models have been created over the years to capture this complex behaviour, following either of the two approaches – micromechanical (microscale) or phenomenological (macroscale).

1.4.4 Role of Martensite Volume Fraction

Stress-induced martensitic transformation involves a gradual change in elasticity. A theoretical study of this was conducted on single crystal NiTi by Sittner et al [86], and found that tension/compression leads to an increase/decrease of Young's modulus depending on the axis orientation of load applied and the crystal. This is due to the martensite variant selection mentioned earlier. It was found that the change in stiffness occurred for {111} grains, as this coincides with the texturing while the wires were manufactured by extrusion or wire drawing. The complex problem in studying the change in stiffness is homogenising the elastic properties and then estimate an effective elasticity of mixture of austenite and martensite phases (variants) in transforming NiTi. Common rule-of-mixtures approaches are Voigt (Equation 1.1) and Reuss average (Equation 1.2) [71,87,88]. These rules can be implemented in FEA code for estimating the change in Young's modulus as the phase transforms from austenite to martensite; marks the upper and lower bounds to the actual strength property.

$$E_{eff} = V_m E_M + (1 - V_m)E_A \qquad (1.1)$$

$$E_{eff} = \left\{ \frac{V_m}{E_M} + \frac{(1 - V_m)}{E_A} \right\}^{-1} \tag{1.2}$$

A phase transformation flow rule was proposed by Auricchio *et al.* [72] involving the martensite volume fraction, $\dot{f}(x, t)$:

$$\dot{f}(x, t) = \frac{\partial f}{\partial t} = V_t(f_t(x, t) - f(x, t)) \tag{1.3}$$

where, $f_t(x, t)$ is the driving force for phase transformation and V_t is the maximum transformation rate. This first order differential equation (Equation 1.3) includes a delay between the driving force and the evolution of martensitic ratio $f(x, t)$. This simple flow rule considers only the two phases and therefore, the complexity of real phase transformation is not fully reproduced.

The initiation and propagation of stress-induced phase transformations was visualised by [89] using a phase shifted Moiré interferometry. The material was tensile loaded, and fringe patterns were observed. The initiation and propagation occurred from the top and bottom sections of the specimen, and progressed towards the centre. The martensite phase can be distinguished by the high fringe density (Figure 1.9).
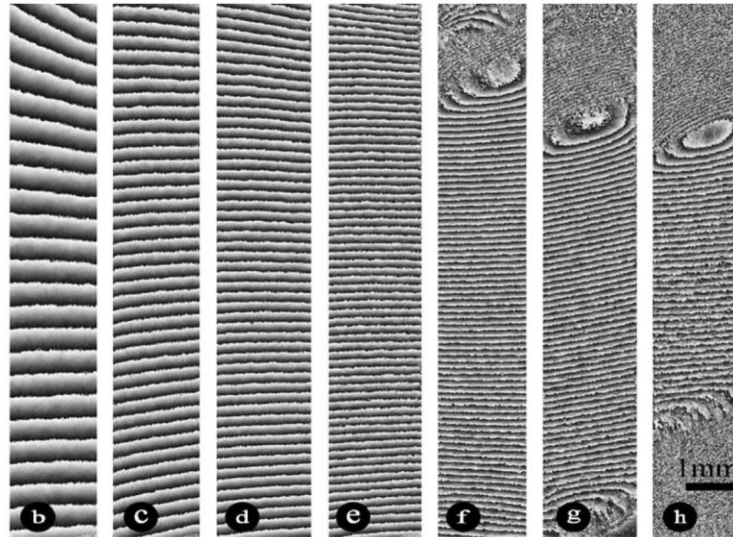
Figure 1.9 Phase shifted Moiré interferometry showing changes in fringe characteristics as stress-induced phase transformation (b to h) occurs during a tensile loading [89].

The initial transformation is partially triggered by the surface energy to create an interface, and partially via the elastic energy of the accommodation of martensite in the

19

austenite matrix. This causes a reduction in free energy and therefore, the nucleation of martensite phase usually requires a higher driving force than that of the subsequent propagation of austenite-martensite interface. The size and shape of martensite nucleus is governed by this free energy reduction [90,91].

An in-depth study [92] found that the energy for martensitic transformation in nanocrystalline NiTi significantly increased when the grain size was reduced, and this caused a reduction in the martensite volume (for same energy levels). In both FEA and experimental study, it was found that the martensitic transformation is totally suppressed when the grain size went below a critical value (50 – 80 nm).

Cyclic loading of NiTi often involves hysteresis, which is a result of the complex interactions between material grains and competing energies between grains and phases. This can degrade stiffness when the material is loaded cyclically. Strength degradation is noted when a reduction in response is observed when the same displacement level is applied. However, permanent strain addition can also happen if any residual martensite exists after each cycle causing incomplete reverse transformation.
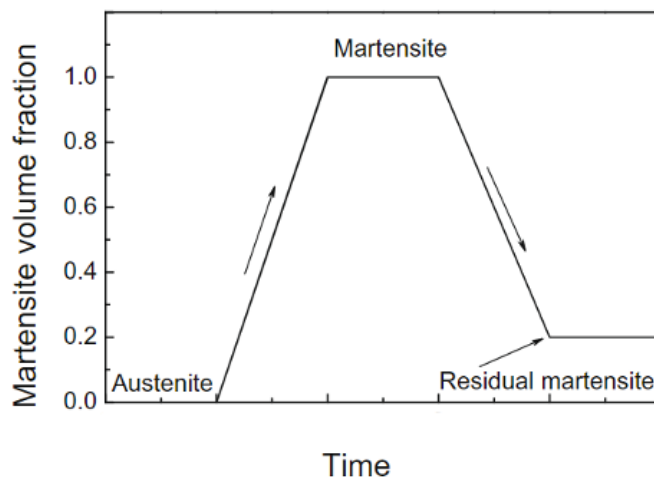
Figure 1.10 The evolution of martensite during mechanical loading and unloading in the first cycle [93].

A schematic representation of the evolution of the martensite volume fraction (MVF) is shown in Figure 1.10. Residual martensite reduces the grain size rearranging the microstructure and hinders the motion of small grains. This ultimately results in a stronger NiTi material [93–95]. The martensite variant selection was also found to affect the mechanical property to a large extent. A study conducted on single crystal NiTi [86] found that tension/compression leads to an increase/decrease of Young's modulus depending

on the axis orientation of load applied and the crystal. This can be attributed to the type of variant selected under the applied force.

1.5 L-PBF Process Parameters

In the additive manufacturing of NiTi, processing parameters have the biggest influence on the final product. This product may require different levels of post-processing such as heat treatment, surface finishing, machining and texturing/painting [96], depending on the quality/design requirements. The various process parameters include laser related, scan related, powder related, and environment (temperature and oxygen concentration) related factors. In L-PBF, melt pool stability is highly critical for fabricating complex functional parts. Melt pool instability can cause micro-particle formations, irregular/discontinuous melt tracks, balling effect, humping and porosities. During the solidification cycle, residual thermal stresses can cause further damages in the form of distortions or delamination of final parts [97]. Optimization of the L-PBF process parameters is, therefore, of high importance to identify a suitable process window. A few of the laser process parameters are represented in Figure 1.11, and introduced below.
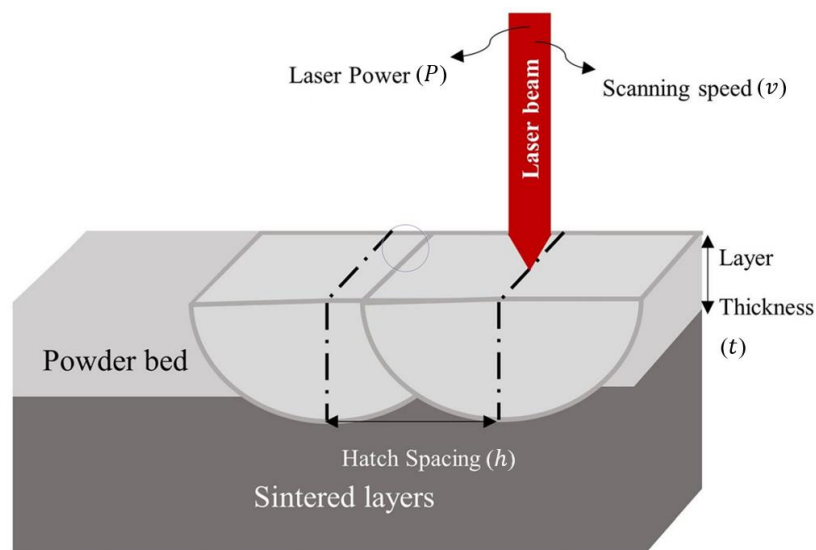
Figure 1.11 Schematic representation of L-PBF process parameters.

Hatch spacing (distance) defines the overlapping gap between two laser scan tracks. Increasing the hatch spacing reduces the overlapping region. The overlap indicates the area undergoing repeated melting. This overlap is necessary in L-PBF to ensure continuous metallurgical bonding. Insufficient overlap causes the formation of unmelted

powder particles between laser scan tracks. Excessive overlaps can cause heat sinks of laser energy and bulging above the powder plane, resulting is deteriorated surface quality and higher chances of porosities. From literature, it can be speculated that a 40 to 60 % overlap can be good, although this is very case-specific [98–101].

Scan speed determines the irradiation time per unit area on the powder bed. The melt pool depth will be higher when the scan speed is lower. This can also result in a wider scan track due to lower solidification rate in the melt pool. Faster solidification rates from higher scan speeds can result in higher thermal gradients, which can cause crack formations and layer delamination. Higher scan speeds can also result in partially melted particles and discontinuous melt pool, increasing the porosity. Better surface roughness and dimensional accuracies are usually achieved under lower scan speeds, however, this may cause spheroidisation phenomenon resulting in agglomeration of powder particles, leading to irregular melt pool cross-sections [102–106].

Layer thickness is another parameter which controls the weldability. This is usually constrained by the minimum feature size in model design and particle size distribution, and is selected differently for different builds. Typically, the layer thickness is chosen between 30 μm and 150 μm. The build rate can be easily made faster by using a higher layer thickness. However, it must be noted that higher laser energy density will be required to melt thicker layers of powders, and this can increase the chances of meltpool instabilities. Therefore, selecting the right levels of layer thickness is essential to determine the moving melt pool characteristics such as mass transfer and heat transfer. This can highly influence the densification levels, microstructural and mechanical properties of the final part [107–112].

1.5.1 Effect on Melt Pool

Laser irradiation causes the powder particles to heat up and melt, forming a melt pool above the previously melted and solidified material. The melt pool size and shape pose a high effect on the track formation quality; primarily controlled by the scanning speed and the laser power. The melt pool behaviour strongly influences the molten material current, surface tension, and heat transfer. Various physical phenomena in the melt pool can affect the formation of a precise structure along the scan direction, rendering detrimental final part properties [113–116].

The Marangoni effect influence the mass and heat transfer in the meltpool, thereby affecting the melt pool geometry. The melt pool becomes wide and shallow in the presence of Marangoni effect, and vice versa [117,118]. The type of melting mode chosen plays a dominant role in controlling the geometry of molten pools; this can be regulated by varying the laser power, scan speed, hatch spacing, and layer thickness. Figure 1.12 illustrates the thermal history in keyhole mode and conduction mode [119]. In keyhole mode, the final part will have reduced porosity and a better combination of ductility and mechanical strength. Whereas, in conduction mode, a wider processing window is availed, with good formability, few forming defects (spatter, porosity and crack) and high process stability. The two modes have their own pros and cons. Therefore, the preference of one over the other is highly dependent on the specific material type, and final part property requirements [118,120]. The following are a few significant melt pool phenomena affecting part properties.
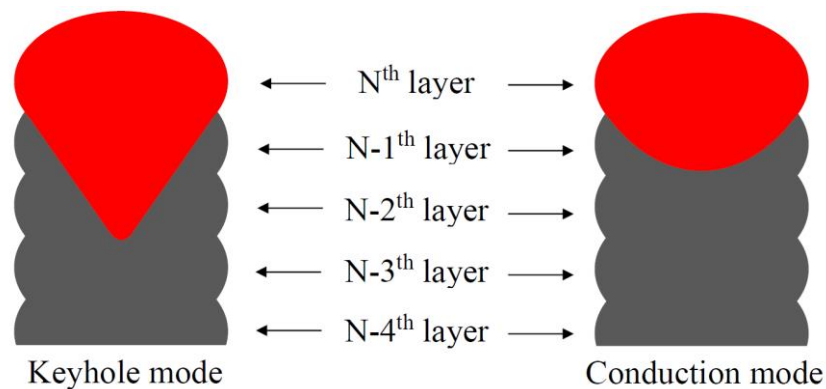
Figure 1.12 Schematic illustration of keyhole and conductive melt pool modes [121].

- *Vaporisation* – In L-PBF process, the laser irradiates high thermal energy into the exposed powder particles, thus forming a melt pool. Above the melt pool, a plasma plume is usually visible which consists of ionised gases and metallic particles as shown in Figure 1.13. When the melt pool temperature exceeds the boiling point of material, vaporisation occurs. This vaporisation creates an immense pressure that can result in a shock wave generating a recoil momentum on the molten particles. This favours nucleation of vapour cavities [122–124]. As a result, the molten material is ejected and causes abrupt changes in the melt pool [125]. These vapours can condense on the lens, causing adverse effects (attenuation or refraction) on the laser beam [126]. Therefore,

the material vaporisation must be avoided, or controlled using the right L-PBF processing conditions.
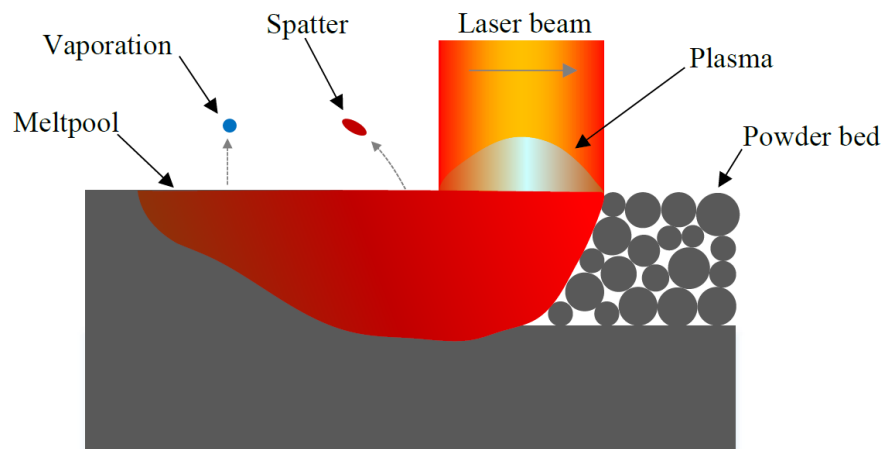
Figure 1.13 Schematic diagram of melt pool phenomena showing laser interaction with powder material [121].

- *Recoil Pressure* – As mentioned earlier, the recoil momentum created during vaporisation creates a laser-induced compressive pressure from the high vapour pressure on the melt pool surface. Previous studies show that this phenomena can improve the part density [127,128]. However, if the recoil pressure exceeds the pressure created by the melt pool surface tension, material might get blown away from the laser-material interaction zone [128]. Therefore, melt pool temperature must be controlled to control the formation of recoil pressure in order to decrease material spattering due to vaporisation. Controlling recoil pressure can also create a flattened melt pool which in turn will improve the surface quality [129].

- *Spattering* – The instability of melt pool can cause spattering of material. It is difficult to define the spattering principle accurately. In general, spatter appears in different forms such as molten droplet, or partially melted powder, or metallic jet, indicating the various formation mechanisms [130,131]. These spatters often degrades the physical and mechanical properties of final parts, by acting as nucleation sites for cracks or pore formations. The chemical composition of spatter are mostly different from that of the powder feedstock [132,133]. The spatter material is also highly influenced by oxygen present in the chamber, resulting in surface oxide formations in volatile elements of the material. Such spatters may adhere to the surface or contaminate clean powders affecting microstructural characteristics in the final part

[134,135]. High velocity inert gas flow can shield or minimise oxidation and contamination of powder bed. It has also been reported that chances of spattering is high when high laser energy densities are used, and suppression of spatters may be favoured when low energy densities are combined with wider laser spot sizes [136].

- *Solidification* – L-PBF is associated with high solidification rates ($10^4 - 10^6$ K/s) [35,137]. The cooling rates are highly controlled by the temperature gradient in the melt pool. This can in turn alter the microstructural formations, in the form of grain refinements, solid solubility, chemical homogeneity and metastable phases' formations [138–140]. The local thermal gradient and the growth rate decides the solidification microstructure and size formation [141,142]. Figure 1.14 shows the various types of solidification fronts formed by a combination of local thermal gradient and growth rate. Therefore, choosing the right process parameters is necessary to control the thermal gradient and cooling rates which in turn produce specific microstructural features.
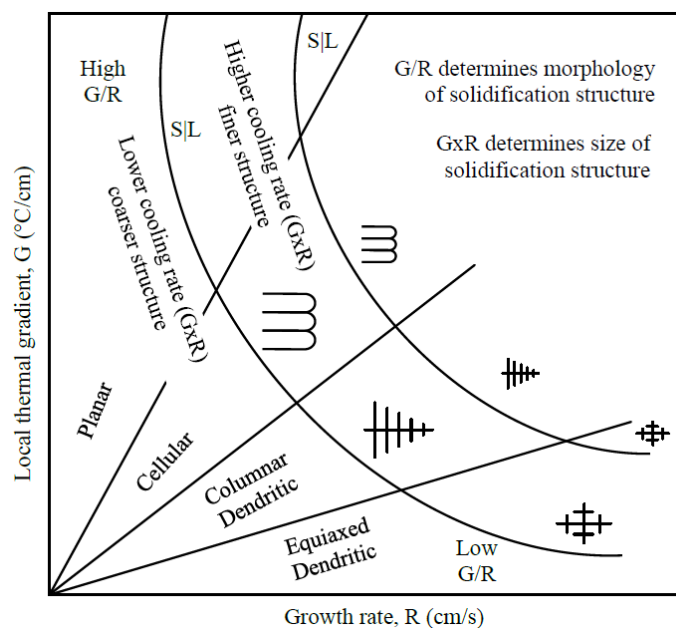
Figure 1.14 Size and morphology of solidified microstructure tailored by thermal gradient and growth rate [143].

The following are a few significant effects imposed on NiTi exclusively, by setting the L-PBF parameters.

1.5.2 Effect on Final NiTi Component Properties

Laser energy density has been found to have a directly proportional relationship with strength and impurity levels of L-PBF fabricated NiTi components. Higher levels of energy density can improve the density of products. However, this can result in higher amounts of impurity pick-ups. Volumetric energy density (VED) can be expressed as given below, where P is laser power, v is scan speed, h is hatch spacing, and t is layer thickness [144].

$$VED = \frac{P}{v \times h \times t} \tag{1.4}$$

Even though L-PBF fabrication is usually conducted in an inert environment, oxygen and nitrogen are sometimes picked up significantly (about 0.14 wt. %) when VED is increased [145]. An energy density of $100 - 200$ J/mm^3 is advised, and a value of 195 J/mm^3 is often recommended [145]. Walker *et al*. [18] demonstrated that very high energy density can form wavy surfaces on parts. Very low energy density was found to cause discontinuous melts. Increasing the energy density beyond a critical value was also found to induce porosity, which led to a drop in relative density [146]. High energy density increases the molten pool volume, hindering the escape of gas bubbles to the surface during solidification, and this often results in pores. Secondly, a balling effect can occur at high energy, and may form voids [26].

The *laser scan speeds* are found to have a direct effect on the thermal hysteresis of the alloy which in turn affects the functional properties. The thermal hysteresis refers to the change in phase transformation temperatures measured through thermal characterisation techniques such as Differential Scanning Calorimetry (DSC), Differential Thermal Analysis (DTA) or Thermogravimetric Analysis (TGA), when the material is heated and cooled. Higher change in martensite-austenite (Ms-As) transition denotes higher thermal hysteresis in the NiTi system. Variations in cooling conditions may result in localized variations in chemical composition [21,147]. During the L-PBF process, the heat distribution is of a non-uniform nature. Due to this and high thermal energies, certain regions are exposed to overheating, and Ni evaporation may occur during processing. This rapid transient processing nature can result in formation of porosity, impurities and precipitates in martensitic NiTi, causing adverse effects on phase transformations and physical properties [16,26,46].

It was also noted that lower scan speeds can exhibit higher thermal memory recovery and improved superelasticity [148]. Other intermetallic phases such as Ti_3Ni_3 and $TiNi_3$ may precipitate, due to a loss of laser control over the synthesis (e.g., during exothermal reaction) for a certain period [149]. Relatively low scan speeds (< 200 mm/s) or high energy densities may create intermetallic phases such as Ti_2Ni, Ti_3Ni_4, or TiO_2 and Ti_4Ni_2O oxides, and result in poor phase transformations affecting the functional properties [150,151,152].

If the operation environment has a high oxygen content ($\geq$ 1800 ppm), brittle oxides may form and exhibit undesirable mechanical responses [26]. Non-metallic elements such as oxygen and carbon are often picked up during the sintering process. NiTi is often sensitive to impurity pick up while processing at high temperatures [63,153]. This results in impurity-related brittle Ti-rich phases such as $Ti_4Ni_2O_x$ which could strongly alter the microstructural properties, and thereby, the functional properties [152,154,155]. Another factor to consider in the L-PBF fabrication process is substrate pre-heating. If the substrate is not heated prior to the sintering process, high residual stresses may appear at the bottom region of the component. This is due to the high thermal gradient between the first few layers and the building platform, and if not attended to properly, may result in a warping effect, causing the fabricated part to separate from the substrate material. Preheating the substrate will decrease the thermal gradient between the first few layers and the substrate [156–158].

Optimization of laser parameters is necessary to ensure high density levels and low impurity concentrations in the fabricated NiTi [145,159–161]. According to ASTM F2063-05 [162], the impurity levels must not exceed 500 ppm. The optimum laser parameters can be identified by creating single NiTi tracks, and modify the parameters until the fabricated tracks meet the desired requirements [159]. A set of optimal process parameters were identified by Walker *et al.* [18] for L-PBF processing of NiTi (Phoenix-PXM machine). The parametric values were: laser power = 250 W, scan velocity = 1.25 m/s, spot diameter = 30 µm, and hatch spacing = 120 µm. They were able to develop a relative part density of 98%, and shape memory functionality. Another set of parameters using the same system were suggested by Shishkovsky *et al.* [149] as: laser power = 50 W, scan velocity = 0.1–0.16 m/s, spot diameter = 70 µm, and hatch spacing = 100 µm. the process obtained 97% relative density. Haberland *et al.* [145] also used an energy density of 200 J/mm (54.7 J/mm^3) and produced a fully dense NiTi containing what were

considered permissible levels of impurity (O_2: 0.03 – 0.04 wt. %; N_2: 0.01 – 0.02 wt. %; C: 0.028 – 0.03 wt. %). The authors also modified the existing energy density relation as follows for simple geometries, to include other parameters such as d_b – beam diameter (mm): d_t – track width (mm): and ρ_r – powder bed relative density.

$$E = \frac{P}{\rho_r \cdot d_b \cdot t \cdot v} \qquad\qquad d_t \leq h \qquad\qquad (1.5)$$

$$E = \frac{P}{\rho_r \cdot d_b \cdot t \cdot v} \cdot \left(2 - \frac{h}{d_t}\right) \qquad 0 < h < d_t \qquad (1.6)$$

Dadbakhsh *et al*. [147] studied the difference in phase formation by producing samples at low laser parameters (LP) and high laser parameters (HP), separately under similar energy densities. The LP parameters were associated with a low power (40 W), and low scanning speed (160 mm/s), with low heating and cooling rates. The HP parameters were based on high power (250 W), and high scanning speed (1100 mm/s), with higher heating and cooling rates. The two combinations produced similar densities (99 %) and chemical compositions. The fabricated samples via LP conditions exhibited martensitic phase with functioning shape memory effect, while the HP combination produced austenitic phase with a superelasticity property, at room temperature.

To retain proper densification levels, a coordinated increment or decrement of the scan speed and laser power was noted as being necessary. It was found that the energy density decreased when laser power was kept constant and scanning speed was increased. Similarly, the energy density decreased when the hatch spacing was increased, while keeping laser power and scanning speed constant [17].

1.5.3 Effect on NiTi Microstructure

Microstructures with different grain morphology, size, and texture can be tailored by adjusting the process parameters [146,163,164]. The layer-by-layer melting and consolidation creates complex thermal gradients, spatially varying grains, and precipitates in the as-fabricated structure. Complex thermal gradients can occur due to high laser power and cooling rates, resulting in a solidification imbalance [165]. The high cooling rates in the range of 103–108 K/s may form finer grains, improving the mechanical properties and density of the final part [166,167]. Khoo *et al*. [168] used repetitive laser scanning technique, in which the second scan imparts lesser energy to the powder compared to a single scan method. Thus, the molten pool acquired a lower

temperature and a shorter solidification time. Various L-PBF research papers have confirmed that grains generally orient in the path of the highest thermal gradient (vertical). Grains may display columnar and equiaxed morphologies with varying sizes [146,169–171]. The thermal stresses during the L-PBF processing of NiTi can generate stress-induced martensitic phases. In L-PBF, the laser power and scanning velocity affects the microstructure distinctly. Even though not much impact on microstructure were reported, change in scan velocities affected the Ni evaporation, altering the phase transformation temperatures [146]. It was further understood that the power density, and complex thermal process during solidification also affects the microstructure.

The melting process in L-PBF involves the re-melting of the formerly sintered layer with bonding of the new layer in an epitaxial solidification manner. Epitaxial solidification is necessary to bond the interlayers strongly, and to prevent undesirable intermetallic phases and porosities in these regions [172,173]. This can result in grain growth in the sublayer, while the current layer grains are sintered [146,165]. Epitaxial growth can result in an increased length and width of the grains. This elongation may be in the form of platelet shape oriented parallel to the laser beam direction (Figure 1.15), following the higher thermal gradient track (scanning direction). A minimum critical energy level is necessary to maintain this epitaxial solidification and a lower cooling rate. The lower cooling rates can lead to the formation of coarser grains [166,174,175]. Grain sizes increase with increasing laser power (Figure 1.16) [174,176]. In an experiment conducted by Bormann *et al.* [146], grain shapes were observed to change from s-shape to rectangular when a high laser power (56–100 W) was used. These grains were also found to orient themselves along the heat direction. Lower levels of cooling rate caused re-orientation and enlargement of the formed grains [166]. High laser power may also increase the porosity. High energy input (> 74 J/mm) is likely to increase the surface roughness and porosity between the adjacent scan tracks. During prolonged melting or high energy, the molten pool becomes unstable, resulting in irregular tracks and vaporization [147,148,177]. When the input energy is less than a critical level (no epitaxial solidification), the sublayer will not be adequately sintered; this could result in reduced area of contact between the layers. The surface tension causes the formation of a cylindrical shape, higher porosity, and weak bonding between layers. Lower cooling rates are often seen in this case, as are re-orientation and enlargement of the formed grains [178].

(a)   (b)
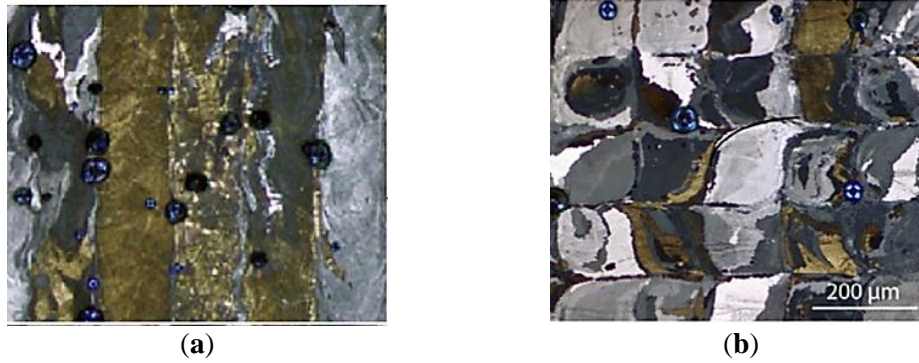
Figure 1.15 (a) Elongated grains as seen in an optical image of L-PBF fabricated NiTi (grid columnar style); and **(b)** formation of S-shaped grains due to the laser scanning motion [146].

(a)   (b)
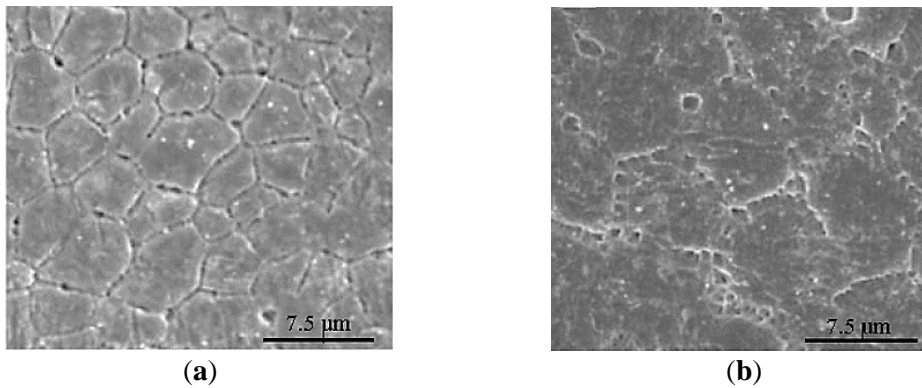
Figure 1.16 SEM images showing an increase in grain sizes when the laser power is increased (constant scan speed), **(a)** P = 300 W **(b)** P = 500 W [174].

1.5.4 Effect on Phase Transformation Temperatures

Dadbakhsh *et al.* [147] reported that the L-PBF parameters can highly influence the transformation temperatures and mechanical response of porous and dense NiTi. In the case of L-PBF processing of NiTi, it was observed that the phase transformation temperatures increase as the energy increases from 45 to 545 J/mm^3 [145,163,179]. This effect is due to the evaporation which occurs during laser processing at high energy. Nickel, which has a lower evaporation temperature (2913 °C), evaporates more readily, leaving more titanium (with an evaporation temperature of 3287 °C) in the matrix composition. This higher titanium content increases the transformation temperature [17,24]. High energy density can also evaporate nickel ions (explained earlier), resulting in higher transformation temperatures [180]. This phenomenon is observable in all the compositions i.e., high Ti content or Ni content, or near equiatomic NiTi [181]. A few studies have discussed the effect of precipitate formations, thermal residual stresses and

30

dislocations on transformation temperatures [147,174]. Solution treatment of as-fabricated L-PBF samples helps to relieve these entities to some extent but the change in phase transformation properties are sometimes not hugely influenced. This can result in functional property actuation being different from build to build [180,182,183]. Another entity affecting the transformation temperatures is the Ni reduction caused during L-PBF. However, in martensitic NiTi, the effect has not been considerable [13,146,180,183].

1.5.5 Effect on Corrosion Properties

The corrosion properties of NiTi are of concern from a cytocompatibility viewpoint. Release of Ni ions from the matrix can cause harmful and adverse effects in biological applications. NiTi is known for its good corrosion resistance, and hence its biocompatibility, due to the rapid development of protective oxide layers (thickness of 2–20 nm) on the surface. The oxides that usually form on the NiTi surface are mostly TiO_2, along with small traces of TiO, Ti_2O_3, NiO and Ni_2O_3 [155,184]. However, Ni ions can still leach in physiological environments when exposed to long service durations [185]. Laser-based processing can lead to higher Ti concentration on the surface, and a thicker oxide layer [184]. Alternatively, controlling the Ti/Ni ratio can also result in higher corrosion resistance due to better stability of the TiO_2 film [186].

In a study performed by [155], both L-PBF fabricated and conventionally-produced NiTi was found to exhibit comparable corrosion properties. The capability of L-PBF in producing a homogeneous and defect-free NiTi structure could further improve the corrosion resistance during service. It was also found that when the porosity was increased, a higher corrosion current was caused due to the presence of larger surface area and an increased number of edges of the porous structures. The corrosion current was observed to increase from about 200 nA (bulk structure) to about 950 nA (35 % porous structure). Higher corrosion currents could result in a higher release rate of Ni ion and corrosion by-products [155]. If the operation environment contains higher oxygen content (e.g., 0.6 %), the L-PBF process can form large oxide film on the porous structure. This can affect the mechanical property; however, it will increase the corrosion resistance and biocompatibility [187,188]. As mentioned in the previous section, low cooling rates can create coarser grains, thus reducing the extent of grain boundaries, which are potential nucleation sites for precipitates or impurities. Therefore, controlling the cooling rates during L-PBF can directly translate into a reduction in corrosion rates for NiTi [187–191].

31

1.6 Powder Properties and Chemical Composition

1.6.1 Effect on Microstructure

Powder shape and particle size distribution are also found to affect the microstructure [192,193]. Laser processing often changes the microstructures and phases of the feedstock alloy powder. Due to the lower heat flux near supports, the grains usually become finer in the regions far away from the base, while coarser grains are formed at the bottom region of the fabricated component [166,175]. In a study conducted by Shiva *et al*. [194], it was observed that equiatomic NiTi (50:50) composition presented the most uniform, finest, and highest packed grains compared to the other two compositions. Ni (45 %) – Ti (55 %) exhibited uniformly distributed grains of irregular shapes and large sizes. Ni (55 %) – Ti (45 %) exhibited smaller grains when compared to Ni (45 %) – Ti (55 %); however, it was still large when compared to NiTi (50:50) composition (Figure 1.17). Finer particles are preferred for denser fabrication, and they also reduce the energy requirement for epitaxial solidification [166]. Particle sizes in the range of 20 – 63 μm or smaller exhibited poor flowability, and a reduced packing density (56 %). When the range was around 25 – 75 μm and 45 – 100 μm, a higher packing density (60 %) was observed. If the particle size falls below 45 μm, packaging density was about 44 %; below 25 μm, the packing density fell even further to about 37 % [145,170]. For L-PBF of NiTi, medium-sized fractions around 25 – 75 µm are the ones with favourable particle size, spherical morphology, flowability and packing density, impurity content, and excellent transformation ability.

| (a) | (b) | (c) |
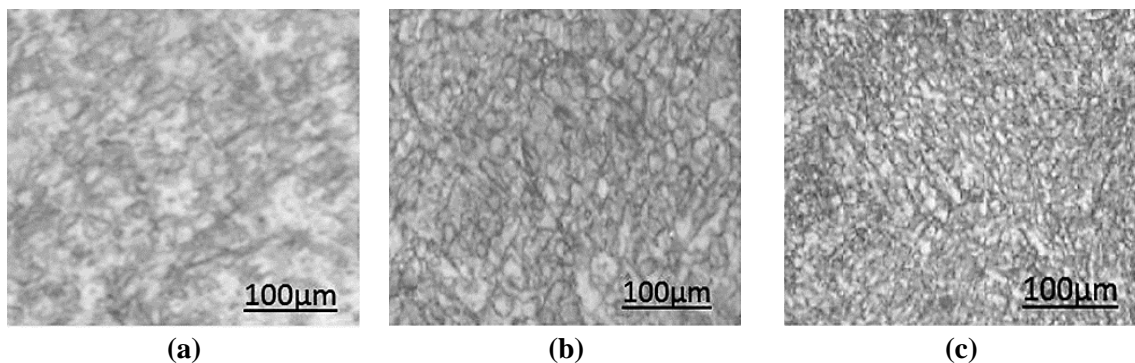
Figure 1.17 Different grain characters as seen in the microstructural images of **(a)** Ni45Ti, **(b)** Ni55Ti, and **(c)** Ni50Ti [194].

1.6.2 Effect on Phase Transformation Temperatures

Transformation temperatures of NiTi are very susceptible to the Ni or Ti content. Near equiatomic NiTi have disadvantages such as lower strength and poor cyclic stability compared to a Ni-rich NiTi. Higher titanium content in the matrix composition will need higher temperature to process, owing to the higher melting point of Ti. Binary NiTi alloys have transformation temperatures between – 40 °C and 100 °C and exhibit a temperature hysteresis of 20 – 40 °C. Higher Ni content (lower Ti content) can decrease the transformation temperatures at a rate of about 93 °C/at. % Ni content. For instance, the effect of nickel content on martensite start (Ms) temperature is shown in Figure 1.18. As nickel content increases, Ms temperature decreases [17,18]. It has been reported that 50 Ni and 50.5 Ni (at. %) NiTi failed to show pseudoelasticity due to low strength [17]. The diffusionless and reversible martensite-austenite transformation takes place in the temperature range of 50–100 °C as a function of the nickel content. This is associated with a variation of transformation temperatures by approximately 10 °C/0.1 at. % change in the nickel content [195,196]. Increasing nickel content also increases the critical stress needed for martensitic transformation and the strain recovery. Therefore, the chemical composition should be maintained very accurately. The transformation temperatures of NiTi alloys are also very sensitive to impurities such as nitrogen, carbon, and oxygen [16]. For instance, if oxygen is present in the NiTi matrix, the transformation temperature will be lowered, and causes the parent phase to be brittle. Studying the phase diagram (Figure 1.19), we can see the existence of few stable phases (Ni_3Ti, $NiTi_2$) besides the main phase NiTi. These additional phases will not exhibit shape memory property and their presence affect the composition of the remnant NiTi portion of matrix. This will also affect the transformation temperature. A metastable Ni_4Ti_3 phase precipitates at lower temperatures owing to the decreased solubility of nickel. This phase is coarsened when annealed at 300 – 600 °C, resulting in the formation of a stable Ni_3Ti phase [16]. Samples lacking these precipitates (high homogeneity) are highly suitable for medical applications. The Ni^+ ion release can be reduced by using a smaller laser spot size, lowering risks of NiTi biomedical implants [26,197].
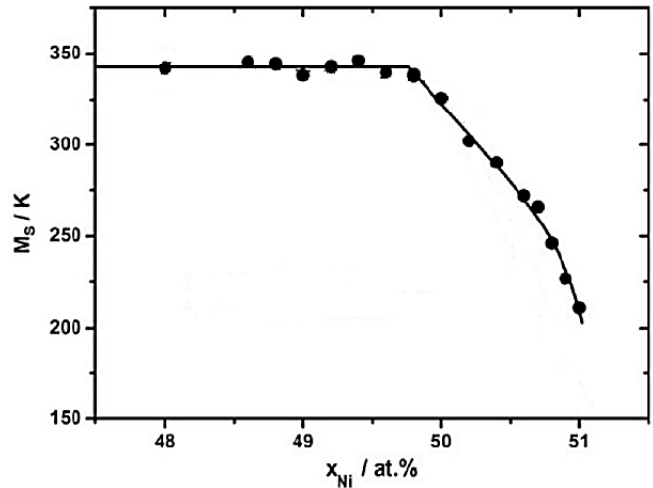
Figure 1.18 Influence of nickel content on martensite start temperature [198].
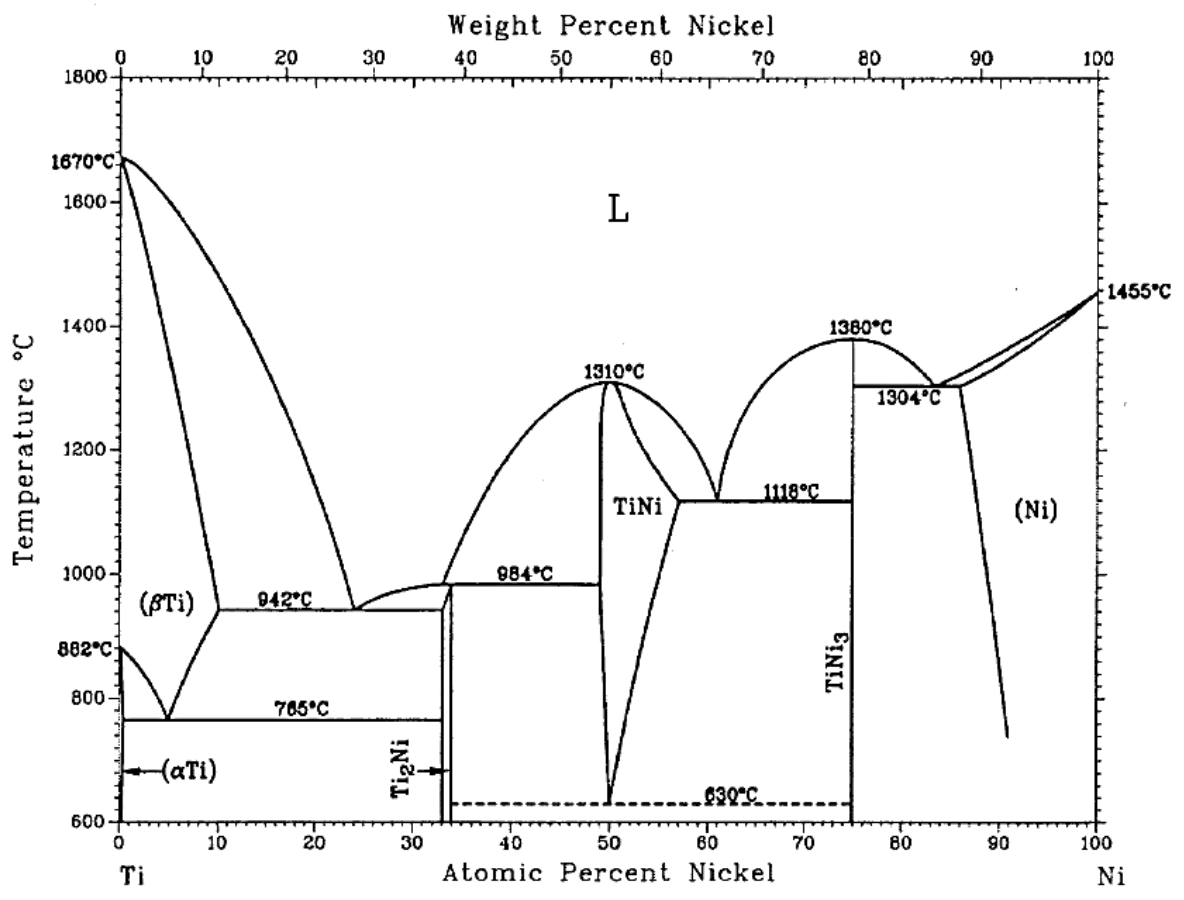
Figure 1.19 Binary phase diagram of NiTi alloy [16].

1.7 Heat Treatment Processes

1.7.1 Effect on Phase Transformations

The as-fabricated Ni-rich Nitinol will not be able to recover the full strength because of the nucleation of martensite in an austenite region [199]. Heat treatments such as solution annealing and aging can be applied after L-PBF fabrication to provide a homogeneous equilibrium state throughout the material, and help in recovering the strength. It also helps in clearing several microstructural defects and residual stresses [200]. Subsequent aging processes can be applied in order to recover strength completely through precipitating Ni-rich phases such as Ni_3Ti, Ni_3Ti_2, and Ni_4Ti_3. Solution annealing followed by water quenching could cause significant decrease in transformation temperatures of Ni-rich Nitinol. The metastable phases such as Ni_3Ti_2 dissolve during solution annealing and this suppresses further precipitation when water quenching is employed. Solution annealing also decreases the transformation features such as peak width (in Differential Scanning Calorimetry). This was confirmed by Andani *et al.* [179] and Saedi *et al.* [201] who reported lower transformation temperatures (about 20 °C) and a single-phase transformation. It was also found that a longer aging duration may increase the transformation temperatures (Figure 1.20). This could be either due to evaporation of Ni in prolonged high temperature conditions, or precipitation of Ni-rich phases at high temperatures [201,202]. Oxidation happens often during the heat treatment processes at high temperatures. This may result in the reduction of Ti, as it is highly reactive to oxygen, and consequently, it decreases the transformation temperatures. This could further result in poor martensite to austenite transformations and an elevation in precipitate formation [203].

When the martensite transformation is suppressed by solution treatment and subsequent ageing processes, formation of R-phase could occur. This is due to the introduction of NiTi precipitates (usually Ni_4Ti_3) which could favour the R-phase growth [53,168]. In the Differential Scanning Calorimetry plots, we may see distinct peaks; the first peak indicates the austenite to R-phase transformation, while the second represents the transformation from R-phase to martensite phase [145,204].
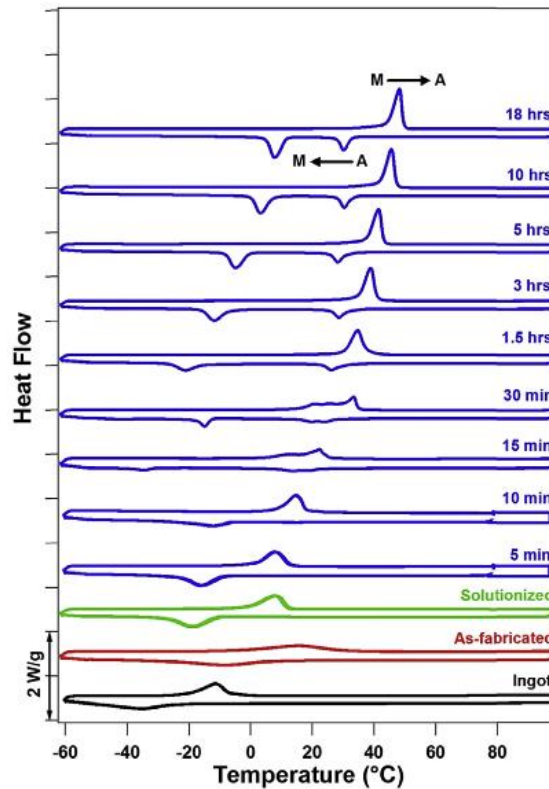
Figure 1.20 Differential Scanning Calorimetry plot showing the effect of solution annealing and ageing time (blue curves) on Ni (50.8 at. %) - Ti [201].

1.7.2 Effect on Mechanical Properties

The thermal stresses during L-PBF can generate stress-induced martensitic phases. Solution annealing can homogenize the composition, dissolve all precipitates, and eliminate all stress-induced phases [13]. Saedi *et al.* [201] conducted a Vicker's hardness tests on L-PBF fabricated NiTi sample, and the hardness value was found to be 224 HV, which is much lower than the ingot hardness (278 HV). Employing solution annealing increased the hardness value to 288 HV. Solution annealing dissolves the brittle Ni4Ti3 precipitates; the increase in the hardness was ascribed to this. A sample which is subjected to an aging process for 18 h at 350 °C. Following this, annealing can eventually exhibit an increase in hardness up to 345 HV. Haberland *et al.* [205] used a Ni-rich specimens to study the effect of orientation on the compressive properties of superelastic NiTi. Their samples were solution annealed at 950 °C for 5.5 h after fabrication, and then quenched under water. The heat treatments generate a flatter loading curve (versus steep curve), and greater stress and strain at failure. This was caused by the dissolution of nucleated Ni4Ti3 phases which had previously formed. Generally, these precipitates hinder plastic

36

deformation. Subsequent aging processes can result in reducing the fracture stress and strain. However, it was found that more severe aging conditions (temperature and duration) create a more ductile curve and higher values of fracture stress and strain [53]. Saedi *et al.* [201] also observed that the subsequent aging also increased the yield stress by about 700 MPa. These observations were because of the precipitation/age hardening effect.

1.8 Challenges in Producing Shape Memory Effect

Achieving an effective shape memory property is challenging, owing to high localized heating, high scan speed, fast heating rates, and rapid solidification rates. The shape memory effect and mechanical responses depend significantly on the microstructural characteristics. Apart from operation parameters, the microstructural characteristics can also be affected by laser solidification tracks, the formation of very small austenitic grains inside melt pools, large plate-like martensitic phases that are thermal stress-induced, and a preferential texture corresponding to the heat flow direction. Compared to DED, these factors are more profound in L-PBF, as scanning velocities are much higher. Figure 1.21 shows these occurrences in an L-PBF processed NiTi. These typical features will eliminate the residual elastic energy among the laser tracks; however, it will reduce the uniformity of martensitic phase transformations. The grains always tend to orient along the build direction (heat flow direction). This can produce large anisotropy in stiffness and shape memory responses. Fine martensitic and austenitic sub-grains formed in laser tracks can also be seen in the Figure 1.21 [13]. The large martensitic plates can be removed by proper annealing and furnace cooling. However, these treatments will not produce isotropic properties. The application of furnace cooling after annealing can result in the segregation of martensite and austenite within the solidified track, leading to further mixed shape memory behaviour [26]. Dadbakhsh *et al.* [169] reported the influence of orientation of austenitic crystals on shape memory response of NiTi fabricated by L-PBF. The structures in which the austenitic crystals are aligned vertically showed the highest elastic recovery. Conversely, the horizontal alignment exhibited lowest elastic recovery and highest shape memory recovery strain. This discrepancy is due to the presence of elongated austenitic crystals, which may destabilize the twinned martensite. The horizontal orientation can also increase the material's resistance to compressive loads [26]. Highly dense L-PBF fabricated equiatomic NiTi showed almost full shape memory recovery, while in porous samples, about 0.5% irrecoverable strain remained. However,

the superelasticity property shows only partial recovery due to low strength property of equiatomic NiTi. The cycling tests will gradually stabilize the shape memory behaviour, and irrecoverable strain becomes negligible [17,205,206].
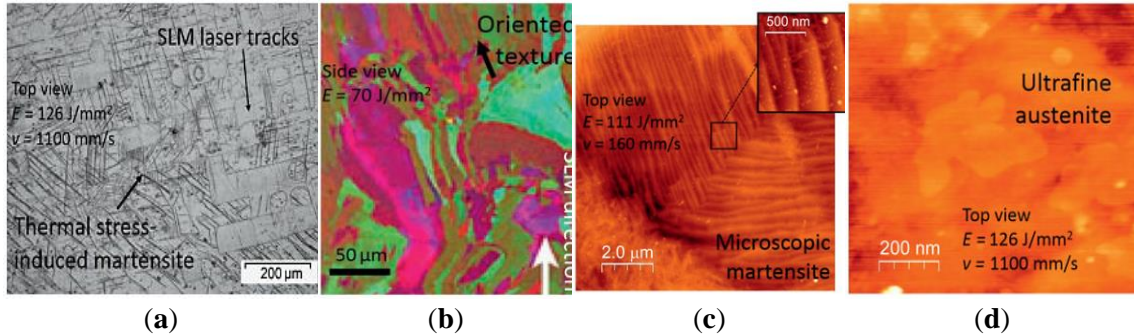
Figure 1.21 (a) L-PBF laser tracks having stress-induced martensite due to high thermal stresses; **(b)** formation of fine austenite sub-grains along L-PBF build direction [163]; **(c)** AFM image showing fine internally twinned martensitic structure; **(d)** AFM image showing ultrafine austenite sub-grains [13].

1.9 Defects in L-PBF NiTi Parts

Defects in L-PBF can be due to several factors, however, the violent rapid transient thermal effects are the primary cause. Depending on the material, these thermal effects can occur due to the improper selection of process parameters and other processing conditions. The product defects may increase the demand for post-processing treatments, reduce reproducibility, process reliability and final product quality.

Lack of fusion defects occur when the incident energy is insufficient resulting in unmelted or partially melted particles. This can result in inconsistent and discontinuous scan tracks, degraded interlayer bonding (delamination) and porosities. *Balling* defect occurs when local powder arrangement is poor, hatch spacing is too high, presence of oxygen or reactive gases in the build chamber, changes in melt pool viscosities, and insufficient laser energy density [207]. Balling can cause porosities, higher surface roughness, and discontinuous melt tracks and scratch the recoater blades. Higher VED and addition of powder de-oxidants can prevent this phenomenon [208–210].

High thermal gradients and cooling rates can increase the chances of formation of columnar grain structures. These columnar grains may lead to shrinkage-related defects such as solidification cracks. This can be controlled by changing the alloy composition

or decreasing the rate of solidification [211]. The lased-based AM processes (L-PBF or DED) are expected to maximize the material density [13]. However, porosity is recognized as one of the most common quality issues. L-PBF can be used to pre-design pore morphology. By engineering the porosity, a desired stiffness value can thereby be achieved [193].

Cracks and *pores* are considered as the two most common structural defects found in L-PBF processed NiTi [207,212]. The porosities can be classified based on the cause of occurrence; gas-induced or process-induced porosity (Figure 1.22a). Gas induced pores are caused by trapped gas in the powder bed. Pores can form near the edge regions due to insufficient melting of powder particles, and they are referred to as "process induced pores" [213]. Based on shape morphology, pores can be of spherical and irregular types [165]. Spherical porosity is due to the mixing of ambient gas with the NiTi powder particles; the trapped gas does not have enough time to escape from the melt pool. Irregular pores are formed due to the balling effect. These pores can be reduced by epitaxial solidification [214]. Strong bonding between layers is necessary to prevent chances of pore formation (optimize laser power and scan speed). It has been reported that energy densities of more than 74 J/mm^3 would increase chances of pores [21]. Irregular pores can be reduced by using an inert gas (Argon) environment to reduce the oxygen levels during processing. This could also reduce the balling effect (oxygen expand between layers) due to less oxygen, further reducing the chances of irregular pores [178,215,216].

Owing to the process nature, L-PBF and DED have a high tendency to create unbalanced stress profiles (residual thermal stresses) between the printed layers. Residual stresses in these processes, usually occur due to the large thermal gradients created by several re-melting and cooling cycles, taking place at inconsistent heat levels or thermal gradient levels. The regions of concern are mainly the exposed layer (top layer) and the interface between the exposed layer and the previously printed layer [217]. Thermal expansion of the top layer creates tensile stress, while the cooler layer below undergoes compressive stresses. This phenomenon occurs throughout the underlying layers and may affect the same layer multiple times. This will eventually result in a stress gradient between the layers. Residual stresses are usually highest in the scan overlap regions. Residual stresses, if high enough, can initiate cracks (Figure 1.22b) throughout the NiTi samples, and reduce

the fatigue strength drastically. This can result in the delamination and/or warpage of feature geometry [201,216,217]. Another reason for crack formation could be the balling effect between layers, or element vaporization. Hence, the process parameters should be such that they favour epitaxial solidification, and provide an inert process atmosphere [214,216,218]. Element vaporization is another cause of crack-initiating pores in the structure. These cracks, however, do not propagate as the L-PBF is inherent to rapid cooling which prevents the propagation mechanism [218–220].

(a)   (b)
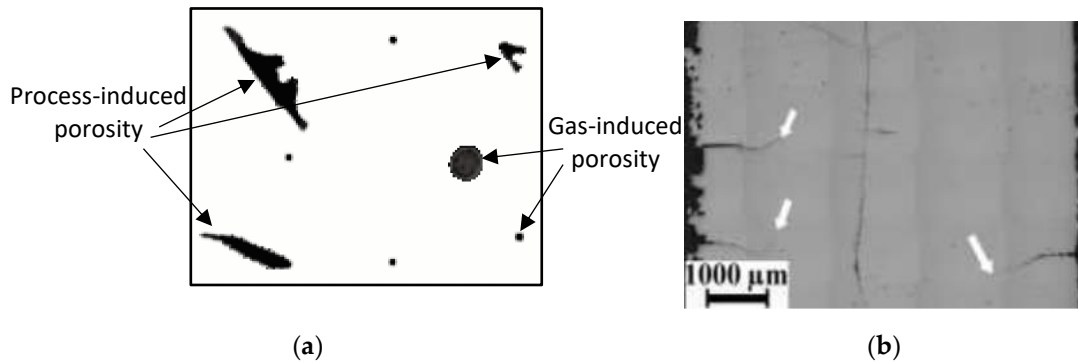
Figure 1.22 (a) Schematic representation of gas-induced and process-induced porosities; **(b)** Optical micrograph showing cracks [220].

1.10 Summary of Existing Knowledge

Previously published work related to the L-PBF processing of NiTi has been reviewed to identify the influential factors involved, process-related issues, and explore possible areas to work on. Based on the findings to date, AM can be used to process NiTi components with high density and near net shape, requiring very little or no post-processing. Out of the two common AM approaches (DED and L-PBF) for NiTi processing, L-PBF has been found to be more effective. The L-PBF process is more capable of producing parts with homogenous and comparable composition to that of the feedstock. The process was also found to be capable of forming uniform microstructure with high aspect ratio columnar grains, uniform strain accumulation and a stable twinned martensite phase structure.

The L-PBF process parameters were found to have a significant impact on the microstructure and phase transformation temperatures. The optimization of several parameters including energy density, scan velocities, and working environment is necessary to attain high density levels and low impurity levels in the fabricated NiTi parts. Too high or low energy densities result in impurity pickup, porosity, and wavy surface finishes. The scan speeds of the laser beam affect the thermal hysteresis due to longer

heat exposure, which in turn influence the shape memory and pseudoelastic properties. The presence of nitrogen, carbon, and oxygen in the work chamber is found to alter the transformation temperatures of NiTi. A high oxygen content can cause degradation of the mechanical and functional properties in the material. Complex thermal gradients affect the microstructure of the as-fabricated structure. Substrate preheating is recommended to reduce the thermal gradient and relieve the residual stresses. Density levels can be managed through coordinated manipulation of scan speed and laser power. High cooling rates were found to generally improve the mechanical properties and density. However, they may result in large thermal gradients affecting the residual stress, grain orientations and phase formations. To avoid undesirable intermetallic phases and porosities, epitaxial solidification has been found to be effective, which could be achieved by controlling the input energy and cooling rate. Higher energy levels cause evaporation of Ni, and therefore, result in higher phase transformation temperatures, as higher Ti content in the composition will increase the transformation temperatures. From the control of cooling rates and oxygen content in the process environment, it was found to be possible to improve the corrosion protection of NiTi. The creation of low density (porous) structures can also increase the chance of corrosion occurring.

The powder quality and material composition also impose a significant effect on the microstructure and phase transformations. Equiatomic NiTi was observed to exhibit the most uniform and finest grains, which is highly recommended for high density fabrication. Particle size was also found to affect the flowability and packing density of the feedstock during fabrication. The martensitic transformation and strain recovery are also influenced by the Ni content in the composition, and therefore maintaining an accurate composition is necessary. Heat treatments performed after L-PBF are also reported to affect the functional and mechanical properties to a great extent. More ductile curves and high fracture characteristics were created when heat treatments involving very high temperatures and durations were used. High localized temperature rise, scan speeds, heating and solidification rates make it difficult to produce the right phase structure for shape memory effect via L-PBF process. The method of solution annealing was found to be effective in homogenizing the composition and dissolving and removing the undesired precipitates and the stress-induced phases.

The difficulties in producing effective shape memory response lies mostly in the microstructural characteristics, which may include formed grain morphologies, stress-

induced phases, and preferential texture formations. Annealing and furnace cooling treatment can improve the functional properties; however, more prospective work is required to completely eliminate the anomalies leading to mixed functional responses in L-PBF fabricated NiTi parts. Furthermore, the common structural defects have also been reviewed. It was found that pores and cracks are two prominent process-related defects which result during L-PBF processing. Common causes may include gas trapping, insufficient melting, high thermal gradients and cooling rates.

In the past, FEA models have been used to study the response of NiTi components, such as when printing stents and actuator springs. Several works have been conducted to evaluate the post-implantation structural and functional response, and degradation and fatigue-related studies. The effect of MVF on Young's modulus of NiTi has not been studied for a step-by-step increment of MVF and compared with the macroscale mechanical responses. A detailed study on this knowledge gap will help in deciding the NiTi processing conditions, model designs, and operational parameters to achieve the appropriate level of porosity for enhanced performance in shock absorption, heat pump, and other related renewable energy applications. Figure 1.23 summarizes the literature of this area, and different aspects of the gap examined.
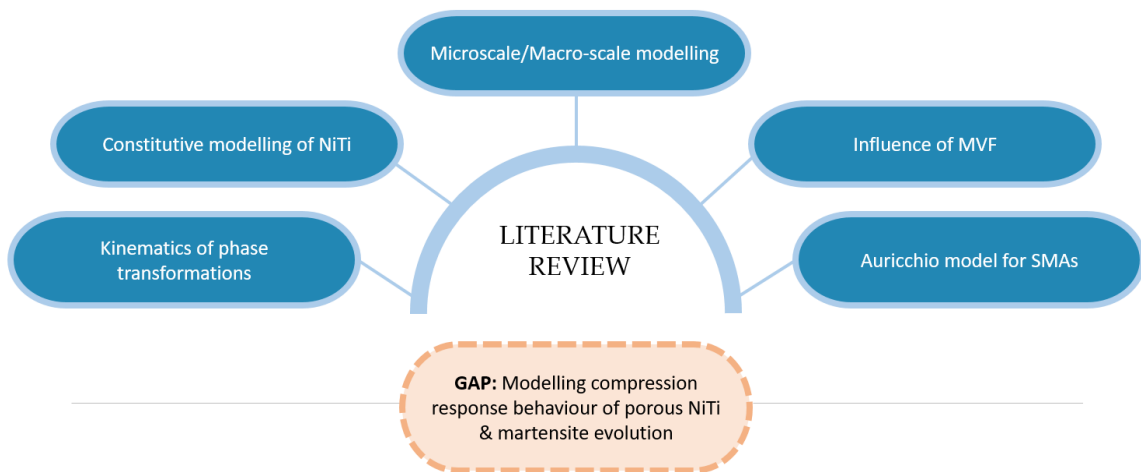
Figure 1.23 Schematic of the literature review content for FEA in the field of NiTi.

The research and development on L-PBF processing of NiTi remains at an early stage, and significant work will have to be conducted to enable NiTi parts to be effectively produced via L-PBF. Over the past years, several researchers have worked on understanding the effect of L-PBF operational parameters on the part properties.

However, the investigation of the sensitivity of the functional characteristics of NiTi to the material composition and L-PBF process control is still in its early stages and requires further research to provide sufficient fundamental understanding in these areas and subsequent end applications. Only a few studies have been conducted to better understand the effect of operation parameters in causing porosity and crack defects. Also, the mechanical behaviour of L-PBF martensitic NiTi has not been explored in much detail, along with how the shape memory properties are affected with changes in L-PBF parameters. A deeper insight into how a set of process parameters interlink the functional and mechanical properties with the microstructural characteristics is also needed to directly correlate the effect of L-PBF with shape memory effect.

There have been no studies to date which have examined the temperature evolution during the metal AM processing of NiTi for measuring the effect of intralayer average temperature differentials on the resulting part densities. In addition, the effect of the process parameters on the Ni loss, phase transformation temperatures, the temperature range of each phase, and transition enthalpies and enthalpy ratios has not previously been presented. The thermal gradients associated with L-PBF makes the microstructural evolution more complex, and influences the phase transformations and shape recovery mechanisms of NiTi alloys. These rapid transient thermal effects are highly controlled by the L-PBF processing parameters. It has been reported by several researchers that phase transformation temperatures elevate with higher levels of laser energy density. However, the underlying mechanisms are not clearly portrayed.

The mechanical properties of L-PBF NiTi measured in compression mode is generally more reliable and exhibits higher stress values than in tension, giving enough headroom to study the effect of L-PBF parameters. Most studies [5,8,13,15,17,26,50,102] in the past focused on investigating the effect of L-PBF parameters in terms of laser energy density on mechanical properties. Many studies have utilised the digital image correlation (DIC) technique to analyse the stress-induced martensitic transformations in austenitic NiTi. The analysis of detwinning and strain recovery in martensitic NiTi is still not fully unexplored, especially how the local strain and strain rates compare with macroscopic strain responses. In most studies, the design space of these process parameters were considerably narrow, and many of them used some sort of post-processing to remove process-induced effects from the as-fabricated samples. The mechanical and functional

responses of L-PBF NiTi fabricated through different processing parameters, build orientations, scanning strategies and laser emission modes is not yet fully understood.

Chapter 2

Influence of Structural Porosity and Martensite Evolution on Mechanical Characteristics of Nitinol via In-Silico Finite Element Approach

2.1 Abstract

Nitinol (NiTi) alloys are gaining extensive attention due to their excellent mechanical, superelasticity, and biocompatibility properties. It is difficult to model the complex mechanical behaviour of NiTi alloys due to the solid-state diffusionless phase transformations, and the differing elasticity and plasticity presenting from these two phases. In this work, an Auricchio finite element (FE) model was used to model the mechanical behaviour of superelastic NiTi and was validated with experimental data from literature. A Representative Volume Element (RVE) was used to simulate the NiTi microstructure, and a microscale study was performed to understand how the evolution of martensite phase from austenite affects the response of the material upon loading. Laser Powder Bed Fusion (L-PBF) is an effective way to build complex NiTi components. Porosity being one of the major defects in Laser Powder Bed Fusion (L-PBF) processes, the model was used to correlate the macroscale effect of porosity (1.4 – 83.4 %) with structural stiffness, dissipated energy during phase transformations, and damping properties. The results collectively summarize the effectiveness of the Auricchio model and show that this model can aid engineers to plan NiTi processing and operational parameters, for example for heat pump, medical implant, actuator, and shock absorption applications.

2.2 Materials and Methods

2.2.1 Constitutive Modelling of Nitinol SMAs

Due to the complex material behaviour in NiTi, models developed to predict the stress strain response need to take account of the major material property parameters of NiTi. The important parameters which define a NiTi material are shown in Figure 1.7. These parameters depend on the material compositions (Ni/Ti ratio), microstructure, mechanical and thermal histories of the material, and results in a wide range of mechanical and functional properties in the literature. A scatter plot of Young's modulus of austenite and martensite phases found from various sources [12,73,77,86,90,91,95,221–242] is shown in Figure 2.1. With a limited availability of sources, no specific trends were found, however, it was seen that the Young's modulus of the martensite phase was always recorded as being below 50 GPa.
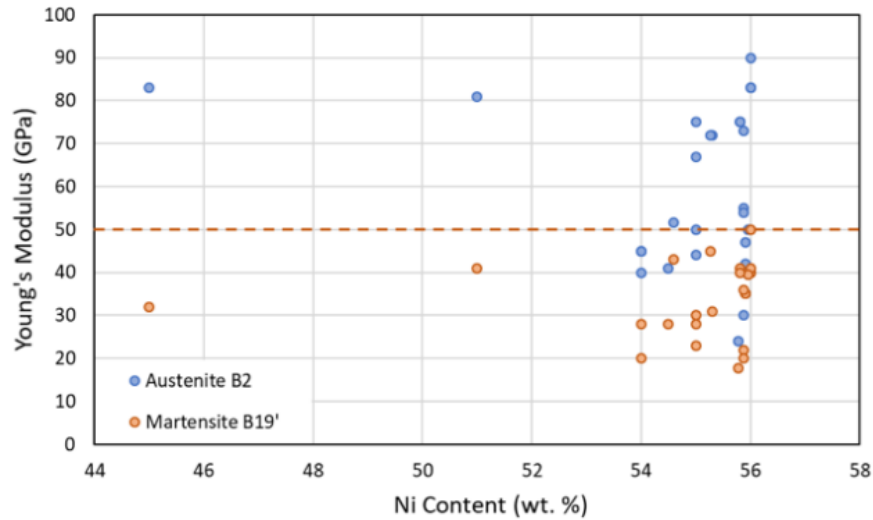
Figure 2.1 Scatter plot showing elastic modulus of the martensite and austenite phases plotted with the Ni content, from past published sources.

Mathematical models have provided a considerable insight into the complex mechanical behaviour of NiTi. Most of the models in the literature have not been able to simulate the following prevalent NiTi phenomena: cyclic instability of superelasticity, actuation instability, shape setting, two-way SME, and functional thermomechanical fatigue [78,85]. Several constitutive models have been created over the years to capture this complex behaviour, following either of the two approaches—micromechanical (microscale) or phenomenological (macroscale).

2.2.2 Microscale Models

The micromechanical model considers the granular microstructure, and describes the concepts such as nucleation, twin growth, and interface motion. The models can be used to utilize the response of single crystal based on variants for creating a polycrystalline model, by assembling single crystal grains [243]. Commonly in NiTi systems, there is a possibility of 12 product variants and 192 habit planes in each grain that constitutes the larger scale. This is often a cumbersome task from a computational perspective, and therefore, numerous constraint equations are employed for minimizing the potential issues in regard to phase fractions, mass conservation, grain boundary conditions, grain interactions, and so on [244–247].

Constitutive models incorporating the habit plane variants (HPVs) and CVPs as basic deformation units were used by researchers in the past [72,244,247–251], assuming

infinitely large material. The primary focus was on evolution of dynamic microstructure during phase transformations. The first transforming grains were those with the highest Taylor and Schmid factor, and highest transformation strain. When plasticity is incorporated, it is often difficult to capture the evolution of static microstructure (dislocation defects, residual strain, austenite twins, etc.) [16,71]. Incorporating additional variables based on experimental data can help translate these micro-scale models to be used in macro-scale analysis [71,252–258]. Prediction models incorporating martensitic microstructure mathematical theory and crystal plasticity was suggested by a more recent research [71] to simulate coupled transformation-plasticity phenomenon. The work involved coupling at intrinsic lattice scale, grain-scale, and macro-scale. Boyd and Lagoudas [259] developed a constitutive model to describe the transformation and reorientation of martensite in a polycrystalline NiTi material. Huang and Brinson [260] used a multivariant model based on micro-mechanics and thermodynamics for single crystal NiTi. Thermomechanical modelling of simultaneous martensitic transformation, coupled with plasticity of NiTi polycrystals, is also an emerging research area.

It is often difficult to create a mathematical model to completely describe the micro-mechanics as there is not a sufficient extent, or easy availability, of microscale details. Additionally, a model for an engineering application often includes millions of grains, demanding large number of constraint conditions and solution variables, which then translates into heavy computational requirements. Due to these reasons, the microscale approach is not commonly used; rather a much larger phenomenological approach is preferred for engineering applications.

2.2.3 Macroscale Models

In comparison to the micromechanical approach, the macroscale constitutive models are much more pragmatic in terms of applicability and features considered. The macroscopic energy functions, which depend on internal state variables, are generally considered to obtain the response in these models. The evolution is simulated via the second law of thermodynamics. These models seek solutions to boundary value problems on the structural level through energy minimization, similar to classical plasticity models [243]. The early models were based on thermodynamics and MVF as an internal state variable to account for microstructure influence [260,261]. These formulations were based on Helmholtz free energy or Gibbs free energy.

One of the most commonly used models was created by Auricchio [72]. 1D and 3D models were created to perform superelasticity, and rate independent models. In this study, the Auricchio model [72] was implemented in the Ansys FEA platform for the shape memory analysis. The rate independent 3D model assumes a single-variant martensite, utilizes an exponential hardening law, and accounts for martensitic transformations and martensitic reorientation. The model also includes the dependency of elastic modulus on MVF. This also facilitates an insight into material strength with respect to MVF at both micro and macroscale in this study. The Auricchio model can be divided into three segments:

1.   1D and 3D constitutive model to reproduce superelasticity

2.   Time-discrete isothermal model

3.   Algorithmic implementation with a finite element (FE) framework.

In the constitutive model, uniaxial loading-unloading history is considered in the time-discrete model to open up the possibility of computing a closed-form solution for evaluating accuracy of FE scheme. In a real uniaxial mechanical test, an asymmetry between tension and compression response (discussed earlier) is possible. The different modes are found to exhibit different strain levels [262]. This concept is proposed using a parameter, $\propto$, which is calculated (Equation (2.1)) from the initial values of phase transformation in tension and compression mode.

$$\propto = \sqrt{\frac{2}{3}} \frac{(\sigma_S^{AS})_C - (\sigma_S^{AS})_T}{(\sigma_S^{AS})_C + (\sigma_S^{AS})_T} \tag{2.1}$$

A few important equations of the constitutive model for the shape memory property of NiTi proposed by Auricchio [72] are presented below. The most important phenomenon considered here is the phase transformation.

Internal variables considered are u, scaled transformation strain, and ξ, single-variant martensite fraction. The phase transformations can be broken down into three as:

•   Conversion of austenite into single-variant martensite (A→S)

•   Conversion of single-variant martensite into austenite (S→A)

•   Reorientation of the single-variant martensite (S→S)

49

During a transformation, u and ξ are subjected to change and the resultant variables are given in Equations (2.2) and (2.3), as below:

$$\dot{u} = \dot{u}^{AS} + \dot{u}^{SA} + \dot{u}^{SS} \tag{2.2}$$

$$\dot{\xi}_s = \dot{\xi}_S^{AS} + \dot{\xi}_S^{SA} \tag{2.3}$$

The reorientation occurs at constant ξ, therefore, $\dot{\xi}_S^{SS} = 0$. Each of these transformations are assumed to occur in a region of the control-variable hyperplane τ-T, where τ is the Kirchhoff stress and T is the temperature.

2.2.3.1 Conversion of Austenite into Single-Variant Martensite (A→S)

To model stress-induced (pressure-dependent) transformation, a Drucker–Prager-type loading function (Equation (2.4)) is introduced:

$$F^{AS}(\tau, T) = \|t\| + 3 \propto p - C^{AS}T \tag{2.4}$$

where, t is the deviatoric stress; $\|t\|$ is the Euclidean norm of the term; p is the pressure; C^{AS} and $\propto$ are material parameters. The initial (Equation (2.5)) and final (Equation (2.6)) transformation functions are expressed as:

$$F_s^{AS} = F^{AS} - R_s^{AS} \tag{2.5}$$

$$F_f^{AS} = F^{AS} - R_f^{AS} \tag{2.6}$$

where,

$$R_s^{AS} = \left[\sigma_s^{AS}\left(\sqrt{\frac{2}{3}} + \propto \right) - C^{AS}T_s^{AS} \right] \tag{2.7}$$

$$R_f^{AS} = \left[\sigma_f^{AS}\left(\sqrt{\frac{2}{3}} + \propto \right) - C^{AS}T_f^{AS} \right] \tag{2.8}$$

where, σ_s^{AS}, σ_f^{AS}, T_s^{AS}, T_f^{AS} are material parameters. The condition for this transformation is assumed to be: $F_s^{AS} > 0$; $F_f^{AS} < 0$; $F^{AS} > 0$.

2.2.3.2 Conversion of Single-Variant Martensite into Austenite (S→A)

Similar to the above transformation, a Drucker-Prager-type loading function (Equation 2.9) is considered here also:

$$F^{SA}(\tau, T) = \|t\| + 3 \propto p - C^{SA}T \tag{2.9}$$

where, C^{SA} is also a material parameter. The initial (Equation (2.10)) and final (Equation (2.11)) transformation functions are expressed as:

$$F_s^{SA} = F^{SA} - R_s^{SA} \tag{2.10}$$

$$F_f^{SA} = F^{SA} - R_f^{SA} \tag{2.11}$$

where,

$$R_s^{SA} = \left[\sigma_s^{SA} \left(\sqrt{\frac{2}{3}} + \propto \right) - C^{SA} T_s^{SA} \right] \tag{2.12}$$

$$R_f^{SA} = \left[\sigma_f^{SA} \left(\sqrt{\frac{2}{3}} + \propto \right) - C^{SA} T_f^{SA} \right] \tag{2.13}$$

where, $\sigma_s^{SA}, \sigma_f^{SA}, T_s^{SA}, T_f^{SA}$ are material parameters. The condition for this transformation is assumed to be: $F_s^{SA} < 0; F_f^{SA} > 0; F^{SA} < 0$.

2.2.3.3 Reorientation of the Single-Variant Martensite (S→S)

To model the reorientation process for non-proportional stress change (directional or rotational), the Drucker-Prager-type loading function (Equation 2.14) is set as:

$$F^{SS}(\tau, T) = \|t\| + 3 \propto p - C^{SS} T \tag{2.14}$$

$$F_s^{SS} = F^{SS} - R_s^{SS} \tag{2.15}$$

where,

$$R_s^{SS} = \left[\sigma_s^{SS} \left(\sqrt{\frac{2}{3}} + \propto \right) - C^{SS} T_s^{SS} \right] \tag{2.16}$$

where, σ_s^{SS} - stress at reorientation of single-variant martensite, C^{SS} and T_s^{SS} are material parameters. The condition for the activation of reorientation is assumed to be: $F_s^{SS} > 0$.

2.2.4 Numerical Simulations

In this study, FE modelling/simulation were performed using the package *ANSYS Workbench 2019*. The Auricchio model which defines the shape memory material properties was utilized coupling with custom material plasticity data implementation.

For an easier understanding of the phase transformations and stiffness variations, the superelasticity concept under pure mechanical effect and isothermal conditions (22 °C) was examined in this work. In other words, the stress-induced martensitic transformation (SIMT) was studied ignoring all thermal effects involved. Initially, a mesh convergence study was implemented to obtain the right mesh size resulting in good result convergence without consuming large computational resources. Tetrahedral elements were used along with an adaptive meshing rule (0.5 times the preceding mesh size) applied to change the mesh size where needed to converge the solution appropriately, especially in the complex

structures (P1 to P7) considered in the study. The model was then validated using a set of experimental data from Jiang & Li [263]. Data from an experimental study by Deurig *et al*. [264], was used to validate the coupled superelastic-plastic behaviour of the model. The validated model was then used to study the effect of porosity in the superelastic region. In the last section, a microscale material model was used to study how the martensite volume fraction could affect the stiffness or Young's modulus of the NiTi material and predictions were compared with the macroscale results.

Table 2.1 shows the three different material data sets that were used for the analyses. The density was assumed to be the same for the three materials as 6.45 g/cm^3. For the macroscale study, a cube of geometry $5 \times 5 \times 5$ mm was modelled with uniaxial mechanical loading/unloading (tension/compression) for a deformation of 0.5 mm (10 % strain in fully dense model) at a constant strain rate of 0.1 min^{-1}. The bottom of the cube was fully constrained (fixed).

Table 2.1 Material data [47,263,264] used in the FEA models for determining the stress-strain responses.

Material	E_A (GPa)	v	σ_s^{AS} (MPa)	σ_f^{AS} (MPa)	σ_s^{SA} (MPa)	σ_f^{SA} (MPa)	ε_L
NT1	71.1	0.3	500	700	400	200	0.044
NT2	41	0.33	380	390	145	110	0.040
NT3	50.3	0.3	556	643	315	246	0.075

To study the effect of porosity, random cavities were incorporated in the $5 \times 5 \times 5$ mm geometry, as shown in Figure 2.2, to represent different porosity levels (presented in Table 2.1). The porosity levels are calculated by taking the fraction of void volume to the cube volume. The two common types of defect-based porosities seen in L-PBF processed NiTi are of process-induced and gas-induced types. Process-induced pores occur due to insufficient melting of powder particles; these are irregularly shaped and found around the edges. The gas-induced pores are usually spherical in shape, and are found well inside the volume; they occur due to the trapping of ambient gases [59]. Apart from these defect-based porosities, engineered porosity is often used in certain applications where porous structures are needed to reduce the amount of material used without affecting the performance of the component. Certain engineered porous structures often improve the biocompatibility performance through bone/tissue adhesion. Structures P1 to P3 can

represent the defect-based pore designs (taking into account the spherical and irregular pore formations). In Figure 2.2, these are presented as wireframe designs to visualise the inside of the cubes. Structures P4 and P5 represent a mix of defect-based and engineered porosities, where inner hollow profiles extend from one face to the other (completely extruded). P6 and P7 represent the engineered porous designs. These wide varieties of shapes are studied to have an overview of how design complexity and porosity levels affect the mechanical performance of NiTi components.

The microscale analysis was performed by creating a representative volume element (RVE) to simulate a NiTi microstructure. The microstructure was designed using a random particle RVE model in the *Material Designer* module in *ANSYS Workbench 2019*. The random particle RVE consists of spherical particles arranged randomly in a matrix material. Besides the position, the particle diameter was also randomly assigned following a uniform distribution between 20 μm to 70 μm (as in real NiTi microstructures).
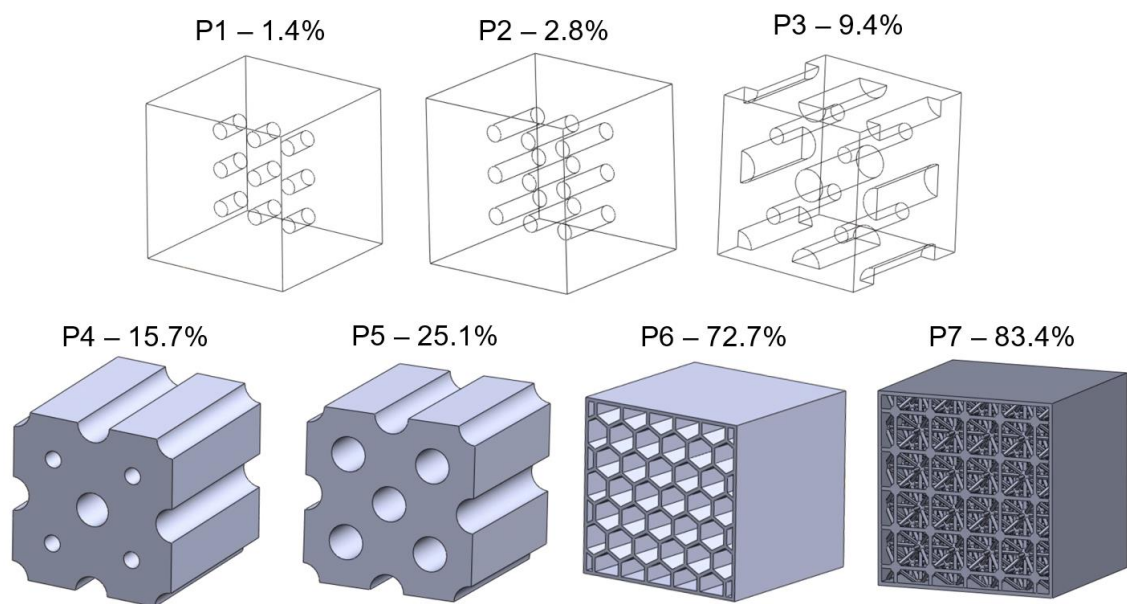
Figure 2.2 Porous structure designs showing the different types of cavities used; P1 to P5 varying degrees of cylindrical cavities; P6 – enclosed honey-comb structure; and P7 – lattice structure with 14-spokes per unit cell.

Table 2.2 Levels of porosity considered in the study; a fully dense cube volume is 125 mm^3.

Sample	Porosity (%)	Void Volume (mm^3)
Fully Dense (FD)	0	0
P1	1.4	1.77
P2	2.8	3.53
P3	9.4	11.78
P4	15.7	19.63
P5	25.1	31.42
P6	72.7	90.85
P7	83.4	104.21

Due to the requirement of RVE periodicity and creating a suitable mesh, the particle diameter was forced to be larger than a program-controlled minimum diameter. It was, however, smaller than half the unit cell size. The periodic displacement boundary conditions are more efficient in converging the results precisely, even if the RVE size is altered. Therefore, the RVE periodicity is essential even if the microstructure is non-periodic. The RVE is also assumed to have isotropic linear elastic matrix and particle properties. It is also assumed that the bonding between the particle and the matrix material is perfect.

Since we needed to simulate a superelastic NiTi, the matrix was considered to be austenite at room temperature. As the material is stressed, the martensitic transformation is expected to reconfigure the microstructure into a fully detwinned martensite. This concept is simulated by gradually increasing the martensite (particle) volume fraction in the austenite matrix from 0.1 to 0.9 (0 being fully austenite; 1 being fully martensite microstructure). To ensure randomness in the position of particles and precise prediction of properties, five sample points were considered in the simulation for each MVF values. A sample meshed RVE containing 0.9 martensite volume fraction (MVF) is shown in Figure 2.3.
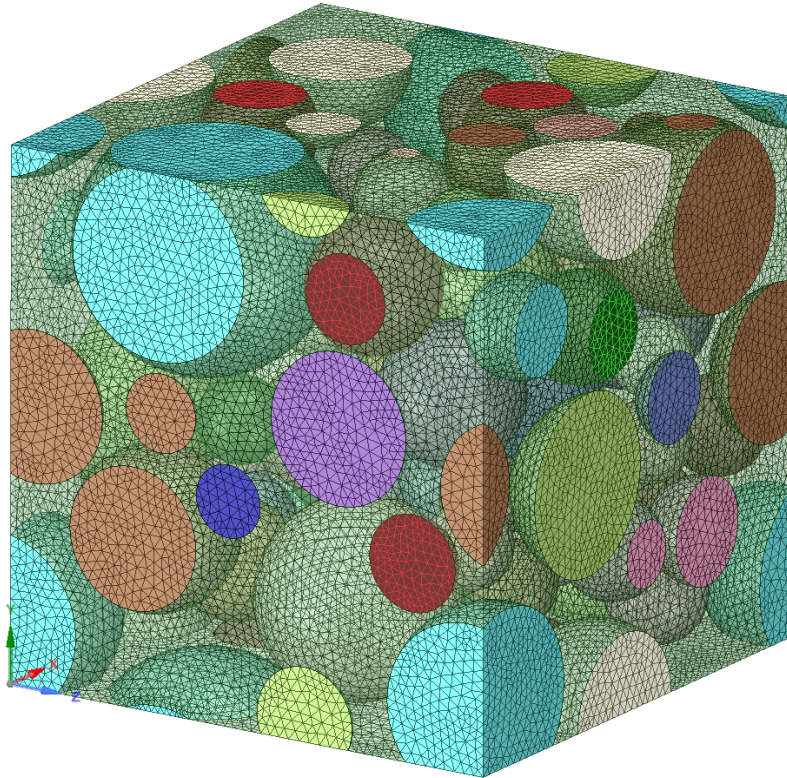
Figure 2.3 Random particle type RVE with a martensitic volume fraction of 0.9.

2.2.5 Mesh Convergence

Mesh convergence is necessary to verify whether the generated mesh is capable of converging an appropriate solution. Material NT1 was used to study the mesh convergence. The superelasticity model considered, traced almost similar curves for the different mesh sizes used (Figure 2.4). Therefore, to distinguish the effect of mesh sizes, two factors were considered based on theoretical observations – insufficient-convergence regions, and stress values at 4 % strain.

Insufficient-convergence regions – As seen in Figure 2.4, larger mesh sizes show some anomaly at the start/end of phase transformations. These can be considered as the non-convergent regions in the solution. It was observed that mesh sizes from 0.5 mm and below did not show any insufficient-convergence region.
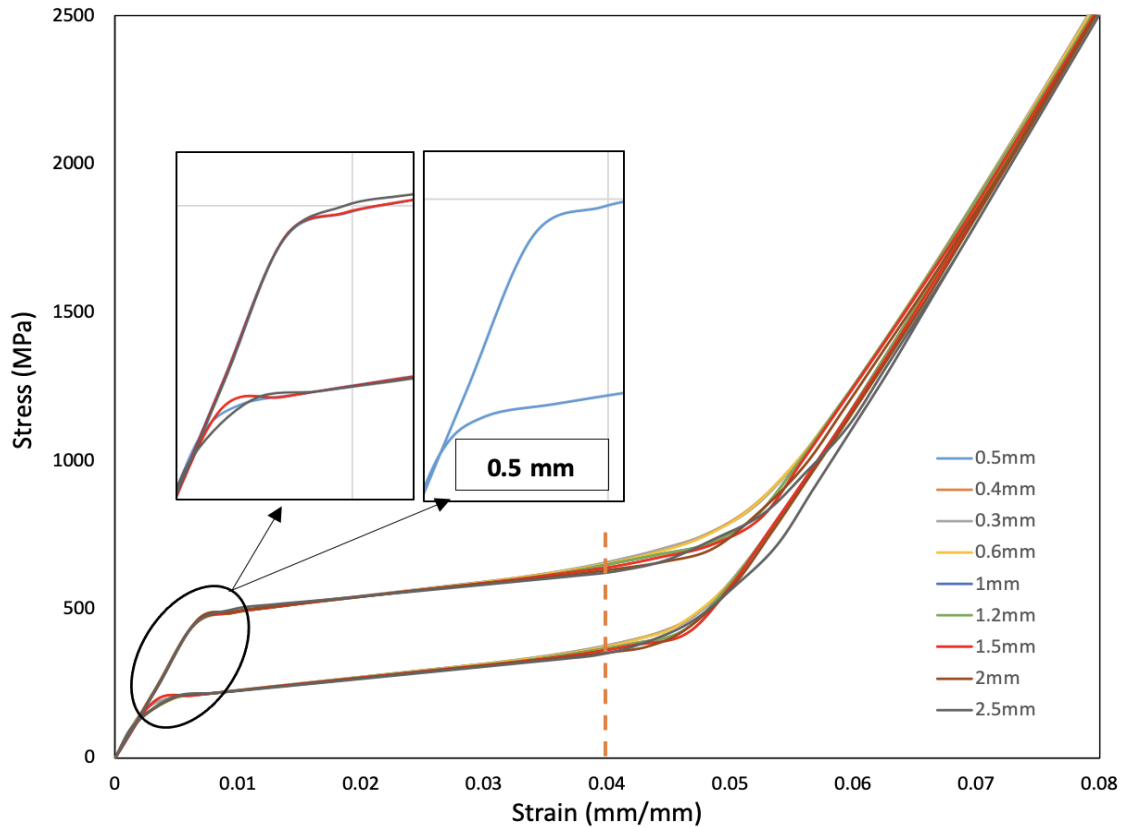
Figure 2.4 Stress-strain graph for mesh convergence study.

Stress at 4 % strain – In Figure 2.4, a noticeable difference in stresses can be seen around the strain value of 0.04 and above. Stress values at 0.04 strain for different mesh sizes are shown in Figure 2.5. It can be seen that the stress values stabilize with low error value around an initial mesh size of 0.6 mm. Even though a mesh size of 0.6 mm was efficient, 0.5 mm showed better convergence and lower error % (Figure 2.5). Lower mesh size gives better prediction; however, the computational time was almost doubled when the initial mesh size was reduced from 0.5 mm to 0.4 mm. Therefore, an initial mesh size of 0.5 mm was selected for macro-scale analysis. While it not fully clear why the error is lower at 0.5 mm, this could be a discretization error from the mesh creation, numerical errors from integration or rounding errors from numerical calculation.
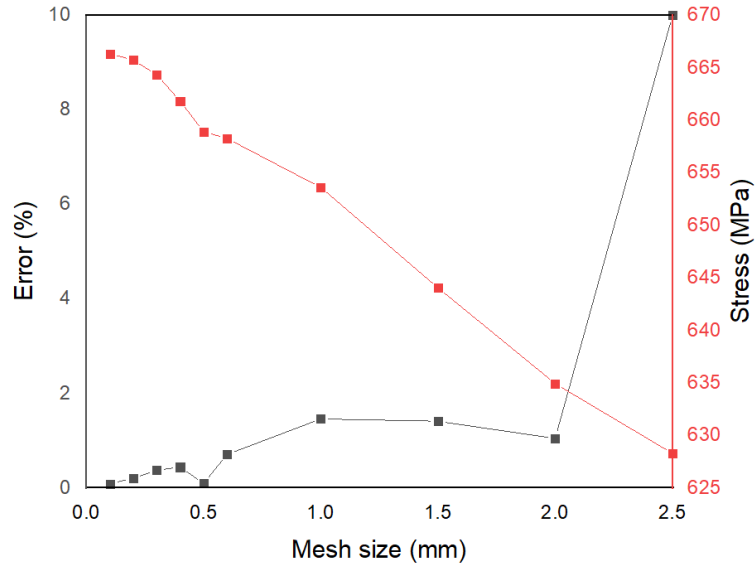
Figure 2.5 Stress values (red) at 4 % strain and respective error % (black) for different mesh sizes.

2.3 Results

2.3.1 Model Validation

Initially, the Auricchio superelasticity model was validated using the experimental data from material NT2 following the same boundary conditions. As seen in Figure 2.6, the FEA model traces a similar curve to that of the experimental one.
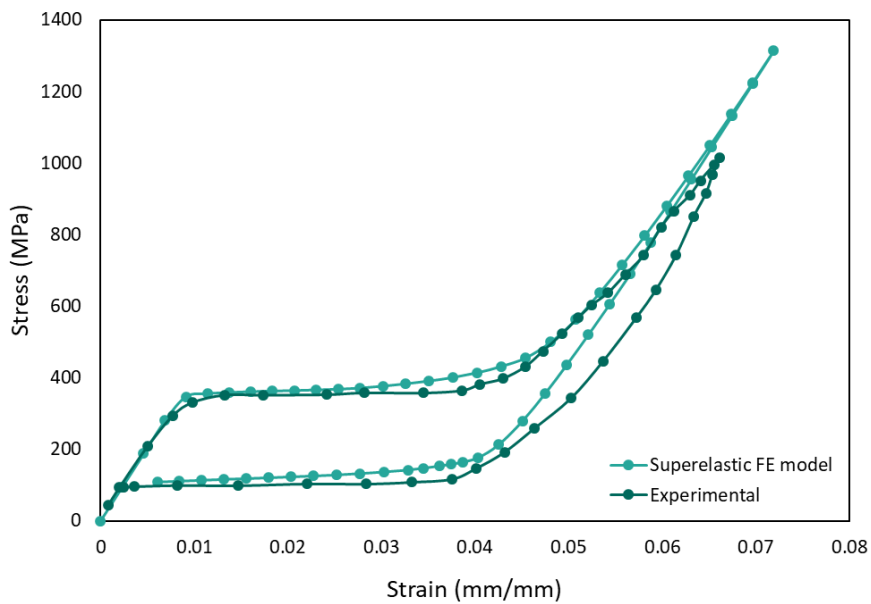
Figure 2.6 Validation of superelasticity model with actual experiment by Jiang & Li [263].

Plasticity in superelastic NiTi is not of a prime interest in most applications as the strain levels applied are generally well within the yield limit of the material. In the current work, a combined superelastic-plastic model was considered to simulate plasticity. The experimental data (NT1) from Deurig *et al*. [264] has been used for this validation. One of the limitations of the Auricchio model is that the plastic data cannot be coupled in the material data, as it is composed exclusively for superelastic behaviour. Therefore, non-linear isotropic hardening data from the experiment was input into the material data to simulate the plastic region, and two discrete simulations were performed with different strain limits under the same straining conditions. After obtaining the plasticity and superelasticity data discretely, the output data were combined to represent the coupled mechanical behaviour. This approach of combining the output data was based on the concept that the initiation and evolution of two distinct yield profiles can be used to fully capture the martensitic transformation and plastic slip yield simultaneously [265–267]. A detailed model can include two limit functions to define both the phase transformation domain and plastic domain for predicting cycling effects and accumulation of inelastic strains. As presented in Figure 2.7, the plastic region always lies after a complete martensitic transformation, inferring that the superelastic phenomenon is distinct (analogous to the elastic region in steel), until the strain limit for plastic deformation has been reached. The plastic deformation was modelled to be triggered after the martensite phase was attained in the matrix (Figure 2.7). The coupled behaviour of the FE model is shown in Figure 2.8; the curve traced is close in shape and magnitude to that of the experiment with slight stress offsets.
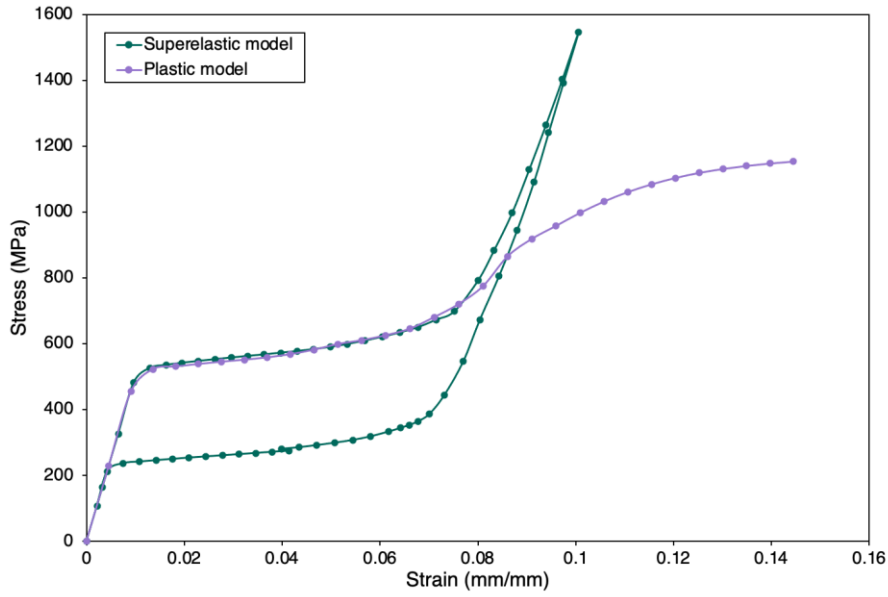
Figure 2.7 Discrete superelastic model and plastic model simulated results.
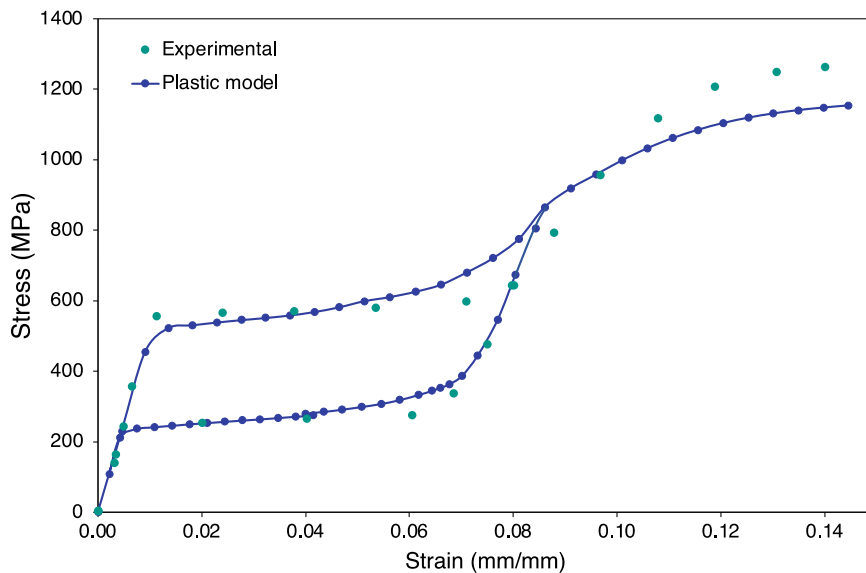
Figure 2.8 Comparison of experimental data and combined plastic model.

2.3.2 Response to Strain Levels

The response of the model to different strain levels was explored under a constant strain rate of 0.1 min^{-1} using the material NT1. As seen in Figure 2.9, when the cube experienced a low strain of 3.5 %, a partial phase transformation occurred, similar to what is found in an actual mechanical test. A 6 % strain generated a complete martensitic transformation, while a 10 % strain progressed with straining in the elastic region of detwinned martensite phase after completing the phase change.
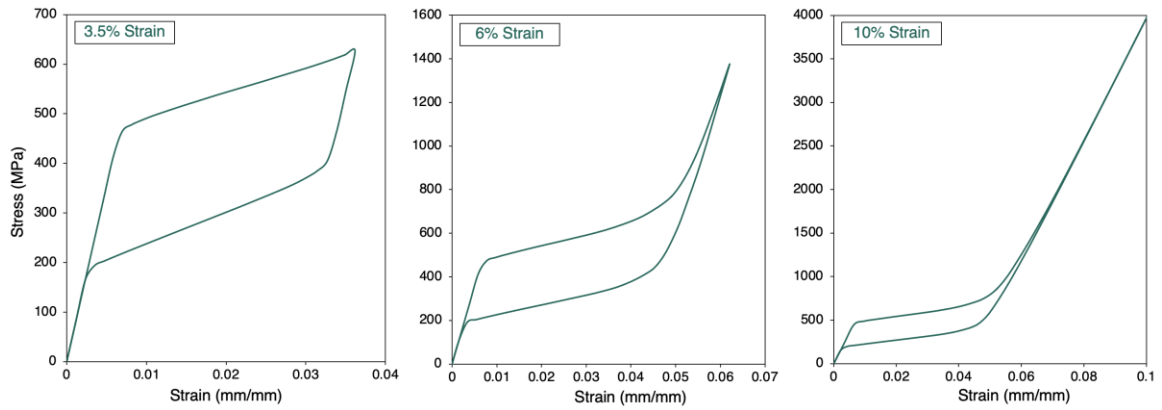
Figure 2.9 Stress-strain curves for different strain levels: 3.5 %, 6 %, and 10 %.

2.3.3 Asymmetry in Tension and Compression

It is often observed that the stress-strain curves generated during actual compression tests are slightly different when compared to the tension tests. This asymmetry can also be simulated in the Auricchio model using a factor, $\propto$ as defined in Equation 2.1. The simulation was performed using material NT1. $\propto$ is varied from 0 (symmetric) to 0.08, where $\propto\; = 0$ represents tension mode stresses. Figure 2.10 shows the asymmetric variation of compression curves with respect to tension, where the compression mode stresses are higher compared to the tension ($\propto\; = 0$).
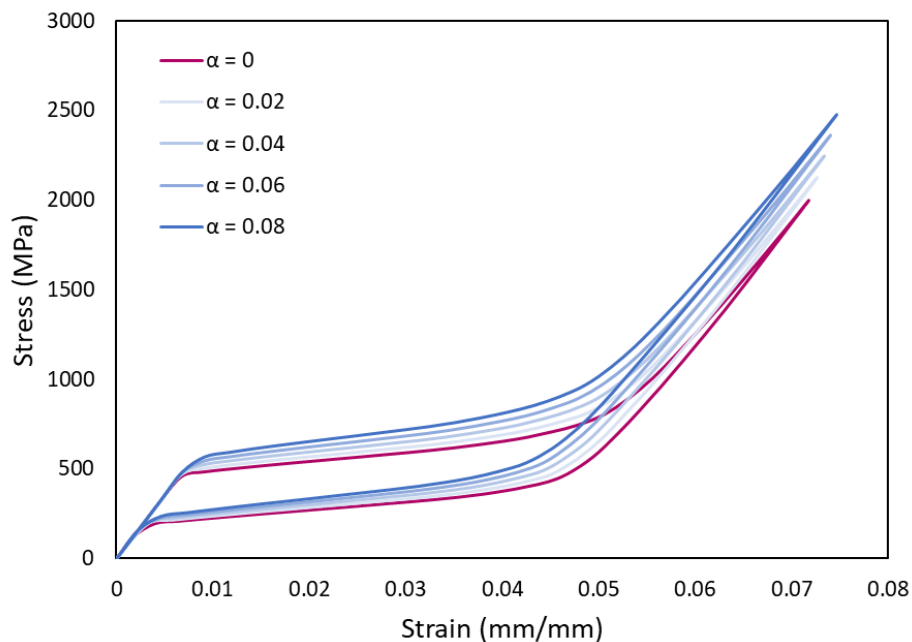
Figure 2.10 Stress-strain curves showing asymmetry between compression and tension.

2.3.4 Compression of Porous Structures

The superelastic FE model was used to simulate the mechanical behaviour of the porous NiTi structures shown in Figure 2.2, using material NT2. All input and boundary conditions were maintained to be similar to that of the fully dense part. The stiffness of the structure was calculated using the slope (martensitic elastic modulus) of the loading curve after complete phase transformation. The unloading curve is of less interest, as this is highly affected by the hysteresis that occurs. The generated stress-strain curves are shown in Figure 2.11.
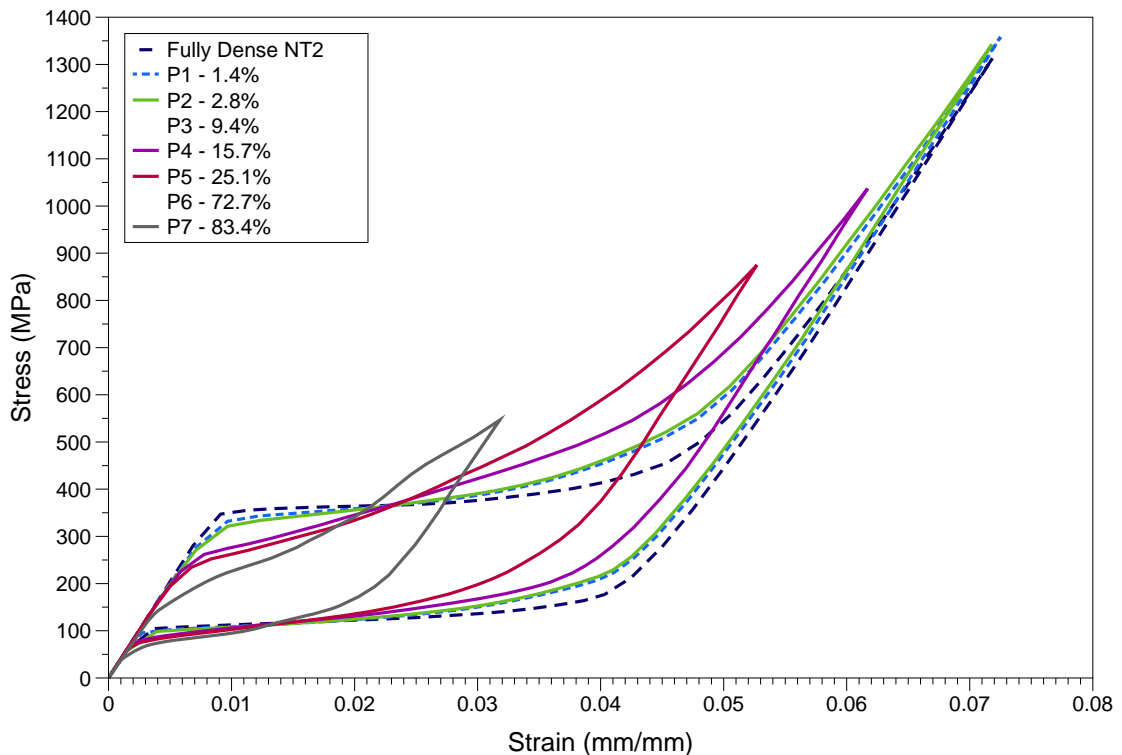
Figure 2.11 Simulated stress-strain curves for fully dense and porous NiTi structures.

As shown in Figure 2.12, the structural stiffness was found to decrease drastically initially until 15 % porosity, after which the gradient lowered and small reductions in stiffness were noted. The reduction in stiffness was found to be about 14 GPa for 83.4 % porosity. Overall, the decrement in elastic modulus of the structure was seen to be more of an exponential trend. In contrast to the Gibson–Ashby analysis [268] of porous structures, which states a quadratic relation between the elastic modulus and porosity, the current study reveals a fourth order polynomial as shown in Figure 2.12. This could be due to some geometric effect (for instance, lattice vs cylindrical voids) in play when the material

deforms. As the porosity levels increased to 83.4 %, the dissipated energy (W_D) decreased by about 8 J/m^3 accompanying a reduction of about 200 MPa in stress levels and a reduction of about 0.063 in strain levels. No particular trend could be interpreted between the levels of porosity and this reduction in dissipated energy. These factors play a major role in depicting the efficacy for heat pump applications.
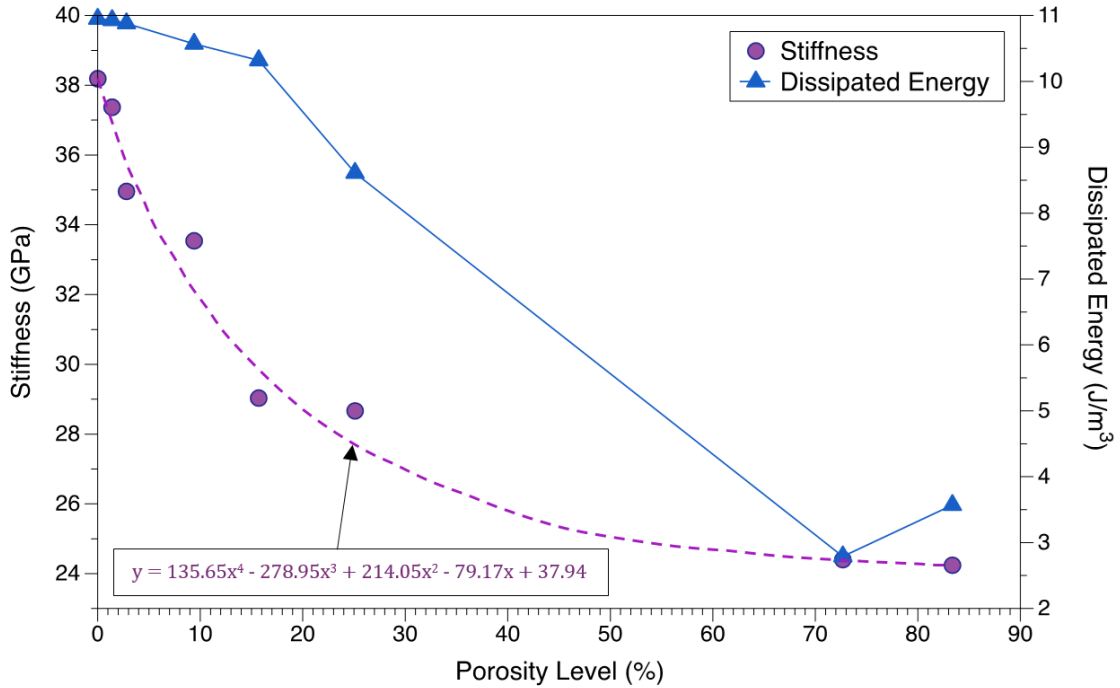
Figure 2.12 Variation of stiffness and energy dissipated per unit volume per cycle, with the increasing levels of porosity.

For the same porous structures, the energy absorbed (W_A) during a linear stress loading for the same maximum force and deformation was also obtained using the methodology shown in Figure 2.13a. W_A and W_D can be used to calculate the damping ratio (ξR), also known as loss factor as in Equation (2.17), to estimate the damping property of the structure when an external stress load is given. The slope of the W_A triangle gives the apparent stiffness of the structure which considers the maximal strain point [269]. The damping ratio and apparent stiffness are of high relevance to shock absorption applications.

$$\xi R = \frac{1}{4\pi} \frac{W_D}{W_A} \tag{2.17}$$

Referring to Figure 2.13b, the damping ratio was generally found to increase when porosity increased, and a sudden fall was noted for 83.4 % porosity. There was also a

minor decrease in ξR for low porosities compared to the fully dense structure. Although no specific trend was found between the apparent stiffness and porosity levels, there was a general rise in stiffness values for structures with more uniformly spread cavities.
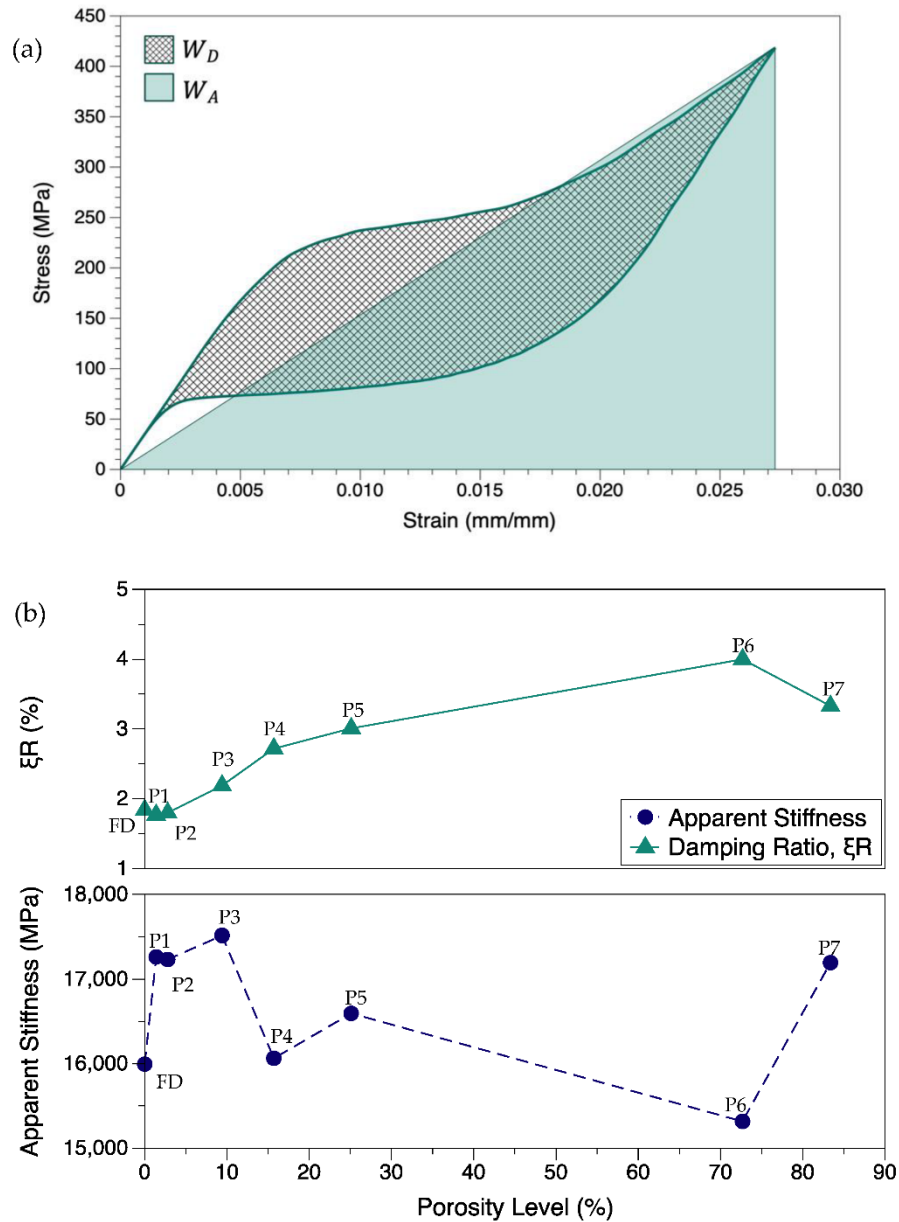
Figure 2.13 (a) Illustration of obtaining the dissipated and absorbed energy from stress-strain curves; **(b)** variation of damping ratio (ξR) and apparent stiffness with the increasing levels of porosity.

2.3.5 MVF vs Elastic Modulus

In this section, the effect of martensitic phase transformation in the matrix on material stiffness was explored using a microscale RVE model. The mechanical properties of NiTi

is primarily dependent on the material composition and phase structures, resulting from various factors including processing techniques, and thermal and mechanical histories. The current study considers the material composition exclusively to estimate an upper bound and a lower bound for the material stiffness of NiTi alloys. As presented in the ASM handbook [224], the composition of Ni varies from 54 to 56 wt. % for NiTi alloys, and therefore these composition limits were taken into account. The Young's modulus for Ti is lower (110 GPa) compared to Ni (210 GPa), hence higher Ni content in NiTi would result in higher elastic moduli. For 56 wt. % NiTi, the stiffness data from ASM handbook [224] was used to represent the upper bound. However, for the lower bound, data from NT3 was used as the material presents a lower E_M and there were no sufficient data for the 54 wt. % NiTi in ASM handbook. Presenting the data using these upper and lower bounds (Table 2.3) will enhance the understanding of how the stiffness may vary within the compositional range and martensite phase volume fraction.

Table 2.3 Upper/lower bound values of stiffness with respect to Ni content in NiTi used in RVEs

	E_A (GPa)	E_M (GPa)	ν
Upper bound (56 wt. % Ni)	83	41	0.3
Lower bound (54 wt. % Ni)	50.30	23.59	0.3

The modulus of elasticity (stiffness) is calculated on the premise that the RVE presents a homogenized microstructure. Initially, the matrix is fully austenite (0 MVF), and the resultant stiffness is equal to E_A. As martensitic transformation takes place, the martensite phase starts to form in the microstructure, gradually decreasing the stiffness as shown in Figure 2.14. When 1 MVF is reached, the material is fully martensite, and the resultant stiffness is equal to E_M. Irrespective of the material composition, a gradual decrease of stiffness was observed until 0.5 MVF, and then the stiffness starts to stabilize until 0.9 MVF, and then decreases rapidly towards 1 MVF point.
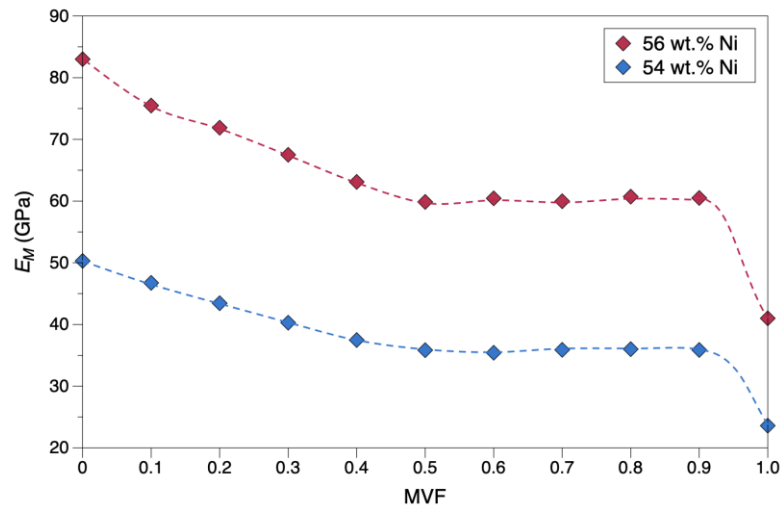
Figure 2.14 Effect of martensite phase evolution on the stiffness of NiTi for the two Ni contents.

2.4 Discussion

In the actual experiment, the hysteresis between loading and unloading curves is more than the simulated results. This can be due to the reorientation of martensite phase (explained in Section 1.2.3 on Kinematics of Phase Transformations) and the presence of residual martensite phase while unloading. In the current FE model, the possibility of residual martensite is ignored, and only the reorientation of martensitic phase is considered, resulting in a lower hysteresis. The hysteresis and stress levels in actual experiments will gradually decline and stabilize after a certain number of cycles [265]. The validated model was then used to study the mechanical behaviour in more detail.

2.4.1 Mechanical Strain

When the compression was simulated (Figure 2.9) for different strain levels, partial and complete transformations were observed. Partial transformation and recovery are also associated with martensite reorientation, as that in complete transformation (within the martensitic elastic limit). Since the plasticity is ignored in this discrete model, the effect of plastic deformation is not accounted for.

When tension and compression modes for the same strain conditions are observed (Figure 2.10), we can see higher stress values in compression compared to the tension mode. Generally, a volume rise is associated with the martensitic reorientation and transformation, that results in a crystallographic asymmetry [77,270]. This induces a

lower stress requirement to generate the transformation in tension than in compression mode. The $\propto$ value depends on the material properties, specifically the thermal and mechanical history that could affect the lattice.

2.4.2 Structural Porosity

Contrary to the 14 GPa drop in stiffness observed as porosity increased to 83.4 %, in bone-implant applications, the reduction in stiffness is much higher for similar levels of porosities. This can be attributed to two reasons. One reason is the fact that the current model does not include the martensite elastic modulus as an input parameter, rather the elasticity of martensite depends on austenite stiffness, elongation strain, and transformation parameters. The second reason is suspected to be the cavities/pore designs considered in the current study. In actual components, these are more lattice-like and uniformly spread throughout the volume, in contrast to the ones considered in the current study.

In renewable energy applications for heat pumps, these porosity levels increase the surface area of the structure that contacts the working fluid, resulting in increased heat conduction/transfers. In conventional designs, the NiTi component is designed with channels inside to facilitate the passage of working fluid. These channels are less efficient compared to the higher porosities that can be engineered via L-PBF. The performance of a heat pump is generally represented by the coefficient of performance (COP) in Equation (2.18). The work done by the material (Q_{out}) can be determined by calculating the area contained within the martensitic transformation region (enclosed by the loading and unloading curve) on the stress–strain curve. This is also referred to as the dissipated energy per cycle or enthalpy [46]. Q_{in} is the latent heat energy required for the martensitic transformation (obtained from Differential Scanning Calorimetry analysis).

$$COP = \frac{Q_{out}}{Q_{in}} \tag{2.18}$$

It was seen that the porosity levels induced lower enclosed area under the martensitic transformation curve (indicating lower Q_{out}). As mentioned earlier, the simulations of these porous structures were conducted for 0.5 mm deformation, similar to that of the fully dense component. Structural porosity results in a lower resultant cross-sectional area and length compared to the fully dense part, and this has contributed towards an effective reduction in the stress and strain levels. No significant trend was noted for energy

dissipation with respect to porosity. This could be attributed to the possibility of different resultant cross-sectional areas and lengths for the same levels of porosity. It should also be noted that a further reduction in mechanical properties takes place when the component is deployed in the high temperature ambient conditions prevalent in heat pumps. For example, a decline of about 10 GPa in ultimate strength was observed when temperature was increased by 200 K from room temperature [271].

The dissipated energy is not a material property as it hugely depends on strain levels, and the associated microscale mechanisms are generally non-linear. When deformation progresses, the strain increases, requiring more energy which, at the end, is dissipated. In a practical aspect, this maximum strain should be decided appropriately to get higher COP. A complex porous structure, which can be realized via L-PBF, is highly beneficial in reducing material volume compared to a fully dense component, however, the lower cross-sectional area affects the Q_{out} and in turn affects the COP. However, a complex structure such as P6 and P7 might have lower stress limits that could affect the structural strength and operational integrity. Compared to most lattice structure topologies, the design of P7 (14-spoke lattice) possesses a higher mechanical strength (Poisson's ratio and elastic modulus) [272]. To summarize, an all-embracing balance should be devised between the surface area (porosity) in contact, stress compensations, and maximum strain levels in order to achieve a high COP.

The dissipated energy due to mechanical hysteresis is also highly relevant in the shock absorption applications such as vibration, impact, and seismic shock dampers. These applications often undergo dynamic loading. The mechanical hysteresis of NiTi enables absorption of the external load. As shown in Equation (2.17), ξR gives an estimate of the damping capabilities of the NiTi structure. The damping is also enabled by martensitic reorientations and is found to depend on the size and structural design [270,273].

The loss factor ξR is usually found to vary between 8 % and 53 % for full-scale analysis. In the current study, due to the small sample size, ξR is much lower (1.8 % to 4.0 %). It can be seen that the porous structures provide better damping property. Besides SIMT, martensitic reorientations and twin boundary motions also mechanize the damping/self-centring effects [270,274]. The two latter mechanisms are not considered in this study. The porous structures are susceptible to anisotropic mechanical responses such as localized plastic deformation or detwinning effects. These can also affect the hysteresis

region, which can affect both W_A and W_D. A higher W_A and lower W_D results in higher ξR. Proper selection of heat treatment parameters can enable lower phase transformation stresses and austenitic elastic moduli. This can enable a lower W_D.

For porous structures, the out-of-plane elastic modulus will be different to the in-plane elastic modulus [274]. Similarly, these could be different from the martensite elastic modulus. Therefore, the apparent stiffness that takes into account the maximum force and deformation represents the effective stiffness of the structure during operation. The apparent stiffness will generally increase, when the material undergoes cyclic loading eventually leading to mechanical stability. This factor helps in identifying the mechanical strength of the structure for shock-related applications. In the current study, the similar deformation input resulted in varying degrees of strains and stresses for different porosity levels. This has resulted in different apparent stiffness values ranging from 15.3 GPa to 17.5 GPa. In general, the values were comparatively higher than that of the fully dense part.

Due to localized deformation heterogeneity in porous structures, the geometry of the component is critical for apparent stiffness and loss factor calculations. This might have played a key role in generating a lower apparent stiffness for P6 and a lower ξR for P7. To summarize, the structures with 10 % to 30 % porosities showed a good balance between structural stiffness, W_D, ξR, and apparent stiffness.

2.4.3 Martensite Evolution vs. Stiffness

An RVE-based analysis of elastic modulus variation with respect to martensite evolution in the microstructure was investigated (Figure 2.14). A gradual reduction until 0.5 MVF and then a level off was seen until 0.9 MVF. This might be because the particle-matrix system is homogenized, and a value of 0.5 MVF denotes martensite phases being uniformly saturated until 0.9 MVF (almost martensite). Referring to the stress–strain curves in Figure 2.15, it can be seen when phase transformation occurs. The crystal structure evolves from BCC to monoclinic structure, causing an increase in strain with a marginal rise in stress. We can see that near the end of martensitic transformation ($0.9 <$ MVF < 1), a larger change in stress occurred compared to initiation (0.1 MVF) or propagation (0.2 to 0.8 MVF) of martensitic transformation. Until the matrix is almost entirely martensite, the austenite stiffness is predominant. This dominance is rapidly degraded as the matrix transforms to complete martensite ($0.9 <$ MVF < 1), and this is

noted by a rapid decrease in stiffness, attaining a value equivalent to the Young's modulus of martensite phase.
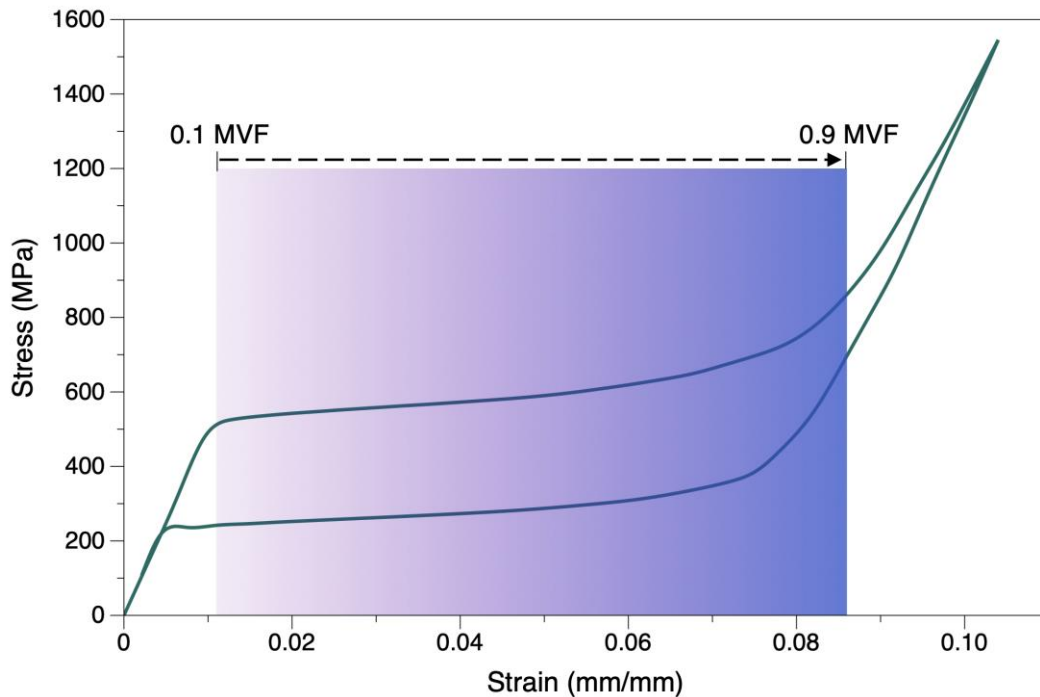
Figure 2.15 Stress-strain curve to illustrate the evolution of martensite phase during stress-induced transformation (SIMT) via stiffness slopes.

The initial transformation in superelastic NiTi is partially triggered by the surface energy to create an interface, and partially via the elastic energy of the accommodation of martensite in the austenite matrix. This causes a reduction in free energy, and therefore, the nucleation of martensite phase usually requires a higher driving force than the subsequent propagation of the austenite-martensite interface. The size and shape of a martensite nucleus is governed by this free energy reduction [90,91]. This could also explain the rapid change in modulus values (0.7 to 0.9 MVF) noted in the stress–strain curves. It is noteworthy that the martensite evolution is high in the regions of stress concentrations in porous structures. Under stresses, these regions will have a higher MVF compared to other regions in the bulk. This principle is also applicable in the case of porous structures, where martensite evolution will be abrupt around the pore regions.

2.5 Conclusions

An Auricchio material model was used to simulate the mechanical behaviour in NiTi alloys and perform macroscale study of the mechanical response at various porosity levels. The model was shown to provide close predictions of real material behaviour,

capable of responding to different strain levels, and asymmetry in tension and compression. It was found that an increase in porosity of up to 83.4 % resulted in a reduction of about 14 GPa in the structural stiffness. The dissipated energy during the phase transformation was reduced by about 8 J/m^3, along with a stress reduction of about 200 MPa and strain decrease of 0.063. The damping ratio increased from 1.8 % to 4.0 % with an increase in porosity. The apparent stiffness for damping operations showed no trend, however, exhibited a general rise in porous samples compared to the fully dense sample.

The stiffness for the austenite phase is generally higher than the martensite phase. The SIMT results in temporary softening of the material. A microscale model using RVE was created to study the gradual decline in stiffness as the martensite phase evolved (increasing the MVF). This was then compared to investigate the response in macroscale analysis; the larger curvature in stress–strain curve near the end of transformation corresponded to a sudden drop in Young's modulus. It is known that L-PBF process parameters affects the microstructure and chemical composition of NiTi. This affects the transformation characteristics, which results in varied energy absorption levels in the structure. This will also affect the operational limits in heat pump applications.

The current model was not built to simulate the thermal or stabilization effect during mechanical cycling. Usually, during the first cycle, the microstructure is modified and self-oriented, and a residual deformation is observed. This residual deformation will propagate until the mechanical curve stabilizes. For shock absorption applications, a lower residual deformation and higher strain recovery is desired. The model is not sufficiently sensitive to the martensite stiffness changes. This low sensitivity was reflected in a lower reduction of structural stiffness for the same porosity levels compared to real-world observations. The developed model does determine how the phase structure results in specific mechanical responses, which can be run in a reasonable period. Thus, this modelling method is highly useful for determining the stress–strain response of NiTi SMAs.

2.6 Contribution to Thesis Objectives

The effect of porosity on mechanical properties was investigated along with how phase fractions affect the elastic modulus of the NiTi structure. Even though the analysis was performed on austenitic NiTi, the findings can be applied to martensitic NiTi also. In later

studies of this project, it was found that the porosities in L-PBF processed NiTi posed a great influence on the material response. In this chapter, the mechanical responses were focused, and the results are used to support the findings in the following chapters. Moreover, the findings from this chapter are applicable in heat pump and shock absorption applications where L-PBF can aid in producing complex NiTi structures. The trend of effect of structural complexity and porosity levels on energy dissipations and shock absorption metrics presented in this work are relevant for engineers.

Chapter 3

Control of NiTi Phase Structure, Solid-State Transformation Temperatures and Enthalpies via Control of L-PBF Process Parameters

3.1 Abstract

In this work, NiTi samples were produced via Laser Powder Bed Fusion (L-PBF) in the horizontal (H-built) and vertical (V-built) orientations with systematic variations in laser power, scan speed and hatch spacing parameters. Increased density was positively correlated with increased laser power, scan speed and hatch spacing for the horizontally built samples but not for the vertically built samples. A smaller difference in the average temperature within a printed layer, associated with the vertically built samples, was linked with reduced porosity and reduced porosity variability between samples. Control of the L-PBF parameters was found to allow control of the resulting part chemical composition which also directly affected phase transformation temperatures, and related phase structures. The laser process parameters were found to have a significant effect ($p < 0.01$) on the martensite start/finish temperature, austenite start/finish temperatures, and the total temperature span. The volumetric energy density was also found to have a direct correlation with both the cooling ($r = 0.52$) and heating ($r = 0.53$) enthalpies, which was found to be due to increased nickel evaporation. Such control of phase change properties afforded from L-PBF is important for many of the end applications for NiTi components including within the energy and precision actuation sectors.

3.2 Materials and Methods

3.2.1 Powder Material

The NiTi powders with a composition of Ni (49.9 at. %) – Ti (50.1 at. %) were supplied by Ingpuls GmbH, Germany. The higher Ti content was chosen in order to ensure that, after L-PBF, the shape memory NiTi phase change temperature was above room temperature. The composition was re-confirmed through an energy dispersive x-ray spectrometry (EDX) unit attached to a *Hitachi S5500* field emission scanning electron microscope (FE-SEM). To produce powders of suitable size and shape for L-PBF, the as-received powders were gas-atomised by electron induction melting inert gas atomisation (EIGA). The particle size distribution (PSD) was $D_{10} = 12.3$ μm; $D_{50} = 28.1$ μm; $D_{90} = 57.3$ μm, where D_{φ} represents the diameter of the powder particles corresponding to the "φ" volume percentage of particles present. The PSD was re-analysed using a *Malvern Mastersizer 3000* with an *Aero S* dispersion unit. The analysis was carried out using a refractive index of 1.958, and a particle absorption index of 1. The air pressure was set to 1 bar to prevent any particle aggregation and searing. Powder morphology was

investigated using a *Zeiss EVO LS-15* SEM machine. The phase transformation temperatures of the as-received powders were also analysed, using a *Netzsch DSC 214* digital scanning calorimetry (DSC) following the ASTM F2004-17 standard, with liquid nitrogen for the sub-zero temperature range.

3.2.2 L-PBF Process

NiTi samples were 3D printed using the *Aconity MINI (GmbH)* SLM machine equipped with a Nd:YAG fibre laser system from *IPG Photonics* having a wavelength of 1068 nm, and a maximum power capacity of 200W. The build chamber was installed with a rubber-based recoater blade. The chamber was flooded with argon gas (99.999 % purity) to ensure minimum oxygen content (< 50 ppm) throughout the printing process to reduce the chance of oxidation during melting and solidification. A powder supply factor of 1.8 (nearly twice the layer thickness) was used throughout the print to ensure a sufficient spreading of powder. In order to reduce spatter on fresh layers, the print sequence started from the inert gas exit side of the build chamber.

In order to reduce time, energy and material consumption, a Box-Behnken (BB) design of experiments (DoE) containing three factors (laser power, scan speed, hatch spacing) with three levels was followed, keeping layer thickness (40 μm) and spot sizes (50 μm) constant. The BB design includes sample production for repeatability analysis with the centre node repeated five times. Due to the intrinsic repeatability (5 repetitions of centre node), this DoE do not require sample repetitions as needed in a full-factorial DoE, thereby reducing material, time and energy consumption. However, the fewer design points in this DoE does not include an embedded factorial design, and this limits the sequential studies of factors and process repeatability of destructive tests. Samples with these 17 sets of process conditions for each build orientation (Prefix: Horizontal – H; Vertical – V) were printed as shown in Figure 3.1. The sample dimensions were $10 \times 10 \times 55$ mm. Laser powers of 120, 150 and 180 W were used along with scan speeds of 600, 800 and 1200 mm/s, and hatch spacings of 40, 55 and 70 μm. The layer thickness of 40 μm was set based on the feedstock particle size distribution, to help ensure good powder spread and flowability on the build platform. The current design space (including the upper/lower levels) was selected based on thorough review of past research works towards achieving shape memory effect in NiTi.
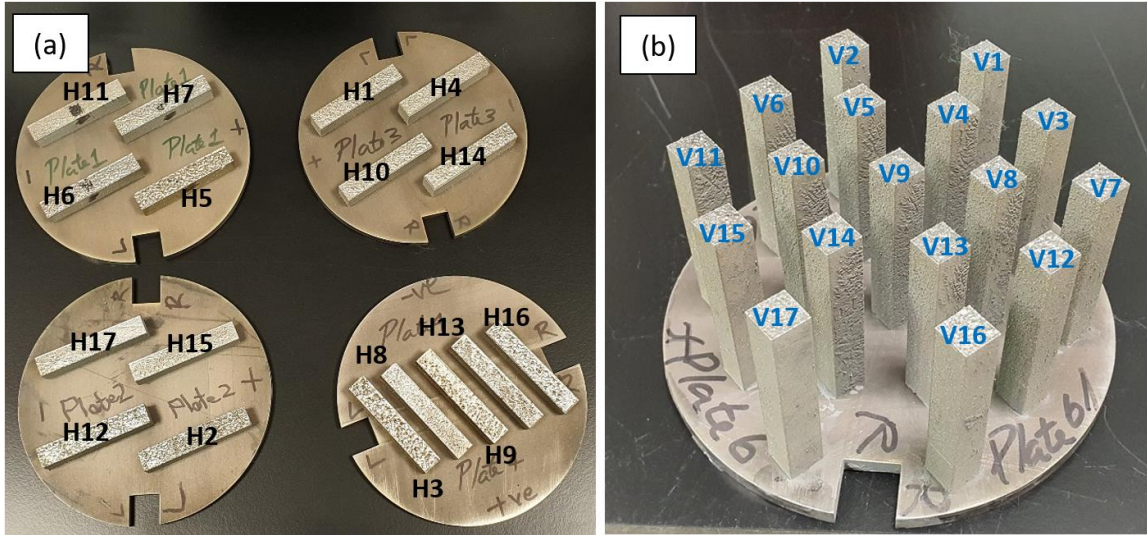
Figure 3.1 NiTi samples as printed on the NiTi build plate - H-built samples (a); V-built samples (b); prefix: H-horizontal / V-vertical.

These parameter sets can be used to calculate the volumetric energy density, VED, which can be calculated as Equation (3.1):

$$VED = \frac{P}{v \times h \times t} \tag{3.1}$$

where, P is the laser power (W); v is the scan speed (mm/s); h is the hatch spacing (µm); and t is the layer thickness (µm). The VED can be explained as the energy released from a unit volume of material during the L-PBF process. It can also be defined as quantifying the thermal energy readily available for the material to transit from powder state to a dense state [275]. For the current range of process parameters, the VED varies from 44.64 to 156.25 J/mm^3. Table 3.1 shows the complete set of process parameters in the DoE that were used to print the samples.

Table 3.1 Laser process parameters used for printing the NiTi samples.

Sample no. (V/H)	Laser power (W)	Scan speed (mm/s)	Hatch spacing (μm)	VED (J/mm³)
1	150	900	55	75.76
2	120	600	55	90.91
3	180	600	55	136.36
4	180	1200	55	68.18
5	150	600	40	156.25
6	150	900	55	75.76
7	150	1200	40	78.13
8	180	900	70	71.43
9	180	900	40	125
10	150	900	55	75.76
11	150	1200	70	44.64
12	120	900	40	83.33
13	150	900	55	75.76
14	150	900	55	75.76
15	120	1200	55	45.45
16	150	600	70	89.29
17	120	900	70	47.62

The samples were arranged on the substrate plate at an in-plane angle of 45° for V-built samples, and 30° for H-built samples, in order to reduce any impact load on the recoater assembly, and to allow a more gradual gas flow/fume removal over the layers in the chamber during print. A simple stripe scanning strategy was maintained as shown in Figure 3.2a with a rotation of 90° for each subsequent layer. This prevents any unwanted overheating around the corners of the sample. The build chamber ambient temperatures during the process were 20 ± 1 °C.
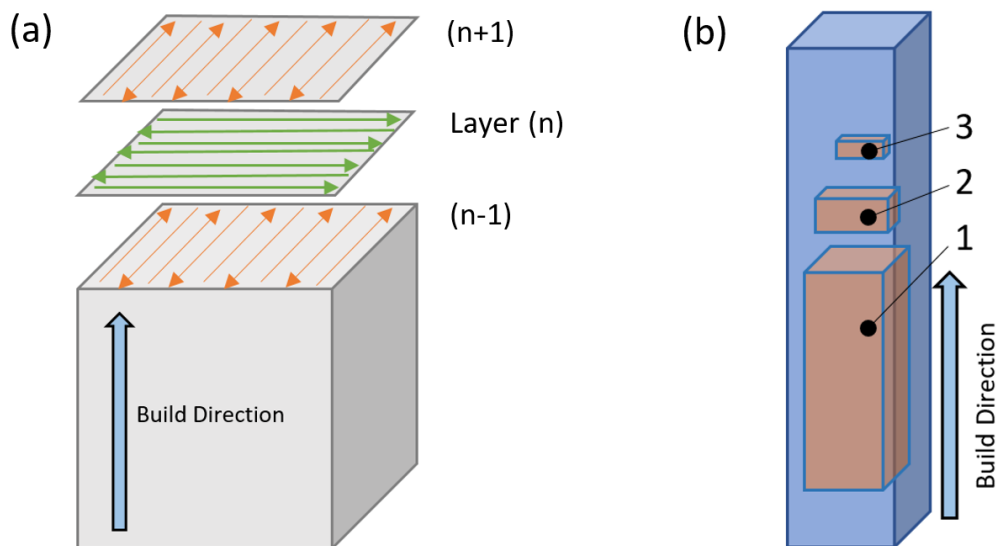
Figure 3.2 (a) Scanning strategy illustrated showing the 90° rotation between each layer and scan direction reversal; **(b)** position of samples cut from the printed parts for various characterisations (1 – dilatometry; 2 – SEM/EDX; 3 – DSC)

3.2.3 Sample Characterisation Methods

The densities of the as-fabricated H/V samples were measured by Archimedes principle following ASTM B962-17 with the help of an analytical balance, *Sartorius Entris II Essential BCE124I-1S*, having an accuracy and repeatability of ± 0.1 mg. The samples were ground lightly to flat on all faces with 240 grit abrasive paper, and cleaned thoroughly. The weights of samples were measured in acetone, and densities were calculated. For the following characterisation methods, only V-built samples were analysed, and no post-fabrication heat treatments were performed prior to analysis. The samples for different characterisation methods were extracted as shown in Figure 3.2b, these sub-parts were cut using diamond-infused blades with at constant slow traverse speed, to avoid excess heat or stress-induced microstructure alteration. DSC thermal analysis was performed on the 17 samples to obtain the heat flow properties and phase transformation temperatures. The thermal cycle conducted was from – 60 °C to 130 °C, and then cooled back to – 60 °C, maintaining a heat/cool ramp rate of 10 °C/min. The sub-zero temperatures were attained using liquid nitrogen. The same process cycle was followed for the powder samples as well. The L-PBF samples were prepared and tested adhering to the ASTM F2004-17 standard.

Dilatometry tests were conducted to identify the thermal expansion coefficients (*CTE*s) and phase changes. For this, samples of dimensions 20 x 10 x 7.5 mm were prepared with

very flat, smooth and parallel surfaces for the dilatometry test which was conducted on *Netzsch DIL 402PC*. The samples were heated from room temperature to 250 °C and held for 10 min and then cooled back to room temperature. The heating/cooling rate was set to 1.5 °C/min. The correction samples, equipment calibration and sample preparation were based on ASTM E228-17 standard.

EDX was performed using the *Aztec Live System from Oxford Instruments NanoAnalysis* on *EVO LS-15* version from *Carl Zeiss* SEM machine, to identify the change in Ni content and investigate its effect on shape memory effect. The samples were cold-mounted and ground using SiC abrasive papers P240, 600, 800 and 1200, and then polished to a high surface finish using 6, 3, 1 μm diamond suspensions and 60 nm colloidal silica. Microstructure was revealed by swabbing with the etchant 15 mL HF + 10 mL HNO_3 + 10 mL CH_3COOH + 5 mL glycerol, for about 2 – 3 s. The above-mentioned SEM and an optical microscope *Keyence VHX2000E 3D Digital Microscope* were used to capture the microscopic images. X-ray diffraction (XRD) was used to analyse the phases present in the printed parts. A *Bruker D8 X-Ray Diffractometer* equipment with CuKα source having a wavelength of 1.5406 Å. The scans were performed in the 2θ range of 35° to 65° under locked coupled mode with an increment of 0.01° and 6.65 sec/step. The scan duration was 6 h for each sample.

3.2.4 Thermal Data and Response Analysis

The thermal data of the melt pool was recorded by two pyrometers (from *KLEIBER Infrared GmbH*) setup in the Aconity SLM machine. The pyrometers detect the light emitted from the region of laser incidence (range of 1500 – 1700 nm), and the output infra-red data is logged in terms of voltage (mV) units and coordinates on the build plate (x, y). In this work, single layer plot was made to illustrate the thermal gradients across the section of the sample. The data acquisition rate was 100,000 samples per second. A single build layer is represented by roughly 6 million data points, each containing the coordinate and temperatures (in mV). The temperature readings were translated to a normalised scale in a range of 0 to 1 to represent the thermal profile.

The output data (responses) from each of the experiments were analysed through *Design-Expert 13* software, and only the models having a high significance and prediction reliability value with no significant lack in data fit, are presented in the results section. The surface response equations are given in terms of actual factors and the levels of each

process parameters used. The equations also include coefficients appropriate to accommodate the actual units of each of the process parameters. The presented response surfaces each show the response to two of the input parameters with the third parameter kept constant at its mid-level.

3.3 Results and Discussion

3.3.1 Particle Analysis

The powders were found to contain a near-equiatomic composition of Ni (49.9 at. %) – Ti (50.1 at. %) through EDX measurement. The particle size distribution shown in Figure 3.3 is an average of three results obtained from the supplied material batch, and this is quantified using the parameter D_φ which represents the diameter of the powder particles corresponding to the volume percentage ($\varphi = 10$, 50 and 90) of particles present. D [4,3] is calculated by the equipment via the weighted average value by volume, and it can be considered as the average particle diameter, and does not depend on the number of particles. $D_{10} = 12.3 \pm 0.8$ µm; $D_{50} = 28.1 \pm 2.2$ µm; $D_{90} = 57.3 \pm 7.7$ µm; D [4,3] = 34.0 $\pm$ 3.1 µm. The powders were observed to have near-spherical shapes as shown in Figure 3.4. Most of them were almost perfect spheres, whereas some particles were ellipsoidal with tiny satellite particles (Figure 3.4b) attached.
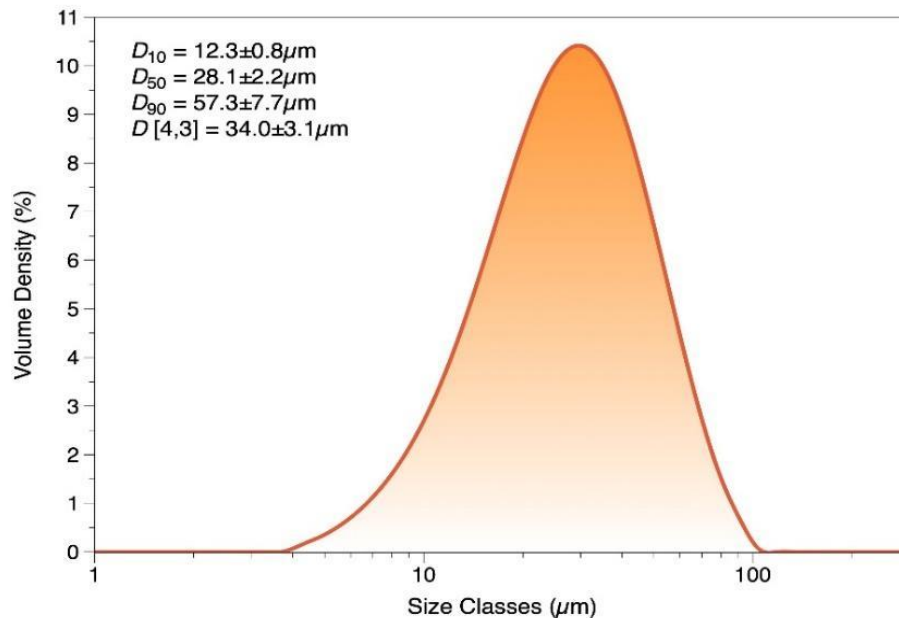
Figure 3.3 Gaussian particle size distribution of raw NiTi powders used.
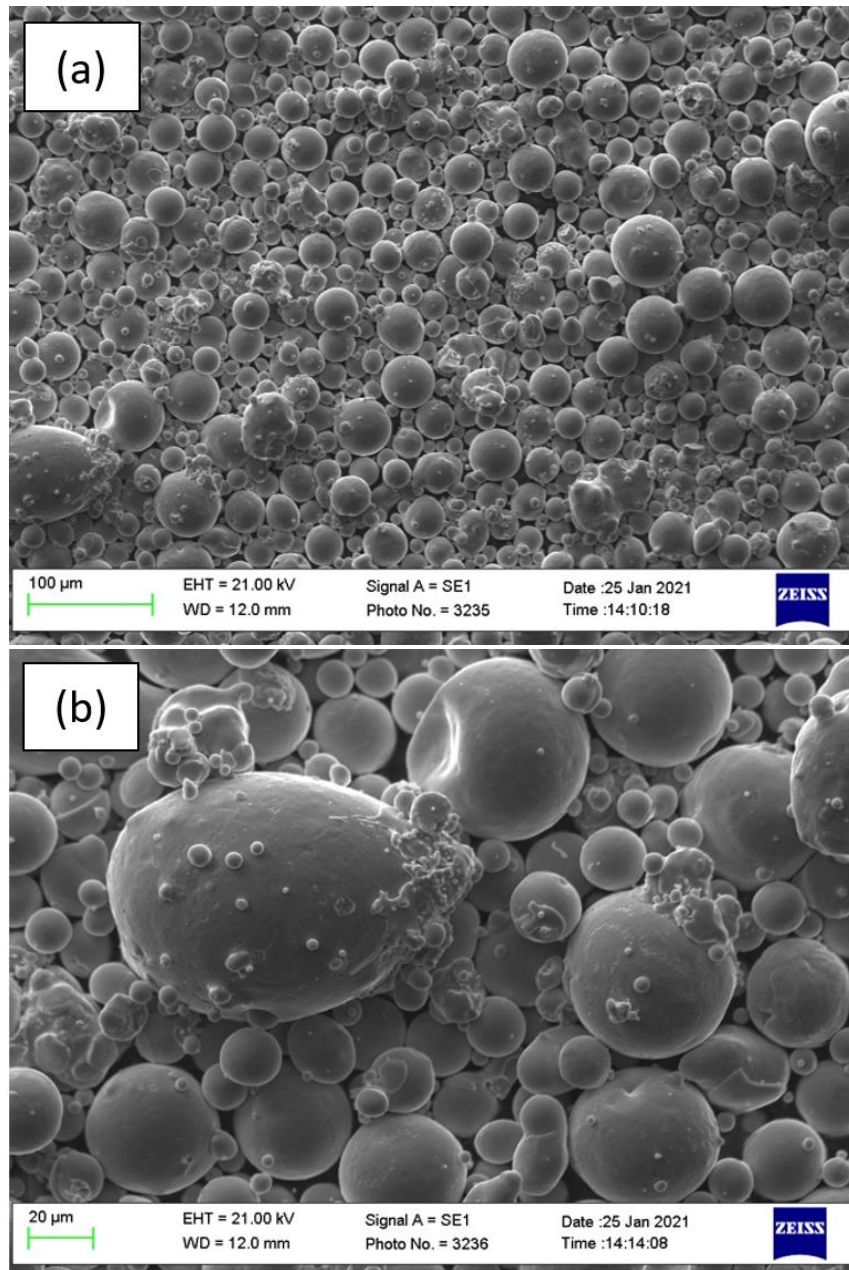
Figure 3.4 Powder morphology as observed in SEM (secondary electron): spherical **(a)** and magnified view of an ellipsoidal particle **(b)** with some attached satellite particles.

3.3.2 Input-Output Correlations

In order to check for possible correlations between the input process parameters and the responses, Pearson correlation and p-value significance parameters were used. Strong or relevant correlation was inferred for the responses that shows a Pearson coefficient (r) of 0.35 or greater, and a p-value of 0.05 or below in the model. A higher value of r and a lower p-value indicates a stronger correlation and a higher degree of significance, respectively. A negative r value indicates inverse relation, and vice versa. From response surface analysis, only models that presented low coefficient of variance and insignificant

lack of fit were considered in the study. The term VED was not an input factor in the BB DoE model, and therefore the p-value is not applicable in the case of VED. All relevant correlations are listed in Table 3.2.

Table 3.2 Pearson coefficients and p-values indicating input-output correlations.

Ms – martensitic start temperature; Af – austenitic finish temperature; $RMTR$ – R phase start to martensitic start transformation range; TTR – total transformation range

Correlation	r	p
V-built Samples		
Laser Power – Ms	0.4063	0.0009
Scan Speed – Ms	-0.5000	0.0009
Hatch Spacing – Ms	-0.6563	<0.0001
Laser Power – Af	-0.7855	<0.0001
Laser Power – $RMTR$	-0.5238	0.0123
Hatch Spacing – $RMTR$	0.5139	0.0136
Laser Power – TTR	-0.6463	0.0007
Scan Speed – TTR	0.5122	0.0039
Scan Speed – Ni Evaporation	-0.5817	<0.0001
Hatch Spacing – Ni Evaporation	-0.6980	<0.0001
VED – Ni Evaporation	0.8585	N/A
VED – Endothermic Enthalpy	0.5333	N/A
VED – Exothermic Enthalpy	0.5155	N/A
H-built Samples		
Laser Power – Density	0.4122	0.0001
VED – Density	-0.4825	N/A
Scan Speed – Density	0.5847	<0.0001
Hatch Spacing – Density	0.4207	0.0001

3.3.3 Density measurements

The densities of the samples were measured using Archimedes' method in acetone medium. The relative densities (with theoretical density value of NiTi = 6.45 g/cm^3) were found to vary between 97.2 % and 97.9 % for the V-built samples, whereas for the H-

built samples, larger variations between 93.4 % and 98.5 % were observed for similar process conditions. As seen in Figure 3.5, most of the samples built in horizontal orientation showed lower densities compared to the V-built samples. However, all of the samples (2, 3, 5, 16) printed using the lower scan speed of 600 mm/s showed high reductions in densities. The other process settings for the H-built samples (sets 4, 8, 9, 11 and 17) resulted in higher densities. These latter samples had a combination of higher laser power and lower energy density with large hatch spacing. It was also seen that for H-built samples, the VED showed high negative correlation with the densities. The selected parameter levels did not cause a large variation in densities of the V-built samples.
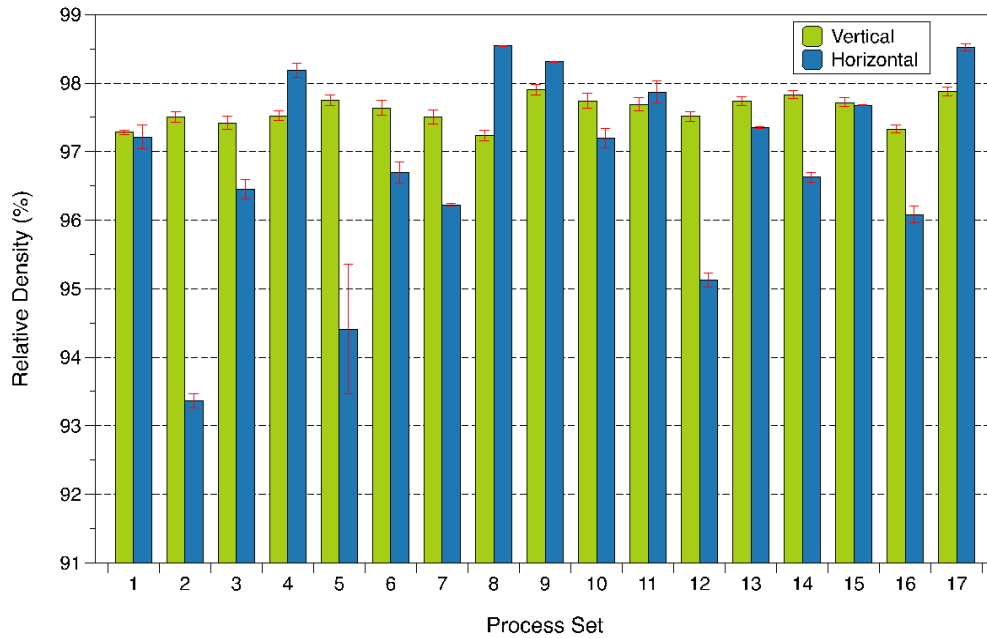
Figure 3.5 Relative densities of samples built vertically and horizontally using the set of 17 process conditions, measured using Archimedes principle; 95% confidence interval implemented based on n=3.

For the relative density responses from 17 H/V samples printed with different laser powers (P), scan speeds (v) and hatch spacings (h), the actual equation for the relative density (RD) of printed samples, the response surface equations are reported as Equation (3.2) and Equation (3.3):

$$RD_{vertical} \ (\%)$$
$$= 94.52953 + 0.032001P - 0.001192v + 0.051402h \qquad (3.2)$$
$$- (3.075E - 06)Pv - 0.000572Ph + 0.000033vh$$

$$RD_{horizontal}\ (\%)$$
$$= 63.82459 + 0.039849P + 0.035340v + 0.321426h$$
$$- 0.000072Pv - 0.001757Ph + 0.000499P^2$$
$$- 0.000011v^2$$

(3.3)

From these, it can be seen that for V-built samples that the laser parameters pose both linear and two-factor interactive effects on the relative density. In the case of H-built samples, additional quadratic effects from laser power and scan speed are also observed. Figure 3.6 shows the response surfaces of the effect of process parameters on vertical and horizontal builds; two process parameters are varied in each of the graphs while the third is kept at the medium levels. As seen in Figure 3.6a and 3.6b, the vertical build showed only slight variations (nearly planar effect) in densities with respect to the process parameters. From the model, it was found that only the interaction between laser power and hatch spacing showed a high level of significance (p = 0.0059) on RD for the V-built samples. Larger variations along with quadratic response surfaces can be seen in the case of the horizontal builds (Figure 3.6c and 3.6d). The scan speed showed the largest effect on the RD compared to laser power and hatch spacing. It was also found that for the current set of parameter levels, the VED has an inverse relationship with the resulting relative densities of the H-built samples.

In most of the earlier studies, more focus had been on understanding the effect of VED on the densification of NiTi samples. However, depending on the parameter levels taken into account and factors that have been considered to remain constant, optimal VED values to obtain high RD varied widely between each of the studies. For instance, a high RD of 99 % and above, were achieved by Saedi *et al*. [276] and Walker *et al*. [277] at a VED of 55 J/mm^3. Meier *et al*. [278] observed high RD at a VED of 85 J/mm^3. Haberland *et al*. [145] achieved an RD of 99 % and higher, using a very high VED of 200 J/mm^3 whereas a VED of 111 – 126 J/mm^3 produced $RD > 99$ % in work reported by Das *et al*. [279]. In the current study, the higher $RD_{horizontal}$ of 97.90 % and 97.88 % were attained using a VED of 125 J/mm^3 and 47.62 J/mm^3 respectively, and high $RD_{vertical}$ of 98.31 % and 98.52 % were achieved for the same VED values respectively. All of these arguments including the results from the current work, point towards the requirement to use more detailed information than just the VED value for generating a correlation with the output RD. Such correlations could for example take into account in a more detailed manner the

process parameters and potentially also other properties such as the powder and inert gas related properties.
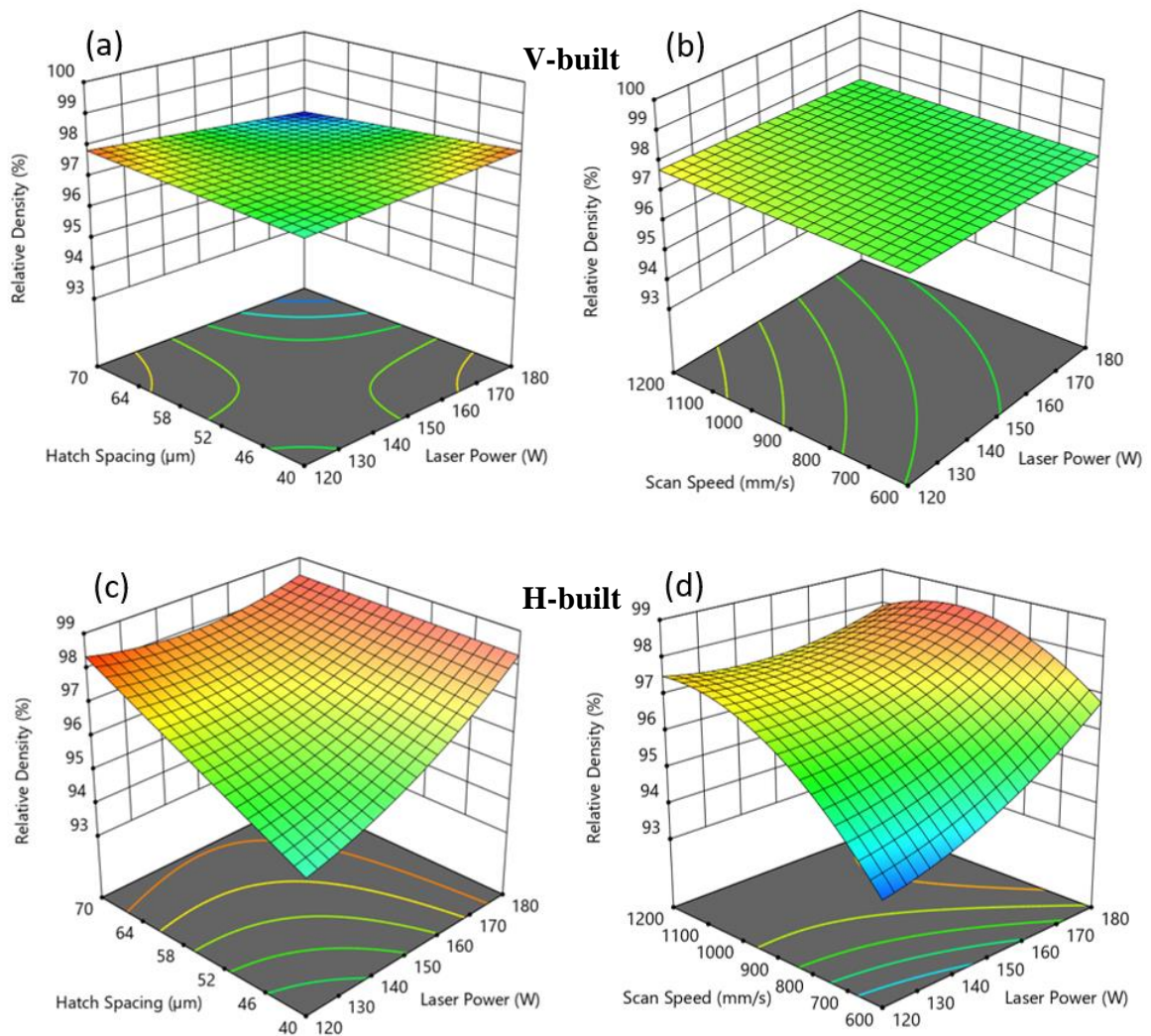
Figure 3.6 Response surfaces showing the effects of the laser process parameters on relative densities of the V-built samples **(a)** with $v = 900$mm/s and **(b)** $h = 55$ μm; and on the H-built samples **(c)** with $v = 900$mm/s and **(d)** $h = 55$ μm.

The RD variations in both H/V samples can be understood in relation to the thermographs plotted in Figure 3.7. The figures show the normalised thermal profiles of the middle layer for one plate of the horizontal builds and one of the vertical build. It can be seen that the H-built samples underwent large thermal variations in the samples across the build plate as compared to the V-built samples with the same process conditions. As seen in Table 3.2, it can be seen that the effect of energy density was substantial in the case of H-built samples. For instance, sample H15 ($VED = 45.45$ J/mm^3) has the least variable overall temperature profile, whereas H17 with 47.62 J/mm^3 has a slightly higher variation in

thermal profile. Sample H12 with 83.33 J/mm^3 and H2 with 90.91 J/mm^3 exhibited the highest variation in temperature profile. This logically follows from the processing conditions, as the horizontal build has a larger surface area and therefore a larger time interval between the print of each layer. This leads to higher extent of heat dissipation increasing the temperature differential across the layer and also would produce larger interlayer thermal gradients when compared to the vertical builds. In the V-built samples, the temperature differential is lower (sample V2; more uniform colour map in Figure 3.7b) than is evident from the H-built sample colour maps (Figure 3.7a), where the rate of change of the temperature gradient from one end of the sample to the other appears to be higher.

The average temperature differentials (TD_{avg}) of each of the samples on the horizontal build shown in Figure 3.7, were also compared to those recorded from the samples printed in the vertical orientation. The average differentials were calculated using the normalized temperature data through the centreline as shown in the enlarged colour maps of H2 and V2 in Figure 3.7. TD_{avg} was calculated by first obtaining the rolling differential of the consecutive data points and then averaging the sum of the differentials. Even though the TD_{avg} did not show a significant correlation with the actual density values, it indicated a noticeable trend with how density varies. As shown in Figure 3.8, it can be seen that the densities are typically higher when the TD_{avg} is lower, and vice versa. As the differences (Δ) in the TD_{avg} of V-built and H-built samples decrease, the difference in RD were also found to decrease. In the case of samples H/V17, the Δ was negative, and this reflected as density being higher for H17 compared to V17. In general, the V-built samples were found to have a lower TD_{avg}, indicating a more uniform intra-layer thermal profile which then translated into smaller density variations and a less significant direct and two-factor interaction relation. In contrast, the higher TD_{avg} in the H-built samples can be seen to have resulted in larger variations in density within the H-built samples, for similar parameter sets. This is also supported by the statistical data shown in Table 3.2.

These larger temperature differentials and interlayer thermal gradients extend to causing various defects in the samples, and are found here to have resulted in lower sample densities. In addition to the density results, this is corroborated by the optical micrographs shown in Figure 3.9c and 3.9d, where porous defects are found to be significantly high in sample H2 compared to sample V2. After the density tests, wire-EDM was performed on

sample H2, and sample V2 is in the same condition (240 grit finish) as used for density tests. These different surface finishes can be ignored at the moment to focus attention on the presence of pores.
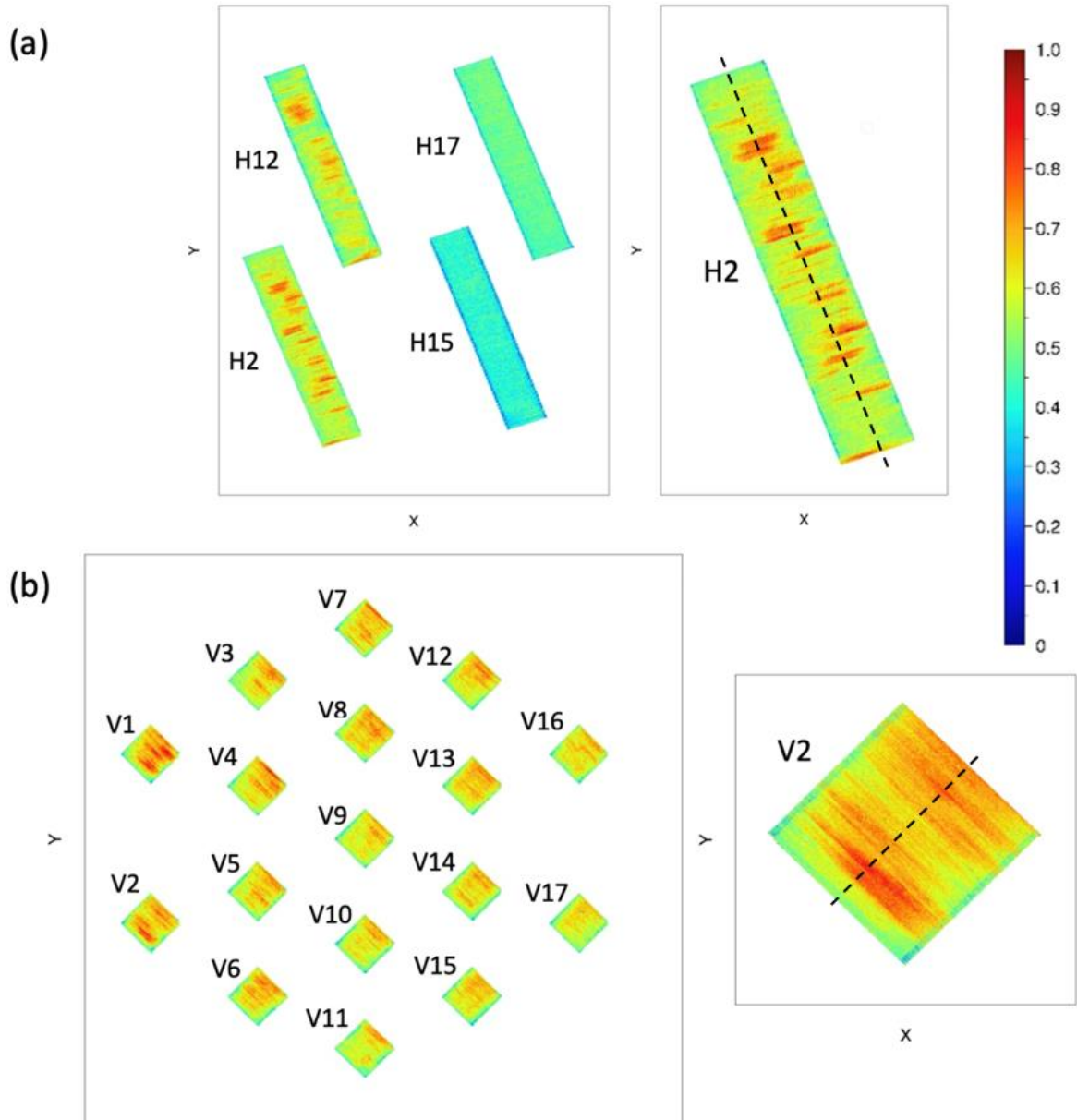
Figure 3.7 Thermal IR data plots showing the temperature variations across the middle layer in: **(a)** horizontal build including the magnified view of samples H2, and **(b)** vertical build including the magnified view of sample V2; normalized temperature scale has been used.
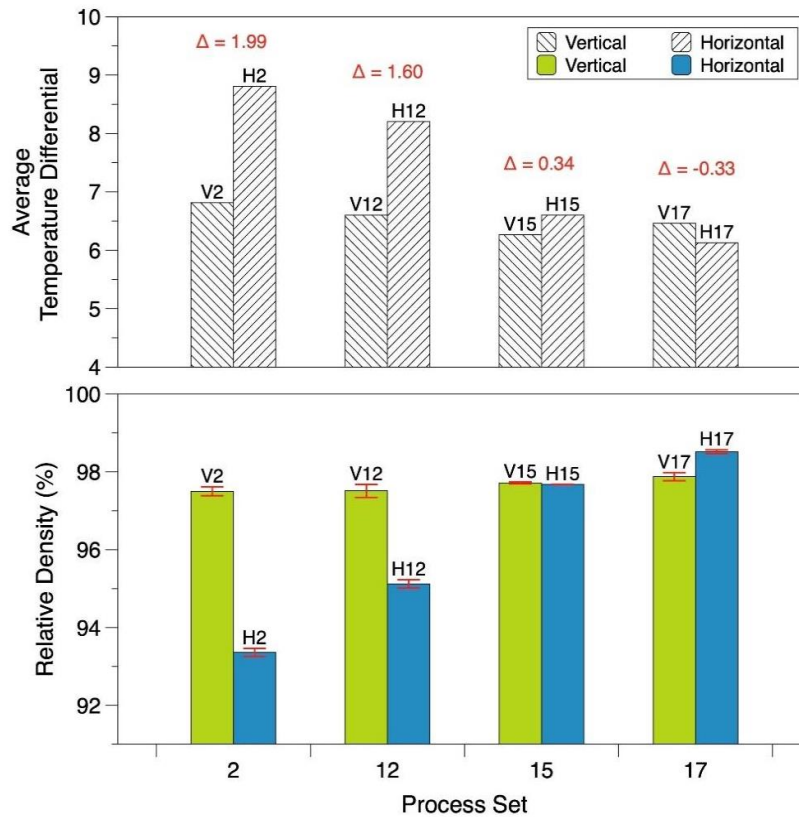
Figure 3.8 Average temperature differential for V-built and H-built samples 2, 12, 15 and 17, difference in differentials of V-built and H-built samples of each set are denoted by Δ.

The porosities found in L-PBF processed parts can be identified based on the causes of occurrence and morphologies. Sufficient laser power and VED is necessary to melt the powder on one layer and re-melt the previous layer, to ensure epitaxial solidification. This is necessary for strong interlayer bonding which helps to prevent undesirable intermetallic phases, and various types of pore formations [35]. Almost all of the samples were found to contain a set of irregular pores or voids. These occur due to various process-induced effects. One of them is the balling defect which occurs due to the expansion of trapped oxygen between layers producing a collapsed region or retention of the pore. Epitaxial solidification and low oxygen levels are necessary to reduce the chances of these irregular pores. The partial pressure at equilibrium for oxygen (near the melting point of Ti) has to be less than 16.2 bar to avoid oxidation. This is generally very impractical, and therefore, oxidation cannot be completely ruled out in L-PBF processes even though the chamber is flooded with argon or other inert gases [279,280]. Irregular pores can also be formed due to lack of fusion. These are found in larger sizes (few hundreds of microns), and is commonly seen spanning along the boundaries of several melt pools. As seen in Figure 3.9a, these defects in some cases accompany unmelted powder particles. This indicates

the lack of fusion due to insufficient laser energy which fails to generate an effective melting and region of fusion overlap.

Many of the porosities found near the edges of the vertically printed samples (sample V2 presented in Figure 3.10) were of gas-induced type. These pores are spherical in shape and occur due to the trapping of ambient gas in the powder bed; not having sufficient time to escape the melt pool. Since a huge fraction of spherical pores were formed near the edge regions, this can be also due to a coupled effect of process conditions (e.g., high scan speed) that could have resulted in poor gas removal and insufficient melting near the edges. The observed sizes of these pores were in the range of $5 - 50 \, \mu m$. The formation of gas induced pores is a dynamic process that involves nucleation and growth of pores, and then an eventual out-gassing (removal/escape of gas) during the rapid solidification of melt pools. Due to insolubility of these gases in liquid metals, the gas pores follow Marangoni convection to escape easily through the melt pool surface. High energy densities tend to generate high temperatures which might evaporate lower melting point constituents (for instance, Ni) accelerating the pore nucleation. At the same time, a higher energy density can induce a higher thermal gradient between the apex and boundary of the melt pool, which in turn boosts the Marangoni convection accelerating the out-gassing process [281,282].

Along with the above-mentioned porosities, some large voids were also observed in samples H2 and V2. These are also a few hundreds of microns in size and more of an irregular spherical morphology. These can be identified as the keyhole porosities. The keyhole pores are caused under high instability in the melt pool due to surface tensions and hydrostatic pressures generated by the high energy density or localized high penetration of laser beam [283]. These are often formed near the bottom region of the melt pool and can be seen in BD view (Figure 3.9c) of sample H2. The formation regions can be somewhat assumed to be melt pool boundaries. It is to be noted that the spot size (50 µm) and hatch spacing (40, 55, 70 µm) in the current work causes laser tracks to overlap to a higher extent than in many previously published works. This can create localized thermal instabilities that could favour the keyhole formation.

The porosity in particles is formed during the gas atomization process, and imperfections such as satellites and skewed sphericity as seen in Figure 3.4 can also lead to porosity. This causes inhomogeneity during powder deposition and could result in air pockets

between the thin layers. Another possible cause of porosity is the presence of spatter/melted droplets from the melt pool produced during the previous scans. As explained by researchers [37,281,284–286], this might occur at higher VED values and lower scan speeds, causing the pressure in the melt pool to exceed the surface tension levels of the molten material.

The L-PBF process tends to create residual thermal (unbalanced) stress profiles between the printed layers. These stresses are usually caused by the large thermal gradients from multiple remelting and solidification cycles. The thermal expansion on one layer creates tensile stress while the layer beneath undergoes compressive stresses. This differential stress phenomenon is induced across the underlying layers, and these layers can be affected in this way multiple times. This can ultimately lead to delamination or warpage of samples from the build plate. As scan overlaps are highly possible with the laser process parameters used in this work, the possibilities of residual stresses are quite high. This can initiate cracks throughout the cross-section of the layer affecting the mechanical properties. The presence of microcracks can be seen in Figure 3.9b. These effects can create pores which could act as crack nucleation sites and end up in crack propagation. However, the rapid cooling in L-PBF can suppress the propagation mechanism in the structure [218,219] and result in shorter microcracks.

Observing the microscopic view of sample cross-section in Figure 3.10c, we can see a rectangular pattern. This pattern can be confirmed as a forefront of the brick-like structures that extend beneath the surface, as seen through a fractured face (Figure 3.10d) of the same sample. At the atomic scale, NiTi forms a cubic lattice structure with almost 90° angles. The right-angle arrangement becomes acute or obtuse under the application of heat, and the shape is deformed. Upon cooling, the molecules regain the right angles, and the original programmed shape is regained (shape memory).
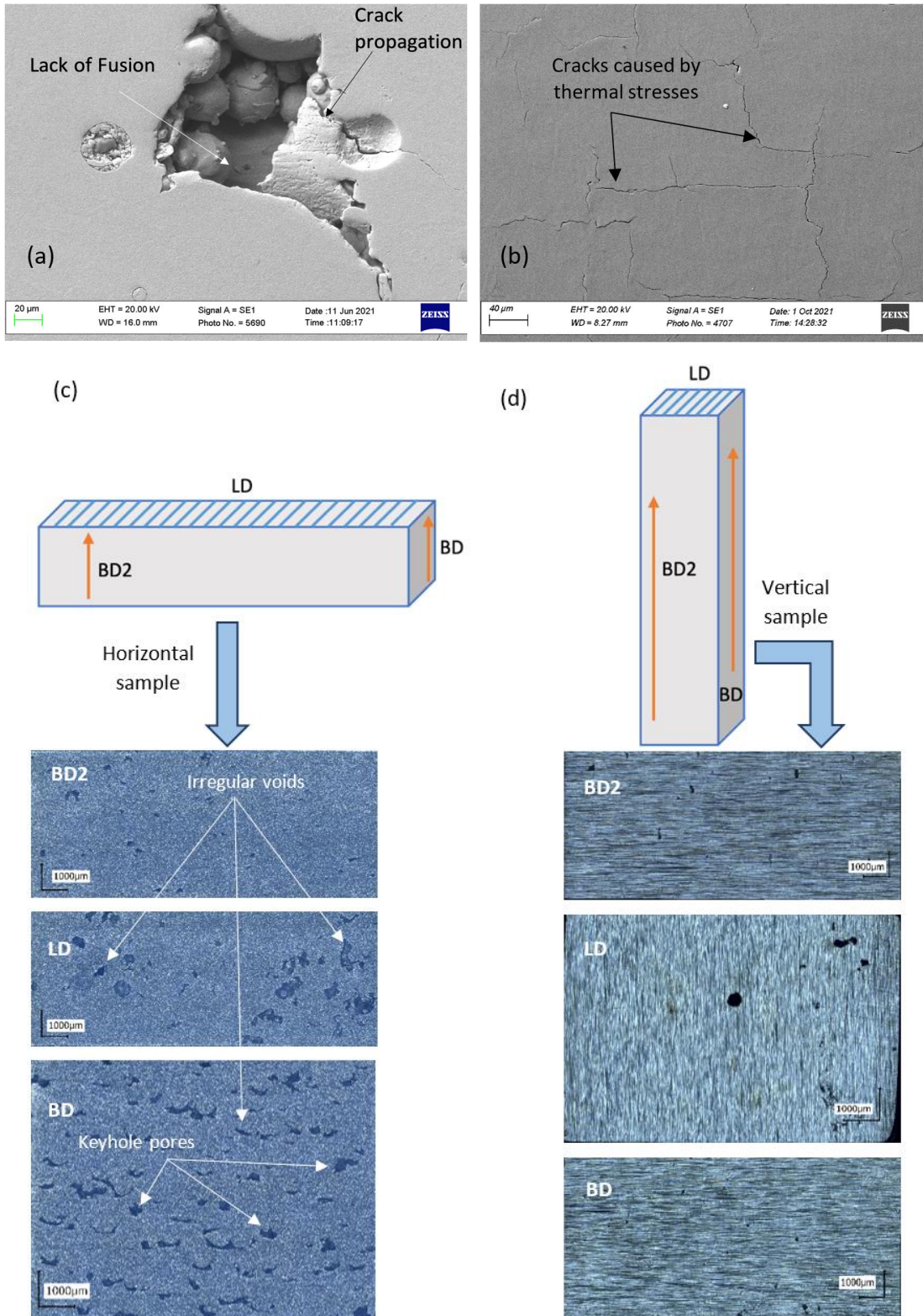
Figure 3.9 (a) SEM image showing porosity found in sample V11 showing keyhole and lack of fusion indicated by unmelted particles trapped between layers; **(b)** microcracks of sample V7; optical micrographs showing the extent of porosities observed on **(c)** horizontally built (H2) and **(d)** vertically built (V2) samples having same process parameters. (LD – sectional lateral face corresponding to print layer; BD and BD2 – faces corresponding to the build direction as illustrated)
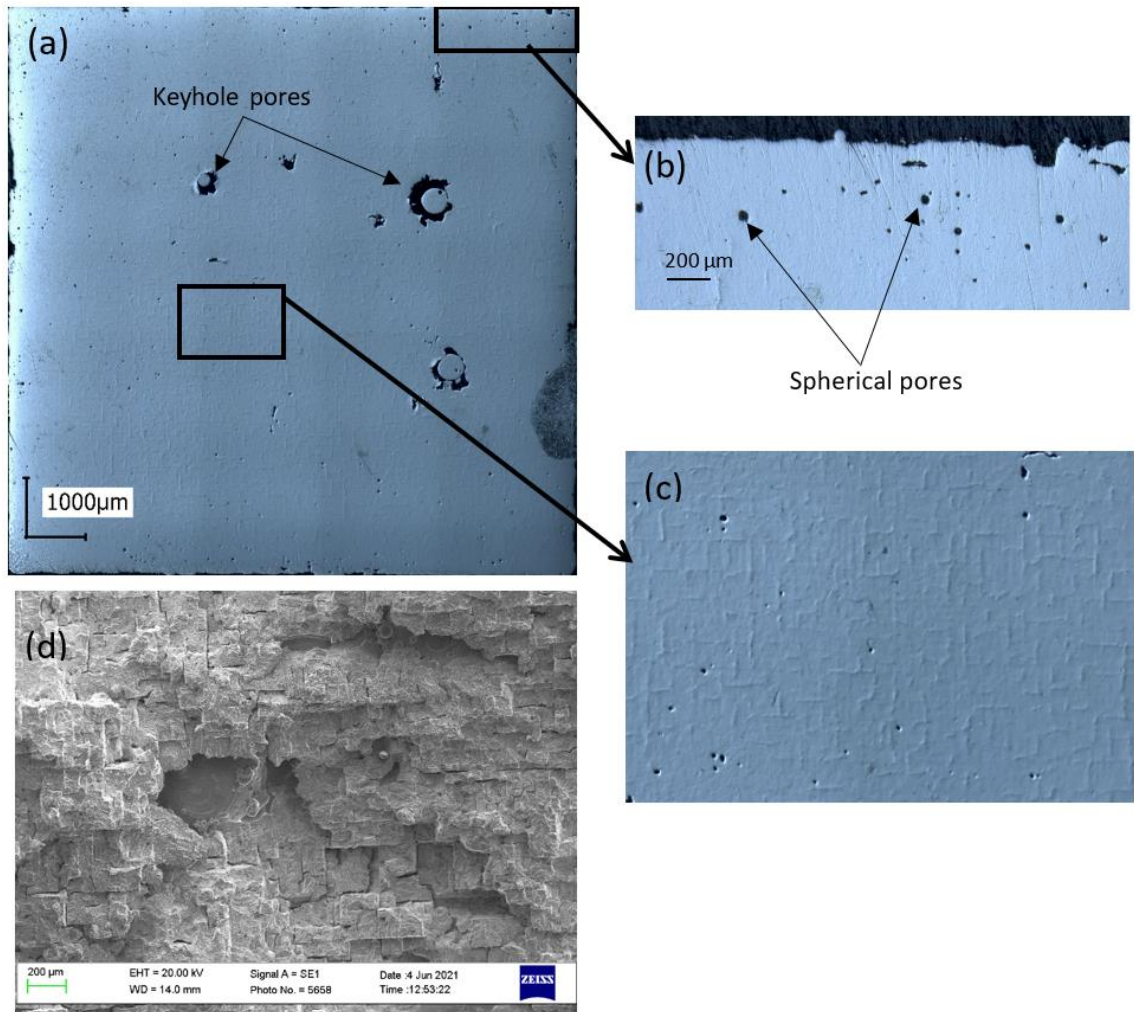
Figure 3.10 (a) Polished LD face of sample V2 showing the presence of keyhole pores; **(b)** detailed view of spherical gas-induced pores formed along the edges; **(c)** magnified view showing the rectangular patterns; **(d)** fractograph showing brick-like structures beneath the rectangular pattern on the surface.

3.3.4 Transformation Temperatures

The transformation temperatures were calculated from the heat flow vs temperature graphs generated through the DSC analysis as shown in Figure 3.11. Each peak starting and ending from the baseline represent the presence of a stable phase. The stable phases found were martensite (low temperature phase with monoclinic B19' crystal structure) and austenite (high temperature phase with body-centred cubic B2 crystal structure). The start and finish temperatures of each of these phases are estimated by plotting tangent lines where the heat flow deviates from the baselines, as illustrated in Figure 3.11.

Compared to the raw powders, most of the as-fabricated samples exhibited an overlapping peak merged with the austenitic transformation region. Due to this, the peaks may appear slightly wider in L-PBF samples. In the raw powders, a shoulder can be seen on either peaks denoting an inhomogeneous heat flow among the powder particles [212]. This indicates the presence of a third unstable intermediary phase; identified as an unstable variant ($R*$) of the R-phase (rhombohedral crystal structure). The $R*$ formation is mainly caused by the cold work performed during the fabrication. This can be further accelerated if Ni-rich precipitates are present [35,287]. A shift of the peaks to the higher side of TTs was observed, see Figure 3.12a. The critical transformation temperatures considered are martensite start (Ms) and finish (Mf) temperatures, R-phase variant start ($Rs*$) and finish ($Rf*$) temperatures, and austenite start (As) and finish (Af) temperatures. Since all of the samples containing $R*$ phase has an overlapping peak, $Rf*$ and As can be considered as the same point.

The transformation temperatures were found to be highly sensitive to the NiTi composition as shown in Figure 3.12, which represents the experimental results from several research works in the past [288]. In the L-PBF process, the high laser energy results in faster evaporation of Ni due to its lower melting point (1455 °C) as compared to that of Ti (1668 °C).
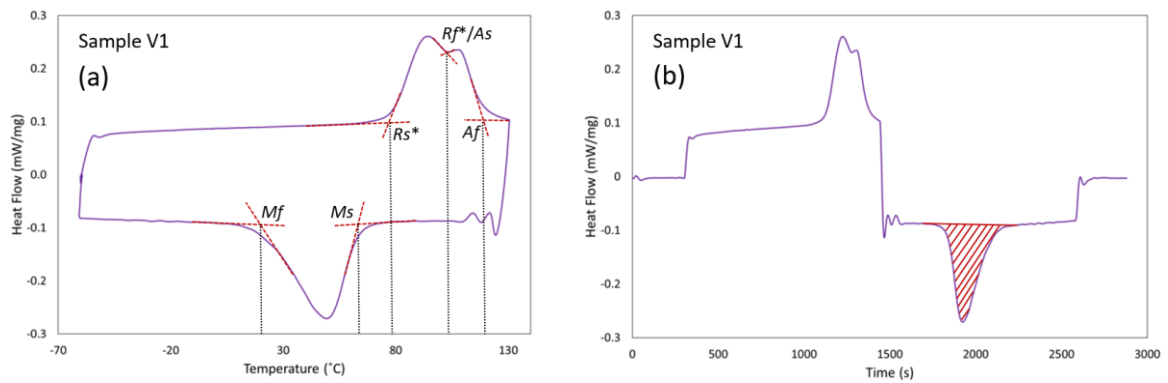
Figure 3.11 Illustration of determining the **(a)** transformation temperatures and **(b)** transition enthalpy from the DSC graphs.

Another possibility of this compositional change owes to the formation of stable phases such as Ni_3Ti or Ni-rich precipitates such as Ni_4Ti_3 (metastable) which ultimately depletes the Ni content in the matrix giving rise to TTs due to the remaining higher Ti content. However, these phases or precipitates generally do not affect the shape memory effect (SME) directly, instead it changes the composition of the matrix [35]. At times, the

distribution of Ni and Ti could be non-uniform in indicated by a number of additional small peaks in DSC curves which can adversely affect the shape recovery [289].
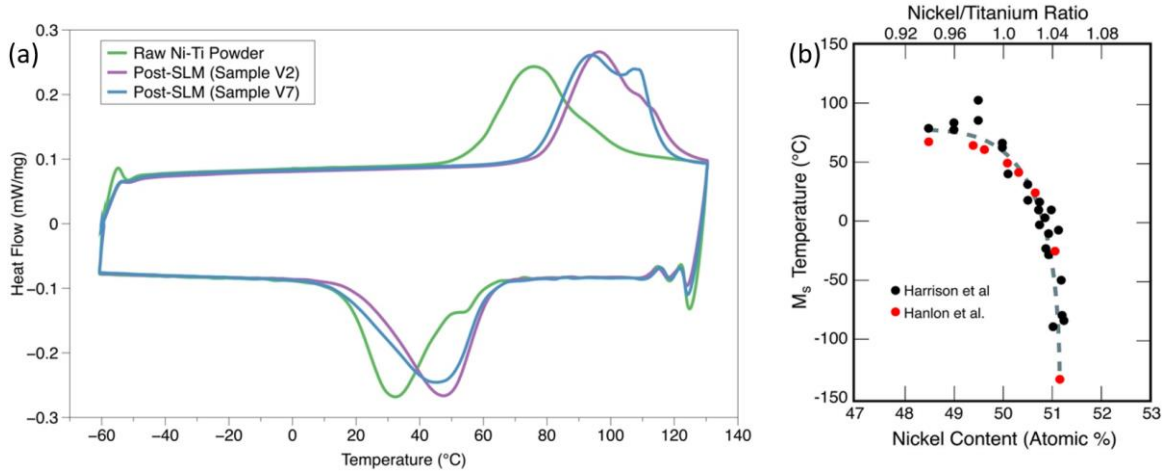
Figure 3.12 (a) DSC plots showing the shift in transformation peaks and the presence of an intermediate phase after L-PBF processing compared to the raw powders; **(b)** variation of martensite start temperature (Ms) with Ni content [288].

All of the current samples in the as-fabricated state exhibited a Ni reduction of 1.2 to 1.8 at. %. The *Ms* for raw powder (Ni - 49.9 at. %) was found to be 49.4 °C which agrees with the literature values seen in Figure 3.12. The Ni reduction that occurred in the current study was found to elevate the transformation temperatures in general compared to the raw powders (Figure 3.13). Since the current feedstock has a higher Ti content, the rise in transformation temperatures are not considerably high, as compared to that of the samples printed using Ni-rich NiTi powders [288,34]. The increased *Ms* temperatures of L-PBF processed samples were found to have very small variations between 61.2 °C and 63.3 °C. This further agrees with the literature findings for corresponding Ni contents (48.1 to 48.7 at. %); the *Ms* temperatures become steady around 60 °C to 65 °C for this compositional range. Further to the L-PBF process, the *Mf* temperatures increased by 1.2 to 9.0 °C, and *Ms* temperatures increased by 11.8 °C to 13.9 °C. *Rs** increased by 20 °C to 25 °C, and *Rf** or *As* increased by 7.0 °C to 19.8 °C, while *Af* increased by 5.0 °C to 13.9 °C. It can be also seen that the martensite transition and R-phase transition temperature span increased in the L-PBF samples as compared to that of the raw powder used.
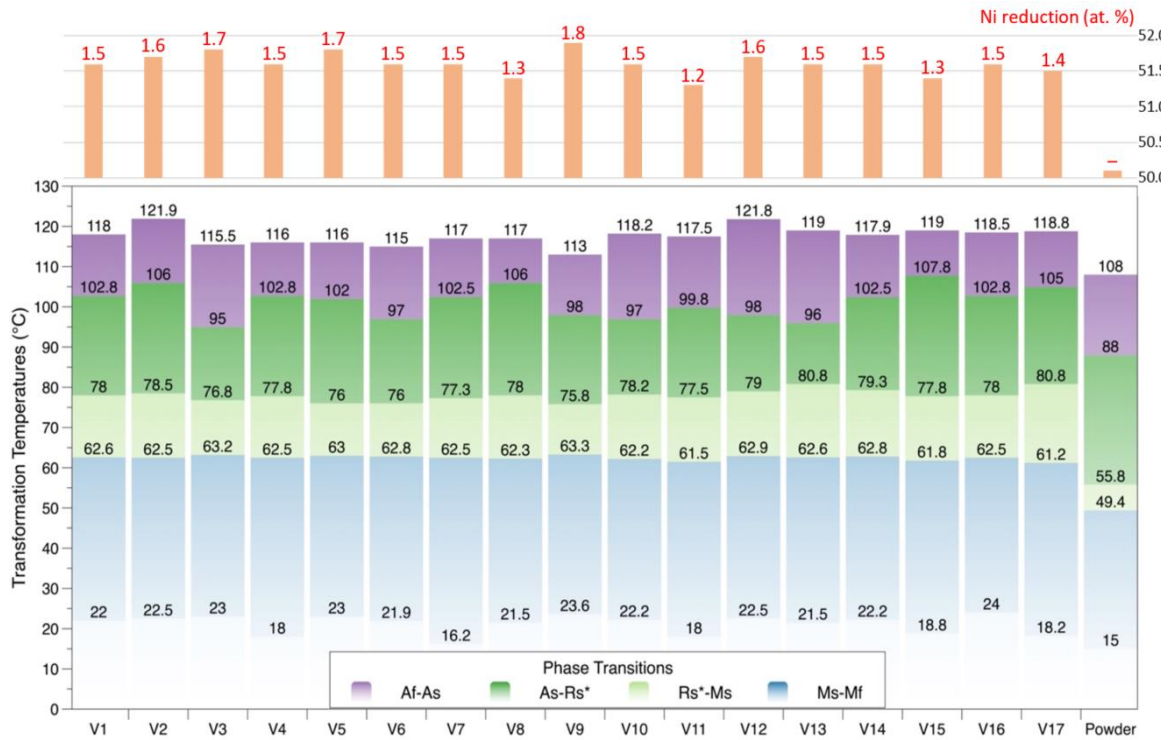
Figure 3.13 Ni evaporation (increase in Ti content) in all samples and their transformation temperatures showing different phases: Austenite transition (*Af-As*); R-phase transition stage 1 (*As-Rs**); R-phase transition stage 2 (*Rs*-Ms*); and Martensite transition (*Ms-Mf*)

An XRD analysis was performed at room temperature (20 °C) on two L-PBF samples and raw powder to identify the different phases present. As observed in Figure 3.14a, the patterns confirm the presence of mostly B19' martensite phases. The presence of martensite phase in the matrix was also confirmed in microscopy, seen in the form of needle-like structure (Figure 3.14b). The peak around 60° indicating an R (222) phase or a B19' (121) was stronger for the raw powders. The peak around 41° showing B19' ($1\bar{1}1$), was weaker in the case of V7, however, it was stronger and wider in the case of V2. Comparatively, most of the B19' peaks were stronger and wider in the case of V2. Some of the minor obscure peaks may indicate the presence of secondary phases such as $NiTi_2$ and Ni_3Ti. The presence of R-phases and precipitates or secondary phases might be caused due to intense thermal stresses generated from the processing conditions. The presence of Ni_4Ti_3 precipitates often results in a stable R-phase [290].
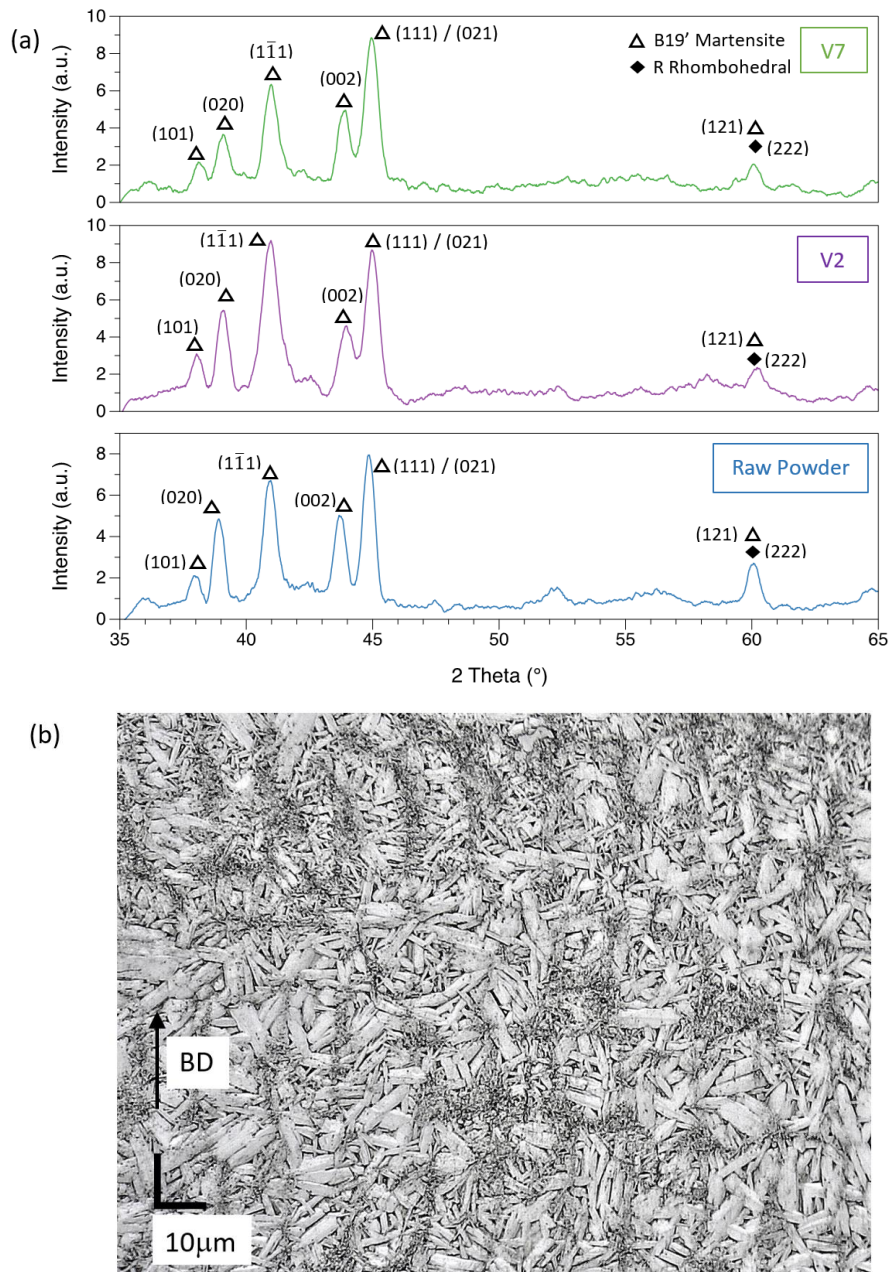
Figure 3.14 (a) X-ray diffraction patterns observed in raw powder, and the L-PBF produced samples V2 and V7; **(b)** martensitic structures as seen in optical micrograph of sample V2.

It has to be noted that the austenitic transformation (heating cycle) is an endothermic process, while the martensitic transformation (cooling cycle) is an exothermic process involving enthalpy changes. This transition enthalpy (J/g) was determined by plotting the heat flow curve (W/g) generated via DSC against the time parameter (seconds). The martensitic transformation peak in the new plot (Figure 3.11) is then isolated, and the area enclosed by the peak is calculated by integrating the curve using MATLAB trapezoidal

numerical integration (*trapz*) function to get the cooling enthalpy ($\Delta H_{cooling}$). A similar method is followed for the austenitic transformation peak to get the heating enthalpy ($\Delta H_{heating}$). As observed in Figure 3.15, the transition enthalpy changes during the heating and cooling cycles are different from each other. In general, the enthalpy change during cooling cycles is higher compared to that of the heating cycles. To better understand this calorific difference, the transition enthalpy ratio (TEr) was calculated using Equation (3.4).

$$TEr = \frac{\Delta H_{heating}}{\Delta H_{heating}} \tag{3.4}$$

Referring to Figure 3.15, it can be seen that after the L-PBF processing, the TEr values dropped from 0.97 (raw powder) to a range of 0.72 – 0.83. Ideally, the net heat inflow or outflow should be equal and balanced ($TEr = 1$), indicating complete phase transformation of the material. However, due to the processing conditions, material inhomogeneity and different entropies in play, the extent of transformation can differ in a real scenario. The entropies are linked to the thermal and dynamic equilibrium, and the entropy production due to phase transformations [291]. This results in a difference in calorific values during heating and cooling cycles. It is interesting to note that the raw powder has a high TEr value close to 1; indicating a good compositional homogeneity and least thermal or dynamic entropies. As mentioned earlier, the TEr value can also point towards the extent or volume of material undergoing phase change. Based on the $\Delta H_{cooling}$ and $\Delta H_{heating}$, it can be implied that the material transformed to austenite (heating) decreased by 10 - 30%, while the transformation to martensite (cooling) increased by 1 – 9 % in the case of L-PBF samples (Figure 3.15). It is interesting to note that VED showed a high positive correlation with the cooling (r = 0.5155) and heating (r = 0.5333) enthalpies, which also positively correlated with a relative increase in Ti content within the alloy.
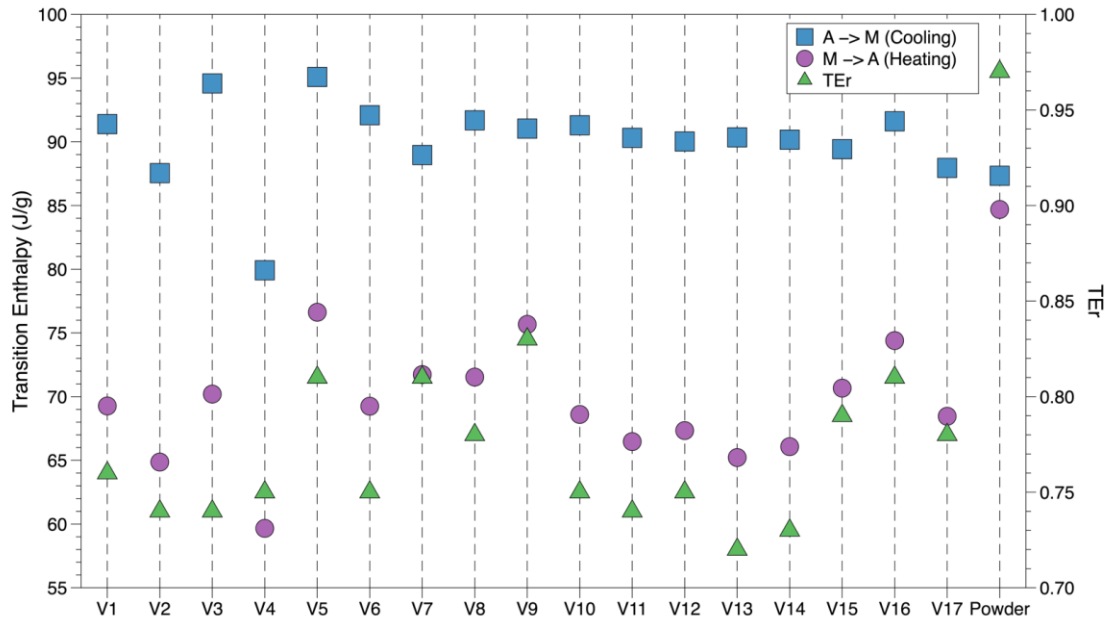
Figure 3.15 Enthalpy changes during austenitic and martensitic transformations, and enthalpy ratio (TEr) for each of the L-PBF samples and raw powder.

Analysing the effect of the laser process parameters on TTs, it can be seen that certain critical temperatures or range of temperatures showed a significant effect on these values. Martensite start temperatures generally lie about halfway across the transition temperatures span, and therefore they can be used as a quick reference to understand the functional property that the material might possess. The full transformation temperature range, $TTR = Af – Mf$, and Af temperatures indicate the boundaries of a transition span. This could help the engineers to identify the operational range of the material for specific applications. $Rs^*{\rightarrow}Ms$ transformation range ($RMTR$) is the transition span where the phases are unstable as the crystal structure tends to change dynamically to the most suitable variant of martensite or R-phase or austenite. In the current DoE, Ms was found to have a linear relationship (Equation 3.5) with the process parameters (Figure 3.16a and 3.16b); scan speed (v) and hatch spacing (h) poses an indirect relationship with higher significance, while the laser power (P) poses a direct impact on Ms. Af was found to have a two-factor interactive (Equation 3.6) relation (Figure 3.16c and 3.16d); however, laser power exhibited a stronger indirect influence on the Af compared to the other two parameters. A linear relationship (Equation 3.7) was found to exist with the $RMTR$ range also. Laser power exhibited an indirect relation with a higher significance, while a direct effect on $RMTR$ was observed with the hatch spacings (Figure 3.16e). In a recent work

by Zhu *et al.* [34], hatch spacing was found to have a linear relationship with TTs, which may be attributed to a reduction in Ni content and increasing dislocation densities. In the case of TTR, the estimated relation (Equation 3.8) was again found to be linear, having the laser power posing a negative relation with high significance, and the scan speed posed a positive relation. The response surface for TTR is shown in Figure 3.16e.

$$Ms\ (°C) = 63.68235 + 0.012083P - 0.001208v - 0.035h \tag{3.5}$$

$$\begin{aligned} Af\ (°C) = 168.55294 &- 0.382222P - 0.009056v - 0.45h + 0.000094Pv \\ &+ 0.003889Ph - 0.000111vh \end{aligned} \tag{3.6}$$

$$RMTR\ (°C) = 15.85245 - 0.044167P + 0.001667v + 0.086667h \tag{3.7}$$

$$TTR\ (°C) = 100.94608 - 0.100417P + 0.007958v + 0.063333h \tag{3.8}$$
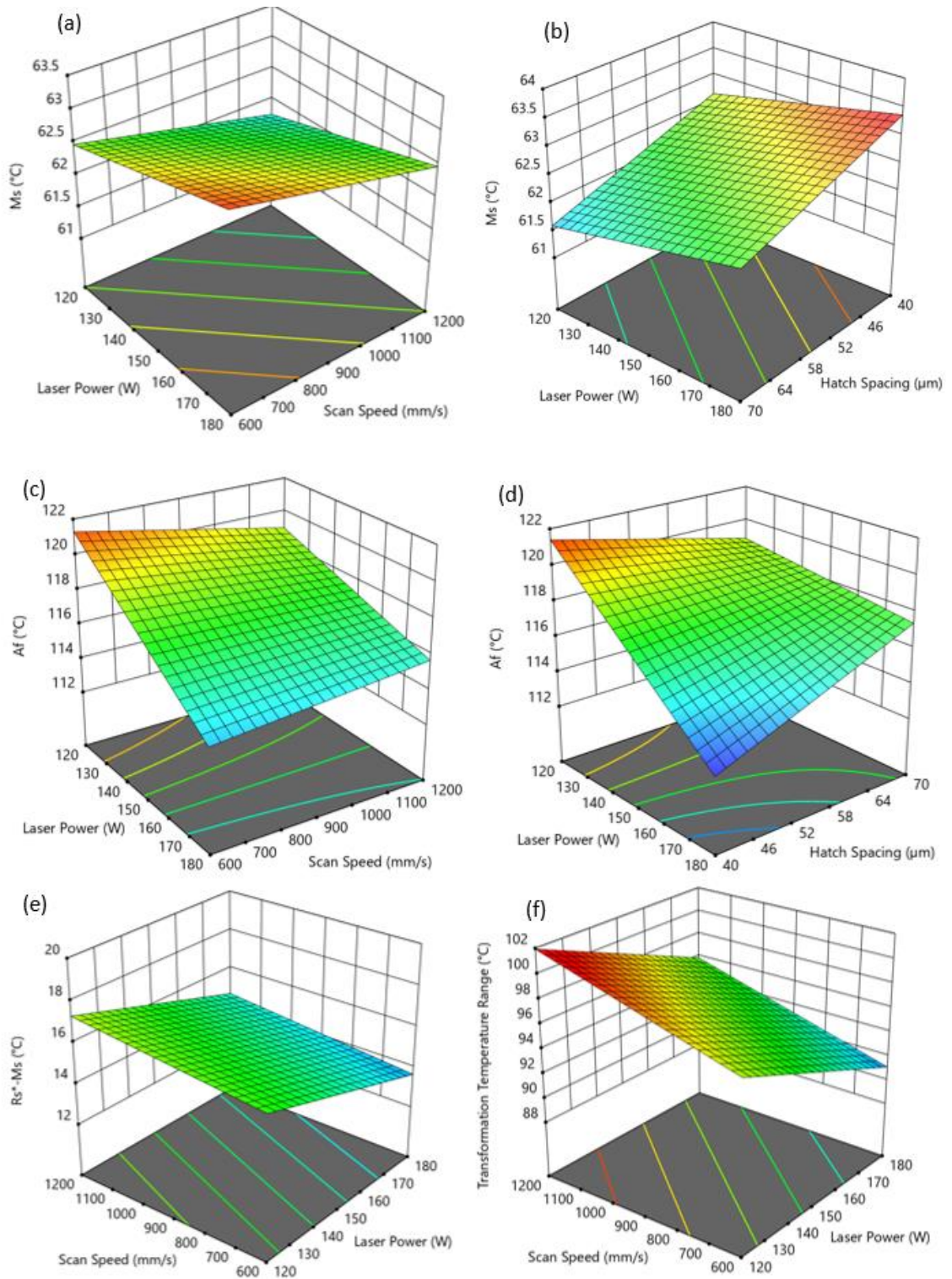
Figure 3.16 Response surfaces of laser process parameters on transformation temperatures of V-built samples keeping the third parameter at middle level: martensite start **(a, b)**; austenite finish **(c, d)**; R-phase to martensite transition range **(e)**; Full transformation temperature range **(f)**

3.3.5 Nickel Evaporation

As discussed in the previous section, Ni evaporation or increase in Ti content in the matrix have a significant effect on the shape memory behaviour of the material by increasing the TTs. In the current work, the raw powder had Ni composition of 49.9 at. % which is just around the corner of the plateau region in the graph shown in Figure 3.12. Therefore, the change in Ni content (1.2 – 1.8 at. %) that occurred in the L-PBF resultant samples did not cause a huge change in the TTs. If the Ni content had been higher in the raw material, the effect of Ni evaporation would have been considerable. Thus, the level of Ni evaporation plays a critical role in determining the performance of the functional property for the specific application. It is necessary to have high input energy to cause this phenomenon, and therefore the effect of laser process parameters needs to be addressed.

From the response analysis, it can be seen that a two-factor interactive relation (Equation 3.9) exists between the Ni evaporation and process parameters in the current DoE. Figure 3.17 shows the response surfaces representing the combined effect of process parameters on Ni evaporation. It was found that the scan speed (v) and hatch spacing (h, with higher significance) posed a negative relation with the output. Laser power (P) showed lower significance. It was also seen that the VED shows a highly significant (> 85 %) direct relation with the Ni evaporation. A narrower hatch spacing causes laser track overlap which ultimately results in high VED, and this finding correlates well.

$$
\begin{aligned}
Ni_{evaporation}(at.\%) \\
= 0.905882 + 0.008333P - 0.000528v + 0.02h \\
+ (2.77778E - 06)Pv - 0.000167Ph - (5.55556E - 06)vh
\end{aligned} \tag{3.9}
$$
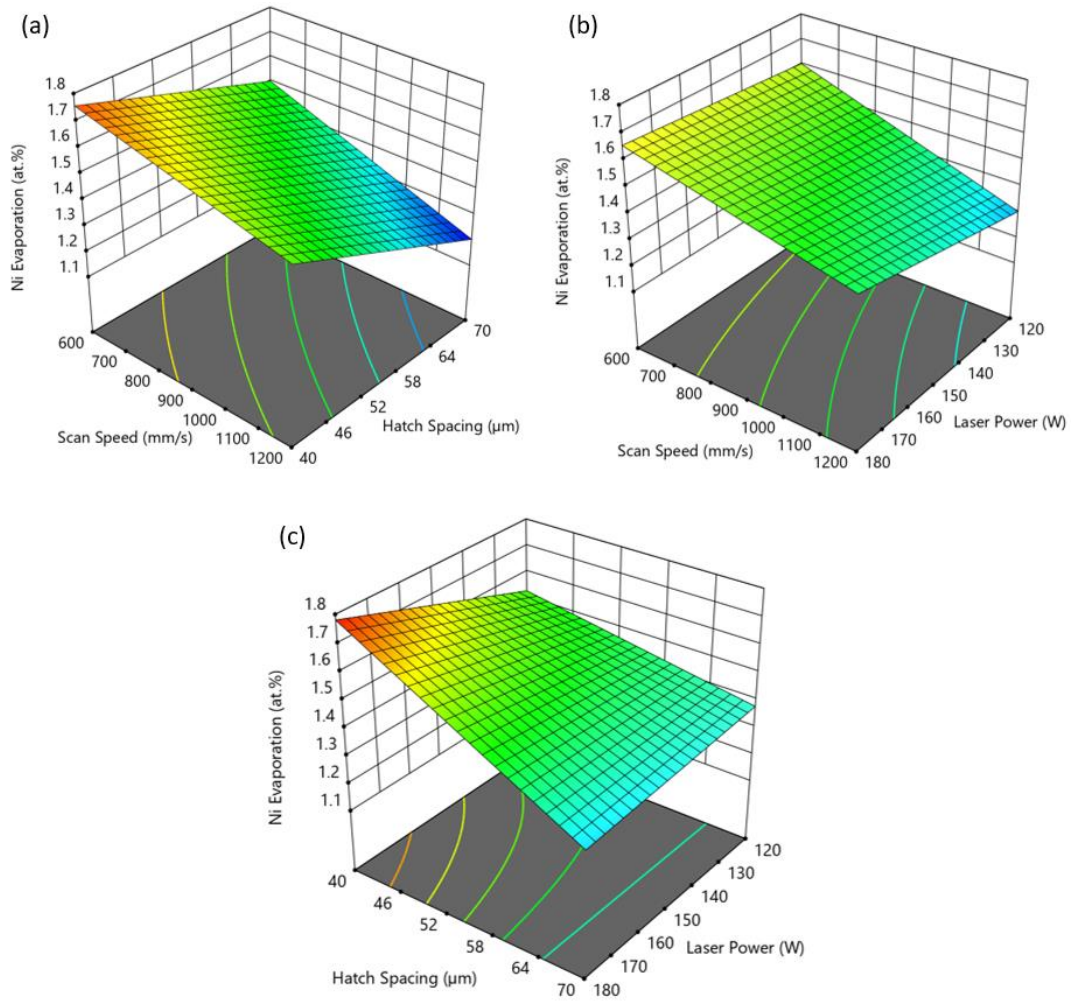
Figure 3.17 Response surfaces for Ni evaporation resulting from the L-PBF process showing the effects of **(a)** scan speed and hatch spacing, **(b)** scan speed and laser power, and **(c)** hatch spacing and laser power.

3.3.6 Thermal Expansion Characteristics

The linear thermal expansion properties of all L-PBF samples were analysed through dilatometry. Thermal strain curves were formulated as shown in Figure 3.18a, based on the thermo-mechanical data generated by the instrument. The linear thermal expansion coefficients (CTEs) were then calculated (Equation 3.10) by taking the slopes of the thermal strain curves around a selected region where the linear expansion is stabilised or where a steady state of stable phase is found. The heating and cooling cycles exhibited slightly different slopes, and therefore an average of these values were used to quantify the resultant CTE values used for the study.

$$CTE = \frac{\Delta L}{L_0 . \Delta T} \qquad (3.10)$$

where, ΔL denotes the change in one linear dimension, L_0 is the original length, and ΔT is the change in temperature causing the linear thermal expansion. The CTE values for the L-PBF samples were found to be between 10.7E – 06 /°C and 12E – 06 /°C; sample V1 was tested to have a CTE of 10.8E – 06 /°C and for V2 and V3, CTE was found to be 11.4E – 06 /°C. These results lie close to the theoretical CTE value of 11E – 06 /°C for austenite (high temperature) phase in NiTi [292]. The CTEs were calculated in the high temperature (austenitic) region. No significant correlations were found between the process parameters and CTE. The thermal expansion coefficients generally decrease with an increase in the bond energy. A higher bond energy also results in a higher melting point. Therefore, the CTE will be lower in a material that has higher melting point. Since, the compositional variation of L-PBF samples in this study are not considerable, this has not caused any significant change in the CTE.
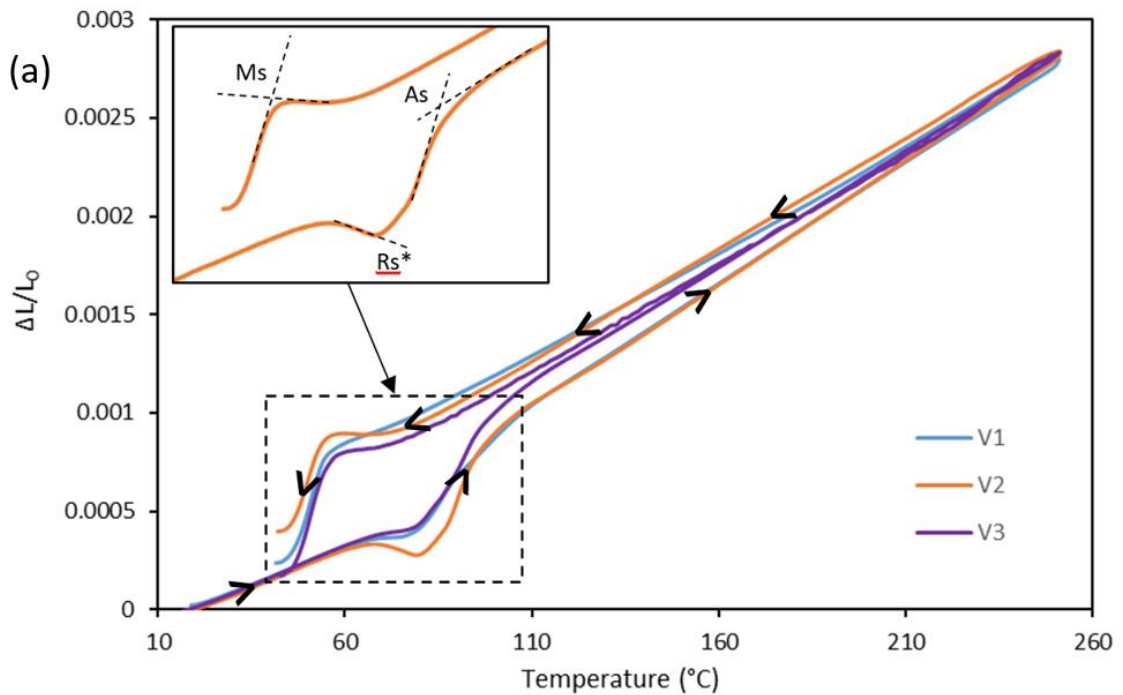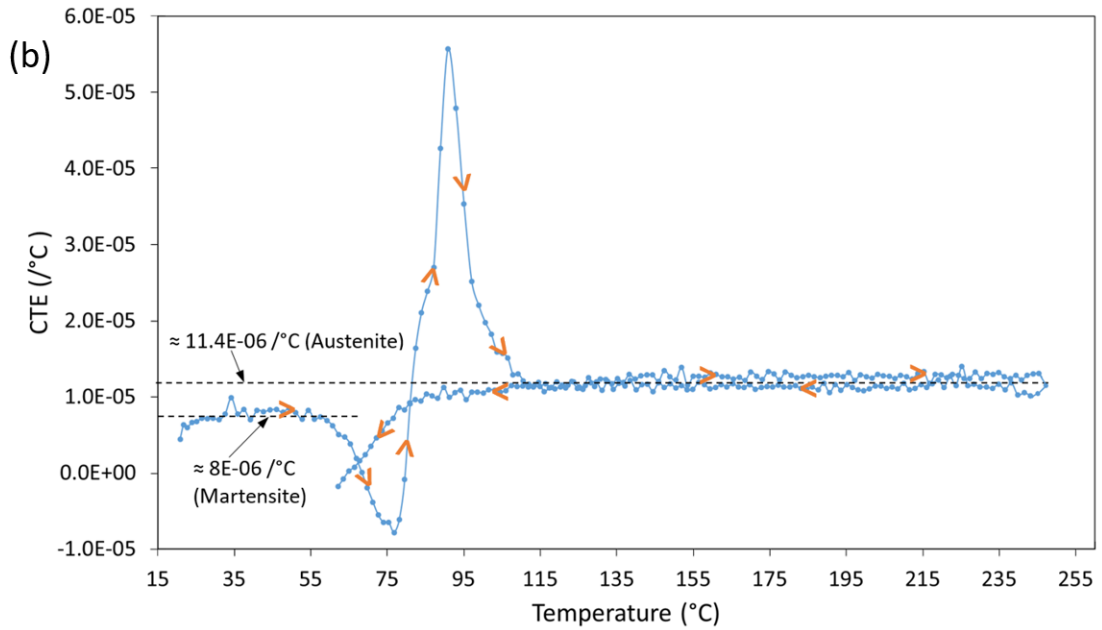
Figure 3.18 Plots of the **(a)** thermal strain curve for samples V1, V2 and V3 showing austenite and martensite phase transformations; and the **(b)** evolution of CTE with temperature for sample V2.

From the *CTE* evolution and thermal strain curves shown in Figure 3.18, we can see abrupt dips or humps during heating and cooling. These dips or humps indicate a sudden shrinkage or expansion of the material. These characteristic dip/hump indicates solid-state phase transformations as the temperature changes causing the instrument probe that is in contact with the sample, to detect an abrupt contraction or expansion of the sample [293]. The entry and exit tangents (Figure 3.18a) of these humps in thermal strain curve give an estimation of the corresponding transformation temperatures. Since the machine could not cool the sample below room temperature, the *Mf* temperatures have been excluded. The transition after the start of austenite phase was not clear enough in heating cycle, and therefore only *Ms*, *Rs**, and *As* were focussed in the study. As seen in Figure 3.19, the temperatures were close enough to the values found through the DSC curves. *Ms* and *Rs** showed high correlations (r = 0.5360 and 0.4730 respectively) between the two methods (DSC and dilatometry). There was no significant correlation between the *As* temperatures obtained by the two methods. The difference in *Ms* values obtained through the two methods ranges between 1.4 and 7.8 °C; difference between *Rs** values ranges 0.2 – 5.5 °C; and for *As* the range was found to be between 0.2 and 15.8 °C. Large variations in *CTE* will be observed when a phase transformation occurs. To explain the expansion phenomenon in NiTi, both the DSC and dilatometry data can be referred to.

103
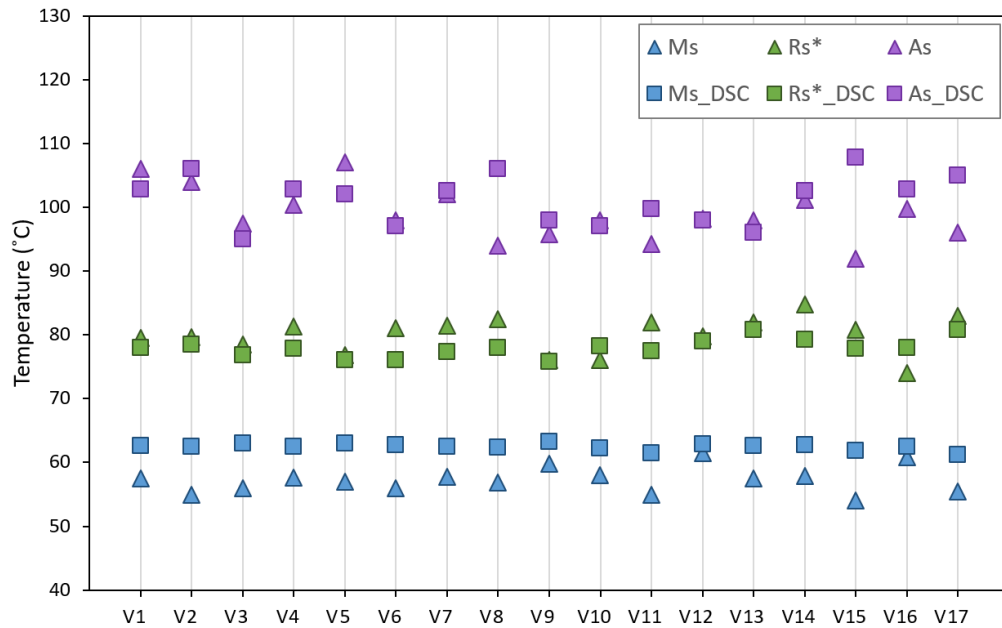
Figure 3.19 Transformation temperatures (martensite start, *Ms*; R-phase start, *Rs**; austenite start, *As*) from dilatometry data compared with the ones obtained from DSC analysis.

Due to the monoclinic structure of the martensite phase, it is possible for the martensite during transformation to form 24 different variants [53,54], and select a crystallographic equivalent variant as it transforms into austenite phase. Since, there is a fractional presence of R-phase in sample V2 as observed in DSC and XRD analysis, when the NiTi is heated crossing *Ms* temperature, the crystal lattice tends to conform to the phase variant that has lower free energy. Martensite phase has been found to have lowest energy, while the R-phase has an intermediate, and austenite having the highest free energies as shown in Figure 3.20. It should be noted that the difference between the free energies of R-phase and austenite is not significant, and the lattice always prefers to choose the phase that has a lower free energy state for stability.

The dips and humps in Figure 3.18b can be explained based on the transformation between each phase, which often results in an expansion or contraction depending on the lattice parameters of the crystal structures. The monoclinic B19' martensite lattice parameters are a = 2.877 Å, b = 4.686 Å and c = 4.099 Å, while the austenite B2 (BCC) structure has a shorter lattice a = 3.014 Å. Therefore, an *M* to *A* transformation results in a change in the lattice parameters: a increases by 7 %, while b and c decreases by 8.8 % and 1.6 %. However, the overall unit-cell volume differs by only 0.4 % [294]. In the case

of rhombohedral R-phase, lattice parameters are defined in terms of hexagonal lattice index having a = 7.358 Å and c = 5.2855 Å. A rhombohedral unit cell is a skewed version of BCC austenite elongated by 0.94 % in the [111] direction [295]. Therefore, a transformation from R^* to A is likely to cause contraction.
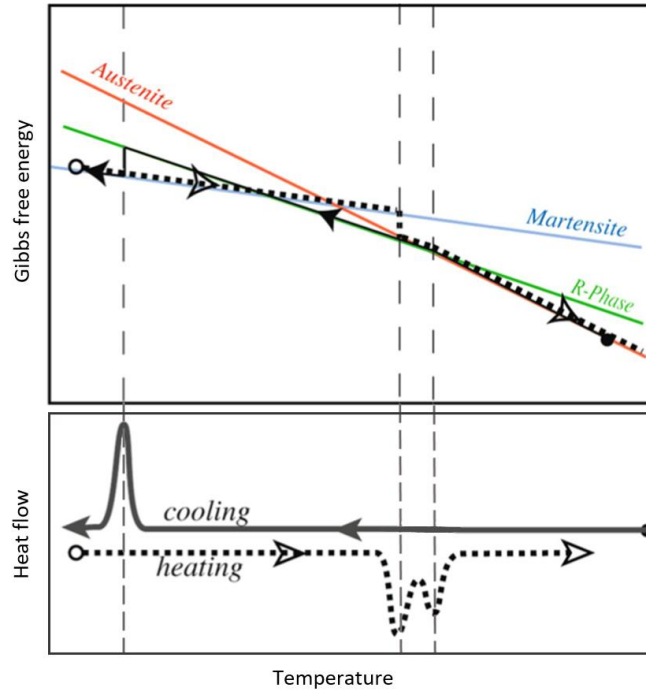
Figure 3.20 Illustration of Gibbs free energy of martensite, R-phase and austenite phases at different temperatures, compared with the DSC curve similar to the L-PBF samples in this work; dotted line represents heating cycle; figure reproduced from Deurig and Bhattacharya (2015) [296].

As observed in Figure 3.18b, the CTE is initially constant ($\approx$ 8E – 06 /°C, close to the theoretical CTE of martensite phase [292]) when heated from room temperature. Once the temperature crosses Ms, the martensite shifts to a lower energy variant while transforming to an R-phase variant. This can result in a dip in the CTE. This dip is further deepened to a few negative CTE values, which indicates a contraction as temperature rises. Depending on the homogeneity of the material, austenite and R-phase can co-exist with clear boundary between them [297]. Owing to this possibility, some of the martensite may start to transform to austenite directly instead of transitioning through an R-phase. This causes a negative CTE as the lattice contracts with an increase in temperature. Moreover, the R^* in sample V2 is an unstable variant, and exists as a shoulder on the

austenitic transformation. This points towards an inhomogeneity in the bulk phase compositions.

When the material is further heated to above R^*, R-phase starts to form indicating a sharp surge in CTE values due to an elongation in the lattice. Once the temperature is around As, the CTE values start to gradually level off and decrease (R^* to A lattice contraction) until Af is crossed, after which the curve gradually stabilises to austenitic CTE value $\approx$ 11.4E – 06 /°C. Both martensitic and austenitic CTE values were found to be very close to the theoretical values. While cooling, due to the incapability of the instrument, the cooling rate could not be maintained. This resulted in the cooling rate decreasing rapidly as natural cooling started to take over from around 70 °C and below. Due to this anomaly, the CTE evolution of the sample could not be properly understood as it highly depends on the cooling rate. However, this would not affect the determination of the Ms from the thermal strain curve, as the peak is dependent on the temperature changes. CTE evolution curve was therefore plotted only till 60 °C for the cooling cycle, to see the trend of the curve. Even though the actual mechanics are not understood, it can be seen that there has been a dip going to the negative CTE region. This indicates a possible lattice transformation from austenite to a martensite, owing to an elongation of the unit cell.

3.4 Conclusions

As-fabricated NiTi samples were 3D printed using the L-PBF (SLM) technique, and the effect of process parameters on the part density, material composition and phase transformation temperatures were analysed. To examine the relative part densities, the effect of build orientations (horizontal and vertical) were also considered. Variation in densities among the L-PBF samples were linked to the thermograph findings, and certain process-related defects. The laser energy input caused Ni evaporation which results in higher transformation temperatures than that of the raw material used. The transformation behaviour was further investigated in detail based on the DSC graphs. The endothermic and exothermic enthalpy changes associated with phase transformations were also compared and investigated to elucidate the extent of transformations. The thermal expansion characteristics for the printed samples were also studied, via dilatometry. The generated results helped in exploring the underlying mechanics of linear expansion in NiTi, and comparing the TTs to that produced via DSC analysis. All significant correlations between the input process parameters and the characterisation results were

presented in the form of response surfaces and actual equations. The following conclusions summarise the important findings from this work:

(1) The relative densities of samples printed horizontally showed higher variations between 93.4 % and 98.5 %, while vertically printed samples showed only small variations resulting in densities of 97.2 % to 97.9 %. For the current parameter levels, the RD of V-built samples presented a linear and two-factor interactive relation, while the RD of H-built samples showed an additional quadratic relation also, with the laser process parameters. For the H-built samples, an inverse effect between RD and VED was also found; highest impact was found to be from the scan speed. Low densities were found to be linked to porosity defects that are caused by trapped/escaped gas voids, keyhole formations, and defective powder particles. The structures also contained microcracks formed from residual thermal stresses.

(2) The difference in densities of the samples printed vertically and horizontally were linked to the intralayer temperature differentials. Higher difference in TD_{avg} causes larger differences in densities of samples printed in either orientation. The V-built samples were found to have a lower TD_{avg}, which resulted in a higher average density and the lower density variability compared to the horizontally printed samples.

(3) In general, L-PBF samples were found to contain an unstable overlapped R-phase with the austenite phase; the finding was corroborated in XRD analysis also. Compared to the raw powders, the L-PBF samples showed higher TTs associated with the reduction in Ni content. The *Mf* temperatures elevated by 1.2 °C to 9.0 °C. *Ms* temperatures increased by 11.8 °C to 13.9 °C; showed a linear relation to the process parameters. *Rs** elevated by about 20 °C to 25 °C, and *Rf*/As* by 7.0 °C to 19.8 °C. *Af* increased by 5.0 °C to 13.9 °C, and showed a linear and two-factor interactive relation to the process parameters. Both $RMTR$ and TTR showed linear relations to the laser parameters.

(4) The transition enthalpies for *A* to *M* and *M* to *A* transitions differed considerably, giving rise to lower transition enthalpy ratios (0.72 to 0.83) whereas the enthalpy ratios for raw powders were quite high (0.97); this was related to the extent of material that has undergone phase transformations.

(5) The Ni content was found to reduce by 1.2 to 1.8 at. % under the parameter levels used in this work. A linear and two-factor interactive relation was found to exist

between the Ni evaporation and the laser parameters. VED exhibited a high direct correlation ($> 85\ \%$) with the Ni evaporation. Scan speed and hatch spacing were found to have a negative correlation to this occurrence. Considering the above findings, we can conclude that the feedstock (pre L-PBF) composition combined with the potential of L-PBF process parameters to cause Ni evaporation (which alters the TTs) can be exploited to process NiTi for specific applications. For instance, for heat pump applications, TTs in the range of 70 to 100 °C is optimal for the operation conditions, whereas, lower TTs in the range of – 20 °C to 10 °C will be optimal for superelastic applications.

(6) The linear $CTEs$ for L-PBF samples were found to vary between 10.7 E – 06 /°C and 12E – 06 /°C under the austenitic region, and be approx. 8E – 06 /°C for the martensitic region, in close agreement to the theoretical values. The transformation temperatures found via dilatometry and DSC were also in good agreement.

The above findings were for the current selection of process parameters and levels. These could differ greatly with respect to the material composition chosen, operation environment, and range of parameters used. For instance, the relationship between VED and part density does not clearly explain how density can be controlled, this strongly encourages the need for a new relationship that considers different aspects of the L-PBF process, such as powder material characteristics, laser processing properties and inert-gas flow properties, in more detail. A few of the defects could be avoided prior to the process itself, for instance, a meticulous preparation and recycling of raw powders processed with good morphology and rheology can help to avoid chances of certain internal porosities. Substrate preheating can help to reduce the residual thermal stresses. Indeed typically, the as-fabricated samples are preferred to undergo annealing or thermal post-processing in order to relieve thermal stresses, and combat the formation of precipitates and secondary phases that affects the matrix composition and/or the SME characteristics.

In future work, it is planned that the resulting physical properties will be examined further. The response surface analysis indicates how the responses vary for the current selection of L-PBF design space. The optimum selection of L-PBF parameters from these surface analyses depends on the end application, for example, biomedical application requires lower TTs and lower Ni reductions whereas in SME applications in aerospace requires higher TTs and higher Ni reductions. Based on this, the current design space can

be widened or skewed to enhance or optimise the required response. In future, the author suggests to widen the borders of design space keeping the centre point same. This can help to visualise how material would behave beyond the current design space.

3.5 Contribution to Thesis Objectives

After thorough analysis of findings from existing literature, the L-PBF design space was determined for this project, accounting the feedstock material properties and machine limitations. Through this chapter, the structural porosities on both vertical and horizontal build were analysed for its formations, cause, and correlated with L-PBF parameters. The reduction in Ni content, phase transformation temperatures and enthalpies, and thermal expansion characteristics were explored on vertically built samples, and correlated with L-PBF parameters. Thus, this chapter has contributed towards analysing the physical, chemical, and thermal characteristics of L-PBF processed NiTi.

Chapter 4

Control of Mechanical and Shape Memory Characteristics in Martensitic NiTi by setting Laser Powder Bed Fusion Parameters and Build Orientation

Publication Status: Published.

4.1 Abstract

The current work encompasses a study of as-fabricated martensitic NiTi samples printed via Laser Powder Bed Fusion (L-PBF) in the horizontal (H-built) and vertical (V-built) build orientations, with systematic variations in the L-PBF process parameters. The sample densities, compositions, thermal characteristics and mechanical responses were analysed and correlated with L-PBF parameters. Mechanical responses measured and analysed included microhardness, impact energies, and elastic modulus. The process parameters were found to have a significant effect on the resulting properties. The variation in physical properties and mechanical responses between each sample of the vertical build were less compared to those measured for the horizontally built samples. The L-PBF samples were compressed to 6 % engineering strain (within elastic limit), and their shape memory strains were thermally recovered. Digital Image Correlation (DIC) based full-field strain analysis was performed during compression to measure local strain fields which revealed in detail the macroscopic effects during detwinning. The shape memory capability of the L-PBF samples was quantised based on strain recoveries attained after thermal recovery. Microstructural variations in submicron scale were also analysed in as-fabricated, post-compression and post-recovery stages, showing the sample response during different deformation mechanisms.

4.2 Materials and Methods

4.2.1 L-PBF Process

The raw NiTi powders were supplied by *Ingpuls GmbH* from Germany, with a nearly equiatomic composition of Ni (49.9) - Ti (50.1 at. %). Higher Ti content was preferred to be used to ensure higher phase transformation temperatures resulting in a martensitic phase at room temperature to achieve SME. The composition was reconfirmed using the EDX module attached to a *Hitachi S5500* FE-SEM. The powders were produced by gas atomisation via an electron induction melting gas atomisation (EIGA) process. The particle size distribution (PSD) was analysed as $D_{10} = 12.3 \pm 0.8$ μm; $D_{50} = 28.1 \pm 2.2$ μm; $D_{90} = 57.3 \pm 7.7$ μm; $D\,[4,\,3] = 34.0 \pm 3.1$ μm, in line with the supplier specifications. Under SEM, the particles were found to be near-spherical in shape, however, a few particles were slightly ellipsoidal attached with tiny satellite particles.

The NiTi samples were 3D printed using a *Aconity MINI (GmbH)* L-PBF machine. The machine is equipped with *IPG Photonics* Nd:YAG fibre laser system, with a maximum

laser power of 200 W and wavelength of 1068 nm. To prevent any oxidation during L-PBF, minimum oxygen content ($<$ 50 ppm) was ensured by flooding the chamber with 99.999 % pure Ar gas. To investigate the effect of L-PBF parameters, a Box-Behnken design of experiments (DoE) was followed. Due to the intrinsic repeatability (5 repetitions of centre node), this DoE do not require sample repetitions as needed in a full-factorial DoE, thereby reducing material, time and energy consumption. However, the fewer design points in this DoE does not include an embedded factorial design, and this limits the sequential studies of factors and process repeatability of destructive tests. The DoE was designed using three factors (laser power, scan speed and hatch spacing) and three levels for each; providing 17 samples in total (as shown in Table 4.1). These 17 samples of dimensions 10 x 10 x 55 mm were printed using 120, 150 and 180 W laser powers with a combination of 600, 900 and 1200 mm/s laser scan speeds and 40, 55 and 70 µm hatch spacings. The layer thickness (40 µm) and spot size (50 µm) were kept constant. These process parameters were used to print samples in two different orientations (horizontal and vertical) to study the effect of build orientation on part properties. The powder layer thickness and supply factor were selected appropriately to ensure good flowability and powder spread on the build platform.

The volumetric energy density (VED) was calculated following Equation 1.4. In the current DoE, the VED was calculated to vary between 44.64 and 156.25 J/mm^3. On the build platform (substrate plate), the samples were arranged at an in-plane angle of 45° for V-built samples and 30° for H-built samples. This was done to reduce impact loads when recoater blades scan each layer and also to allow more uniform gas flow (fume removal and cooling) over each sample. As shown in Figure 4.1a, a simple stripe scanning strategy was followed with 90° rotation between each subsequent layer. The ambient temperature of the build chamber was monitored to be 20 $\pm$ 1 °C.

Table 4.1 Laser process parameters used for printing the NiTi samples.

Sample no. (V/H)	Laser power (W)	Scan speed (mm/s)	Hatch spacing (μm)	VED (J/mm^3)
1	150	900	55	75.76
2	120	600	55	90.91
3	180	600	55	136.36
4	180	1200	55	68.18
5	150	600	40	156.25
6	150	900	55	75.76
7	150	1200	40	78.13
8	180	900	70	71.43
9	180	900	40	125.00
10	150	900	55	75.76
11	150	1200	70	44.64
12	120	900	40	83.33
13	150	900	55	75.76
14	150	900	55	75.76
15	120	1200	55	45.45
16	150	600	70	89.29
17	120	900	70	47.62

Figure 4.1 (a) Illustrative image of L-PBF printing strategy along the build direction, and sample extraction from V-built and H-built samples for various characterisations (1 – compression tests, EBSD, AFM, Nanoindentation; 2- SEM/EDX, optical microscopy, microhardness test; 3 – DSC), **(b)** speckle pattern generated on L-PBF sample for DIC analysis.

4.2.2 Physical and Thermal Characterisation

The relative densities of the as-fabricated H/V samples were measured via Archimedes method following ASTM B962-17 standards. Analytical balance *Sartorius Entris II Essential BCE124I-1S* having an accuracy and repeatability of ± 0.1 mg was used. The samples were ground flat using 240 grit abrasive paper on all faces, to any remove spatter particles and surface roughness occurred through AM. The samples were then cleaned thoroughly and weighed in acetone, and densities were calculated. These densities were then fractioned with the theoretical density value (6.45 g/cm^3) of a fully dense NiTi to calculate the relative densities.

The prepared samples used for density tests were then precision-cut into sub-parts as shown in Figure 4.1a, using diamond-infused blades at constant slow feed rate and speed with flood coolant to avoid excess heat or stress-induced alterations to microstructure. Differential Scanning Calorimetry (DSC) technique was used via *Netzsch DSC 214* to determine the calorific heat flow properties and phase transformation temperatures following ASTM F2004 − 17. Two thermal cycles were pursued on all 34 samples (H-built/V-built) using a cool/heat ramp rate of 10 °C/min; controlled cooling was achieved using liquid nitrogen. The first cycle was designed to run from – 60 °C to 130 °C to – 60

°C, and then brought back to room temperature. In the second cycle, temperatures were readjusted for more economic operation; – 20 °C to 140 °C to – 20 °C, and back to room temperature.

4.2.3 Mechanical Characterisation

Charpy impact tests were conducted on the *Denison Mayes 6705* impact equipment for sub-size specimens (as per ASTM E23-18) having dimensions of $10 \times 7.5 \times 55$ mm with a V-notch cut 2 mm $\times$ 45° and 0.25 mm base radius. The fractured surfaces were observed under SEM to capture the fractography. For Vicker's microhardness, a *Leitz Wetzlar Miniload* Hardness Tester equipment was used with a 300 g load. Five measurements were carried out and the average value was used.

Mechanical uniaxial compression tests were performed using a computer-controlled *Zwick 50kN* universal testing machine. The compression involved a strain-controlled loading cycle and an unloading cycle, at a crosshead speed of 1 mm/min. Each sample (of dimensions 7.5 x 10 x 20 mm) was subjected to one cycle of loading and unloading. A maximum strain limit of 0.09 was assigned in the machine which resulted in an actual material (engineering) strain of 0.06 ± 0.001 in all samples. The strain recorded/applied by the machine is typically prone to multiple bending forces from the crosshead and combination of engaged components, especially during compression of hard materials. Therefore, actual material strain was obtained through data from Digital Image Correlation (DIC) based strain analysis.

The DIC technique works on the basis of analysing the evolution of displacements of each pixels between each frames. For this, speckle patterns were created on one face of each of the L-PBF samples (Figure 4.1b), through laser marking using a *NKT Origami XP 1030* nm wavelength femtosecond laser, with 400 fs pulse width, 20 µs/pixel exposure time, 4W average power, and a pulse repetition rate of 1000 kHz. The laser system used a galvanometer scanner (*Focusshifter-15* by *Raylase GmbH*) and an F-theta lens to focus the beam (working distance = 200 mm).

The frames were recorded via a 4K (3480×2180) resolution camera at 60 Hz, with a 2x optical magnification. The camera was aligned with the centre of the surface of sample. The external lighting and focus was manually adjusted to control the exposure and image contrast; focal zone mapping was used to prevent any parallax error. The region of interest

(surface component) from the recorded frames were then locked and analysed via *Zeiss GOM Correlate* software. Spatial resolution was set by a facet size of 18 pixels and grid spacing of 12 pixels. The computation was based on bi-cubic subpixel interpolation with maximum residual of 20 values, accuracy of 0.1 pixels, and a 0.1 % strain uncertainty. Time synchronization between the stress data from Zwick machine and strain/displacement data from GOM Correlate was performed to interpret the actual engineering strain data.

The compressed samples were then subjected to thermal treatment as an attempt to recover the original shape. The heating was performed from 20 °C (room temperature) to 125 °C at a ramp rate of 2 °C/min in an argon atmosphere. The maximum temperature was held for 120 s before cooling back down to room temperature. This heat-based strain recovery was performed using a *Netzsch DIL 402 PC* dilatometer, and recoveries at different temperatures were measured. The dilatometer was not equipped with cooling system, so once the maximum temperature was reached, the sample was allowed to cool naturally. And the final dimensions were measured using high-precision micrometre with 5 repetitions, and an accuracy of 10 µm.

4.2.4 Microstructural Characterisation

The samples were ground using abrasive SiC papers P240, P600, P800 and P1200, and then polished using 6, 3, 1 µm diamond suspensions and 60 nm colloidal silica. The samples were then etched by swabbing the surface with 15 mL HF + 10 mL HNO_3 + 10 mL CH_3COOH + 5 mL glycerol for approx. 2 – 3 s, to visualise the microstructure. Microscopic images were captured using *Keyence VHX2000E 3D* Digital microscope. Before etching, the chemical composition of the L-PBF samples was analysed through an *Aztec Live System* from *Oxford Instruments NanoAnalysis* EDX unit attached to a *Zeiss EVO LS-15* SEM. Backscattered electron (BSE) imaging was also obtained using a CZBSD semiconductor (with four diode segments) detector installed in the SEM.

The crystallographic features including phases and crystal structures were analysed through Electron Backscatter Diffraction (EBSD) equipment. The detector used was an *Oxford Instruments Symmetry S2* under 20 kV and 10 nA with a 70° tilt. The working distance was kept at 14 mm and a FOV map size of 200 µm and 50 µm was scanned with a step size of 0.1 – 0.3 µm and 0.03 – 0.08 µm, respectively. The samples were coated with thin carbon coating to improve conductivity. The samples were prepared using the

same polishing routine explained earlier, followed by an additional vibro-polishing for 8-10 hours using 60 nm colloidal silica. The same samples were again used for optical profilometry and AFM.

Atomic Force Microscopy (AFM) equipment *Bruker Dimension Icon* was used to study the topological variations at submicron scale. The scan was performed under *ScanAsyst* imaging mode (peak force tapping) with a scan size of 20 x 20 μm, 256 sample points, and a drive frequency of 0.5 kHz. The *ScanAsyst* is used to automatically control the force setpoint. A silicon tip on nitride lever with cantilever spring constant = 0.4 N/m and resonance frequency = 70 kHz was used. Thermal tuning method was followed to determine the spring constant and deflection sensitivity. The samples were analysed in conjunction with an *FRT MicroProf 200* optical profilometry equipment using white light and a 3 mm probe. The surface elevations were contour mapped over the top surface at a resolution of 10 μm. The final data was normalised to analyse the difference in samples and after each functional stage.

4.3 Results

4.3.1 Correlation & Significance

Studying the effect of L-PBF parameters on material responses is an integral part of this work. All possible correlations and significances between the input parameters and output responses were analysed. Pearson correlation coefficient (r) and model significance (p-value) were used to quantise the relationship between L-PBF parameters and response factors. Table 4.2 shows all significant correlations found. A strong and significant correlation is identified when r ≥ 0.35, and a p-value ≤ 0.05; higher r and lower p-value indicates stronger correlation and higher significance, respectively. If r is negative, the correlation is considered inverse. VED is not a control-parameter in the current BB DoE model, hence p-value is not applicable where VED is correlated.

Table 4.2 Pearson coefficients and p-values indicating input-output correlations.

Correlation Factors	r	p
V-built Samples		
Composition		
Scan Speed – Ni Evaporation	-0.5817	<0.0001
Hatch Spacing – Ni Evaporation	-0.6980	<0.0001
VED – Ni Evaporation	0.8585	N/A
Mechanical Properties		
Laser Power - Microhardness	0.4193	0.0117
VED – Impact Energy	-0.3769	N/A
VED – Young's Modulus (E_M)	-0.5300	N/A
Laser Power – Irrecoverable Strain	0.7622	0.0003
Laser Power – Irrecoverability	0.7375	0.0013
H-built Samples		
Physical Properties		
Laser Power – Density	0.4122	0.0001
Scan Speed – Density	0.5847	<0.0001
Hatch Spacing – Density	0.4207	0.0001
VED – Density	-0.4825	N/A
Composition		
Laser Power – Ni Evaporation	0.5997	0.0006
Scan Speed – Ni Evaporation	0.4361	0.0050
Thermal Characteristics		
Laser Power - TTR	0.6593	0.0002
Hatch Spacing - TTR	-0.4069	0.0066
VED - TTR	0.5531	N/A
Laser Power – Endothermic Enthalpy	-0.3958	0.0139
Laser Power – Exothermic Enthalpy	-0.4483	0.0066
Hatch Spacing - TEr	0.8811	<0.0001
Mechanical Properties		
Scan Speed – Impact Energy	0.4766	0.0243
Hatch Spacing – Impact Energy	0.5632	0.0100
VED – Impact Energy	-0.7172	N/A

4.3.2 Relative Densities

The relative densities (RD) of as-fabricated V-built samples were found to vary between 97.2 % and 97.9 %. In H-built for similar processing conditions, larger variations in RD between 93.4 % and 98.5 % were noted (Figure 4.2). Most of the H-built samples were found to have lower densities than their V-built counterparts. The results from the 17 process parameters were used to identify the response surfaces and actual equations capable of finding the optimum process parameter configuration; results originally

published in Chekotu *et al.* [46]. From the response surface model of V-built samples, it was found that the interaction between laser power and hatch spacing was highly significant (p = 0.0059) on RD. In the case of H-built, it can be seen (Table 4.2) that the scan speed exhibited the highest positive correlation with RD, however, VED showed an inverse correlation.
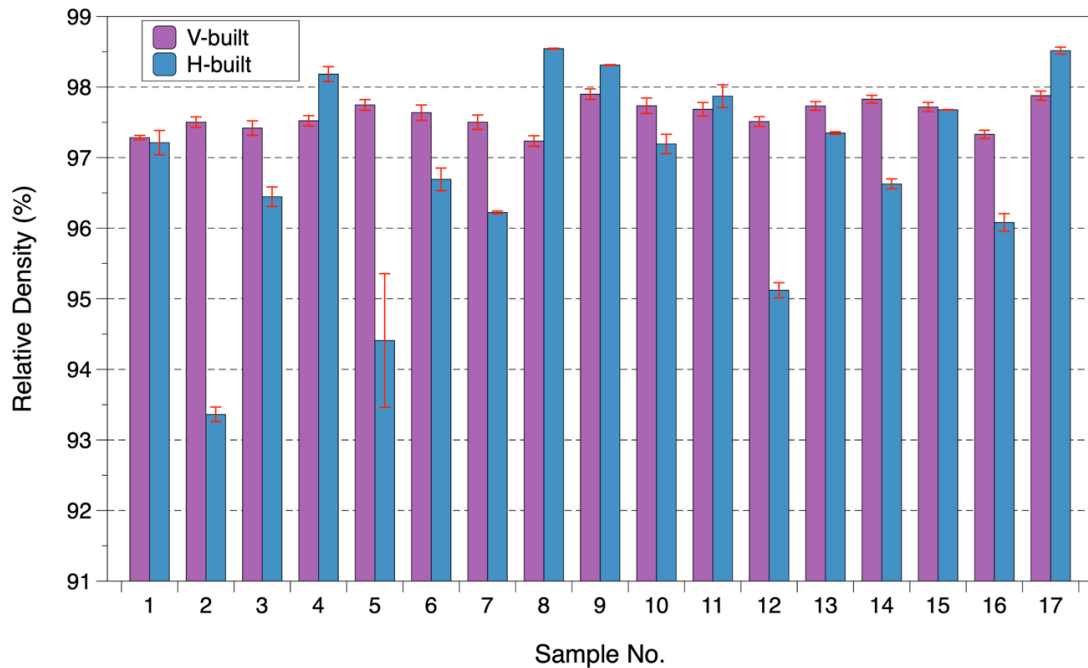
Figure 4.2 Relative densities of V-built and H-built samples printed using the set of 17 process conditions; 95% confidence interval implemented based on n = 3; samples 1, 6, 10, 13, 14 were produced with the same processing parameters.

4.3.3 Phase Transformation Characteristics and Ni Evaporation

As mentioned earlier, two thermal cycles were conducted using DSC for each of the L-PBF samples. The phase transformation temperatures (TTs) were calculated [46] from the heat flow vs temperature graphs generated by DSC analysis. The first cycle showed the presence of two stable phases (identified as peaks in DSC, starting and ending from the baseline) – martensite and austenite along with a third unstable variant (*R**) of intermediary R-phase (rhombohedral crystal structure). In-depth detail of the first cycle was originally reported in Chekotu *et al*. [46]. In the second cycle, the unstable phases were no longer observed, instead the profile showed only fully stable phases. The difference between first and second cycles can be seen clearly in Figure 4.3. The heat flow profile generated during the first thermal cycle was irregular and unrepeatable, whereas the profile generated in the second thermal cycle was repeatable. A shift in TT

of about 10 – 25 °C on the endothermic side was also noted between the first and second thermal cycles. This was also seen in a previous work by Turner [52].
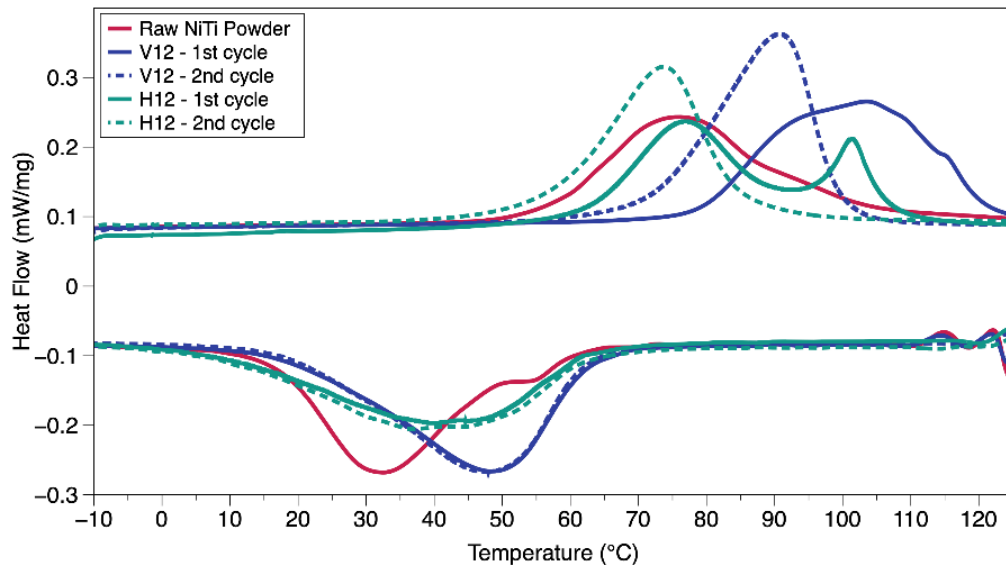
Figure 4.3 DSC thermal profiles showing shift in transition peaks of H/V samples compared to that of the raw powders. In both H/V-built samples, profiles of second thermal cycle show smooth behaviour compared to the ill-behaved first thermal cycle.

The critical TTs considered are martensite start (*Ms*), martensite finish (*Mf*), austenite start (*As*) and austenite finish (*Af*). These temperatures were noted and presented in Figure 4.4 from the profile of second thermal cycle (Figure 4A1 in Appendix A) of all H/V-built samples. The *Mf* temperatures were higher for V-built samples: range of 12.2 – 21.1 °C, and lower (0.8 – 13 °C) for H-built samples. For H-built samples, it was found that *Mf* exhibited high inverse correlation with laser power, and a marginal inverse correlation with VED. *Ms* temperatures were also higher (61 – 63 °C) for V-built samples, and lower in the range of 59.4 – 66.5 °C for H-built samples.

For V-built samples, *As* temperatures were higher in the range of 68.7 – 73.9 °C. On the contrary, in H-built samples, the *As* temperatures (50.5 – 62.2 °C) fell below their corresponding *Ms* temperatures; indicated by the dark peach shade in Figure 4.4. The *As* temperatures in V-built samples showed negative correlation with laser power and VED, and a positive correlation with hatch spacing. *Af* temperatures were in the range of 94.8 – 102.6 °C for V-built samples, and 83 – 90.5 °C for H-built samples.

An additional measure, called full transformation temperature range, $TTR = Af - Mf$, is considered to indicate the boundaries of transition span of a sample. This helps to determine the operational field of the NiTi material. TTR varied between 76.5 °C and 84.3 °C for V-built samples. For H-built samples, TTR varied from 72.2 to 83.7 °C, and showed positive correlations with laser power and hatch spacing, and an inverse correlation with VED.
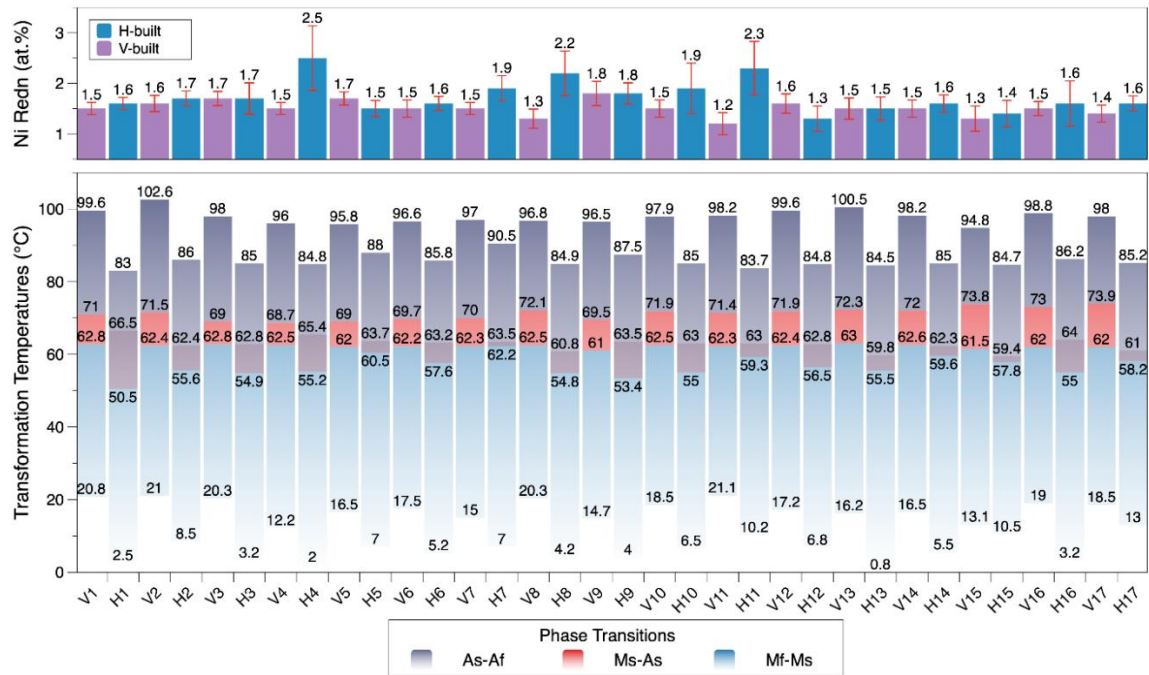
Figure 4.4 Top - Ni reduction observed in V-built and H-built samples along with error bars representing standard deviation (n = 10) for each samples; Bottom - Transformation temperatures showing different phase transition ranges: martensite (*Mf-Ms*), transition (*Ms-As*), and austenite (*As-Af*); In all H-built samples, Ms overshot As, indicated by darker peach shade.

Each of the phase transitions involve enthalpy changes. The $M \rightarrow A$ austenitic transformation (heating cycle) is associated with an endothermic enthalpy ($\Delta H_{heating}$), while the $A \rightarrow M$ (cooling cycle) involves exothermic enthalpy ($\Delta H_{cooling}$). These enthalpy changes are determined by calculating the area enclosed by the peaks with the baseline in heat flow (W/g) vs time parameter (seconds) graph from DSC analysis. The enclosed area was calculated by isolating each peaks and conducting MATLAB trapezoidal numerical integration using *trapz* function. A third analysis parameter called transition enthalpy ratio (TEr), Equation 3.4, was also used to better understand the

calorific-difference implications during the phase transitions. The enthalpies and ratios for L-PBF samples are plotted in Figure 4.5.
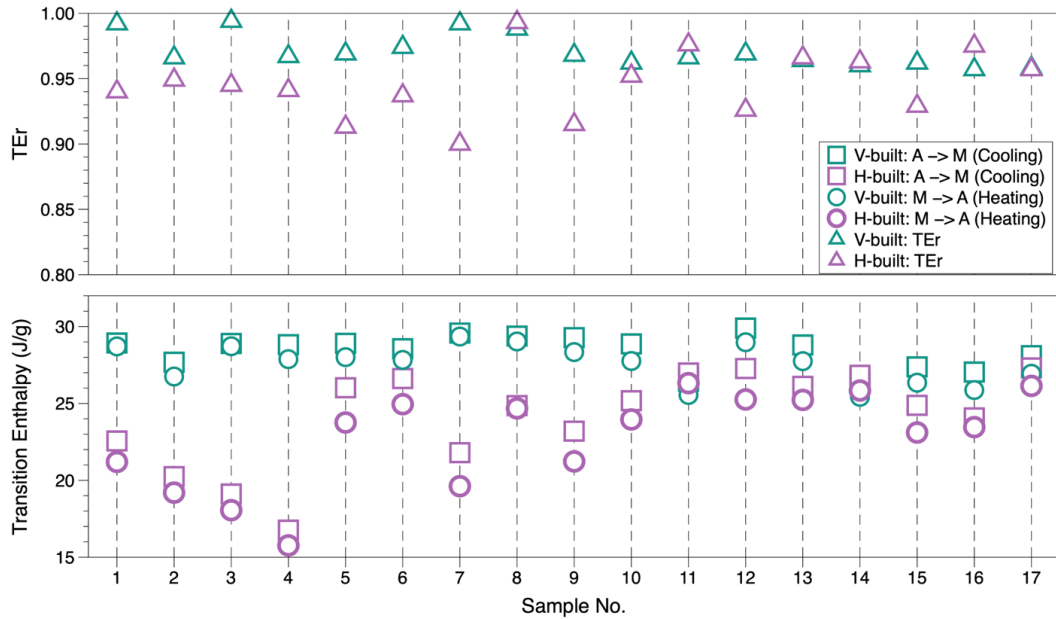
Figure 4.5 Enthalpies of horizontally (H-built) and vertically (V-built) oriented samples, recorded during austenitic and martensitic transformations, and their corresponding enthalpy ratios (TEr).

In general, the transition enthalpies and ratios were higher for V-built compared to H-built samples. $\Delta H_{heating}$ varied from 25.4 to 29.35 J/g for V-built, and 15.77 to 26.32 J/g for H-built samples. $\Delta H_{cooling}$ varied from 26.45 to 29.90 J/g for V-built, and 16.76 to 27.31 J/g for H-built samples. In both build orientations, the endothermic enthalpy was found less when compared to the exothermic enthalpy. For V-built samples, TEr ranges from 0.96 to 0.99, whereas in H-built, TEr ranges from 0.90 to 0.99. For H-built samples, both the endothermic and exothermic enthalpies exhibited an inverse correlation with laser power; hatch spacing posed high direct correlation with TEr with high significance ($p < 0.0001$).

The transformation temperatures are also linked to the Ni/Ti composition. The post - L-PBF composition of each sample was analysed to see the change in Ni content with respect to laser process parameters. Ni evaporation is a common occurrence in L-PBF processes due to the high energy input and differences in boiling point temperatures between Ni (2,730 °C) and Ti (3287 °C) [36]. 10 measurements were taken for each sample and standard deviation was also measured (Figure 4.4). The standard deviation for H-built samples was found to be generally higher than the V-built samples.

From response analysis, it was found that the scan speed and hatch spacing posed a high negative correlation with Ni evaporation in V-built samples, while laser power and scan speed showed positive correlation with Ni evaporation in H-built samples. The response analysis returned a two-factor interaction correlation for both V-built (Equation 4.1) and H-built (Equation 4.2) samples, between Ni evaporation and the L-PBF process parameters, where P = laser power; v = scan speed; h = hatch spacing. Figure 4.6 shows the response surfaces of both V-built and H-built samples. In H-built samples, the effect of hatch spacing was found to be less significant (0.0230) compared to that of the V-built (< 0.0001).

The raw NiTi powders contained 49.9 at. % Ni. This composition is highly relevant, as reduction in Ni beyond this composition shows a minimal effect in elevating the TTs (specifically *Ms*) [46,288]. It can be noted that in V-built samples where the Ni evaporation was in the range of 1.2 to 1.8 at. %, the change in TTs was somewhat influential and has caused an increase in *Ms* by about 14 °C compared to the raw powder [46]. *Mf*, *As* and *Af* also showed elevation as well. The increase in TTs after L-PBF processing has also been noted in the past by other researchers [298,145].

However, in the case of H-built samples where 1.3 to 2.5 at. % Ni evaporation was noted, the TTs (specifically *Mf*, *As* and *Af*) were found to decrease compared to the raw powder. Despite this decreasing trend, the *Ms* temperatures were found to increase (more than that of V-built). This has also resulted in Ms overshooting *As* temperature, and the endothermic and exothermic heat flow profiles overlap at this temperature region.

$$
\begin{aligned}
Ni_{evaporation}\ (at.\%) \\
= 0.905882 + 0.008333P - 0.000528v + 0.02h \\
+ (2.77778E - 06)Pv - 0.000167Ph - (5.55556E - 06)vh
\end{aligned} \tag{4.1}
$$

$$
\begin{aligned}
Ni_{evaporation}\ (at.\%) \\
= 4.63039 - 0.021389P - 0.004833v - 0.013333h \\
+ (3.1E - 05)Pv + (5.6E - 05)Ph + (1.7E - 06)vh
\end{aligned} \tag{4.2}
$$
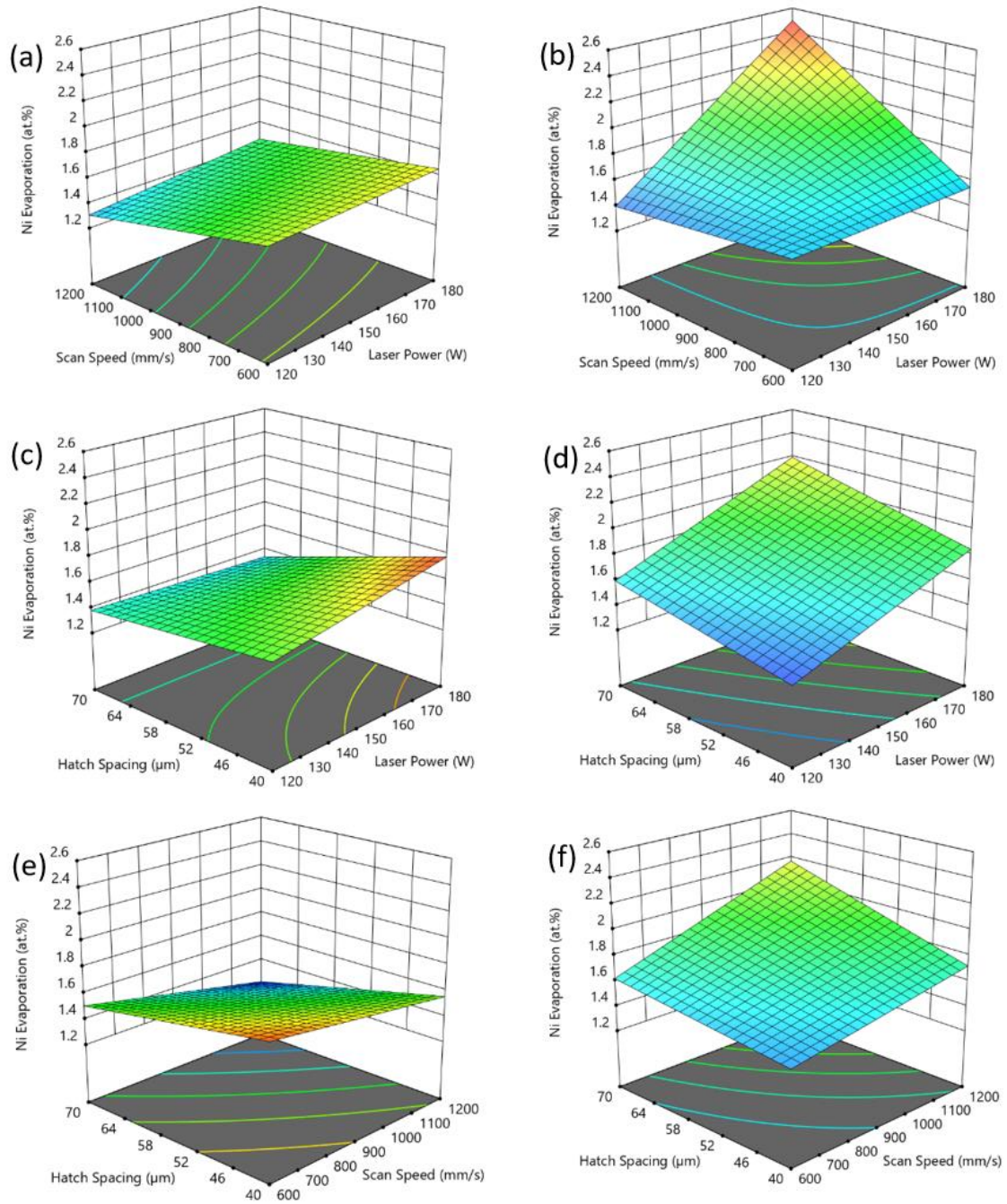
Figure 4.6 Response surfaces of Ni reduction due to L-PBF process parameters, in V-built **(a, c, e)** and H-built **(b, d, f)** samples; each response surface is plotted while the third parameter is at mid-level.

4.3.4 Vickers Microhardness

The microhardness test was conducted around the centre of a cross-sectional surface parallel to the longest length as shown in Figure 4.7a. This cross-sectional plane is the plane used for compression tests also. From microhardness tests, it was seen (Figure 4.7b) that the V-built samples were slightly softer (248 – 362 HV) compared to the H-built

124

samples (290 – 454 HV). The standard deviation was also found to be generally larger in H-built.
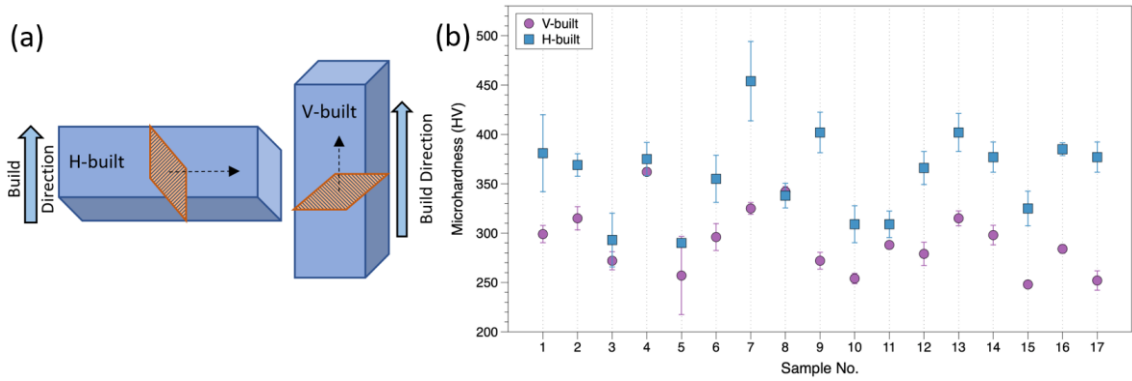
Figure 4.7 (a) Illustration of cross-sectional plane where microhardness indents were made in V-built and H-built samples (sample was extracted as per Figure 4.1); axis of compression represented by arrows, **(b)** Vickers microhardness results for all 17 V-built and H-built samples; error bars represent standard deviations (n = 5).

For V-built samples, a direct positive correlation was found between laser power and microhardness. From the response surface analysis, a two-factor interaction relation (Equations 4.3 and 4.4) was found between microhardness and the responses of V-built and H-built samples, respectively. Here also, the model was more significant in the case of V-built (p = 0.0033) compared to the H-built (p = 0.0115). For V-built orientation, interaction between laser power and scan speed was highly significant, whereas in H-built, interaction between scan speed and hatch spacing was observed to be highly significant. The responses based on two-factor interactions for both V-built and H-built are presented in Figure 4.8.

$$Microhardness\ (HV) = 1001.98 - 6.247P - 0.419v - 4.608h$$
$$+0.004361Pv + 0.053889Ph - 0.003556vh$$

(4.3)

$$Microhardness\ (HV) = 359.24 - 3.62P + 15.75v - 12.88h +$$
$$31.50Pv - 18.75Ph - 60vh$$

(4.4)
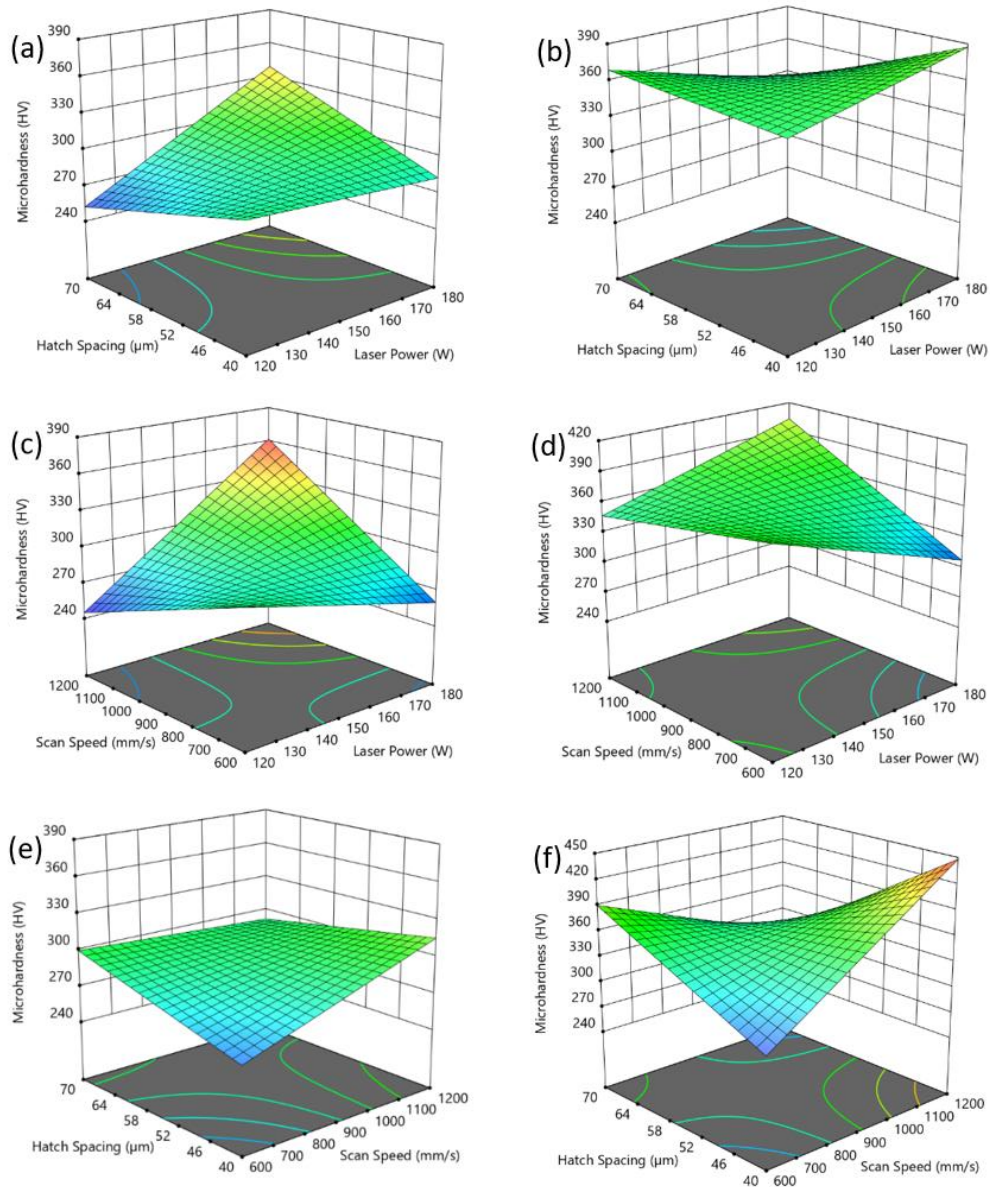
Figure 4.8 Response surfaces of microhardness levels due to L-PBF process parameters, in V-built **(a, c, e)** and H-built **(b, d, f)** samples; each response surface is plotted while the third parameter is at mid-level.

4.3.5 Charpy Impact Energy

Looking at the fractographs (Figure 4.9), we can see brittle fracture (agrees with the high hardness values obtained) in both V-built and H-built samples along with an extraordinarily ordered brick-like arrangement (Figure 4.9b) inherent to NiTi. There were sites of open pores, un-melted particles and process-induced porosities (primarily keyholes) as seen in Figure 4.9c – 4.9f that might have further weakened the structure.
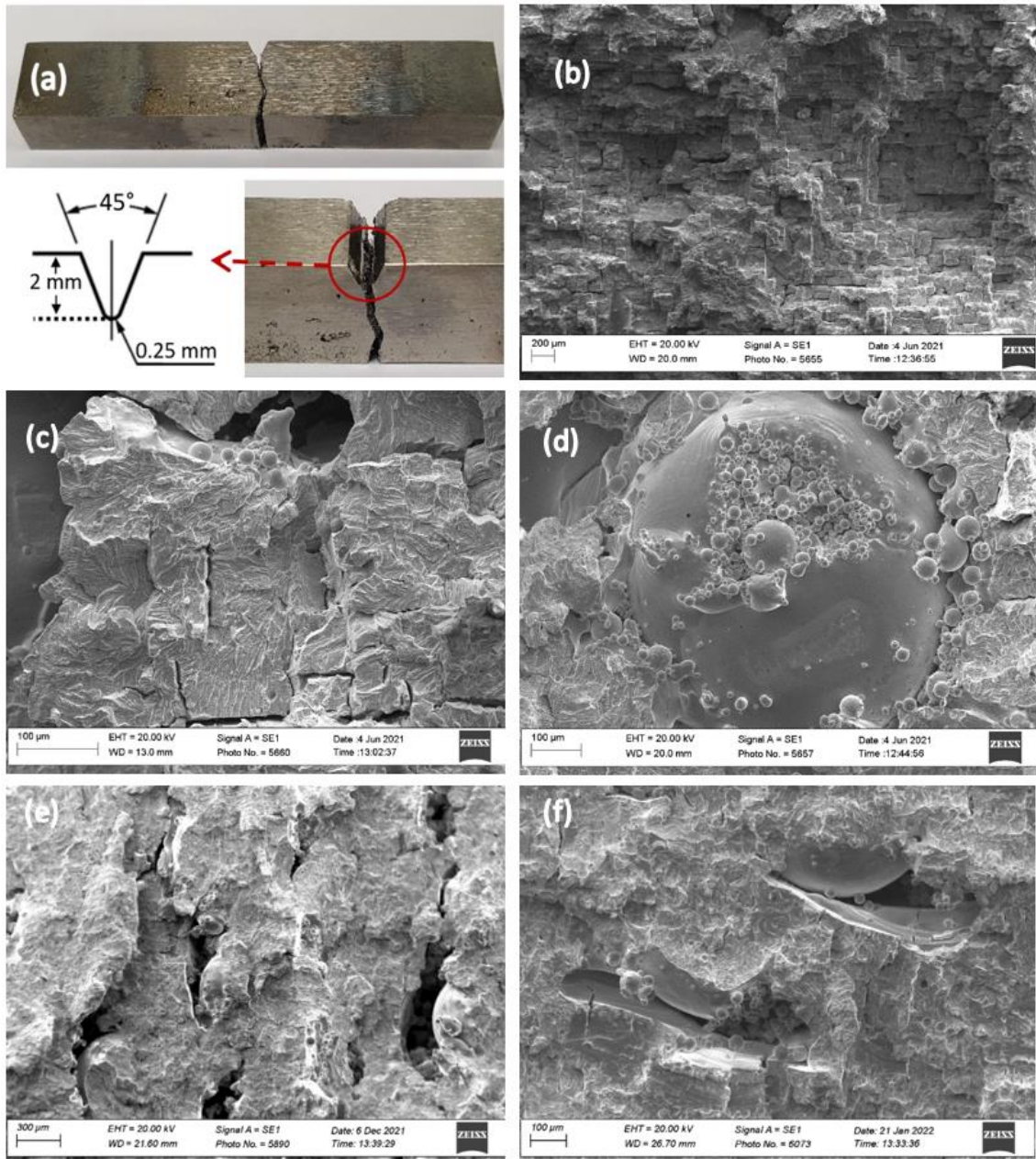
Figure 4.9 (a) Sub-size specimen V1 after impact test with V-notch specifications; SEM fractographs after Charpy impact tests of sample V1: **(b)** brick-like ordered cuboidal arrangement **(c)** brittle characteristics, **(d)** un-melted powders; sample H1: **(e)** process-induced porosities **(f)** brittle characteristics and un-melted particles.

In general, the impact energies were found to be low due to the brittle nature of as-fabricated L-PBF samples (Figure 4.10). The impact energies were higher, 4.8 to 6.2 J, for V-built samples when compared to the H-built samples, where it varied from 3.2 J to 6 J. For H-built orientation, scan speed and hatch spacing posed a significant direct linear correlation and an inverse relation with VED. However, the response analysis with respect to L-PBF parameters returned no significant model with low variance. In the case of V-

127

built samples, the L-PBF process parameters exhibited a quadratic relation (Equation 4.5) with the impact energy. High significance was shown by laser power, scan speed, and an interaction between laser power and hatch spacing. In addition, a weak negative correlation with VED was found. Figure 4.11 presents the response surfaces obtained from the model.

$$Charpy\ Impact\ Energy\ (J)$$
$$= -11.628 + 0.103P + 0.013v + 0.152h - (2.8E - 05)Pv$$
$$-(6.67E - 04)Ph + (4.4E - 05)vh - (1.61E - 04)P^2 - (6.06E - 06)v^2$$
$$- (8.67E - 04)h^2$$

$$(4.5)$$
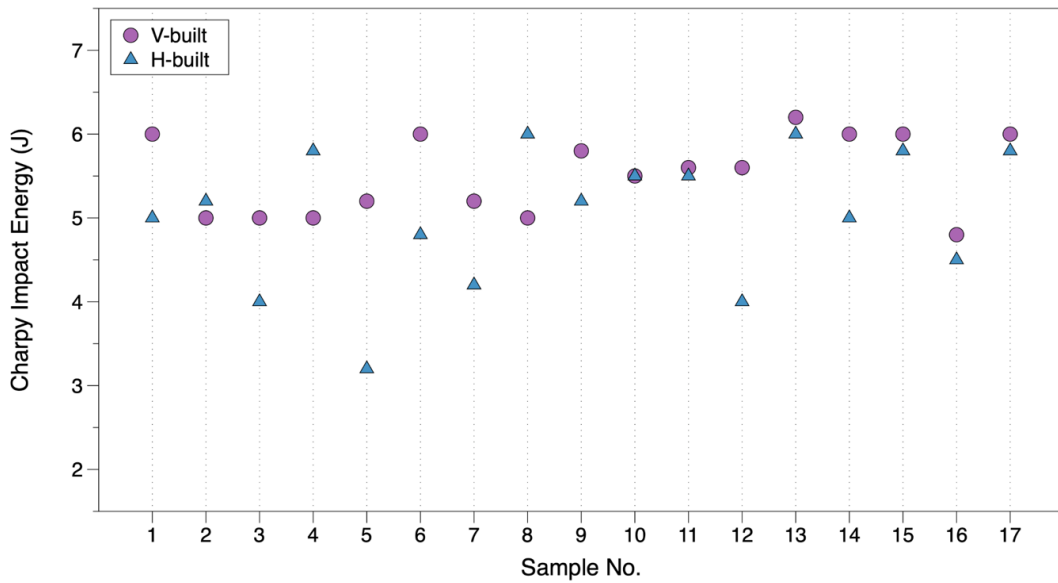
Figure 4.10 Charpy impact energies for V-built and H-built samples.
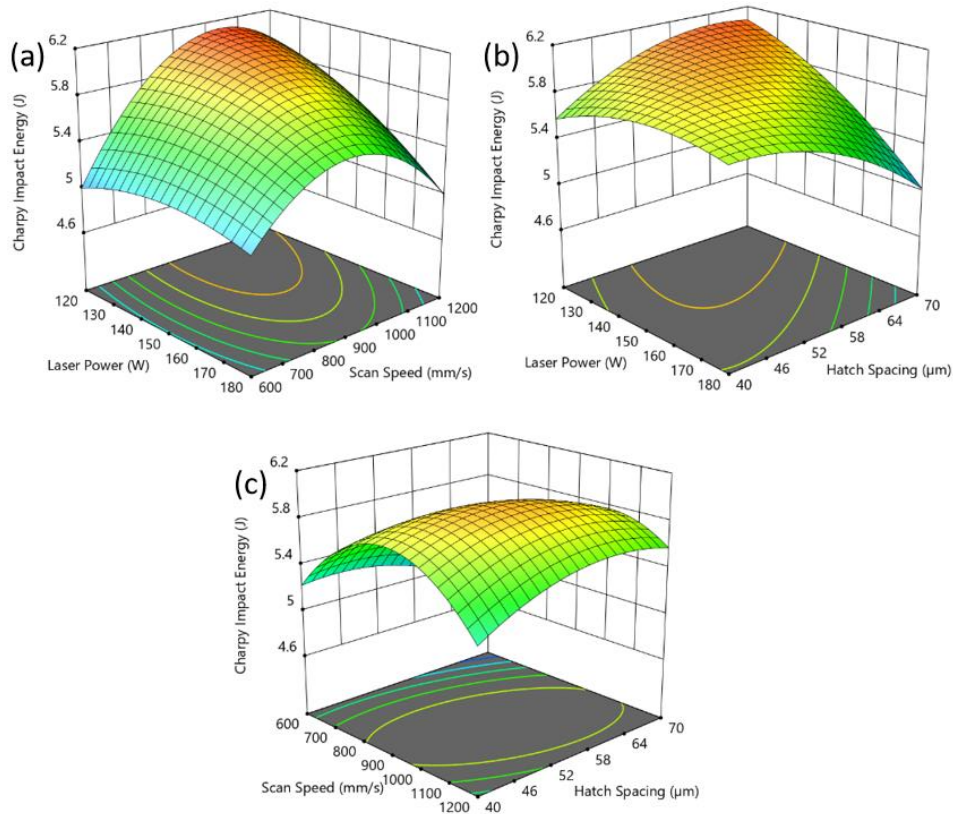
Figure 4.11 Response surfaces of L-PBF parameters on Charpy impact energy in V-built samples at mid-level of **(a)** hatch spacing (55 µm), **(b)** scan speed (900 mm/s), and **(c)** laser power (150W).

4.3.6 Compression and Full – Field Strain Analysis

The stress-strain characteristics in martensitic NiTi involves detwinning mechanism to accommodate the induced deformation in the early stages. The strain chosen was within the elastic limit of the detwinned martensite. Several trial runs were conducted with contingency L-PBF samples to finalise and ensure the chosen strain limit is well within the detwinning region, but is still sufficient to induce detwinning. The material was axially compressed to 6% strain. To comprehend the full-field stress-strain characteristics of the material, macroscopic strain, local axial strain, local axial strain rate, and maximum local strain rate were analysed. Macroscopic strain refers to the average uniaxial engineering strain (ε) measured. Local axial strain is the strain measured across a specific axis (near centreline - in this study) along the gauge length. Local axial strain rate refers to the rate of deformation occurring at a particular location within a specific time interval. It can also be defined as the rate at which strain occurs or changes instantaneously. To note, all readings showing + ve values are in relation to an expansion or strain release in

the material, and – ve values refer to compression or contraction of the material. Accurate strain rate measurements are highly significant in metallurgy, especially for L-PBF NiTi, as process-induced residual stresses and detwinned clusters can highly affect the strain distribution. A low strain rate was followed to effectively evaluate the material response against stress.

Figure 4.12a shows the general trend of stress-strain curves generated through compression of H-built and V-built L-PBF samples. The maximum stresses for H-built samples varied between 360 and 420 MPa. In general, the V-built samples showed higher max. stresses in the range of 395 – 430 MPa. The variation in max. stresses between L-PBF samples was less in V-built samples compared to the H-built. A similar trend can also be seen in the relative density measurements that might have influenced the structural integrity of the samples (Figure 4.12b). The Young's moduli (E_M) of L-PBF samples were obtained from the strain release side of detwinned martensite, as this is more significant in engineering applications. Overall, the moduli varied within 23 – 33 GPa. For V-built samples, the E_M variation was found to be more significant compared to their H-built counterparts. Samples built with low VED exhibited better stiffness readings. Curve fitting revealed the existence of a highly significant quadratic relationship (r = 0.5300) between E_M and VED in V-built samples. In previous studies [45,268], it can be seen that porosity plays a major role in material stiffness; shows a quadratic or higher order relationship between porosity and density. The effect of relative density on E_M of V-built samples is significantly low (r = 0.2031), as the density variations are minimal between samples (Figure 4.12b). This proves that the quadratic relation found in V-built samples is solely due to the variation in L-PBF process parameters. In the case of H-built samples, although a significant quadratic relation (r = 0.3880) is seen, the effect of density variation is considerably higher (r = 0.3560) on E_M. Therefore, the quadratic relation between E_M and VED in H-built samples can be ignored.

The macroscopic stress-strain response of sample H5 is detailed in Figure 4.13. The macroscopic response is divided into 14 timestamps each representing the time and macroscopic strain at that instant. Timestamps 1 to 3 represent the elastic region in twinned martensite; 4 to 6 represents the region of detwinning; 7 to 8 represents the beginning of detwinning saturation and deformation through elasticity in the detwinned structure; 9 to 12 mark the strain release region where strain is regained elastically from

the detwinned structure; 13 to 14 represent the unrecovered strain due to the presence of detwinned structures in the matrix.
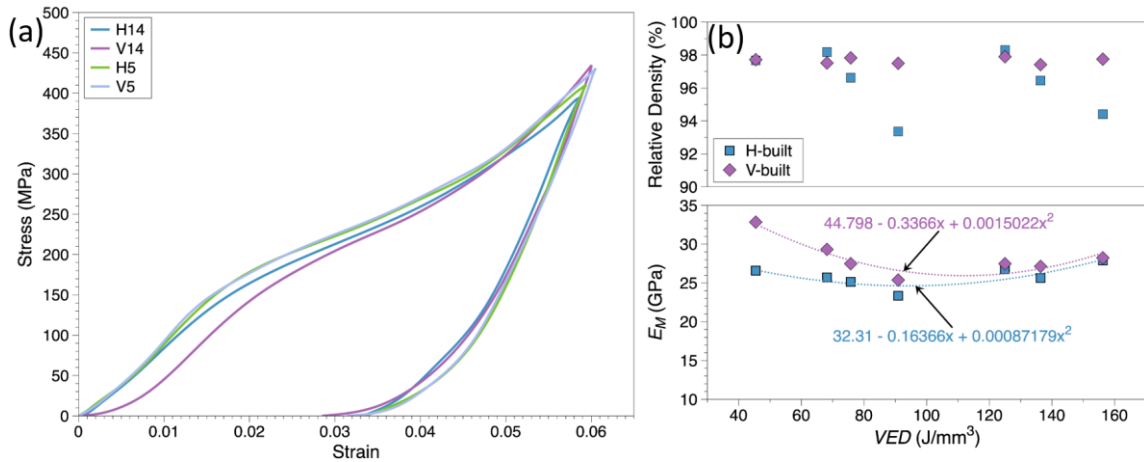
Figure 4.12 (a) Typical stress-strain characteristics of H-built and V-built samples; **(b)** Martensitic Young's modulus vs volumetric energy density (x) compared to the relative density of samples, includes curve-fitting for both H-built and V-built.

In addition, Figure 4.13 represents the deformation contour and strain contour generated via Digital Image Correlation (DIC) analysis. Samples used for compression/DIC analysis were speckle patterned as shown in Figure 4.1b. Initially, the samples were 20 mm high, and it can be seen how the height reduces (as compression progresses), and height recovers (as strain releases) towards the end of the cycle. The local strain distribution at each deformation stage is portrayed along with the associated timestamps. It can be seen clearly from the early stages of deformation (1 to 3), local strains are randomly developed and the intensity increases as the macroscopic strain progresses. This is due to the high levels of porosity seen on the surface and sub-surface. The regions near/around the pores are prone to high levels of local strains and strain rates. This can be seen evidently in Figure 4.14a, where local axial strains are plotted for different levels of macroscopic strains.

131
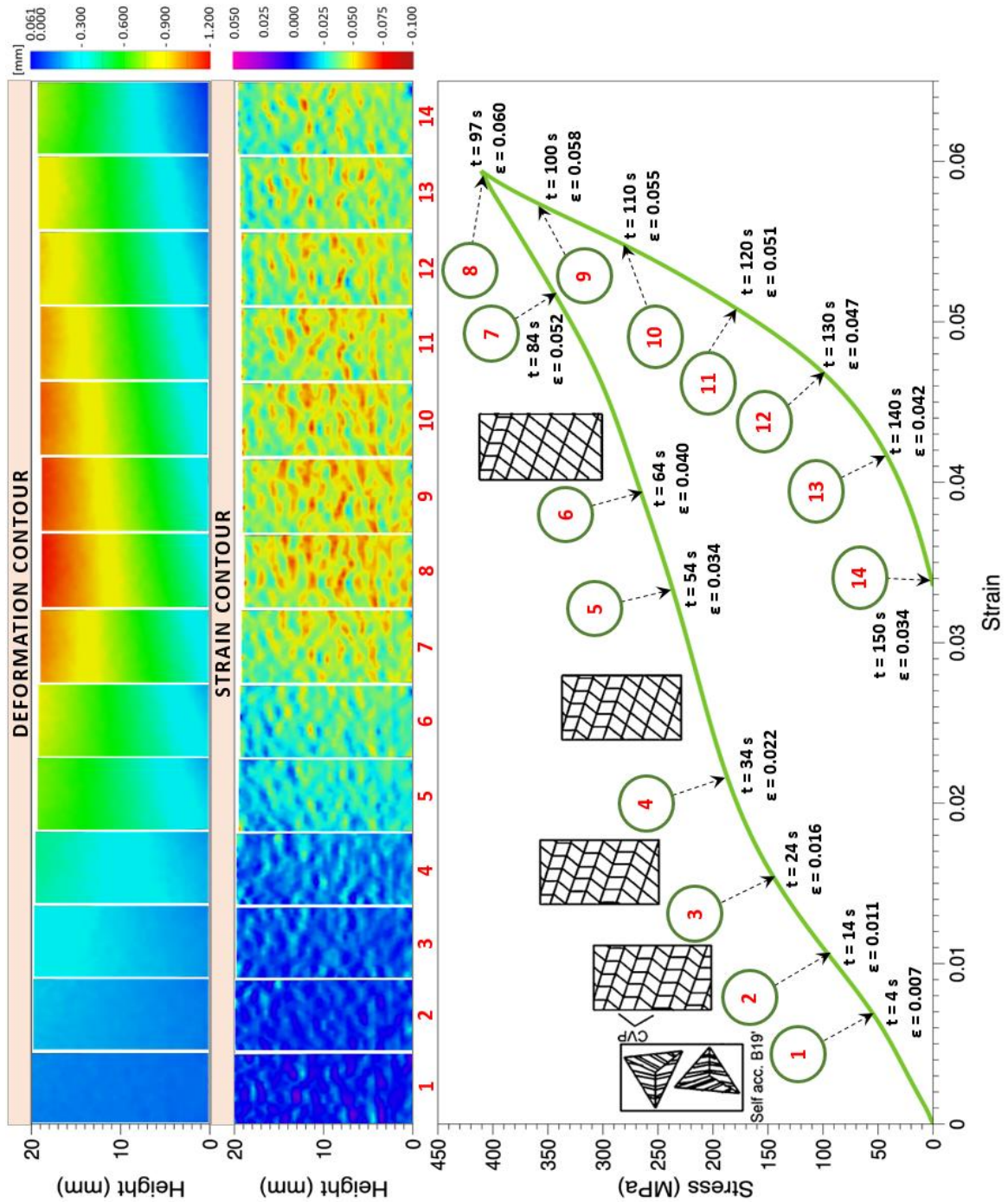
Figure 4.13 Stress-strain curves and full-field DIC contour plots generated via compression of sample H5. Deformation contour indicates the progression of material displacement during compression (downward direction); strain contour plots indicate progression of local strains over the full-field. Timestamps 1 to 14 are marked in the stress-strain curves to compare the full-field response with the macro-response.

132
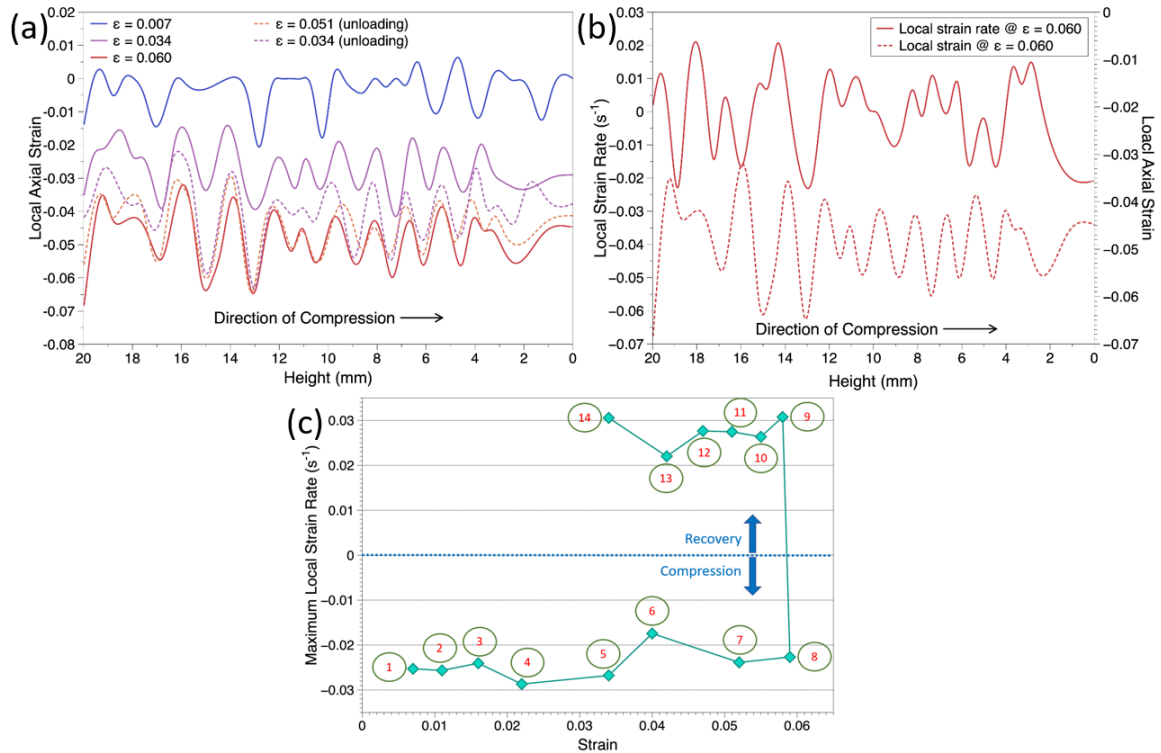
Figure 4.14. Local strain profiles along a line section (near centreline of gauge length): **(a)** local strain field for macroscopic strains ε = 0.007, 0.034 and 0.060 while loading, and strains of ε = 0.051 and 0.034 during unloading; **(b)** distribution of local strain rates and local strains observed at ε = 0.060; **(c)** Evolution of max. local strain rates as detected at various timestamps (1 to 14), represents the compression stage (1 to 8) and recovery stage (9 to 14) during strain release (indicated by positive readings).

Referring Figure 4.14a, it can be seen that the local strain profile resembles a complex superposed sinusoidal waveform, as the axial line of analysis passes through the inhomogeneous porous surface. The clusters of pores result in localised weaker mechanical strength. In the case of ε = 0.007, a few local strains are seen to slightly cross into tension (+ ve readings). This could be due to the upsetting of the sample as the compression begins. This trend becomes invalid from ε = 0.011. In general, the sinusoidal profile shifts to higher mean value as macroscopic strain levels increase. The profile waveform at different strain levels is consistently coherent (crests and troughs), exhibiting variation in amplitude only. This confirms the acquired data is not a noise, rather it represents the actual local strain fluctuations.

Figure 4.14b presents the local strain rates extracted from DIC analysis for ε = 0.060. As observed, the strain rates may be + ve or – ve and imitates a first order differential of the local strain waveform. The maximum local strain rate detected for each value of ε, is

133

extracted and plotted in Figure 4.14c. In compression mode, the extreme – ve value was selected and in recovery mode, extreme + ve reading (resembling expansion) was selected. The plot shows how local strain rate varies at each stage of compression. Under the twinned structure elastic region (1 to 3), the strain rates remain almost same at about $- 0.024$ to $- 0.025$ s^{-1}. In the detwinning region (4 to 6), where rapid crystal rearrangement begins (4), the strain rate increases to $- 0.029$ s^{-1} and then gradually decreases to $- 0.027$ s^{-1} and at timestamp 6, the rate further drops to $- 0.017$ s^{-1}. This drop is due to sparser detwinning than at timestamp 4, as most of the matrix are now detwinned, and more energy is required to elastically (in detwinned state) deform the material. From 6 to 8, where the detwinned structure is elastically deformed, the strain rate increases again to roughly $- 0.023$ s^{-1}.

During unloading, the strain recovery happens at a higher strain rate compared to loading. From $\varepsilon = 0.058$ to 0.040, there is a gradual decrease in strain rate, from $0.031 - 0.022$ s^{-1}. The strain rate increases back to 0.031 s^{-1} towards the end of the cycle. This trend is also reflected in Figure 4.14a, where it can be seen at $\varepsilon = 0.034$, that the amplitudes of local strains during loading stage is more compared to the amplitude in the waveform seen during unloading stage. It is quite obvious from the plots, that the local strains with higher strain rates exhibit shorter amplitudes. Even though the amplitudes are lower, the mean value of local strains in the unloading cycle seems to be higher compared to the loading cycle.

4.3.7 SME Strain Recovery

The shape memory capability of the L-PBF samples were measured through thermal strain recovery. During shape memory activation, the recovered strain is due to a collective sum of elastic strain and shape memory effect strain. To better understand this strain recovery, the following terminologies have been used. Unrecovered strain (U) is the strain that did not recover (Equation 4.6) when the compression load was released and stress was diminished to zero. Unrecovered strain indicates a matrix that underwent elastic strain recovery under a detwinned state, and partly a very minor cluster of dislocations around regions of stress concentrations (porosities). H_o is the original length (along compression axis) of the sample before compression; H_f represents the final length of the sample at the end of compression cycle; H_{sr} represents the length of the sample after thermal strain recovery.

$$U = \frac{H_f - H_o}{H_o} \tag{4.6}$$

Irrecoverable strain (I) is defined as the strain that is left unrecovered (Equation 4.7) after thermal shape memory activation. This unrecovered strain cannot be regained, and thus indicates the extent of shape memory strain for the material; leaves a residual strain in the material. If followed by any further cyclic loadings, this residual strain marks the start of the next loading cycle, and so on. Lower I values indicate high recovery capabilities in the material.

$$I = \frac{H_{sr} - H_o}{H_o} \tag{4.7}$$

Irrecoverability (IR) can be referred as the ratio (I/U) of irrecoverable strain to the unrecovered strain. This indicates the extent of irrecovery in a material; higher IR indicates lower shape memory recovery capabilities. In Figure 4.15, a typical stress-strain-temperature curve observed in current study has been plotted; sample V5 demonstrated having an unrecovered strain of 0.0314. It can be seen that until the As temperature (69 °C) there is no significant recovery, denoting a lack of energy to initiate austenitic phase transformation. From As, we can see an exponential strain recovery which then stabilises after Af (95.8 °C), indicating a fully austenitic matrix. Due to the absence of cooling system, controlled cooling was not achieved, and therefore the strain data during cooling cycle was not obtained. Hence, when the sample reached room temperature, the length was measured with high repeatability using a high precision micrometre. It was found that the length (or recovered strain) noted after Af was retained. Irrecoverable strain of 0.0049 was noted at the end, showing a 99.51% recovery of the original dimensions for an applied engineering strain of 6%.
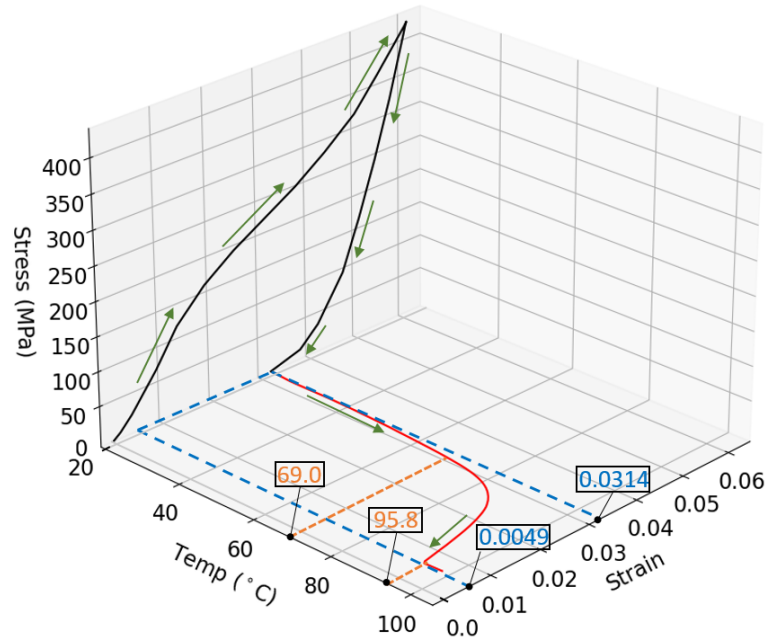
Figure 4.15 Typical stress-strain-temperature characteristics observed (sample V5 shown) representing the unrecovered strain and irrecoverable after thermal excitation.

The three measures (I, U or IR) for each of the 17 sets of H-built and V-built samples were analysed after compressing the samples with an engineering strain of 6 %. The results are tabulated in Table 4A1 in Appendix A. It was found that the H-built samples showed a recovery in the range of 98.96 % to 99.80 % of the original dimensions, whereas V-built samples exhibited less inter-sample variations with a recovery between 99.31 % and 99.56 %. In the case of H-built samples, no much significant relation was found between the L-PBF parameters and I, U or IR. However, for V-built samples, laser power showed high significant linear correlations with I (r = 0.7622) and IR (r = 0.7375).

Additionally, as shown in Figure 4.16a, the irrecoverable strain exhibits a linear correlation with irrecoverability with varying significance: r = 0.9672 for V-built and r = 0.9921 for H-built samples. IR was plotted against I in Figure 4.16a, and this shows how irrecoverability affects the irrecoverable strain. The IR values vary less (between 0.155 and 0.236) in V-built samples compared to that of the H-built samples (between 0.066 and 0.296). The slope of the fitted line is found to be steeper in the case of V-built samples compared to that of the H-built samples.
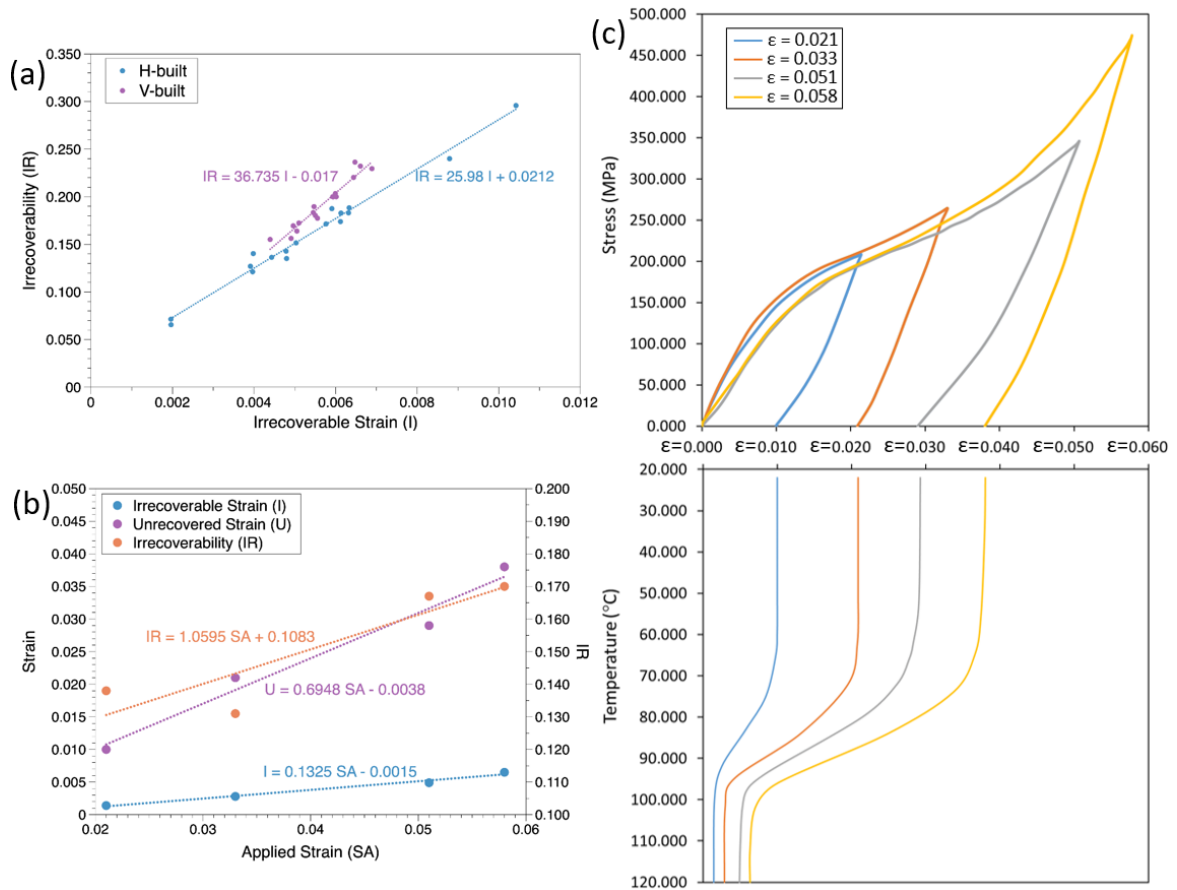
Figure 4.16 (a) Dependence of irrecoverable strain with respect to irrecoverability for V-built and H-built samples; **(b)** linear effect of applied engineering strain on irrecoverable strain, unrecovered strain and irrecoverability; **(c)** Stress-strain-temperature characteristics observed in V-built samples at different levels of applied engineering strain ($\varepsilon = 0.021$, 0.033, 0.051, 0.058).

To investigate the effect of imparted compression strain on strain recovery, four V-built samples printed via mid-levels of L-PBF parameters (150 W, 900 mm/s, 55 μm) were used. The samples were compressed to different engineering strain levels: 2.1 %, 3.3 %, 5.1 % and 5.8 %. The samples were heated to 125 °C at a constant ramp rate of 10 °C/min, and the recovered strain data was recorded. Basic physical properties including density and transformation temperatures of these samples were also obtained.

From the results (Figure 4.16c), the material behaviour at certain strain levels can be clearly seen. The strain levels of 0.021 and 0.033 indicate a region (yielding plateau) of reoriented twinned and partly detwinned matrix, whereas, levels of 0.051 and 0.058 shows the material approaching the elastic limit of detwinned martensite indicated by the rapid rise in stress after yield plateau. The effect of density can also be clearly seen on the

stress-strain curves. For similar strains, the sample (used for $\varepsilon = 0.033$) with high density ($RD = 97.9$ %) has higher overall stress profile compared to other samples ($\varepsilon = 0.021$, 0.051 and 0.058) that has relatively lower densities ($RD = 97.83$ %, 97.05 % and 97.70 %, respectively).

Similar to the trend seen in Figure 4.15, irrespective of the strain levels, the strain recoveries in all samples were activated around the *As* temperatures, and the recovered strains were found to stabilise after *Af* temperatures. As in Figure 4.16b, the irrecoverable strain showed a high linear correlation with applied engineering strain (r = 0.9916) and unrecovered strain (r = 0.9898) levels. The unrecovered strain grew larger (r = 0.9840) when applied strain was increased. The irrecoverability of the material was also found to have linear positive correlation with applied strain (r = 0.9003) and irrecoverable strain (r = 0.8958).

4.3.8 Microstructural Variations

The differences in densities of H-built and V-built samples were caused by the different levels of porosities/defects observed in the samples. These include lack of fusion pores, keyhole pores, gas (spherical) pores, and thermal-induced cracks as shown in Figure 3.9. Overall, the number of defects seen in H-built samples were considerably higher than that in the V-built samples; more details can be referred to an earlier work by authors [8]. To compare quantitatively, the melt-pool thermal data was plotted for H-built and V-built samples as shown in Figure 3.7. In addition to this, the intra-layer average temperature differential (TD_{avg}) of each sample was calculated by averaging the sum of rolling differential of consecutive data points along the broken lines drawn in the samples. As presented in Figure 3.8, the values of TD_{avg} indicated a noticeable trend of how density values vary with thermal profiles. The number of porosities were typically higher when TD_{avg} is higher, and vice versa. When the differences (Δ) in the TD_{avg} of V-built and H-built samples decreased, the differences in relative densities were also found to decrease.

The Inverse Pole Figures (IPF) Z maps (Figure 4.17a – 4.17c) reveal the presence of twinned microstructures along with, a few detwinned structures or a mix of possible plastic dislocations inherited from the thermal stresses during L-PBF process. The grain sizes of these martensitic structures are difficult to determine due to multiple geometric features associated with these needle-like structures. However, the size can be qualitatively observed to be in the range of 1 – 10 μm. Also, it was observed from a larger

Field of View (FOV) area (200 μm) that the L-PBF process did not favour a particular grain orientation.
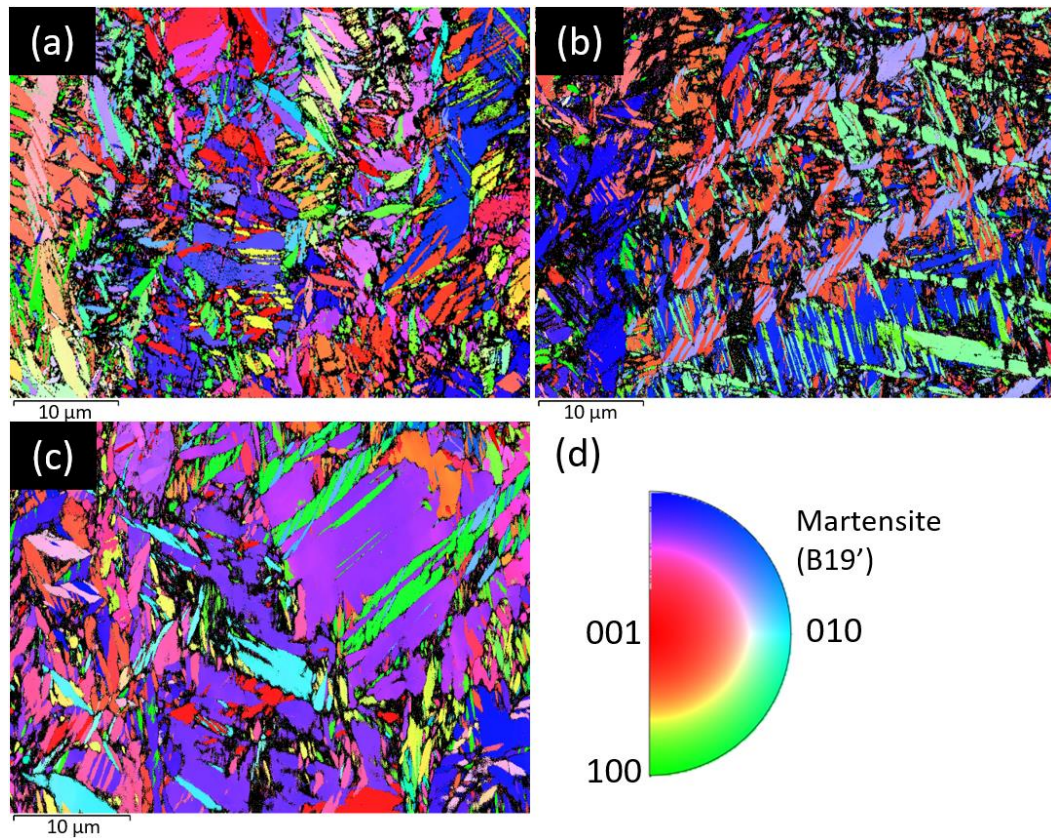
Figure 4.17 Different twinned martensitic structures as seen in H7 **(a & b)** and H11 **(c)** through IPF Z maps; the microstructure reveals primarily a twinned NiTi matrix with the presence of very few detwinned or possibly dislocated grains, **(d)** index maps.

The microstructural topological variations in the L-PBF samples at submicron scale were investigated through AFM at multiple stages: as fabricated, post-compression and after thermal strain recovery. Samples used for EBSD analysis (with finest mirror-like finish) were used for this analysis also. Optical profilometry was used to analyse the macroscopic surface topology at a 10 μm resolution, as shown in Figure 4.18. The macroscopic topography reveals a better overview of how the deformation (or extent of detwinning) has taken place across the sample surface. This is comparable to the DIC-based deformation contour seen in Figure 4.13. As expected, the surface looks more uniform in as-fabricated stage compared to the other two stages. In sample H6, along the direction of compression, the left edge where the ram contacts with and compresses the sample, exhibits the highest deformation. In H11, this edge was slightly curved towards one corner (due to machining), and the scale used was normalised between samples. This has

resulted in the surface topography being slightly skewed to one side. However, the trend is similar between both samples where the left edge is more deformed and after strain recovery, the same edge shows the highest unrecovered deformation.
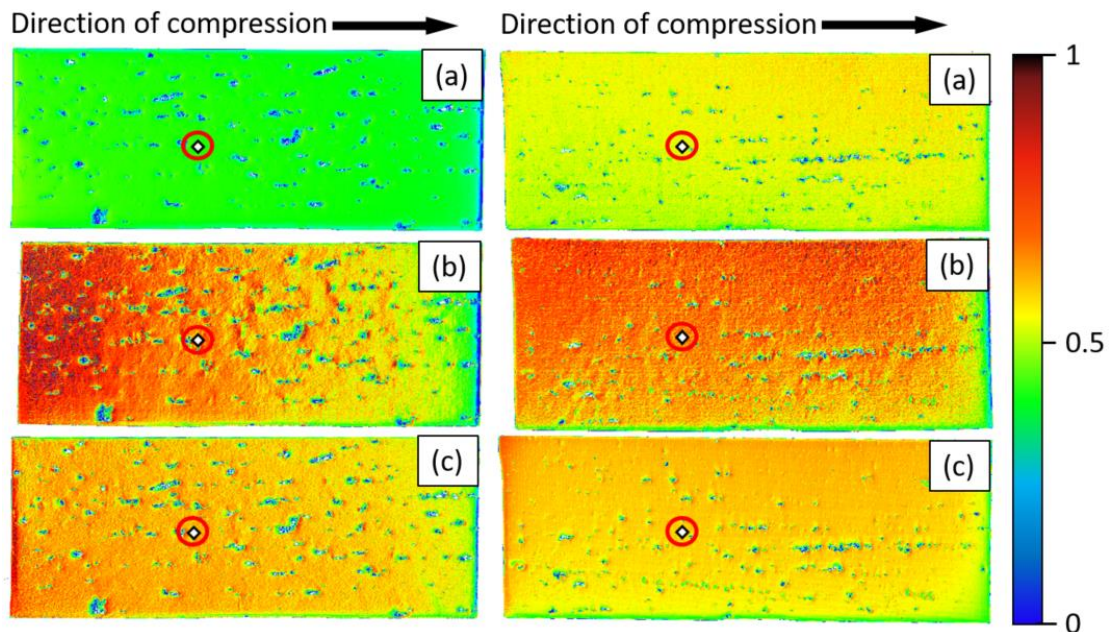
Figure 4.18 Macroscopic topography as measured on samples H6 (left) and H11 (right) via optical profilometry at different stages: **(a)** as-fabricated, **(b)** post-compression, **(c)** after thermal strain recovery; single normalised scale used to represent the changes in samples. White quadrilaterals encircled red represents the location where AFM scans were conducted to observe the topography at a submicron scale.

For submicron investigation, a location was chosen (as shown in Figure 4.18) in both samples where the changes in strains are more profound. During the scans after each stages, the same locations were located with the help of micro-indents. In Figure 4.19a – 4.19f, we can see the changes in submicron topography after each stages. The topographies of as-fabricated stages (Figure 4.19a – 4.19b) can be used as the references for each samples. It can be clearly seen in Figure 4.19c – 4.19d that post-compression stages show higher peaks and deeper ridges compared to the as-fabricated. Counterintuitively, the post-recovery microstructure (Figure 4.19e – 4.19f) was found to be even more rugged compared to post-compression stage. The twinning features can be seen in as-fabricated stage more explicitly; at a scale range of 0 – 40 nm. In post-compression and post-recovery stages, these features are not clearly visible due to larger scale range (100 – 300 nm).

To analyse the topology, the following roughness parameters were considered: mean roughness (Sa), root mean square roughness (Sq), maximum height (Sz) and *median*. Sa represents the arithmetic mean and indicates an overview of surface roughness. Sq represents roughness as a standard deviation of heights. Sz indicates the maximum variation on the surface, calculated as the sum of deepest ridge height and highest peak height. *Median* indicates a more average roughness trend along with waviness of the surface. The values of these parameters for H6 and H11 are plotted in Figure 4.19g and Figure 4.19h, respectively.

In the case of H6, the Sa and Sq values varies in the range of 4 to 32 nm and 5 to 41 nm, respectively as the L-PBF sample is compressed and recovered, whereas the variation is lower in the case of H11, where it varies in the range of 0.7 to 26 nm and 1 to 32 nm, respectively. When the samples are compressed, the *median* values jump significantly by 86 nm and 82 nm for H6 and H11, respectively. After strain recovery, a further increase in the *median* values is noted (49 nm for H6 and 28 nm for H11). However, this increment is lower compared to the initial jump. In the case of Sz, which indicates the maximum irregularity, the values jump by 143 nm and 158 nm for H6 and H11, respectively when the sample is compressed. Once strain is recovered, the Sz increases by a lower value, 124 nm for H6 and 48 nm for H11. To summarise the findings, compression results in a rough topography compared to the fine microstructure. This rough topography is expected to relieve or become smooth when strain is recovered, however, the topography becomes significantly wavier but with more or less the same Sa or Sq (smoothness), as when it had been compressed.

4.4 Discussion

4.4.1 Effect of L-PBF Build Orientation

Referring to Table 4.2, it can be understood that the effects of the process parameters on the output responses are different depending on the build orientations. In general, the H-built and V-built samples exhibited a similar trend of variation among each of the responses measured. The H-built samples however generally showed larger variations in responses compared to their V-built counterparts. From the relative density analysis, it is evident that the effect of L-PBF parameters are more significant for H-built samples causing relatively higher amounts of porosities compared to the V-built samples. The variation of RD for V-built samples is approx. 0.7 % while it is 5.2 % for H-built samples.

H-built and V-built samples (2, 3, 5, 16) printed using low scan speed (600 mm/s) showed larger reductions in RD. H-built and V-built samples (4, 8, 9, 11, 17) built using a combination of higher laser power, low VED, higher scan speeds (at 900 and 1200 mm/s) and large hatch spacing showed higher sample densities.
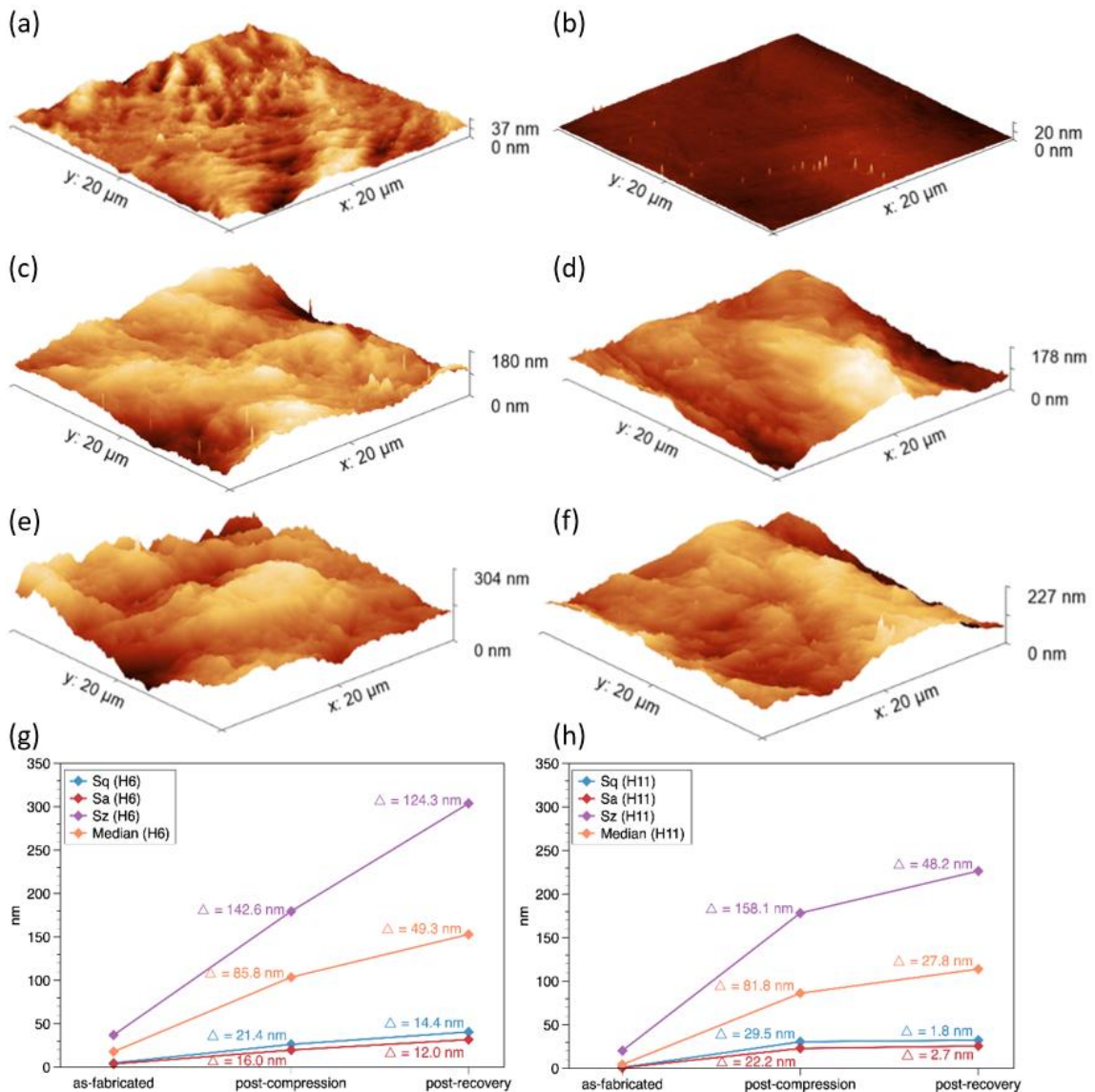
Figure 4.19 Microstructural surface topography as observed through AFM in: as-fabricated (**a** – sample H6, **b** – H11), post-compression (**c** – H6, **d** – H11); after thermal strain recovery (**e** – H6, **f** – H11) stages; Submicron topology measurements (roughness in nm) from AFM scanning of sample (**g**) H6 and (**h**) H11.

Samples with higher densities exhibited better energy responses during Charpy impact testing. This positive correlation was noted with higher confidence (r = 0.6817) for H-built samples and lower (r = 0.5802) for V-built samples, following a similar trend to the

RD responses. Sample H5 has the lowest impact energy, and H8 has the highest impact energy (highest *RD*, Figure 4.2). The correlation between *RD* and impact energies can be seen clearly. Additionally, the variation of Charpy impact energy for H-built samples was found to be higher (2.8 J) compared to that (1.4 J) of the V-built, which is also comparable to the *RD* trend. The porosity levels and low impact energies (3.2 – 6.2 J) observed in L-PBF samples can indicate a brittle character also. This was confirmed by the fractographs (Figure 4.9c) where we can see brittle fractures in the form of cleavages/river-like patterns. Vickers microhardness results were also found to be high for these samples, which reconfirms the brittle nature of fracture. As shown in Figure 4.7b, the H-built samples are harder than the V-built samples. Sample 7 processing conditions resulted in high hardness, and sample 5 presented low hardness for V- built and H-built samples. The lowest hardness was recorded for H5 with larger standard deviation; this trend was also seen in Figure 4.2, where sample H5 has lower *RD* with large standard deviation. The high hardness readings noted in H-built samples has possibly originated from the high internal thermal stresses during L-PBF process. The high hardness with brittle nature/low fracture toughness has led to lower impact energy readings in H-built samples (Figure 4.10). The standard deviation in H-built samples can also be seen higher, and this could be linked to the porous nature (lower *RD*) of H-built samples resulting in varying depths during indentation. As seen in fractographs, the porosities were mainly of process-induced types, and they induce rough edges which can act as stress concentration zones. This can further reduce the impact energy and fatigue life of L-PBF NiTi samples, by facilitating crack formation and hardness, by producing porosity with a poor shape to resist deformation.

RD also posed an inverse correlation with irrecoverable strain (r = -0.5553), unrecovered strain (r = -0.4495) and irrecoverability (r = -0.5205) of H-built samples. This indicates better shape memory activation and deformation recovery when sample densities are high. In the case of V-built samples, this correlation is not profound, which could be due to the low variation in *I*, *U*, and *IR* (0.0025, 0.0040, and 0.0812 respectively), compared to the wider variation in H-built samples (0.0085, 0.0092, and 0.2302 respectively).

Ni evaporation was found to have more inter-sample variation (1.2 at. %) in H-built orientation compared to 0.6 at. % variation in V-built samples. From the response surface analysis of V-built, it is clear that *VED* has a direct influence on Ni evaporation.

Maximum evaporation is observed when laser power is high, and hatch spacing and scan speed are low (Figure 4.6c – 4.6e). Whereas, in H-built samples, high Ni evaporation is noted when laser power and scan speeds are high (Figure 4.6b). From the previous study [46] of the same H-built samples, high average temperature differential and random hot spots were noted. These phenomena could lead to localised high energy density, hence, resulting in high melt pool temperatures leading to higher Ni evaporation of up to 2.5 at. %. The lower boiling point of Ni, along with high heating/cooling rates are sufficient to suppress element diffusion that results in chemical homogenization. This can cause enrichment of Ti along grain boundaries due to the limited evaporation of Ni, especially in the molten pool boundary areas. In the current study, these Ti enrichments were seen in the form of pure Ti phases in H-built samples (Figure 4A2 in Appendix A). A few thermographs are presented in Figure 5A4 in Appendix A, where we can observe the thermal gradients, melt pool hot spots, and global intra-layer temperature for V-built and H-built samples.

Reduction in Ni (or raised Ti content) in the matrix pose a significant effect on the shape memory property of the material via elevating the TTs for phase transformations. As mentioned earlier, this effect is minimal in the current study as the raw powder has lower Ni content. Samples H4, H8 and H11 underwent high Ni reduction comparatively; all of these samples were processed at higher laser powers. The elevation of Ms temperatures in H-built samples was more than that of the V-built samples, agreeing with higher Ni evaporation in H-built. However, the fall in Mf, As, and Af noted in H-built samples, was interesting to be observed. This decrease in TTs has also been noted in some studies [299,163]. This also can be correlated to the Ti enrichment discussed earlier. The enrichments can deplete Ti locally from NiTi matrix and thus result in lower TTs globally, even though Ni evaporation was noted to be high.

Referring the second cycle plots in Figure 4.3 and Figure 4.4, the As lies above the Ms in V-built samples, whereas in H-built samples As lies below Ms. Looking at two cycles in Figure 4.3, we can also see that the endothermic peak shifts to lower temperatures during the second cycle, lowering the thermal hysteresis. At the same time, there is no change observed in exothermic peaks during second cycle. With the above observations, we can infer that the austenitic transformation occurs over a shorter temperature range and this also indicate better shape recovery actuation in H-built samples due to overlapping Ms – As transition region (indicated by dark peach shade in Figure 4.4). This Ms – As transition

overlap is larger for samples H1, H4 and H9. In V-built samples, the hysteresis is lower for V3, V4 and V5. These six samples are likely to exhibit the best thermal strain recovery response from a thermal excitation perspective. The TTs are highly dependent on any internal thermal stresses (as dislocations) or precipitate phases [298]. Reduction in Ni need not be only through Ni evaporation, but also through stable Ni-rich precipitate phases such as Ni_3Ti, Ni_2Ti, or metastable phase Ni_4Ti_3 that depletes the Ni content in the matrix thereby increasing TTs because of the remaining high Ti content. Inhomogeneity in Ni and Ti distribution can also cause irregular DSC heat flow profiles, which can also result in poor shape memory properties.

The start and finish TT hysteresis (TTR) for phase transitions was found comparable in both V-built and H-built samples. This can indirectly indicate somewhat similar levels of homogeneity in NiTi matrix [36,180,298]. From Figure 4.5, we can see that the H-built samples showed lower transition enthalpies and enthalpy ratios compared to V-built samples. Additionally, the variations in H-built samples were more significant compared to V-built samples. In an ideal sample, it is expected that the endothermic and exothermic enthalpies are equal/balanced ($TEr = 1$), and this indicates complete phase transformation in the material. Due to the presence of material inhomogeneity and different entropies [300] caused by L-PBF parameters, the extent of transformation (via TEr) was found to vary between 0.90 to 0.99 for H-built, and 0.96 to 0.99 for V-built samples. This indicates that during DSC heating or $M \rightarrow A$ transformation, the material that did not transform varies in the range of $1 - 10$ % for H-built samples, while it is $1 - 4$ % in the case of V-built samples; when compared to that of $A \rightarrow M$ transformation.

Due to the play of different factors such as residual strains or dislocations, and reorientation of martensitic twins, it is difficult and perhaps inappropriate to compare TEr with actual strain recovery data to understand the shape memory recovery through austenitic phase transformation [45,46]. Still, the variation in TEr data was comparable with the irrecoverability data; H-built samples showed significant variations in irrecoverability between samples compared to the V-built, similar to the trend seen in TEr data. For V-built samples, VED exhibited a positive correlation with endothermic (r = 0.3732) and exothermic (r = 0.3700) enthalpies. Ni evaporation also poses a direct effect (r = 0.4034 and r = 0.4550, respectively) with these enthalpies. These findings agree with earlier work by Chekotu [46].

In general, the differences between variation in responses of H-built and V-built samples were noteworthy in all material and physical properties. The primary elements causing these varying responses are: (1) thermal processing each build orientation underwent during L-PBF, (2) area exposed to heat dissipation, (3) probability of each build layer containing spatter particles. The thermographs (Figure 4A3 in Appendix A) aid to visualise the thermal gradients, melt pool hot spots, and global intra-layer temperature differences in V-built and H-built samples. The effect of these thermal profiles on porosity formations was discussed earlier in section 3.8.

4.4.2 Functional Characteristics and Microstructural Variations

The characteristics of macroscopic stress-strain response and local strain distributions are discussed in this section with the help of uniaxial compression tests and DIC analysis. As compression progresses, due to surface-exposed porosities, the local strains are initially developed at regions of stress concentrations (regions of pore-clusters or pores) on the surface as shown in strain contour maps in Figure 4.13. It was observed in L-PBF samples, that these process-induced pores form periodically across a layer as well as in the build direction between layers. These periodic pore formations occur due to the periodic high temperature gradient profile generated across a layer and between layers during printing. In Figure 4A3 in Appendix A, the location of maximum compressive local strain rates are compared with the location of the pores on the sample surface. These pores are likely to be contained inside the bulk, in the same vicinity as indicated by blue broken lines. The thermograph shown is Figure 4A3c is for the middle build layer, while the pores seen in Figure 4A3b are from the top layer. Therefore, the blue markings indicate an approximate region where the pores are located. . This clearly indicates a correlation of thermal profile to the pore formation (as discussed earlier in Section 3.3.3 - Figure 3.7 and Figure 3.8), producing the local strain and strain rate variations as observed in Figure 4.14.

Under cool (near/below *Mf*) stress-free conditions where the martensite phase is stable, the B19' martensitic structure in martensitic NiTi contains multiple self-accommodated martensite variants, shown in Figure 4.13 (timestamp 1). In the case of austenitic NiTi where martensitic transformation is stress-induced, the formation of martensite variants is based on favourable orientation under applied stress. The low symmetry martensitic lattice may exist in 12 correspondence variant pairs (CVP). These 24 possible martensitic variants can be classified into 6 plate groups with 4 plate variants. Since L-PBF often

imparts some thermomechanical history to the samples (viz. residual stresses). These residual stresses can assist in stabilising the martensite variants, and may also help to form detwinned or dislocated structures that may reside in stress-free state [301,302]. In IPF-Z maps (Figure 4.17) of stress-free state, we can see the formation of twins, and a few regions where twins are absent (possibly detwinning or slip). From the AFM z-map in Figure 4.19a – 4.19b and Figure 4.19g – 4.19h, we can refer the twinned structures to a topology *median* of 18 nm (H6) and 4.4 nm (H11).

Certain regions in the strain contour map (Figure 4.13), are seen to undergo a local strain of about 6.5% to 8%, compared to the 6% engineering strain applied. It should be noted that, in polycrystalline NiTi, martensite detwinning to a single preferred variant cannot occur without concurrent plastic dislocations [6]. This is more profound due to the presence of stress-concentrating pores, which could further contribute to these dislocations. This can also be compared with local axial strain/strain rate variation with respect to direction of compression (Figure 4.14a – 4.14b). The intensities go higher as macroscopic strain increases from 0.007 to 0.060. The threshold for detwinning is much lesser near or around pores compared to the denser regions, which results in earlier detwinning and leads to localised microscopic slip formations as the material deformation results in crossing the elastic limit of detwinned martensitic structure [63-65].

When the sample is gradually stressed, only one of these four variants in an associated plate group will begin to develop (timestamp 2). This happens by initially reorienting the martensite plates to form one set of favourite twinning system. This variant is chosen in alignment with largest partial shear stress (preferentially oriented) [45,303,304]. This variant undergo detwinning (timestamps 3 - 6), where multiple self-accommodating variants are transformed to a single variant (after timestamp 6). This can be seen in the strain contours of respective timestamps in the form of turquoise blue to yellow/amber transitions. Once the single variant has mostly saturated the matrix, we can see these regions turn from amber to deep red (timestamps 7 - 8). Certain regions in the strain contour map, are seen to undergo a local strain of about 6.5 % to 8 %, compared to the 6 % engineering strain applied. It should be noted that, in polycrystalline NiTi, martensite detwinning to a single preferred variant cannot occur without concurrent plastic dislocations [40]. This is more profound due to the presence of stress-concentrating pores, which could further contribute to these dislocations.

This can also be compared with local axial strain/strain rate variation with respect to direction of compression (Figure 4.14a – 4.14b). The intensities go higher as macroscopic strain increases from 0.007 to 0.060. The threshold for detwinning is much lesser near or around pores compared to the denser regions, which results in earlier detwinning and leads to localised microscopic slip formations as the material deformation results in crossing the elastic limit of detwinned martensitic structure. Previous investigations [303,305] have observed that at lower strain levels (6 %, similar to the current study), the matrix contains both twinned and detwinned B19' variants. At high strain levels (12 %), the deformation was observed to be accommodated by reorientation, detwinning, and high density of dislocations. Since thermal strain recovery can only recover detwinned deformations, microscopic slips can ultimately result in non-recovery of strain when thermal strain recovery is performed.

It is interesting to note in Figure 4.14c that the maximum local strain rate during elastic deformation in both twinned (1 - 3) and detwinned (7 - 8) structures are less compared to the detwinning stage (4 - 5). This indicates that the maximum strain during deformation of martensitic NiTi is achieved through detwinning. Also, the strain rate in elastic region of detwinned matrix is lower than that of the twinned structure. This indicates three possibilities – firstly the difference in stiffness of self-accommodated twins and detwinned B19' state; secondly, it could represent the reorientation of martensite to favour low energy state, and thirdly it could point towards a slip condition where higher energy is required to cause slip (plastically deform the detwinned matrix).

When stress is released (timestamps 8 - 14), we can see the strain is recovered under the elasticity of detwinned martensite. This was also associated with partial reverse detwinning, where a few detwinned structures disappear due to insufficient energy to stabilise a single variant. In a previous study by Nishida *et al.* [306], the twins were seen to disappear gradually while stress is applied, leaving only a fraction or none towards the end, depending on the applied strain levels. For the same macroscopic strain levels ($\varepsilon = 0.051$ and 0.034), the local axial strain was seen to be higher (Figure 4.14a) during unloading cycle, compared to the loading cycle. Along with this, some roughening due to dislocations were also observed. This residual strain (unrecovered strain, *U*) left behind, can be evidently seen via AFM, Figure 4.19c – 4.19d and Figure 4.19g – 4.19h, where the topology *median* got elevated to 104 nm (H6) and 86 nm (H11).

During thermal recovery, the stress-strain-temperature behaviour was found very much similar in all H-built and V-built samples. The factors which consistently differed were the As and Af temperatures, around which the sudden jump in strain recovery occurred. These TTs were comparable with the temperatures measured via DSC analysis. Even though the applied strain was identical, the H-built samples were found to have more variability in I, U, and IR, compared to the V-built samples. Referring Figure 4.16a, the L-PBF process parameters influenced I and IR of H-built substantially. The difference between minimum and maximum readings was almost similar to the difference noted when V-built samples were strained at varying levels (2.1 % to 5.8 %) of engineering strain. This indicates a significant variation of SME capabilities in NiTi when samples are built in different orientations under similar processing conditions. For H-built orientation, the IR values were highest for samples with low relative densities, and gradually decreases and stabilise as densities increase. In general, better shape memory effect (low IR) was exhibited by H-built samples as seen in Table 4A1 in Appendix A. This could be due to the overlapping $Ms - As$ region (darker peach shade in Figure 4.4), indicating lower hysteresis between phase transitions (seen in Figure 4.3). Overall, the similar trend of recovery mechanics mentioned earlier along with comparable TTs, indicate high controllability of shape memory property via L-PBF.

When the L-PBF samples were strained at different levels (2.1 % to 5.8 %), the I, U, and IR were found to increase consistently (Figure 4.16b). As strain increases, more detwinning happens and any internal stress induced structures will lead to martensitic reorientations, or plastic slip at regions of stress concentrations. Therefore, I and IR increases as more of these lattice defects increase. Unrecovered strain, U can be highly influenced by structural stiffness [45,307]. This was seen clearly in Figure 4.16c, where three of the samples showed comparable E_M values (slope at initial load release), while sample used for $\varepsilon = 0.051$ showed lower E_M (due to lower density). This also resulted in a lower U value in Figure 4.16b. In an ideal single crystal NiTi, detwinning occur at a constant stress level (flat-plateau), however, from Figure 4.12a and Figure 4.16c, we can see the detwinning stage is associated with a slightly tilted-plateau. This indicates the heterogeneity in grain orientations, and the presence of lattice defects, caused by L-PBF processing [308].

Since strain recovery relieves the compressed bulk structure, one may expect the submicron topology measurements in the post-recovery stage to show alleviation, compared to post-compression. However, the case was found to be entirely different as seen in AFM topography (Figure 4.19e – 4.19f). The *median* increased to 153 nm and 114 nm in H6 and H11, respectively. The jump in post-recovery topology measurements from post-compression readings were significantly less compared to the jump measured post-compression from polished as-fabricated state. This implies that the increase in surface distortion is solely due to crystallographic rearrangements, which occurred during *detwinned M → A* and then *A → twinned M* transformations. It has also been reported that the fraction of martensitic twins after thermal recovery is much lower (up to three times) in compressed samples. This lower fraction of detwinning could be due to higher dislocation densities that occur during compression [69,70].

It is highly probable that the deeper ridges or higher peaks seen in post-compression and post-recovery AFM topography are regions of stabilised detwinned martensite inter-dispersed with plastic slip. Referring Figure 4.19c – 4.19f, these ridges/peaks which formed in post-compression tends to remain in post-recovery. While most of the martensite transforms to austenite, some is hindered from undergoing transformation due to plastic zones. These regions remain stabilised by any prevalent internal stresses which are elevated when heating is progressed beyond *Af* [309].

During *detwinned M → A*, the nucleation of B2 austenitic structures happens only in one variant, recovering the compression strain as atoms are rearranged to a B2 structure. However, during the *A → twinned M* transformation, the nucleation of martensitic variants occurs by self-accommodation in the crystal [40,301,308]. B2 austenite possess higher crystal symmetry, and the atomic shifts in B2 variant relative to the monoclinic B19' variants are noted to be marginal. As austenite transforms to martensite, this symmetry gets reduced significantly, and multiple B19' variants with crystallographic equivalence having different habit planes are generated. This self-accommodation also results in significantly less volume change requiring a small energy barrier for transformation. Whereas in steel which has a tetragonal martensitic structure, this volume change is significant, elevating these energy barriers too high to activate SME [40,310,311]. In other words, the structural change in NiTi occurs via small diffusionless coordinated shift of atomic positions. Despite having different crystal structures for B2 and B19', the habit planes allow a lattice orientation relation between the two phases.

150

These habit planes neither rotate nor deform during martensitic transformation, resulting in a buoyancy-like force exerted when variants are formed. This phenomenon often results in surface distortion when smooth austenite surface transforms to martensite [310]. This was also reflected in an increase of 12 nm and 2.7 nm in *Sa* and increase of 14.4 nm and 1.8 nm in *Sq* for H6 and H11, respectively. Comparing the two L-PBF samples (Figure 4.19g – 4.19h), it was also noted that the change in surface parameters (*Sa*, *Sq*, *Sz* and *median*) during post-compression and post-recovery, are directly dependant on the initial submicron topology of as-fabricated condition.

4.5 Conclusions

The effect of laser process parameters and build orientations on as-fabricated L-PBF NiTi part properties was studied in detail. Relative densities and Ni reductions recorded for each of the H-built and V-built samples were analysed, and significant correlations were found to exist with the L-PBF parameters. Phase transformation temperatures and their corresponding enthalpies were analysed following two thermal cycles. The austenitic start temperatures in V-built samples, and total transformation range and enthalpy properties in H-built samples showed high correlations with laser parameters. The microhardness levels of H-built samples were found to be relatively higher, while the impact energies in V-built samples were slightly better. However, the impact energies recorded for H-built samples showed better correlations with L-PBF parameters.

Compression tests at 6 % strain were performed on both H-built and V-built L-PBF samples. The samples exhibited stress plateauing and elastic recovery in the martensitic phase, leaving behind a certain residual unrecovered strain. This trend was investigated in detail using DIC-based full-field strain analysis. Local strain behaviours were analysed to see the effect of applied macro-strains on the SME. The shape memory capabilities of these samples, measured in terms of irrecoverability, revealed a high correlation with applied strain levels. The DIC technique helped to better understand the nucleation and evolution of detwinning mechanism, and also shed light on reverse detwinning mechanism. The L-PBF parameters also resulted in a higher variation in SME functionality for H-built samples compared to the V-built samples.

Through EBSD, the L-PBF samples were confirmed to contain twinned martensitic structures mostly, in as-fabricated conditions. The samples showed fine and smooth

submicron topology in this stage when scanned via AFM. The changes in submicron topology that occurred during compression and recovery were also reported in this study.

In general, the variations in responses caused by L-PBF parameters were considerably lower in V-built samples when compared to their H-built counterparts. This trend was uniformly seen in all physical and mechanical characterisations. However, these variations in H-built samples were found to be meaningful, while correlating with L-PBF parameters. Therefore, the H-built orientation in L-PBF processing can be suggested to have better control over material properties and shape memory functionality, under the selected set of parameters. Due to the inherent high laser spot processing speeds, high thermal gradient and stochastic nature of L-PBF, these properties can differ substantially under different processing conditions or scanning strategies.

4.6 Contribution to Thesis Objectives

In this chapter, a few pending responses (chemical and thermal) of horizontally built samples were analysed. In Chapter 3, a few issues in regard to thermal analyses were found; these were addressed in this chapter. Apart from these, this chapter presents the mechanical responses and shape memory capabilities of both vertically and horizontally built samples, along with full-field strain analysis. The changes in submicron topologies after each stage of processing was also explored and reported in this chapter, along with other microstructural analysis including fractography. Data from Chapters 2 and 3 were used to support and validate the results/findings in this chapter.

4.7 Supplementary Data

4.7.1 Appendix A

Table 4A1 Strain recovery data for all V-built and H-built samples (better SME readings highlighted in red).

Sample ID	Irrecoverable Strain (I)	Unrecovered strain (U)	Irrecoverability (IR) = I/U
V1 / H1	0.005 / 0.006	0.030 / 0.032	0.172 / 0.187
V2 / H2	0.010 / 0.004	0.035 / 0.028	0.296 / 0.155
V3 / H3	0.006 / 0.005	0.030 / 0.036	0.200 / 0.135
V4 / H4	0.006 / 0.005	0.029 / 0.033	0.220 / 0.143
V5 / H5	0.005 / 0.006	0.031 / 0.034	0.156 / 0.183
V6 / H6	0.005 / 0.006	0.030 / 0.035	0.183 / 0.174
V7 / H7	0.005 / 0.002	0.029 / 0.030	0.190 / 0.066
V8 / H8	0.007 / 0.006	0.030 / 0.034	0.230 / 0.183
V9 / H9	0.006 / 0.004	0.027 / 0.028	0.236 / 0.140
V10 / H10	0.006 / 0.004	0.030 / 0.032	0.200 / 0.136
V11 / H11	0.006 / 0.006	0.034 / 0.031	0.188 / 0.177
V12 / H12	0.005 / 0.009	0.029 / 0.037	0.169 / 0.240
V13 / H13	0.006 / 0.006	0.029 / 0.034	0.203 / 0.171
V14 / H14	0.007 / 0.005	0.028 / 0.033	0.232 / 0.152
V15 / H15	0.005 / 0.002	0.031 / 0.027	0.164 / 0.071
V16 / H16	0.006 / 0.004	0.030 / 0.033	0.200 / 0.121
V17 / H17	0.006 / 0.004	0.031 / 0.031	0.180 / 0.127
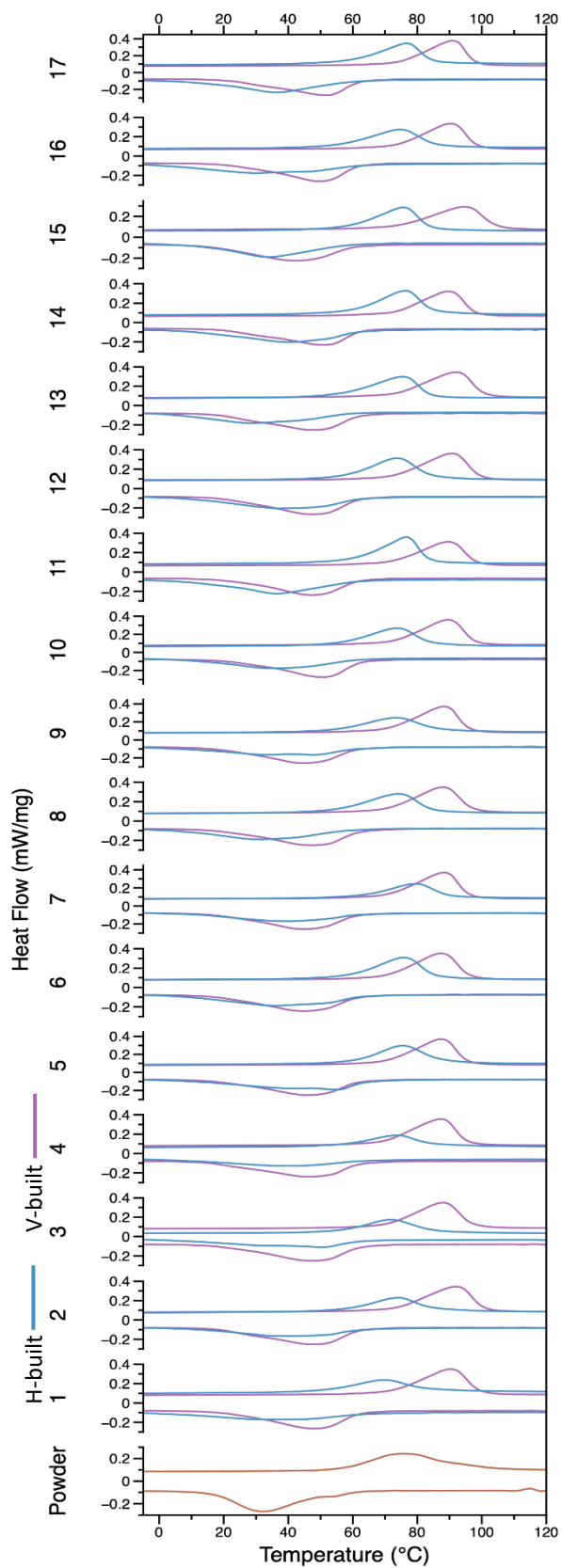
Figure 4A1 DSC heat flow profiles of all H-built and V-built samples from the second thermal cycle, compared to that of the raw powders.

154
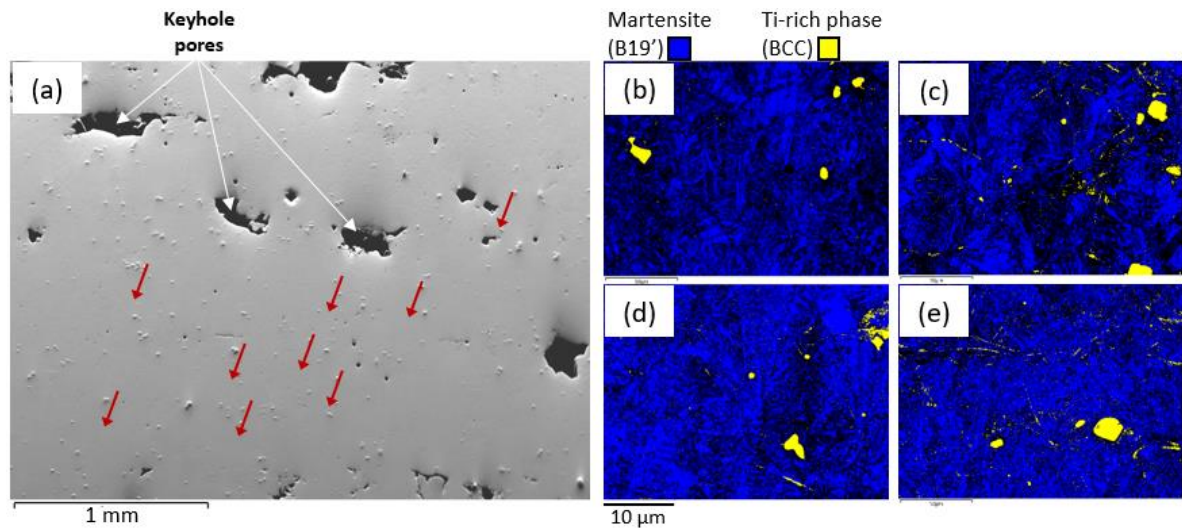
Figure 4A2 (a) Optical micrograph of a H-built sample (H11) showing the random distribution of Ti-enriched protrusions on the finely polished surface, **(b-e)** phase maps as obtained from EBSD indexing these protrusions as nearly-pure Ti phase with BCC structure indicating β – Ti phase; EDX composition analysis revealed that the protrusions contain Ti: 99.2 at. % and Ni: 0.8 at. %.
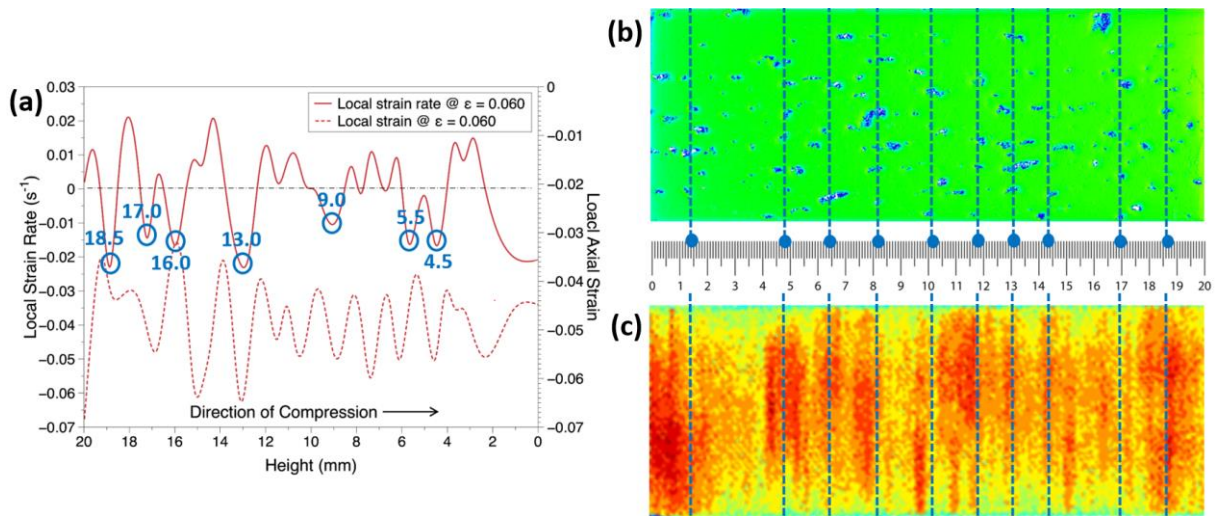
Figure 4A3 (a) Location (in mm) of maximum compressive local strain rates in sample H5 indicated by blue markers; **(b)** optical profilometry image showing presence of pores in sample H5, blue broken lines indicate regions of cluster formation of pores in the lateral direction; (c) thermograph of sample H5 plotted using pyrometric data obtained during L-PBF, blue broken lines helps to locate/compare regions of pore formations with the regions of high temperature or thermal gradient.

Chapter 5

Formation of β – Ti Phase during L-PBF Processing of Martensitic NiTi

5.1 Abstract

Shape memory activations in martensitic NiTi are highly influenced by the processing technique used. Laser Powder Bed Fusion (L-PBF) is a metal additive manufacturing method being investigated for NiTi processing. The rapid transient thermal effects involved in L-PBF processing are found to cause microstructural anomalies which can result in unfavourable mechanical and functional properties. In this paper, anomalous hard protrusions observed in L-PBF processed NiTi microstructure were investigated in detail. The spatial distribution and cause of these protrusions were analysed. Studies were conducted using EDX, BSE, EBSD, TEM, DSC, AFM and nanoindentation, to identify the compositions, crystal structures, thermal characteristics and nanomechanical properties of these protrusions. The protrusions which were identified as hard β – Ti phase, were found to influence the phase transformation properties of the NiTi samples.

5.2 Materials and Methods

NiTi samples of cuboidal dimensions (10 x 10 x 55 mm) were 3D printed using a *Aconity MINI (GmbH)* L-PBF machine, equipped with *IPG Photonics* Nd:YAG fibre laser system having a wavelength of 1068 nm. The NiTi powders were supplied by *Ingpuls GmbH* from Germany with a nearly equiatomic composition of Ni (49.9) – Ti (50.1) at. %. The powder particles were spherical in shape and were produced by electron induction melting gas atomisation (EIGA) process with a particle size distribution of $D_{10} = 12.3 \pm 0.8$ μm; $D_{50} = 28.1 \pm 2.2$ μm; $D_{90} = 57.3 \pm 7.7$ μm; $D\ [4,\ 3] = 34.0 \pm 3.1$ μm.

Multiple NiTi samples were printed using a combination of L-PBF parameters under constant layer thickness (40 μm) and laser spot size (50 µm). Laser parameters included were three laser powers (120, 150 and 180 W), three levels of scan speeds (600, 900 and 1200 mm/s) and three levels of hatch spacings (40, 55 and 70 µm). A Box-Behnken design of experiment (DoE) was followed to print the samples (Table S1 is supplementary). The samples were printed in horizontal (H-built; longest axis of the cuboid parallel to build plate surface) and vertical (V-built; longest axis of cuboid perpendicular to build plate surface) orientations, following a simple stripe scanning strategy with 90° rotation between each consequent layer. The volumetric energy density (*VED*) of L-PBF processing was calculated following Equation 1.4. The *VED* varied between 44.64 and 156.25 J/mm^3, following the combination of the above-mentioned laser parameters. The samples were arranged on the build plate at an angle of 45° for

vertical orientation build, and 30° for horizontal build. The build chamber ambient temperature was 20 ± 1 °C for all builds.

After fabrication, samples were ground using abrasive SiC papers P240, P600, P800 and P1200, and then polished using 6, 3, 1 μm diamond suspensions and 60 nm colloidal silica. To reveal the microstructure, samples were etched with 15 mL HF + 10 mL HNO$_3$ + 10 mL CH$_3$COOH + 5 mL glycerol for approx. 2 – 3 s. Optical images of microstructures were obtained using *Keyence VHX2000E* 3D Digital microscope. Prior to etching, the chemical composition of the samples was analysed through an *AZtec Live System* from *Oxford Instruments NanoAnalysis* EDS module attached to a *Zeiss EVO LS-15* SEM. Backscattered electron (BSE) imaging was achieved by plugging in a CZBSD semiconductor detector (with four diode segments) to the SEM. Differential Scanning Calorimetry (DSC) thermal analysis was followed using *Netzsch DSC 214* equipment to analyse the phase transformation temperatures. Thermal cycling was conducted from – 60 °C to 130 °C and back to – 60 °C maintaining a ramp rate of 10 °C/min.

The crystal structure of martensitic NiTi was analysed at *The Open University*, using an Electron Backscatter Diffraction (EBSD) detector (*Oxford Instruments Symmetry S2*) on a *Zeiss Crossbeam 550* FIB-SEM. Analytical conditions were: a 20 kV accelerating voltage, a 10 nA current, a 14 mm working distance, and a 70° sample tilt. A minimum of two EBSD maps were acquired for each sample: an overview map with horizontal width of 200 μm and a step size of 0.1 μm; and a detail map with horizontal width of 50 μm and step size of 0.03 μm. An additional vibro-polishing was performed on the metallographic samples for 8 – 10 hours using 60 nm colloidal silica prior to EBSD analysis. The same samples were used for AFM and nanoindentation. Atomic Force Microscopy (AFM) equipment *Bruker Dimension Icon* was used to study the topology of the protruded particle at submicron scale. A silicon tip on nitride lever with resonance frequency = 70 kHz and cantilever spring constant = 0.4 N/m was used, in conjunction with *ScanAsyst* imaging mode (peak force tapping) with a scan size of 20 x 20 μm, 256 sample points, and a drive frequency of 0.5 kHz.

The specimen cross-sections for scanning/transmission electron microscope (S/TEM) analysis were prepared using a focused ion beam (FIB) instrument with a Gallium source (*Zeiss Auriga, Carl Zeiss AG, Germany*). Final polishing was performed using a *Fischione 1040 NanoMill* Argon ion beam polisher. To obtain selected-area electron

diffraction (SAED) patterns, TEM images and high-resolution annular dark-field (HAADF) TEM images, a S/TEM *FEI Titan 80 – 300 kV* (*Thermo Fisher Scientific, USA*) with Schottky field-emission gun (operated at 300kV) was used. A camera length of 380 mm was used to determine the SAED patterns. These were then analysed in the *Single Crystal 4* software package.

Nanoindentation was performed using *Bruker Hysitron TI Premier* to reveal the localized property variation using a three-sided Berkovich indenter. A resolution of $\pm$ 0.02 mN for indentation load, and $\pm$ 2 nm for indentation depth was implemented. The high resolution ensured a precise nanomechanical property evaluation. The area function of the indenter configuration was calibrated using standard fused silica. The z-axis movement and indenter tip to microscope head were calibrated to precisely locate the position for the indentation. The piezo automation mode with scanning probe microscopy (SPM) attached in nanoindentation attachment was employed to obtain the surface morphology, and then precisely trace the region for indentation. Prior to indentation, the sample was kept inside the nanoindentation chamber for more than 3 hours to diminish the influence of thermal drift on the P – h data. Subsequently, the indentation was performed at a maximum indentation load of 3 mN with a loading-unloading rate of 300 µN. A holding time of 10 seconds was used to diminish the influence of creep on the unloading characteristics.

5.3 Results and Discussion

Raw powders having higher Ti content were used to ensure higher phase transformation temperatures and a stable martensitic phase at room temperature. This ultimately favours shape memory property in the L-PBF processed samples. In phase composition analysis, the powders were found to contain fully martensitic phase with no precipitate phases, and near equiatomic composition with higher Ti content (refer Figure 5A1 in Appendix A). Hard protruding particles (Figure 5.1a) were found scattered within the NiTi matrix after L-PBF processing. During fine vibro-polishing, these protrusions were detected due to being hard and more resistant to polishing than the surrounding matrix (NiTi). Therefore, the protruded particles indicated phases with an unyielding hard mechanical property, different from the surficial NiTi matrix. As seen in Figure 5.1a – 5.1b, the V-built samples showed no, or significantly less, traces of protrusions on the polished surface compared to the H-built samples. However, all of the H-built samples showed a large number of these protruded particles randomly distributed in the NiTi matrix. More images of other

H-built and V-built samples in the DoE can be seen in Figure 5A2 in Appendix A. To study these protrusions in detail, the H-built samples H2, H6, H8 and H11 were considered. The L-PBF processing parameters of these samples are shown in Table 5.1.
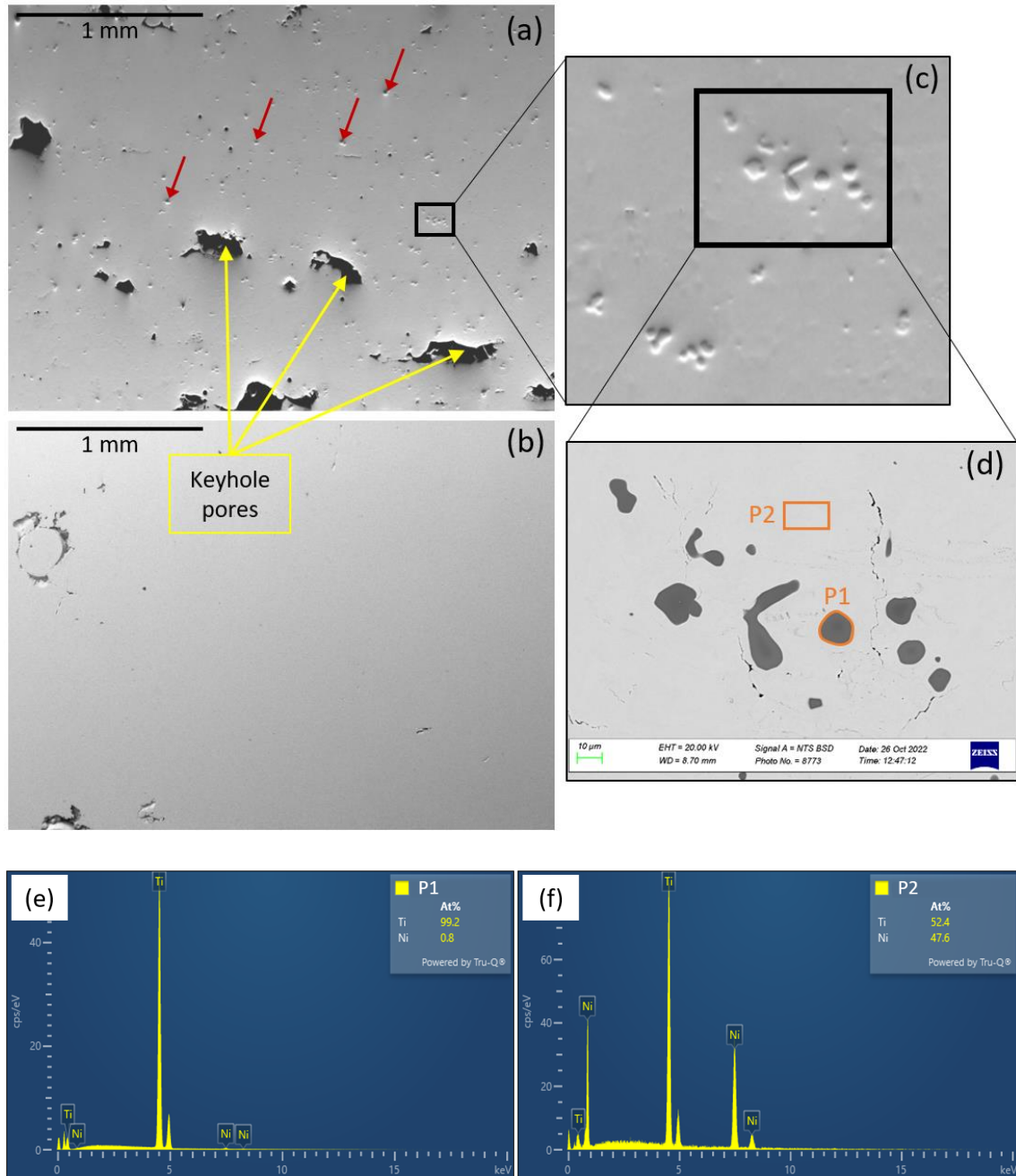
Figure 5.1 SEM image of (a) protruded particles as seen in sample H11: overview of random distribution of protruded inclusions and typical keyhole pores seen in H-built L-PBF samples, (b) vertically built V11 sample, (c) close-up secondary electron emission image of H11, (d) Back-Scattered Electron (BSE) emission image of the same region, (e) EDX compositional analysis of protruded particle P1 from BSE image, (f) EDX compositional analysis of NiTi matrix P2 from BSE image.

Table 5.1 L-PBF processing conditions used to print the NiTi samples (H-built/V-built).

Sample	Laser power (W)	Scan speed (mm/s)	Hatch spacing (µm)	VED (J/mm^3)
H2/V2	120	600	55	90.91
H6/V6	150	900	55	75.76
H8/V8	180	900	70	71.43
H11/V11	150	1200	70	44.64

The protruding particles seen in the highly polished samples were revealed to be Ti-rich (98.6 – 99.5 at. %) from EDX analysis (Figure 5.1e – 5.1f), so these particles are referred as Ti protrusions for discussion. BSE imaging was also conducted to confirm the composition. Heavier elements (higher atomic number) appear brighter in BSE mode as they deflect incident electrons more strongly compared to the lighter elements. From the BSE image (Figure 5.1d), the protrusions can be seen as darker, compared to the matrix surrounding it, which further confirms the Ti-rich composition in the protrusions. Through image analysis, the area fractions of Ti protrusions with respect to the total areas were analysed; Figure 5A3 in Appendix A. The area fractions were found to be between 0.5 % and 2 % for H-built samples. No correlation was found between the extent of the area fractions and the L-PBF parameters. Also, the morphology of these particles was found to be irregular throughout the microstructure.

Figure 5.2a – 5.2d shows the predominance of monoclinic B19' twinned martensite phase as woven fabric of needle-like structures. The Ti protrusions were indexed as a BCC structure. The findings from EBSD, EDX analysis and BSE imaging reveals that these protrusions are composed of some form of Ti.

These protrusions can be seen, as short needle-like peaks in AFM scans (Figure 5.2e – 5.2f) of polished as-fabricated L-PBF samples. Through analysis of the peak force error diagrams, these protrusions were flagged as a different entity compared to the NiTi matrix.
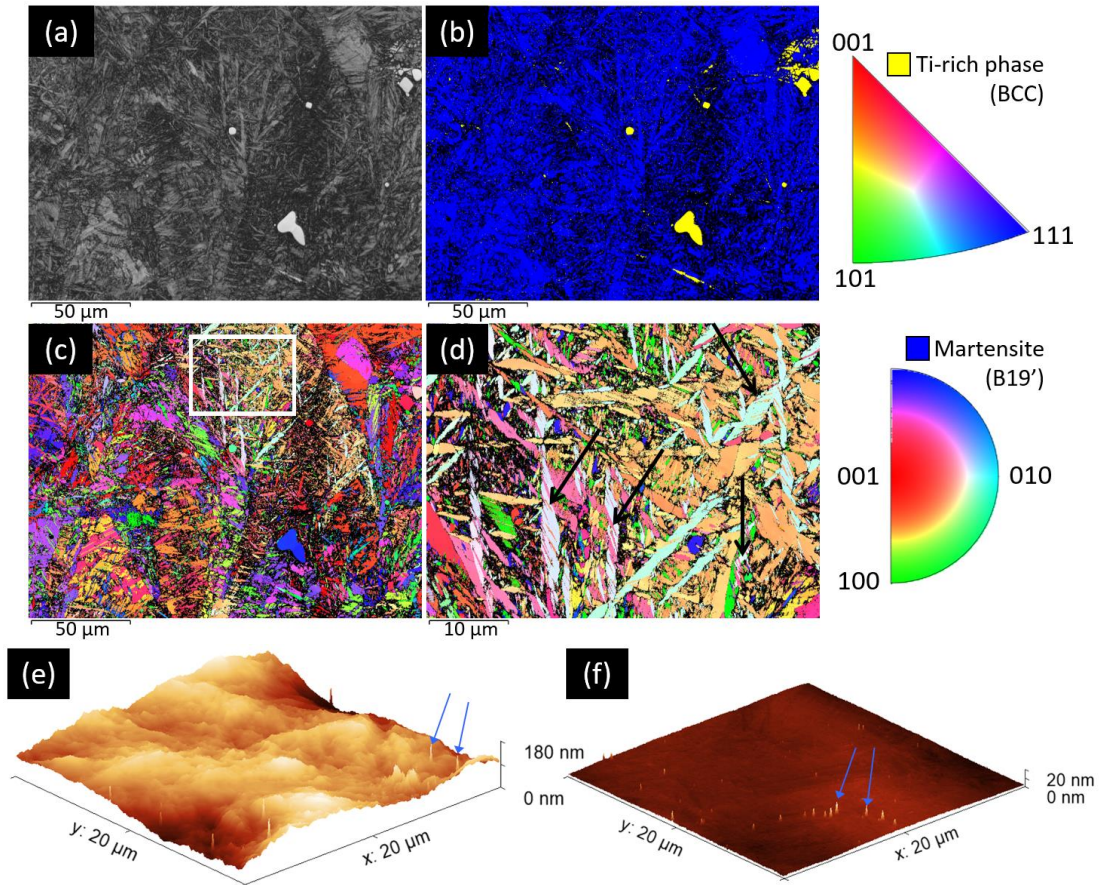
Figure 5.2 Microstructure of H11 through EBSD: **(a)** Band contrast map, **(b)** phase map showing martensitic B19' NiTi (blue) and Ti-rich BCC phase (yellow), **(c)** IPF Z map showing grain orientations (index maps shown right), **(d)** 50 μm close-up image of white-border region in IPF map showing random twinned structures; AFM scans showing protrusions: **(e)** sample H6, **(f)** sample H11.

TEM analysis was conducted to substantiate the crystallographic details of Ti protrusions found through EBSD. The boundary of one of such Ti protrusions was located, and a specimen cross-section was prepared. In Figure 5.3a, the HAADF TEM image is presented with darker shade representing the Ti protrusion, and lighter shade representing the NiTi matrix. Using the software package and previously reported [312] Ti crystal structures as a reference, SAED analysis was performed. The analysis confirmed BCC structure with a zone axis of [310] for the Ti protrusion; indexed region named P1. Figure 5.3b shows the SAED patterns.
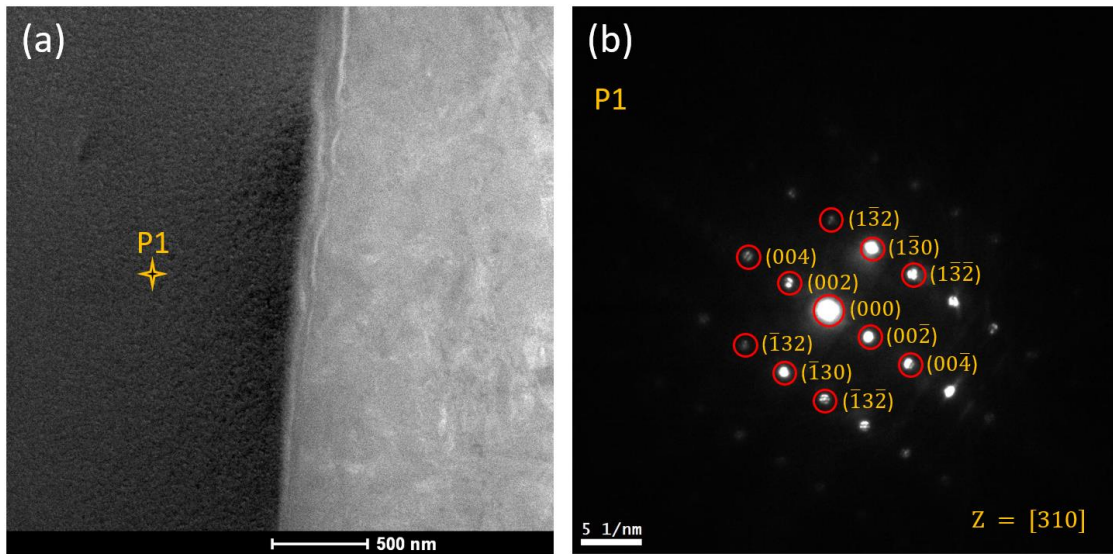
Figure 5.3 (a) High-angle annular dark-field (HAADF) TEM image showing boundary between Ti protrusion (darker shade) and NiTi matrix (lighter shade); **(b)** selected area electron diffraction (SAED) pattern acquired in TEM at point P1 along with analysed zone representation.

The random distribution of Ti protrusions is independent of the locations of the pores. Further microstructural analysis revealed via optical microscope images (Figure 5.4a – 5.4b) show that these protrusions are formed in regions of overlapping scan tracks and epitaxial melting (deep in the melt pool overlapping the previous scanned layer). Either way, it is certain that these regions are exposed to continuous high thermal energy. From examination of the thermographs of middle layer of the L-PBF samples (Figure 5A4 in Appendix A), it can be seen that the effect of the same L-PBF parameters was much less for the V-built samples. In the V-built samples (samples V2, V6, V8 and V11 in Figure 5A4 in Appendix A), the temperature profiles are similar with only slight variations between samples, however, in the case of H-built samples, the effect of the different VED can be clearly seen to have resulted in more variation in the global average temperatures (samples H2, H6, H8 and H11). The H-built samples also exhibited several regions of high temperature or hotspots across the layer, and higher intralayer thermal gradients. The surface area for heat build-up and for heat dissipation, as well as inter-layer laser scanning delays, can affect the thermal profiles of L-PBF samples produced in the different orientations. These temperature profiles would produce higher local cooling rates in the H-built samples which can be seen to have caused the more precipitation and the significant number of Ti-rich protrusions found in the H-built samples compared to V-built samples.

In NiTi system, high Ni evaporation is possible, which could lead to precipitate formations or change in functional properties [35,46,313–315]. However, the formation of nearly pure Ti particles has not previously been reported. From EBSD band contrast maps and IPF-Z maps (Figure 5.2a – 5.2d), and microscopic images (Figure 5.4a – 5.4b), it was also noticed that these protrusions occur mostly in regions of very fine martensitic grains. Regions with large grain size rarely showed the presence of these kind of protrusions. The formation of small martensite grains is often caused due to high energy exposure [37]. This was also confirmed from pyrometric infra-red data where localised high temperatures were detected. The melt pool temperatures are significantly high in L-PBF and the process itself is susceptible to high cooling rates (10^7 °C/s) [35,316]. At times the melt pool temperature can go severely high in the range of 3000 – 5000 °C, depending on material, laser power and scan speed. The boiling point of Ni (2,730 °C) is lower compared to that of Ti (3,287 °C). When the Ni content is higher (> 50.5 at. %), Ni_4Ti_3 and $NiTi_3$ precipitates are often formed. However, in martensitic NiTi, where the Ti content is marginally higher, high temperatures can lead to Ti_2Ni (Ti-rich) precipitate formations. Such precipitates, as well as dislocations or other local stress fields can alter the phase transformation temperatures (TTs) of L-PBF NiTi [35,36,163,317,318].

These Ti_2Ni formations can also occur due to a eutectoid reaction between Ni and Ti, which overcomes the influence of Ni evaporation, and thereby decreases the TTs overall. A similar trend was observed in Figure 5.4c, where the H-built samples exhibit lower TTs. The Ni reductions are high for these samples compared to V-built ones, and this should generally induce higher TTs in H-built samples. However, a reduction in TTs along with an overlapping *Ms – As* transition region (indicated by darker peach shade), where the *As* temperature lies below the *Ms* temperatures. This coinciding martensite – austenite phase transition can result in better shape memory activation and fatigue resistance [319]. A better shape memory capability in H-built samples was indeed recorded from strain recovery testing conducted on the L-PBF samples (Table 4A1 in Appendix A).
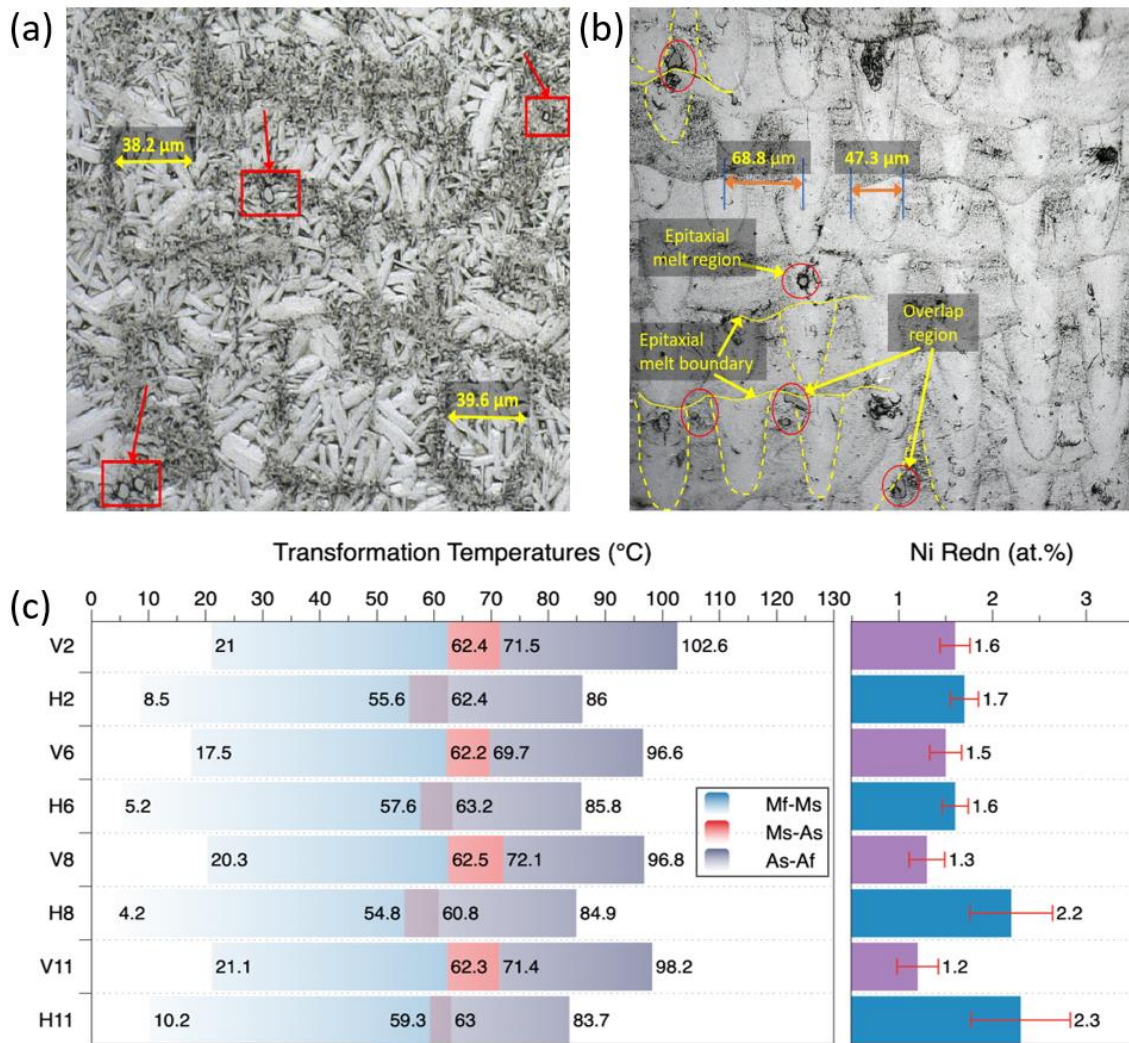
Figure 5.4 (a) Optical microscope images showing melt pools, scan tracks, large/small martensitic features in fully-etched H2 (hatch spacing = 55 μm), **(b)** features as seen in partially-etched H8 (hatch spacing = 70 μm); laser spot size used: 50 μm, **(c)** Phase transformation temperatures of V-built (V) and H-built (H) samples and their corresponding Ni reductions recorded after L-PBF processing; *Mf* – Martensitic finish, *Ms* – Martensitic start, *As* – Austenitic start and *Af-* Austenitic finish temperatures (each gradient shows corresponding phase transitions).

Referring to the binary phase diagram of NiTi [35], the reaction temperature for Ti_2Ni is 984 °C lower than that of the NiTi phase which is 1310 °C, and the Gibbs free energy for Ti_2Ni reaction has been found as 78.03 kJ/mol indicating a high spontaneity during the L-PBF process [320,321]. During high cooling rates and repeated heating, elemental diffusion is often suppressed to obtain chemical homogeneity, and this can result in Ti enrichments (as Ti_2Ni) along grain boundaries or melt pool boundaries. These Ti

enrichment phases were also reported to create local stress fields, which can affect the transformation temperatures [36].

Understanding the spontaneity of Ti-enriched phases, these protrusions were initially suspected to be Ti_2Ni phase. The Ti_2Ni phase has a face centred cubic (FCC) structure in space group $Fd\bar{3}m$. However, from crystal structure analysis, these Ti protrusions were indexed as BCC structures in TEM analysis and EBSD analysis (Figure 5.2b & Figure 5.3). Since EDX showed nearly pure Ti content, the protrusions were hypothesised to be a β phase Ti or β – Ti phase. β – Ti is a stable high temperature phase of titanium having a BCC structure, therefore the formation of β – Ti was further investigated. In β – Ti phase, Ti is bonded in a distorted BCC geometry of 8 equivalent atoms with $a = 2.82$ Å; space group $Im\bar{3}m$. The phase specifications used to detect B2 austenite was based in space group $Pm\bar{3}m$. P is for primitive cells, and I is for the BCC arrangement.

Referring the binary phase diagram of NiTi (Figure 1.19 in section 1.6.2), it is evident that at high melt pool temperatures (e.g., 942 °C), with high Ti content (> 90 at. %), the preferred phase is β-Ti. It is considered that the thermal kinetics from the L-PBF process stabilised this phase during solidification. This may be due to extensive local evaporation of the Ni due to exceeding a critical local evaporation temperature; see Figure 5A4 in Appendix A. It is also noted that there are increased chances for the high temperature β – Ti phase to stabilise at high cooling rates [322]. One of the Ti protrusions from sample H6 was observed under AFM to see the topographical features. As seen in Figure 5.5a, the protrusion was surrounded by deep and shallow ridges. The difference in height between the Ti protrusion and the surrounding ridges were about 150 – 180 nm. These ridges can indicate a sudden elimination (rather than reduction) of Ni in the region, and formation of a nearly pure Ti phase. The region also seems to contain fine grains and therefore indicate localised prolonged heating (high melt pool temperature).
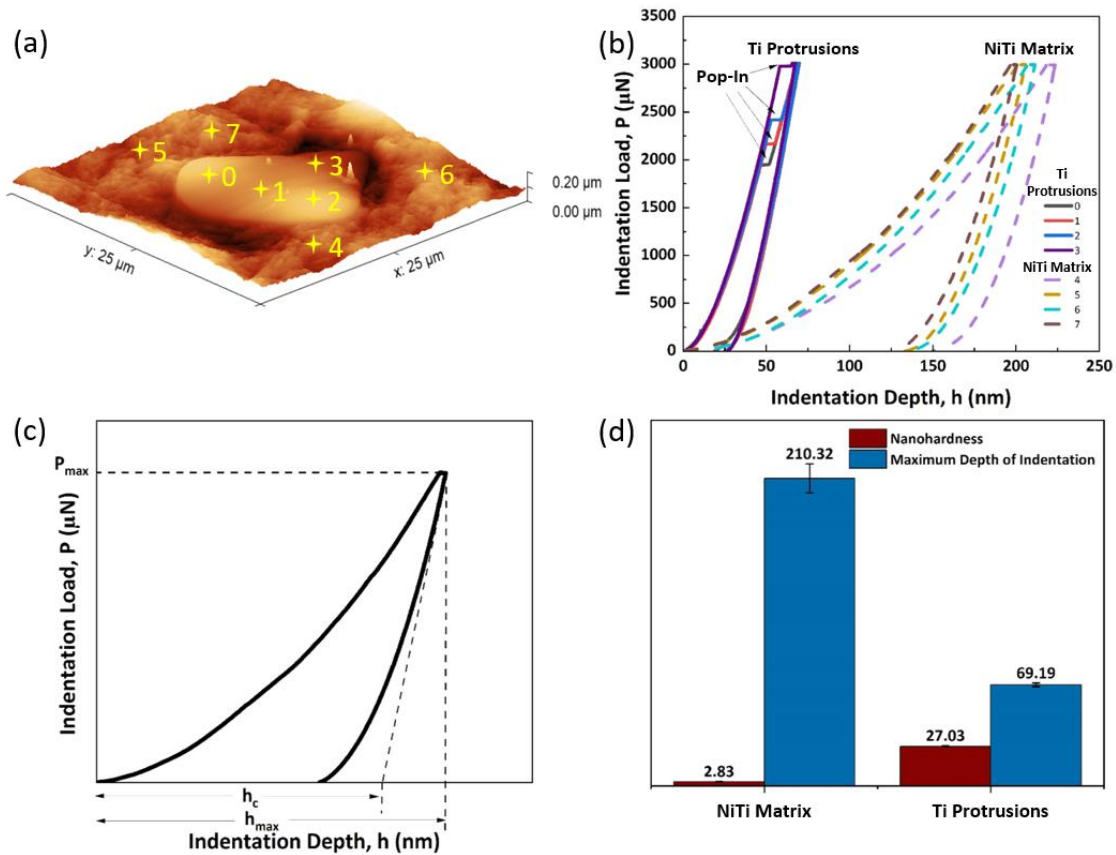
Figure 5.5 (a) AFM image of Ti-enriched particle showing locations of nanoindentation, **(b)** P – h characteristics recorded through nanoindentation, **(c)** terms used in OPM method for hardness estimation, **(d)** nanohardness and depth of indentation for concerned entities.

In order to study the mechanical properties of the protrusions, nanoindentation was performed. Nanoindentation has been widely used to understand the localized functional and mechanical property changes in NiTi system [323–326]. To evaluate the associated deformation response of these Ti protrusions, the nanoindentation response was measured. Figure 5.5a highlights the indentation points where measurements were taken from the Ti protrusions and the surrounding NiTi matrix. As presented in Figure 5.5b, the P – h characteristics acquired from the NiTi matrix can be seen to be entirely different to that of the protrusion. Under the exact same indentation load, the depth of indentation achieved in the protrusion was significantly lower compared to the NiTi matrix. Along with low penetration, the indents on Ti protrusion were seen to undergo a sudden plunge (conventionally termed as pop-in) after certain depth of indentation. At a P_{max} of 3 mN, h_{max} of 200 – 220 nm was noted in the NiTi martensitic phase. This is more than three times the h_{max} (67 – 70 nm) found on the Ti protrusion (Figure 5.5d). To convert such

depth variation into quantitative terms of hardness (H), the Oliver and Pharr method (OPM), Equation 5.1, is employed on the P – h curve [327].

$$H = \frac{P_{max}}{A_c}$$

(5.1)

In the above term, A_c signifies the projected contact area of indentation at P_{max} and it is measured using the relation 24.5 h_c^2. Figure 5.5c represents the characteristic terms associated with OPM method for hardness estimation. By following the OPM, the nanohardness values of the martensitic NiTi matrix and Ti protrusion were estimated (Figure 5.5d) to be 2.84 ± 0.29 and 27.03 ± 0.51, respectively. The Ti protrusions were found to be nearly 9 times harder than the martensitic NiTi matrix. Previous studies show β – Ti as a hard material with a ferritic iron-like BCC structure having a ductile-brittle transition temperature. This temperature in generally above room temperature, which can result in cleavage fracture at ambient conditions [328]. As seen in Figure 5.5b, the pop-ins noted during indentation on Ti protrusions can be due to this cleavage fracture in brittle and hard β – Ti. It can also be due to an underlying porosity (beneath the protrusion) that is created during drastic Ni evaporation. The variation in P – h curve of indents made on Ti protrusions was found to be negligible, while the variation in NiTi matrix was found to be considerable. Nanoindentation is well-known for its high sensitivity to microstructural inhomogeneity [324,329]. Therefore, these variations in P – h curves can indicate a high heterogeneity in NiTi martensitic matrix, whereas the Ti protrusions are more homogeneous. This further supports the premise of these protrusions being a single entity of β – Ti. All of the above characterisations help to summarise that the protrusions are a hard β – Ti phase. A comparative study based on some previous studies shows that β – Ti exhibits a higher hardness than the NiTi system [330,331]. However, based on processing conditions and formation mechanics this can vary in each scenario. Also, during processing or indentation, a martensitic transformation can occur inside β – Ti resulting in α'– Ti which further leads to increased hardness characteristics. These small fractions of α'– Ti are generally not indexed in EBSD [331–333].

5.4 Conclusions

The formation of hard protrusions in NiTi caused by L-PBF processing has been investigated in detail. These protrusions were found in as-fabricated NiTi samples after fine polishing. The entities were significantly present in H-built samples, whereas they

were scarce/not seen in samples built in the vertical orientation. Further investigation revealed these to be nearly pure Ti phases which precipitated in the regions of high-temperature exposures such as melt pool boundaries, scan track overlaps and epitaxial melt region. Localised high melt pool temperatures can also locally eliminate Ni from fine grained martensitic regions, promoting the formation of Ti-rich precipitates. Upon detailed analysis, these particles were found to be β – Ti. Even though the presence of precipitates and secondary phases in L-PBF NiTi has been reported in the past by several researchers, the presence of a β – Ti phase observed in the current study is novel from the metal additive manufacturing route. A suggestion for future investigation is a systematic analysis of how the powder properties, L-PBF parameters and scanning strategies affect the formation of the β – Ti phase in L-PBF processed NiTi.

5.5 Contribution to Thesis Objectives

The particles analysed in this chapter was first discovered during the microstructural analysis of L-PBF processed NiTi in Chapter 4. Further investigation revealed the effect of these phases on phase transformation properties and shape memory capabilities. The findings were validated using the results from the study conducted in Chapter 4 on shape memory responses. Thus, the Chapters 4 and 5 collectively report the significance of tailoring the microstructure for shape memory responses in L-PBF NiTi.

5.6 Supplementary Data

5.6.1 Appendix A
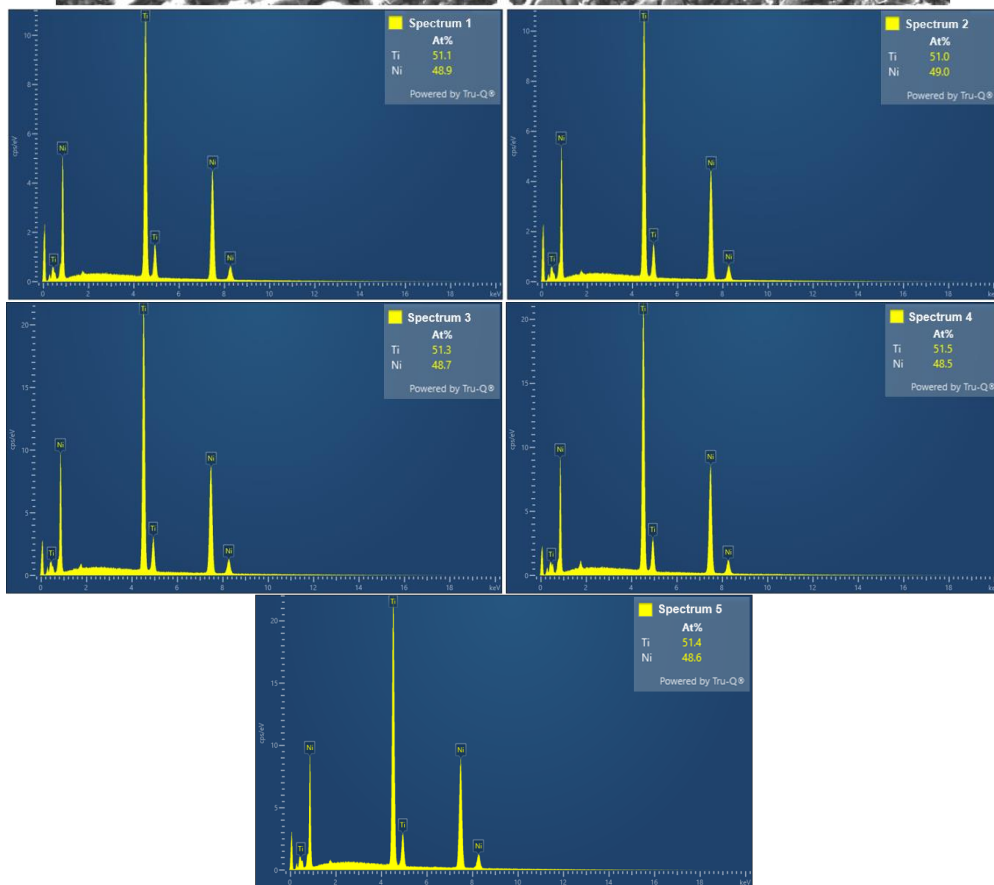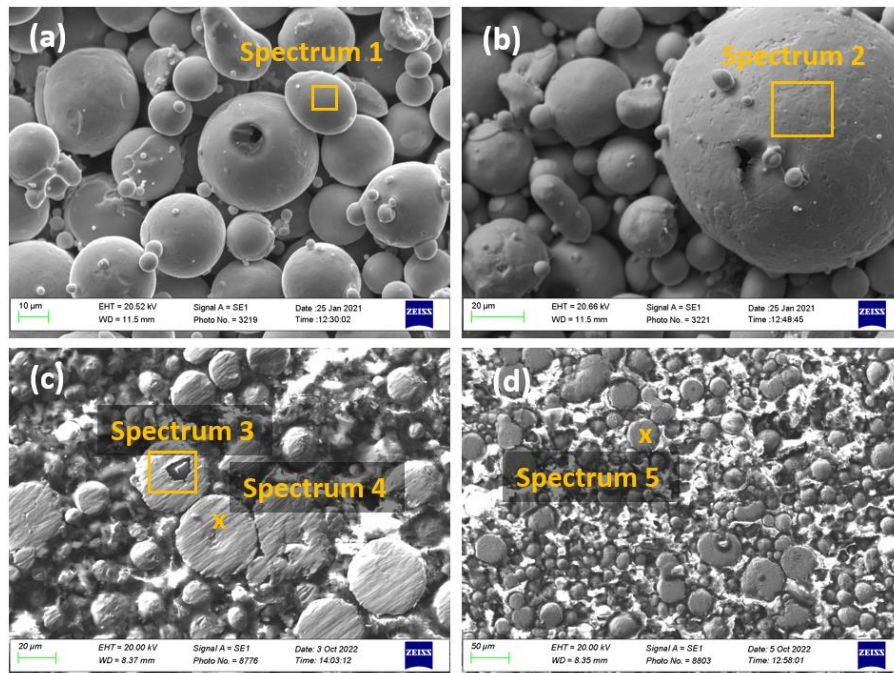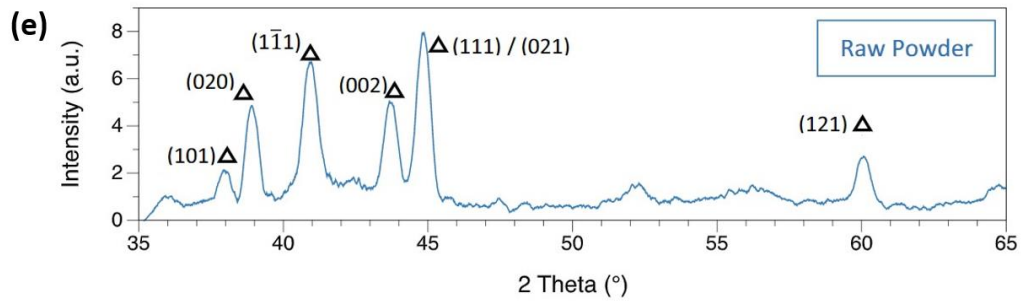
Figure 5A1 EDX indexed regions of raw powders **(a,b)** and sectioned raw powders in cold mounted resin **(c,d)** along with their respective spectrums showing Ni-Ti compositions; **(e)** X-ray diffraction patterns observed in raw powders showing fully martensitic phases (Δ).
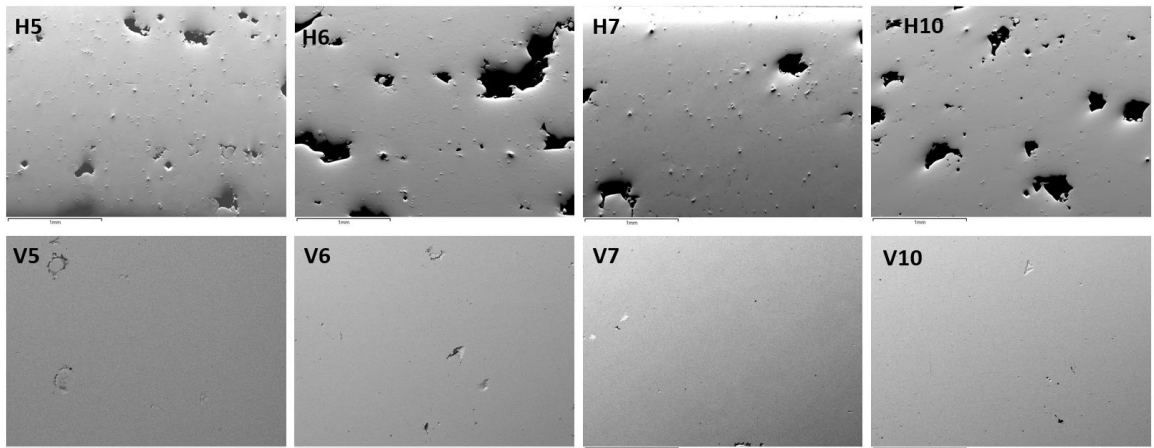
Figure 5A2 Polished surfaces of H-built and V-built samples processed with same L-PBF parameters compared.

Sample	H5	H6	H7	
Mean Area (μm²)	3.02	3.28	1.62	
Ti Protrusions Area (μm²)	14.77	9.98	13.39	
Total Area (μm²)	29763	33400	29502	2
Area Fraction (%)	0.87	0.53	1.57	
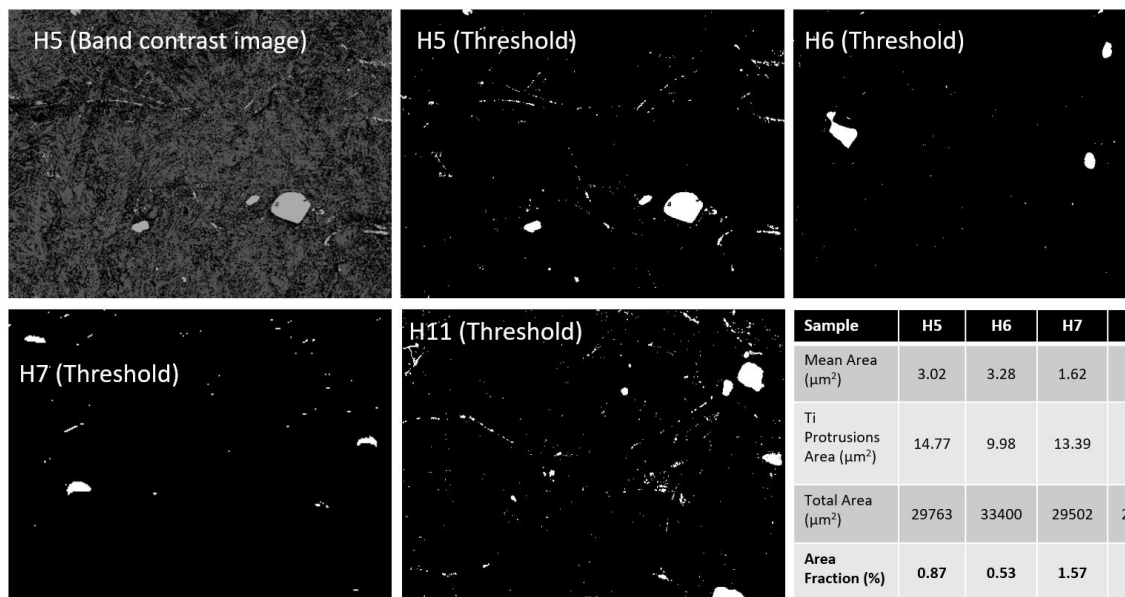
Figure 5A3 Band contrast images of each sample were used to study the area fraction of Ti protrusions – these images were analysed by thresholding the grey colour tones

171

thus highlighting the Ti particles (white in colour). The table shows the calculated area fractions.

Melt-pool thermographs

The thermal data of the melt pool (as seen in Figure 5A4) was logged by two pyrometers (from *KLEIBER Infrared GmbH*) setup in the *Aconity Mini* SLM machine. The emitted light from the laser incidence region (range: 1500 – 1700 nm) is detected by the pyrometers, and the output infrared data is recorded terms of voltage (mV) units and (x, y) coordinates of the build plate. A single layer plot was produced to illustrate the thermal gradients and hot spots across the section of the samples. The data acquisition rate used was 100,000 samples per second. A single build layer is represented by approx. 6 million data points, each containing the coordinate and temperatures (in terms of voltage, mV). The temperature readings were then translated to a normalised scale (0 to 1), to represent the thermal profile.
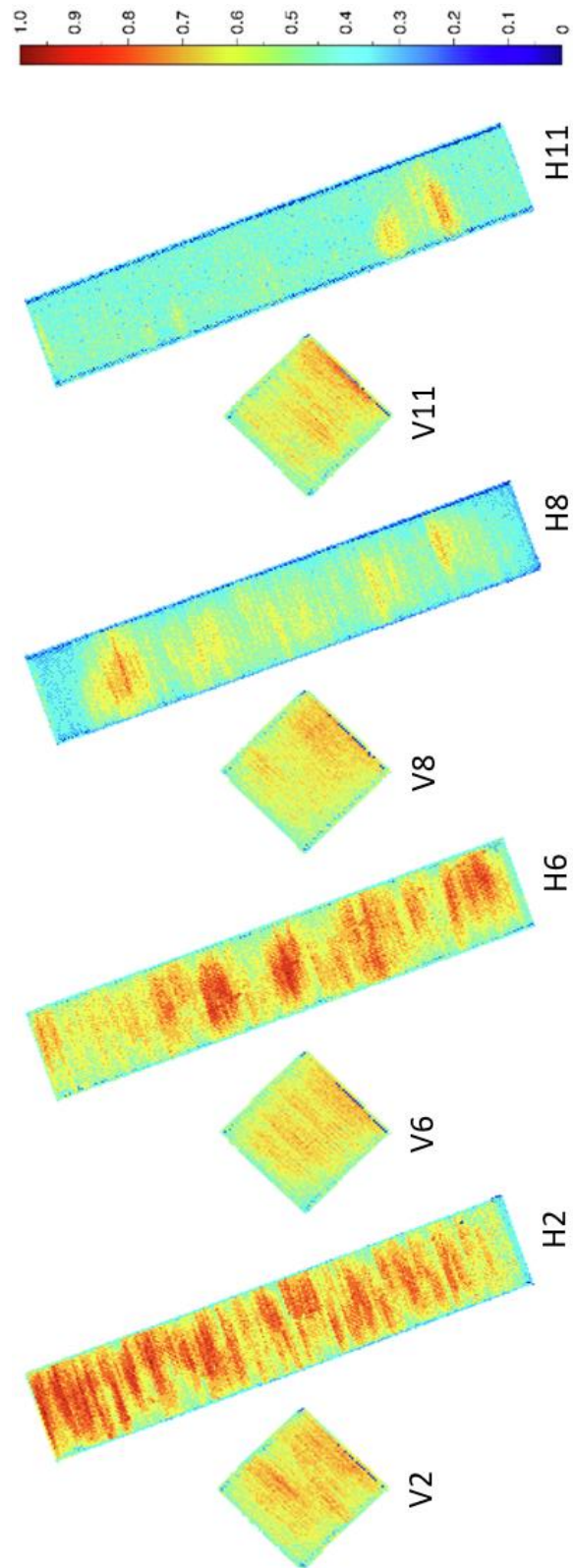
Figure 5A4 Thermographs showing temperature variations and hotspots across the middle layer in V-built (V2, V6, V8, V11) and H-built (H2, H6, H8, H11) samples; normalised temperature scale has been used.

173

Chapter 6

Conclusions and Future Work Directions

6.1 Investigation Summary

To achieve the research aims in this study, the objectives were successfully completed to gain a comprehensive understanding on how L-PBF parameters and build orientations affect the physical, mechanical, and functional properties of NiTi. The original contribution and remarks corresponding to each of the investigations performed are summarised as below:

I. The Auricchio finite element model and representative volume element model were implemented to study the mechanical responses of porous NiTi structures, and provided close predictions to the experimentally measured austenitic NiTi behaviour.

The model responded well to different strain levels and exhibited as expected asymmetric responses in tension and compression modes. The structural stiffness showed an inverse fourth order polynomial relationship with porosity levels. As porosity levels were increased, the structural stiffness and the dissipated energy during martensitic transformation was reduced. Studying the shock absorption performance of porous NiTi, the damping ratio or loss factor was found to increase when porosity increased, while the apparent stiffness showed no observable trend, although the porous structures showed better values than the fully dense structure. In the microscale study, as martensite phase evolution occurs, the elastic modulus of NiTi material was observed to gradually decrease, and then level off as it progressed towards a saturated martensitic matrix, after which a sudden decrease occurred attaining the martensitic elastic modulus.

II. Control of physical, chemical and thermal properties of NiTi was investigated by varying the L-PBF process parameters and build orientations.

In the L-PBF design space, the vertically build presented less variation in densities compared to the horizontal build. In both orientations, higher amounts of porosities were recorded when laser scan speeds were low. However, the higher densities were recorded in horizontal build, printed using a combination of higher laser powers, lower energy densities, and large hatch spacings. The response surface analysis

showed two-factor and linear correlations of vertical build densities with L-PBF parameters, while an additional quadratic relation existed for horizontal build. These effects arose from a variety of porous features including spherical (gas) voids, keyhole formations, lack of fusion and microcracks. These were linked to the higher intralayer average temperature differentials calculated from pyrometric data in horizontal build compared to that of the vertical build. The global intralayer temperatures and differentials are affected by geometric effects (surface area) including thermal conduction, scanning time, and raster time delay of laser beam after each layer of print.

The Ni reduction in vertical build showed lesser variation compared to the horizontal build, and the highest Ni reduction was recorded in horizontal build. From the response surface analysis, the Ni reduction showed a two-factor interaction with L-PBF parameters in both vertical and horizontal builds. Scan speed and hatch spacing posed high correlation with vertical build, while laser power and scan speed exhibited high correlation with horizontal build. Additionally, the laser energy density showed high correlation with Ni reduction seen in vertical build.

While analysing the phase transformation temperatures of both vertical and horizontal builds, it was found that the second cycle in thermal analysis returned more reliable results. The first cycle of the vertical build was analysed to understand the behaviour of unstable variant (R^*) of rhombohedral phase that might have been induced during in-process entrained thermal stresses. The second cycle results were used to study the correlations between L-PBF process parameters and phase transformation properties. The austenitic start temperatures in vertical build, and total transformation range and transition enthalpy properties in horizontal build exhibited high correlations with laser parameters. The total transformation range that determines the operational range of NiTi material was found comparable in both builds. The transition enthalpies and enthalpy ratios were found to be relatively lower in horizontal build, indicating a lower microstructural homogeneity. This was later confirmed during the microstructural study.

Results from the thermal expansion test revealed no significant correlation between the L-PBF parameters and coefficient of linear thermal expansion. The thermal expansion characteristics showed distinct regions of austenitic and martensitic phase

transformations, indicated by humps or dips in thermal strain curves. These can be linked to the crystal lattice rearrangement that occurs between B2, R* and B19' phases during expansion/contraction.

III. Control of mechanical properties and shape memory capabilities was achieved through the control of L-PBF process parameters and build orientations.

In general, the horizontal build showed higher microhardness values, and the vertical build showed higher impact energies. A two-factor interaction correlation was found between microhardness values and L-PBF parameters in both builds. The microhardness values and impact energies recorded for horizontal build presented high correlations with scan speed and hatch spacing. In both build orientations, the recorded impact energies presented an inverse correlation with the laser energy density. The impact energies in vertical build presented a quadratic relation with L-PBF parameters with the laser power and hatch spacing posing a higher effect than scan speed. Overall, the hatch spacing effect was found to be important for tailoring impact energies. It must also be noted that there was a high correlation between sample density and impact energies; hence tailoring of density also plays an important role here.

From the compression tests characterised with full field strain analysis, it was seen that both horizontal build and vertical build showed comparable characteristics while deforming and recovering elastic strains. The maximum stresses recorded for 6 % strain in horizontal built samples were relatively lower compared to the vertically built samples. The variations in these values were less in the vertical builds, a similar trend was seen in the density analysis of both builds. In the vertical build, the structural stiffness (elastic moduli) correlated well with the laser energy density. From the strain analysis, it was found that the maximum local strain rate was recorded during the progression of detwinning compared to fully twinned or fully detwinned states. This conveys that maximum strain under deformation is accommodated during the detwinning stage. It was also found that the elastic strain rate in the detwinned state is lower than that of the twinned matrix. The porosity formations were also found to influence the local strain profiles.

The shape memory capabilities measured in terms of irrecoverable strain and irrecoverability, revealed good linear correlations with laser power in the case of the

vertical builds. The horizontal builds showed relatively less shape memory effect, with higher variation in responses to changes in L-PBF parameters. However, no significant correlations were found during response analysis between the process parameters and shape memory response. As the applied strain level was increased from one sample to the next, but produced with the same process parameters, there was a clear reduction in the total percentage of shape memory functionality, as observed via an increased irrecoverability. This implies the importance of choosing the right strain levels for optimum shape memory responses.

IV. Microstructural features in L-PBF processed NiTi and their effects on shape memory capabilities were investigated.

All of the L-PBF samples were seen to contain mostly twinned martensitic microstructures when characterised through different methods including phase analysis, microscopy and crystal structural analysis. From the fractographs, it was clearly seen that the samples were brittle, this was supported by microhardness and impact test results. Changes in submicron topologies were analysed and reported for each stage of compression and shape memory recovery. It was also interesting to find that the horizontal build contained randomly spread pure Ti phases precipitated in the microstructure. These formations were not or were scarcely present in vertical build. These precipitates were found to affect the phase transformation characteristics and shape memory functionality. The horizontal build showed better shape memory capabilities in general due to the lower thermal hysteresis these features induced. Even though precipitates and secondary phases in L-PBF processed NiTi has been reported by several researchers, the presence of a pure Ti phase observed in the current study is novel from the metal additive manufacturing route.

To summarise, the variations in all responses caused by L-PBF parameters were considerably lower in vertical build. This trend was consistently seen in all physical, chemical, thermal, mechanical, and functional characterisations. However, the higher variations found in horizontal build correlated well with the L-PBF parameters. Therefore, the produced sample properties could be altered more by the L-PBF process parameters in the horizontal build orientation. The inherent stochastic nature of the L-PBF is due to the high thermal gradients, variations in feedstock powder properties, recoater blade degradation, spatter formations, and variations in process environment

temperature and inert gas flow properties. The resulting part properties can also differ substantially due to different process parameter settings including scanning strategies. In this work, the effects of laser powder, scan speed, hatch spacing, and build orientation, were examined in detail, and reported herein.

6.2 Recommendations for Further Research

The current project achieved the aim of evaluating the effects of L-PBF process parameters on NiTi for mechanical properties and retained shape memory functionality, and provides a significant level of novel results in this area. However, there still remains a number of challenges and critical areas that have to be addressed in future work. The following recommendations are proposed for future research.

- A better finite element model integrating the microstructural evolution during phase transformations needs to be developed to understand the thermally-induced shape memory response in martensitic NiTi. Also, the residual deformation in each loading cycle must be accounted for to test the stabilisation effect. Ideally, a combined multi-physics-based model that accounts for stabilization effect, thermal effect, martensitic phase evolution and local heterogeneity must be created to accommodate the L-PBF effect.

- The presence of residual thermal stresses in the as-fabricated L-PBF NiTi has to be measured. Under certain aspect ratios of part geometry, the effect of residual stresses on vertical build is minimal, however, it is highly influential in horizontal build. Different types of support structures need to be analysed for their effectiveness to efficiently reduce the effects of thermal gradients from the bottom layers of the build. Substrate preheating is another route to effectively reduce the thermal gradients. Studying the effect of preheated build plate on part properties and using the pyrometric thermal data can give insight into resulting thermal fields would help to address this critical issue. The as-fabricated samples are often annealed or heat treated in order to relieve thermal stresses, and reduce the extent of precipitates and secondary phases which affects the microstructure and reduce the shape memory functionality. In-situ heat treating of samples on build plate using substrate heating during or after L-PBF processing is another relevant area to investigate in this regard.

- The design space in the current DoE is suggested to be widened and/or skewed keeping the centre node same, to explore how the L-PBF parameters can be optimised

for end applications. The required levels of density, phase transformation temperatures, compositions, and mechanical/functional properties are different for various end applications. The current response models can be used as a reference to develop the optimisation strategy.

- The formation of β – Ti phase in L-PBF processing of NiTi was due to the higher temperature (as observed within the horizontal builds) resulting in a higher thermal cooling gradient. This needs further investigation to understand why the thermal profile of the horizontal builds differed from the vertical builds. It would be interesting also to explore whether the presence of spatter particles landing on a built layer (adjusting the inlet gas flow) could influence β – Ti phase formations. Along with these, a systematic analysis of how powder properties, L-PBF parameters scanning modes (pulse and continuous), and scanning strategies affect the formation of the different phases, the shape memory response and the cyclic stability, will be interesting to pursue in the future.

References

[1]   S.C. Dutta, R. Majumder, Shape memory alloy (SMA) as a potential damper in structural vibration control, in: S. Hloch, D. Klichová, G. Krolczyk, S. Chattopadhyaya, L. Ruppenthalová, (Eds.), Advances in Manufacturing Engineering and Materials, Springer, 2019, pp. 485-492.

[2]   K.S. Senkevich, Prospects of production and application of hybrid structures and composites made of titanium alloys and nitinol: Overview, Rus. J. Non-Ferr. Met. 60 (2019) 101-105.

[3]   Neng Li, Shuai Huang, Guodong Zhang, RenyaoQin, Wei Liu, Huaping Xiong, Gongqi Shi, Jon Blackburn, Progress in additive manufacturing on new materials, J. Mater. Sci. Technol. 35 (2019) 242-269.

[4]   T. Ikeda, The use of shape memory alloys (SMAs) in aerospace engineering, in: K Yamauchi, I Ohkata, K. Tsuchiya, S Miyazaki (Eds.), Shape Memory and Superelastic Alloys, Woodhead Publishing Limited, 2011, pp. 125-140.

[5]   J.P. Oliveira, A.J. Cavaleiro, N. Schell, A. Stark, R.M. Miranda, J.L.Ocana, F.M. Braz Fernandes, Effects of laser processing on the transformation characteristics of NiTi: Acontribute to additive manufacturing, Scr. Mater. 152 (2018) 122-126.

[6]   J.W. Mwangi, L.T. Nguyen, V.D. Bui, T. Berger, H. Zeidler, A. Schubert, Nitinol manufacturing and micromachining: A review of processes and theirsuitability in processing medical-grade nitinol, J. Manuf. Proc. 38 (2019) 355-369.

[7]   Z. Yang, X. Wei, P. Cao, W. Gao, Surface modification of nitinol by chemical and electrochemical etching, Mod. Phys. Lett. B 27 (2013) 1341012.

[8]   D. Gu, B. He, Finite element simulation and experimental investigation of residualstresses in selective laser melted Ti–Ni shape memory alloy, Comp. Mater. Sci. 117 (2016) 221-232.

[9]   J. Combs, E. Levin, C. Cheng, S. Daly, S. Yeralan, T. Duerig, Effects of heat treatment on the magnetic properties of nitinol devices, Shap. Mem. Superelast. 5 (2019) 429-435.

[10]   B. Almeida, F. Ormiga, M. Araujo, R. Lopes, I. Barbosa Lima, B. Dos Santos, H. Gusman, Influence of Heat Treatment of Nickel-Titanium Rotary Endodontic Instruments on Apical Preparation: A Micro-Computed Tomographic Study, J. Endod. 41 (2015) 2031-2035.

[11] X. Liu, Y. Wang, D. Yang, M. Qi, The effect of ageing treatment on shape-setting andsuperelasticity of a nitinol stent, Mater. Charact. 59 (2008) 402-406.

[12] D. Depriester, A. Maynadier, K. Lavernhe-Taillard, O. Hubert, Thermomechanical modelling of a NiTi SMA sample submitted to displacement-controlled tensile test, Int. J. Solids Struct. 51 (2014) 1901–1922.

[13] S. Dadbakhsh, M. Speirs, J. van Humbeeck, J.P. Kruth, Laser additive manufacturing of bulk and porous shape-memory NiTi alloys: From processes to potential biomedical applications, MRS Bull. 41 (2016) 765–774.

[14] C.M. Jackson, H.J. Wagner, R.J. Wasilewski, 55 Nitinol—The Alloy with a Memory: Its Physical Metallurgy, Properties, and Applications, NASA SP-5110, NASA: Washington, DC, USA, 1972.

[15] M.H. Elahinia, M. Hashemi, M. Tabesh, S.B. Bhaduri, Manufacturing and processing of NiTi implants: A review, Prog. Mater. Sci. 57 (2012) 911–946.

[16] M. Bram, A. Ahmad-Khanlou, A. Heckmann, B. Fuchs, H.P. Buchkremer, D. Stöver, Powder metallurgical fabrication processes for NiTi shape memory alloy parts, Mater. Sci. Eng. 337 (2002) 254–263.

[17] S. Saedi, Shape Memory Behavior of Dense and Porous NiTi Alloys Fabricated by Selective Laser Melting, University of Kentucky, Lexington, KT, USA, 2017. Ph.D. Thesis.

[18] J.M. Walker, C. Haberland, M.T. Andani, H.E. Karaca, D. Dean, M. Elahinia, Process development and characterization of additively manufactured nickel-titanium shape memory parts, J. Intell. Mater. Syst. Struct. 27 (2016) 2653–2660.

[19] K. Khanlari, M. Ramezani, P. Kelly, 60NiTi: A review of recent research findings, potential for structural and mechanical applications, and areas of continued investigations, Trans. Indian Inst. Met. 71 (2018) 781–799.

[20] W.S.W. Harun, M.S.I.N. Kamariah, N. Muhamad, S.A.C. Ghani, F. Ahmad, Z. Mohamed, A review of powder additive manufacturing processes for metallic biomaterials, Powder Technol. 327 (2018) 128–151.

[21] A. Baran, M. Polanski, Microstructure and properties of LENS (laser engineered net shaping) manufactured Ni-Ti shape memory alloy, J. Alloys Compd. 750 (2018) 863–870.

[22] M. Wang, X. Lin, W. Huang, Laser additive manufacture of titanium alloys, Mater. Technol. 31 (2016) 90–97.

[23] K.H. Leitz, P. Singer, A. Plankensteiner, B. Tabernig, H. Kestler, L.S. Sigl, Multi-physical simulation of selective laser melting, Metal Powder Rep. 72 (2017) 331-338.

[24] Y. Zhang, L. Wu, X. Guo, S. Kane, Y. Deng, Y.G. Jung, J.H. Lee, J. Zhang, Additive manufacturing of metallic materials: A review, J. Mater. Eng. Perform. 27 (2018) 1–13.

[25] R.F. Hamilton, B.A. Bimber, M.T. Andani, M. Elahinia, Multi-scale shape memory effect recovery in NiTi alloys additive manufactured by selective laser melting and laser directed energy deposition, J. Mater. Process. Technol. 250 (2017) 55–64.

[26] Z.X. Khoo, Y. Liu, J. An, C.K. Chua, Y.F. Shen, C.N. Kuo, A review of selective laser melted NiTi shape memory alloy, Mater. 11 (2018) 519.

[27] B. Zheng, Y. Zhou, J.E. Smugeresky, J.M. Schoenung, E.J. Lavernia, Thermal behavior and microstructural evolution during laser deposition with laser-engineered net shaping: Part I. numerical calculations, Metal. Mater Trans. A 39 (2008) 2228-2236.

[28] R. McCann, M.A. Obeidi, C. Hughes, E. McCarthy, D.S. Egan, R.K. Vijayaraghavan, A.M. Joshi, V.A. Garzon, D.P. Dowling, P.J. Mcnally, D. Brabazon, In-situ sensing, process monitoring and machine control in laser powder bed fusion: a review, Addit. Manuf. 45 (2020) 102058.

[29] A. Mussatto, R. Groarke, A. O'Neill, M.A. Obeidi, Y. Delaure, D. Brabazon, Influences of powder morphology and spreading parameters on the powder bed topography uniformity in powder bed fusion metal additive manufacturing, Addit. Manuf. 38 (2021) 101807.

[30] G.M. Volpato, U. Tetzlaff, M.C. Fredel, A comprehensive literature review on laser powder bed fusion of Inconel superalloys, Addit. Manuf. 55 (2022) 102871.

[31] D.W. Brown, V. Anghel, L. Balogh, B. Clausen, N.S. Johnson, R.M. Martinez, D.C. Pagan, G. Rafailov, L. Ravkov, M. Strantza, E. Zepeda-Alarcon, Evolution of the microstructure of laser powder bed fusion Ti-6Al-4V during post-build heat treatment, Metall. Mater. Trans. A 52 (2021) 5165–5181.

[32] A.S. Tehrani, M.H. Korayem, S. Shao, M. Haghshenas, N. Shamsaei, Ti-6Al-4V powder characteristics in laser powder bed fusion: The effect on tensile and fatigue behaviour, Addit. Manuf. 51 (2022) 102584.

[33] P. Bayati, K. Safaei, M. Nematollahi, A. Jahadakbar, A. Yadollahi, M. Mahtabi, M.Elahinia, Toward understanding the effect of remelting on the additively manufactured NiTi, Int. J. Adv. Manuf. Technol. 112 (2021) 347–360.

[34] J.N. Zhu, E. Borisov, X. Liang, R. Huizenga, A. Popovich, V. Bliznuk, R. Petrov, M. Hermans, V. Popovich, Controlling microstructure evolution and phase transformation behavior in additive manufacturing of nitinol shape memory alloys by tuning hatch distance, J. Mater. Sci. 57 (2022) 6066–6084.

[35] J.C. Chekotu, R. Groarke, K. O'Toole, D. Brabazon, Advances in selective laser melting of nitinol shape memory alloy part production, Mater. 12 (2019) 809.

[36] D.C. Ren, H.B. Zhang, Y.J. Liu, S.J. Li, W. Jin, R. Yang, L.C. Zhang, Microstructure and properties of equiatomic Ti–Ni alloy fabricated by selective laser melting, Mater. Sci. Eng. A 777 (2020) 138586.

[37] M.A. Obeidi, M. Monu, C. Hughes, D. Bourke, M. Nur Dogu, J. Francis, M. Zhang, I. Ul Ahad, D. Brabazon, Laser beam powder bed fusion of nitinol shape memory alloy (SMA), J. Mater. Res. Technol. 14 (2021) 2554–2570.

[38] M. Speirs, H.B. Van, H.J. Van, J.P. Kruth, Fatigue behaviour of NiTi shape memory alloy scaffolds produced by SLM, a unit cell design comparison, J.Mech. Behav. Biomed. 70 (2017) 53–59.

[39] W. Guo, B. Feng, Y. Yang, Y. Ren, Y. Liu, H. Yang, Q. Yang, L. Cui, X. Tong, S. Hao, Effect of laser scanning speed on the microstructure, phase transformation and mechanical property of NiTi alloys fabricated by LPBF, Mater. Des. 215 (2022) 110460.

[40] J.A. Shaw, C.B. Churchill, M.A. Iadicola, Tips and tricks for characterizing shape memory alloy wire: Part 1-differential scanning calorimetry and basic phenomena, Exp. Tech. 32 (2008) 55-62.

[41] K. Otsuka, X. Ren, Physical metallurgy of Ti–Ni-based shape memory alloys, Prog. Mater. Sci. 50 (2005) 511–678.

[42] L. Contardo, G. Guenin, Training and two-way memory effect in Cu-Zn-Al alloy, Acta Metall. Mater. 38 (1990) 1267–1272.

[43] F. Nematzadeh, S.K. Sadrnezhaad, Finite element analysis of mechanical performance of Nitinol biliary stent: Effect of material properties, Mater. Res. Innov. 17 (2013) S53–S59.

[44] K.I. Aycock, J.D. Weaver, H.M. Paranjape, K. Senthilnathan, C. Bonsignore, B.A. Craven, Full-field microscale strain measurements of a nitinol medical device using digital image correlation, J. Mech. Behav. Biomed. Mater. 114 (2021) 104221.

[45] J.C. Chekotu, D. Kinahan, R. Goodall, D. Brabazon, Influence of structural porosity and martensite evolution on mechanical characteristics of nitinol via in-silico finite element approach, Mater. 15 (2022) 5365.

[46] J.C. Chekotu, R. Goodall, D. Kinahan, D. Brabazon, Control of Ni-Ti phase structure, solid-state transformation temperatures and enthalpies via control of L-PBF process parameters, Mater. Des. 218 (2022) 110715.

[47] G. Costanza, M.E. Tata, Shape memory alloys for aerospace, recent developments, and new applications: A short review, Mater. 13 (2020) 1856.

[48] S.D. Leonardo, G. Pitarresi, G. Burriesci, Standard mechanical testing is inadequate for the mechanical characterisation of shape-memory alloys: Source of errors and a new corrective approach, Mater. Des. 216 (2022) 110538.

[49] E. Ryklina, A. Korotitskiy, I. Khmelevskaya, S. Prokoshkin, K. Polyakova, A. Kolobova, M. Soutorine, A. Chernov, Control of phase transformations and microstructure for optimum realization of one-way and two-way shape memory effects in removable surgical clips, Mater. Des. 136 (2017) 174-184.

[50] M. Elahinia, M.N. Shayesteh, A.M. Taheri, A. Amerinatanzi, B.A. Bimber, R.F. Hamilton, Fabrication of NiTi through additive manufacturing: A review, Prog. Mater. Sci. 83 (2016) 630–663.

[51] P. Šittner, E. Iaparova, L. Kaderávek, Y. Chen, O. Tyc, Tensile deformation of NiTi shape memory alloy thermally loaded under applied stress, Mater. Des. 226 (2023) 111638.

[52] T.L. Turner, Thermomechanical Response of Shape Memory Alloy Hybrid Composites, NASA, Langley Research Center, Virginia, USA, 2001.

[53] M.W. Han, H. Rodrigue, S. Cho, S.H. Song, W. Wang, W.S. Chu, S.H. Ahn, Woven type smart soft composite for soft morphing car spoiler, Comp. Pt. B: Eng. 86 (2016) 285-298.

[54] Y. Guo, A. Klink, C. Fu, J. Snyder, Machinability and surface integrity of Nitinol shape memory alloy, CIRP Ann. 62 (2013) 83–86.

[55] J. Eaton-Evans, J.M. Dulieu-Barton, E.G. Little, I.A. Brown, Observations during mechanical testing of Nitinol, J. Mech. Eng. Sci. 222 (2008) 97–105.

[56] S.Y. Yang, G.S. Dui, Temperature analysis of one-dimensional NiTi shape memory alloys under different loading rates and boundary conditions, Int. J. Solids Struct. 50 (2013) 3254–3265.

[57] J. Laeng, Z. Xiu, X. Xu, X. Sun, H. Ru, Y. Liu, Phase formation of Ni–Ti via solid state reaction, Phys. Scr. T129 (2007) 250–254.

[58] S. Barbarino, E.I. Saavedra-Flores, R.M. Ajaj, I. Dayyani, M.I. Friswell, A review on shape memory alloys with applications to morphing aircraft, Smart Mater. Struct. 23 (2014) 063001.

[59] J. Liu, Compliant Mechanisms Using Superelastic Nitinol, MS Thesis, Pennsylvania State University, State College, PA, USA, 2012.

[60] A. Skalitzky, P. Caleb, A. Gurley, D. Beale, Woven Nitinol Fabric Strips Characterized in Tension via Finite Element Analysis and Geometric Modelling, In Proceedings of the ASME 2019 Conference on Smart Materials, Adaptive Structures and Intelligent Systems, Louisville, KY, USA, 2019.

[61] M.N. Shayesteh, Toward Patient Specific Long Lasting Metallic Implants For Mandibular Segmental Defects, MSc Thesis, University of Toledo, USA, 2015.

[62] I.V. Shishkovsky, L.T. Volova, M.V. Kuznetsov, Y.G. Morozov, I.P. Parkin, Porous biocompatible implants and tissue scaffolds synthesized by selective laser sintering from Ti and NiTi, J. Mater. Chem. 18 (2008) 1309–1317.

[63] M.T. Andani, N.S. Moghaddam, C. Haberland, D. Dean, M.J. Miller, M. Elahinia, Metals for bone implants part 1 – powder metallurgy and implant rendering, Acta Biomater. 10 (2014) 4058–4070.

[64] N.S. Moghaddam, R. Skoracki, M. Miller, M. Elahinia, D. Dean, Three dimensional printing of stiffness-tuned, nitinol skeletal fixation hardware with an example of mandibular segmental defect repair, Proc. CIRP 49 (2016) 45–50.

[65] B. O'Brien, M. Bruzzi, Shape Memory Alloys for Use in Medicine, in: P. Ducheyne (Ed.), Comprehensive Biomaterials, Elsevier, USA, 2011.

[66] D. Stoeckel, A. Pelton, T. Duerig, Self-expanding nitinol stents: material and design considerations, Eur. Radiol. 14 (2004) 292–301.

[67] G. Florian, A.R. Gabor, C.A. Nicolae, A. Rotaru, N. Stanica, N.G. Bizdoaca, P. Rotaru, Thermomechanical, calorimetric and magnetic properties of a Ni-Ti shape-memory alloy wire, J. Therm. Anal. Calorim. 140 (2020) 527–544.

[68] J.G. Fuentes, P. Gümpel, J. Strittmatter, Phase change behavior of nitinol shape memory alloys, Adv. Eng. Mater. 4 (2002) 437–452.

[69] Y. Liu, Z. Xie, Progress in Smart Materials and Structures, Nova Science Publishers, UK, 2007.

[70] Y.I. Yoo, Y.J. Kim, D.K. Shin, J.J. Lee, Development of martensite transformation kinetics of NiTi shape memory alloys under compression, Int. J. Solids Struct. 64-65 (2015) 51-61.

[71] P. Šittner, P. Sedlák, H. Seiner, P. Sedmák, J. Pilch, R. Delville, L. Heller, L. Kadeřávek, On the coupling between martensitic transformation and plasticity in NiTi: Experiments and continuum based modelling, Prog. Mater. Sci. 98 (2018) 249–298.

[72] F. Auricchio, R.L. Taylor, J. Lubliner, Shape-memory alloys: Macromodelling and numerical simulations of the superelastic behaviour, Comput. Methods Appl. Mech. Eng. 146 (1997) 281–312.

[73] X. Wang, B. Xu, Z. Yue, Phase transformation behavior of pseudoelastic NiTi shape memory alloys under large strain, J. Alloys Comp. 463 (2008) 417-422.

[74] A. Paiva, M.A. Savi, An overview of constitutive models for shape memory alloys, Math. Prob. Eng. 2006 (2006) 56876.

[75] T. Duerig, The metallurgy of Nitinol as it pertains to medical devices, in: Titanium in Medical and Dental Applications, Woodhead Publishing: Sawston, UK, 2018.

[76] N. Rebelo, M. Perry, Finite element analysis for the design of Nitinol medical devices, Minim. Invasive Ther. Allied Technol. 9 (2000) 75–80.

[77] D.K. Gara, S. Potnuru, Quandaries during numerical analysis on shape memory product, Int. J. Mech. Prod. Eng. Res. Dev. 10 (2020) 271–282.

[78] A. Zaccaria, F. Migliavacca, G. Pennati, L. Petrini, Modeling of braided stents: Comparison of geometry reconstruction and contact strategies, J. Biomech. 107 (2020) 109841.

[79] F. Auricchio, M. Conti, M. De Beule, G. De Santis, B. Verhegghe, Carotid artery stenting simulation: From patient-specific images to finite element analysis, Med. Eng. Phys. 33 (2011) 281–289.

[80] L. Derycke, D. Perrin, F. Cochennec, J.N. Albertini, S. Avril, Predictive numerical simulations of double branch stent-graft deployment in an aortic arch aneurysm, Ann. Biomed. Eng. 47 (2019) 1051–1062.

[81] F. Sturla, M. Ronzoni, M. Vitali, A. Dimasi, R. Vismara, G. Preston-Maher, G. Burriesci, E. Votta, A. Redaelli, Impact of different aortic valve calcification patterns on the outcome of transcatheter aortic valve implantation: A finite element study, J. Biomech. 49 (2016) 2520–2530.

[82] D. Gastaldi, V. Sassi, L. Petrini, M. Vedani, S. Trasatti, F. Migliavacca, Continuum damage model for bioresorbable magnesium alloy devices - Application to coronary stents, J. Mech. Behav. Biomed. Mater. 4 (2011) 352–365.

[83] M. Azaouzi, N. Lebaal, A. Makradi, S. Belouettar, Optimization based simulation of self-expanding nitinol stent, Mater. Des. 50 (2013) 917–928.

[84] L. Petrini, A. Trotta, E. Dordoni, F. Migliavacca, G. Dubini, P.V. Lawford, J.N. Gosai, D.M. Ryan, D. Testi, G. Pennati, A computational approach for the prediction of fatigue behavior in peripheral stents: Application to a clinical case, Ann. Biomed. Eng. 44 (2016) 536–547.

[85] S.Y. Yang, J. Escobar, R.J. Clifton, Computational modeling of stress-wave-induced martensitic phase transformations in NiTi, Math. Mech. Solids, 14 (2009) 220-257.

[86] P. Šittner, L. Heller, J. Pilch, C. Curfs, T. Alonso, D. Favier, Young's modulus of austenite and martensite phases in superelastic NiTi wires, J. Mater. Eng. Perform. 23 (2014) 2303–2314.

[87] J.L. Gugat, C. Bechtold, C. Chluba, E. Quandt, R.L. de Miranda, High-cycle mechanical fatigue performance of sputtered Nitinol, J. Mater. Eng. Perform. 29 (2020) 1892-1900.

[88] N. Tucker, K. Lindsey, An Introduction to Automotive Composites, Rapra Technology Limited, UK, 2002.

[89] K.E. Perry, P.E. Labossiere, E. Steffler, Measurement of deformation and strain in nitinol, Exp. Mech. 47 (2007) 373-380.

[90] A. Sengupta, P. Papadopoulos, Constitutive modeling and finite element approximation of B2-R-B19′ phase transformations in Nitinol polycrystals, Comput. Meth. Appl. Mech. Eng. 198 (2009) 3214-3227.

[91] A. Sengupta, P. Papadopoulos, R.L. Taylor, Multiscale finite element modeling of superelasticity in Nitinol polycrystals, Comput. Mech. 43 (2009) 573-584.

[92] H.S. Liu, L. Mishnaevsky, Martensitic transformations in nanostructured nitinol: Finite element modeling of grain size and distribution effects, Comput. Mater. Sci. 76 (2013) 27-36.

[93] Q. Kan, G. Kang, Constitutive model for uniaxial transformation ratchetting of superelastic NiTi shape memory alloy at room temperature, Int. J. Plast. 26 (2010) 441–465.

[94] V. Chiroiu, M. Florinel Ionescu, T. Sireteanu, R. Ioan, L. Munteanu, On intrinsic time measure in the modeling of cyclic behavior of a nitinol cubic block, Smart Mater. Struct. 24 (2015) 035022.

[95] D. Song, G. Kang, Q. Kan, C. Yu, C. Zhang, Non-proportional multiaxial transformation ratchetting of superelastic NiTi shape memory alloy: Experimental observations, Mech. Mater. 70 (2014) 94–105.

[96] I. Gibson, D. Rosen, B. Stucker, Additive Manufacturing Technologies: 3D Printing, Rapid Prototyping, and Direct Digital Manufacturing, Springer, 2014.

[97] V. Gunenthiram, P. Peyre, M. Schneider, M. Dal, F. Coste, R. Fabbro, Analysis of laser melt pool powder bed interaction during the selective laser melting of a stainless steel, J. Laser Appl. 29 (2017) 022303.

[98] X. Su, Y. Yang, Research on track overlapping during selective laser melting of powders, J. Mater. Process. Technol. 212 (2012) 2074–2079.

[99] Z. Dong, Y. Liu, W. Wen, J. Ge, J. Liang, Effect of hatch spacing on melt pool and as-built quality during selective laser melting of stainless steel: modeling and experimental approaches, Mater. 12 (2019) 50.

[100] M.H. Hong, B.K. Min, T.Y. Kwon, The influence of process parameters on the surface roughness of a 3D-printed Co–Cr dental alloy produced via selective laser melting, Appl. Sci. 6 (2016) 401.

[101] T. Peng, C. Chen, Influence of energy density on energy demand and porosity of 316L stainless steel fabricated by selective laser melting, Int. J. Precis. Eng. Manuf. Green Technol. 5 (2018) 55–62.

[102] W. Xiong, L. Hao, Y. Li, D. Tang, Q. Cui, Z. Feng, C. Yan, Effect of selective laser melting parameters on morphology, microstructure, densification and mechanical properties of supersaturated silver alloy, Mater. Des. 170 (2019) 107697.

[103] M.A. Taha, A.F. Yousef, K.A. Gany, H.A. Sabour, On selective laser melting of ultra high carbon steel: effect of scan speed and post heat treatment, Mater. Sci. Eng. Technol. 43 (2012) 913–923.

[104] J.H. Wang, J. Ren, W. Liu, X.Y. Wu, M.X. Gao, P.K. Bai, Effect of selective laser melting process parameters on microstructure and properties of Co-Cr alloy, Mater. 11 (2018).

[105] A.H. Maamoun, Y.F. Xue, M.A. Elbestawi, S.C. Veldhuis, Effect of selective laser melting process parameters on the quality of Al alloy parts: powder characterization, density, surface roughness, and dimensional accuracy, Mater. 11 (2018) 2343.

[106] L. Junfeng, W. Zhengying, Process optimization and microstructure characterization of Ti6Al4V manufactured by selective laser melting, IOP Conf. Ser. Mater. Sci. Eng. 269 (2017).

[107] M. Ma, Z. Wang, M. Gao, X. Zeng, X., Layer thickness dependence of performance in high-power selective laser melting of 1Cr18Ni9Ti stainless steel, J. Mater. Process. Technol. 215 (2015) 142–150.

[108] V. Sufiiarov, A.A. Popovich, E.V. Borisov, I.A. Polozov, D.V. Masaylo, A.V. Orlov, The effect of layer thickness at selective laser melting, Proc. Eng. 174 (2017) 126–134.

[109] X. Shi, S. Ma, C. Liu, C. Chen, Q. Wu, X. Chen, J. Lu, Performance of high layer thickness in selective laser melting of Ti6Al4V, Mater. 9 (2016) 975.

[110] J.M. Pizarro, M.M. Savalani, Effect of preheat and layer thickness on selective laser melting (SLM) of magnesium, J. Rapid Prototyp. 22 (2016) 115–122.

[111] S. Dadbakhsh, L. Hao, Effect of layer thickness in selective laser melting on microstructure of Al/5 Wt.%Fe2O3 powder consolidated parts, Sci. World J. 2014 (2014) 106129.

[112] S.A. Fatemi, J.Z. Ashany, A.J. Aghchai, A. Abolghasemi, Experimental investigation of process parameters on layer thickness and density in direct metal laser sintering: a response surface methodology approach, Virtual Phys. Prototyp., 12 (2017) 133–140.

[113] A.V. Gusarov, I. Yadroitsev, Ph. Bertrand, I. Smurov, Heat transfer modelling and stability analysis of selective laser melting, Appl. Surf. Sci. 254 (2007) 975–979.

[114] L. Bian, J. Usher, N. Shamsaei, Laser-Based Additive Manufacturing of Metal Parts: Modeling, Optimization, and Control of Mechanical Properties, Taylor & Francis Incorporated, Florida, 2017.

[115] A.V. Gusarov, I. Smurov, Modeling the interaction of laser radiation with powder bed at selective laser melting, Phys. Procedia 5 (2010) 381–394.

[116] M.R. Alkahari, T. Furumoto, T. Ueda, A. Hosokawa, Melt pool and single track formation in selective laser sintering/selective laser melting, Adv. Mater. Res. 933 (2014) 196–201.

[117] P. Yuan, D. Gu, Molten pool behaviour and its physical mechanism during selective laser melting of TiC/AlSi10Mg nanocomposites: simulation and experiments, J. Phys. Appl. Phys. 48 (2015) 035303.

[118] Y.C. Wu, C.H. San, C.H. Chang, H.J. Lin, R. Marwan, S. Baba, W.S. Hwang, Numerical modeling of melt-pool behavior in selective laser melting with random powder distribution and experimental validation, J. Mater. Process. Technol. 254 (2018) 72–78.

[119] H. Yang, J. Yang, W. Huang, Z. Wang, X. Zeng, The printability, microstructure, crystallographic features and microhardness of selective laser melted Inconel 718 thin wall, Mater. Des. 156 (2018) 407–418.

[120] J. Yang, J. Han, H. Yu, J. Yin, M. Gao, Z. Wang, X. Zeng, Role of molten pool mode on formability, microstructure and mechanical properties of selective laser melted Ti-6Al-4V alloy, Mater. Des. 110 (2016) 558–570.

[121] A. Mussatto, Re-Inforcing Nano-Particle Integration into Metal AM and Produced Part Characterisation, Dublin City University, Dublin, Ireland, 2022. Ph.D. Thesis.

[122] J.H. Tan, W.L.E. Wong, K.W. Dalgarno, An overview of powder granulometry on feedstock and part performance in the selective laser melting process, Addit. Manuf. 18 (2017) 228–255.

[123] A. Ladewig, G. Schlick, M. Fisser, V. Schulze, U. Glatzel, Influence of the shielding gas flow on the removal of process by-products in the selective laser melting process, Addit. Manuf. 10 (2016) 1–9.

[124] W. O'Neill, C.J. Sutcliffe, R. Morgan, A. Landsborough, K.K.B. Hon, Investigation on multi-layer direct metal laser sintering of 316l stainless steel powder beds, CIRP Ann. 48 (1999) 151–154.

[125] Q. Han, Y. Geng, R. Setchi, F. Lacan, D. Gu, S.L. Evans, Macro and nanoscale wear behaviour of Al-Al2O3 nanocomposites fabricated by selective laser melting, Compos. Part B Eng. 127 (2017) 26–35.

[126] T.G. Spears, S.A. Gold, In-process sensing in selective laser melting (SLM) additive manufacturing," Integrating Mater. Manuf. Innov. 5 (2016) 16-40.

[127] W. O'Neill, C.J. Sutcliffe, R. Morgan, K.K.B. Hon, Investigation of short pulse Nd: YAG laser interaction with stainless steel powder beds, Proc. Solid Free. Fabr. Symp. 9 (1998) 147–160.

[128] W.E. King, H.D. Barth, V.M. Castillo, G.F. Gallegos, J.W. Gibbs, D.E. Hahn, C. Kamath, A.M. Rubenchik, Observation of keyhole-mode laser melting in laser powder-bed fusion additive manufacturing, J. Mater. Process. Technol. 214 (2014) 2915–2925.

[129] J.P. Kruth, L. Froyen, J. Van Vaerenbergh, P. Mercelis, M. Rombouts, B. Lauwers, Selective laser melting of iron-based powder, J. Mater. Process. Technol. 149 (2004) 616–622.

[130] D. Wang, S. Wu, F. Fu, S. Mai, Y. Yang, Y. Liu, C. Song, Mechanisms and characteristics of spatter generation in SLM processing and its effect on the properties, Mater. Des. 117 (2017) 121–130.

[131] A.B. Anwar, Q.C. Pham, Study of the spatter distribution on the powder bed during selective laser melting, Addit. Manuf. 22 (2018) 86–97.

[132] M. Taheri Andani, R. Dehghani, M.R. Karamooz-Ravari, R. Mirzaeifar, J. Ni, Spatter formation in selective laser melting process using multi-laser technology, Mater. Des. 131 (2017) 460–469.

[133] M. Taheri Andani, R. Dehghani, M.R. Karamooz-Ravari, R. Mirzaeifar, J. Ni, A study on the effect of energy input on spatter particles creation during selective laser melting process, Addit. Manuf. 20 (2018) 33–43.

[134] M. Simonelli, C. Tuck, N.T. Aboulkhair, I. Maskery, I. Ashcroft, R.D. Wildman, R. Hague, A study on the laser spatter and the oxidation reactions during selective laser melting of 316L stainless steel, Al-Si10-Mg, and Ti-6Al-4V, Metall. Mater. Trans. A 46 (2015) 3842–3851.

[135] Y. Liu, Y. Yang, S. Mai, D. Wang, C. Song, Investigation into spatter behavior during selective laser melting of AISI 316L stainless steel powder, Mater. Des. 87 (2015) 797–806.

[136] V. Gunenthiram, P. Peyre, M. Schneider, M. Dal, F. Coste, I. Koutiri, R. Fabbro, Experimental analysis of spatter generation and melt-pool behavior during the powder bed laser beam melting process, J. Mater. Process. Technol. 251 (2018) 376–386.

[137] P. Konda Gokuldoss, S. Kolla, J. Eckert, Additive manufacturing processes: selective laser melting, electron beam melting and binder jetting—selection guidelines, Mater. 10 (2017) 672.

[138] M. Zavala-Arredondo, H. Ali, K.M. Groom, K. Mumtaz, Investigating the melt pool properties and thermal effects of multi-laser diode area melting, Int. J. Adv. Manuf. Technol. 97 (2018) 1383–1396.

[139] Y. Birol, Microstructural characterization of a rapidly-solidified Al-12 Wt% Si alloy," J. Mater. Sci. 31 (1996) 2139–2143.

[140] E.J. Lavernia, T.S. Srivatsan, The rapid solidification processing of materials: science, principles, technology, advances, and applications, J. Mater. Sci. 45 (2010) 287–325.

[141] T. DebRoy, H.L. Wei, J.S. Zuback, T. Mukherjee, J.W. Elmer, J.O. Milewski, A.M. Beese, A. Wilson-Heid, A. De, W. Zhang, Additive manufacturing of metallic components – process, structure and properties, Prog. Mater. Sci. 92 (2018) 112–224.

[142] J.C. Ion, Laser Processing of Engineering Materials: Principles, Procedure and Industrial Application, Elsevier, Butterworth-Heinemann, USA, 2005.

[143] S. Kou, Welding Metallurgy, John Wiley & Sons, New Jersey, USA, 2003.

[144] H. Meier, C. Haberland, Experimental studies on selective laser melting of metallic parts, Mater. Werk. 39 (2008) 665–670.

[145] C. Haberland, M. Elahinia, J.M. Walker, H. Meier, J. Frenzel, On the development of high quality NiTi shape memory and pseudoelastic parts by additive manufacturing, Smart Mater. Struct. 23 (2014) 104002.

[146] T. Bormann, B. Muller, M. Schinhammer, A. Kessler, P. Thalmann, M. de Wild, Microstructure of selective laser melted nickel-titanium, Mater. Charact. 94 (2014) 189–202.

[147] S. Dadbakhsh, M. Speirs, J.P. Kruth, J. Schrooten, J. Luyten, J.V. Humbeeck, Effect of SLM parameters on transformation temperatures of shape memory nickel titanium parts, Adv. Eng. Mater. 16 (2014) 1140–1146.

[148] S. Dadbakhsh, M. Speirs, J.P. Kruth, J. van Humbeeck, Influence of SLM on shape memory and compression behaviour of NiTi scaffolds, CIRP Ann. Manuf. Technol. 64 (2015) 209–212.

[149] I.V. Shishkovsky, I.A. Yadroitsev, I.Y. Smurov, Manufacturing three-dimensional nickel titanium articles using layer-by-layer laser-melting technology, Tech. Phy. Lett. 39 (2013) 1081–1084.

[150] S.F. Ou, B.Y. Peng, Y.C. Chen, M.H. Tsai, Manufacturing and characterization of NiTi alloy with functional properties by selective laser melting, Metals 8 (2018) 342.

[151] M. Bram, M. Bitzer, H. Buchkremer, D. Stover, Reproducibility study of NiTi parts made by metal injection molding, J. Mater. Eng. Perform. 21 (2012) 2701–2712.

[152] J. Mentz, M. Bram, H. Buchkremer, D. Stover, Improvement of mechanical properties of powder metallurgical NiTi shape memory alloys, Adv. Eng. Mater. 8 (2006) 247–252.

[153] Y. Zhao, M. Taya, Y. Kang, A. Kawasaki, Compression behavior of porous NiTi shape memory alloy, Acta Mater. 53 (2005) 337–343.

[154] K. Johansen, H. Voggenreiter, G. Eggeler, On the effect of TiC particles on the tensile properties and on the intrinsic two-way effect of NiTi shape memory alloys produced by powder metallurgy, Mater. Sci. Eng. 27 (1999) 410–414.

[155] H. Ibrahim, A.R. Jahadakbar, A. Dehghan, N.S. Moghaddam, A. Amerinatanzi, M. Elahinia, In vitro corrosion assessment of additively manufactured porous NiTi structures for bone fixation applications, Metals 8 (2018) 164.

[156] K. Kempen, L. Thijs, B. Vrancken, S. Buls, J. van Humbeeck, J.P. Kruth, Producing Crack-Free, High Density M2 HSS Parts by Selective Laser Melting: Pre-Heating the Baseplate: in Proceedings of the Solid Freeform Fabrication Symposium, Austin, TX, USA, 2013.

[157] P. Vora, K. Mumtaz, I. Todd, N. Hopkinson, AlSi12 in-situ alloy formation and residual stress reduction using anchorless selective laser melting, Addit. Manuf. 7 (2015) 12–19.

[158] P. Aggarangsi, J.L. Beuth, Localized Preheating Approaches for Reducing Residual Stress in Additive Manufacturing: in Proceedings of the Solid Freeform Fabrication Symposium, Austin, TX, USA, August 2006.

[159] T. Srivatsan, T. Sudarshan, Additive Manufacturing: Innovations, Advances, and Applications, CRC Press: Baca Raton, FL, USA, 2015.

[160] L. Machado, M. Savi, Medical applications of shape memory alloys, Braz. J. Med. Biol. Res.36 (2003) 683–691.

[161] N. Morgan, Medical shape memory alloy applications—The market and its products, Mater. Sci. Eng. 378 (2004) 16–23.

[162] ASTM F2063-05, Standard Specification for Wrought Nickel-Titanium Shape Memory Alloys for Medical Devices and Surgical Implants, ASTM International: West Conshohocken, PA, USA, 2005.

[163] T. Bormann, R. Schumacher, B. Muller, M. Mertmann, M. de Wild, Tailoring selective laser melting process parameters for NiTi implants, J. Mater. Eng. Perform. 21 (2012) 2519–2524.

[164] T. Bormann, M. de Wild, F. Beckmann, B. Muller, Assessing the Morphology of Selective Laser Melted NiTi Scaffolds for a Three-Dimensional Quantification of the One-Way Shape Memory Effect: in Proceedings of the SPIE, San Diego, CA, USA, August 2013.

[165] B. Song, X. Zhao, S. Li, C. Han, Q. Wei, S. Wen, J. Liu, Y. Shi, Differences in microstructure and properties between selective laser melting and traditional manufacturing for fabrication of metal parts: A review, Front. Mech. Eng. 10 (2015) 111–125.

[166] E.O. Olakanmi, R.F. Cochrane, K.W. Dalgarno, A review on selective laser sintering/melting (SLS/SLM) of aluminium alloy powders: Processing, microstructure, and properties, Prog. Mater. Sci. 74 (2015) 401–477.

[167] D. Gu, Laser Additive Manufacturing of High-Performance Materials, Springer: New York, NY, USA, 2015.

[168] Z.X. Khoo, J. An, C.K. Chua, Y.F. Shen, C.N. Kuo, Y. Liu, Effect of heat treatment on repetitively scanned SLM NiTi shape memory alloy, Mater. 12 (2018) 77.

[169] S. Dadbakhsh, B. Vrancken, J.P. Kruth, J. Luyten, J. van Humbeeck, Texture and anisotropy in selective laser melting of NiTi alloy, Mater. Sci. Eng. 650 (2016) 225–232.

[170] S. Saedi, A.S. Turabi, M.T. Andani, N.S. Moghaddam, M.H. Elahinia, H.E. Karaca, Texture, aging, and superelasticity of selective laser melting fabricated Ni-rich NiTi alloys, Mater. Sci. Eng. 686 (2017) 1–10.

[171] K. Wada, Y. Liu, Shape recovery of NiTi shape memory alloy under various pre-strain and constraint conditions, Smart Mater. Struct. 14 (2005) 273–286.

[172] J.M. Walker, Additive Manufacturing towards the Realization of Porous and Stiffness-Tailored NiTi Implants, Ph.D. Thesis, University of Toledo, Toledo, OH, USA, 2014.

[173] B.V. Krishna, S. Bose, A. Bandyopadhyay, Fabrication of porous NiTi shape memory alloy structures using laser engineered net shaping, J. Biomed. Mater. Res. 89 (2009) 481–490.

[174] B.V. Krishna, S. Bose, A. Bandyopadhyay, Laser processing of net-shape NiTi shape memory alloy, Phys. Metall. Mater. Sci. 38 (2007) 1096–1103.

[175] E. Olakanmi, R. Cochrane, K. Dalgarno, Densification mechanism and microstructural evolution in selective laser sintering of Al–12Si powders, J. Mater. Process. Technol. 211 (2011) 113–121.

[176] J.J. Marattukalam, A.K. Singh, S. Datta, M. Das, V.K. Balla, S. Bontha, S.K. Kalpathya, Microstructure and corrosion behavior of laser processed NiTi alloy, Mater. Sci. Eng. 57 (2015) 309–313.

[177] T.I. Hsu, C.M. Wei, L.D. Wu, Y.P. Li, A. Chiba, M.H. Tsai, Nitinol powders generate from plasma rotation electrode process provide clean powder for biomedical devices used with suitable size, spheroid surface and pure composition, Sci. Rep. 8 (2018) 13776.

[178] R.H. Morgan, A.J. Papworth, C. Sutcliffe, P. Fox, W. O'Neill, High density net shape components by direct laser re-melting of single-phase powders, J. Mater. Sci. 37 (2002) 3093–3100.

[179] M.T. Andani, C. Haberland, J. Walker, M. Elahinia, An Investigation of Effective Process Parameters on Phase Transformation Temperature of Nitinol Manufactured by Selective Laser Melting: in Proceedings of the ASME Conference on Smart Materials, Adaptive Structures and Intelligent Systems, Newport, RI, USA, September 2014.

[180] M. Speirs, X. Wang, S. Van Baelen, A. Ahadi, S. Dadbakhsh, J.-P. Kruth, J. VanHumbeeck, On the transformation behavior of NiTi shape-memory alloy produced by SLM, Shape Mem. Superelast. 2 (2016) 310–316.

[181] M.T. Andani, Modeling, Simulation, Additive Manufacturing, and Experimental Evaluation of Solid and Porous NiTi, Ph.D. thesis, University of Toledo, Toledo, OH, USA, 2015.

[182] X. Wang, J. Yu, J. Liu, L. Chen, Q. Yang, H. Wei, J. Sun, Z. Wang, Z. Zhang, G. Zhao, J. Van Humbeeck, Effect of process parameters on the phase transformation behavior and tensile properties of NiTi shape memory alloys fabricated by selective laser melting, Addit. Manuf. 36 (2020) 101545.

[183] X. Wang, M. Speirs, S. Kustov, B. Vrancken, X. Li, J.-P. Kruth, J. Van Humbeeck, Selective laser melting produced layer-structured NiTi shape memory alloys with high damping properties and Elinvar effect, Scr. Mater. 146 (2018) 246–250.

[184] N. Eliaz, Corrosion of metallic biomaterials: A review, Mater. 12 (2019) 407.

[185] C. Ma, M.T. Andani, H. Qin, N.S. Moghaddam, H. Ibrahim, A. Jahadakbar, A. Amerinatanzi, Z. Ren, H. Zhang, G.L. Doll, Improving surface fifinish and wear resistance of additive manufactured nickel-titanium by ultrasonic nano-crystal surface modifification, J. Mater. Process. Technol. 249 (2017) 433–440.

[186] C.W. Chan, H.C. Man, Laser welding of thin foil nickel-titanium shape memory alloy, Opt. Lasers Eng. 49 (2011) 121–126.

[187] Z.G. Karaji, M. Speirs, S. Dadbakhsh, J.P. Kruth, H. Weinans, A.A. Zadpoor, S.A. Yavari, Additively manufactured and surface biofunctionalized porous nitinol, ACS Appl. Mater. Interfaces 9 (2016) 1293–1304.

[188] H.C. Man, Z.D. Cui, T.M. Yue, Corrosion properties of laser surface melted NiTi shape memory alloy, Scr. Mater. 45 (2001) 1447–1453.

[189] D. Landolt, Corrosion and Surface Chemistry of Metals, CRC Press: Baca Raton, FL, USA, 2007.

[190] Y. Hedberg, M.E. Karlsson, E. Blomberg, I.O. Wallinder, J. Hedberg, Correlation between surface physicochemical properties and the release of iron from stainless steel AISI 304 in biological media, Colloids Surf. B Biointerfaces 122 (2014) 216–222.

[191] F. Wedian, M.A. Al-Qudah, A.N. Abu-Baker, The effect of Capparis spinosa L. extract as a green inhibitor on the corrosion rate of copper in a strong alkaline solution, Port. Electrochim. Acta 34 (2016) 39–51.

[192] S.A. Rizvi, T.I. Khan, A novel fabrication method for Nitinol shape memory alloys, Key Eng. Mater. 442 (2010) 309–315.

[193] H. Meier, C. Haberland, J. Frenzel, R. Zarnetta, Selective Laser Melting of NiTi Shape Memory Components: in Proceedings of the International Conference on Advanced Research in Virtual and Rapid Prototyping, Leiria, Portugal, October 2009.

[194] S. Shiva, I.A. Palani, S.K. Mishra, C.P. Paul, L.M. Kukreja, Investigations on the influence of composition in the development of Ni–Ti shape memory alloy using laser based additive manufacturing, Opt. Laser Technol. 69 (2015) 44–51.

[195] L. Kalman, I. Meszaros, Analysis of a NiTi shape memory alloy, Mater. Sci. Forum 812 (2015) 89–93.

[196] W. Tang, Z. Sandstrom, G. Wei, S. Miyazaki, Experimental investigation and thermodynamic calculation of the Ti-Ni-Cu shape memory alloys, Metall. Mater. Trans. A 31 (2000) 2423–2430.

[197] T. Habijan, C. Haberland, H. Meier, J. Frenzel, J. Wittsiepe, C. Wuwer, C. Greulich, T.A. Schildhauer, M. Köller, The biocompatibility of dense and porous nickel–titanium produced by selective laser melting, Mater. Sci. Eng. C 33 (2013) 419–426.

[198] J. Frenzel, E.P. George, A. Dlouhy, Ch. Somsen, M.F.X. Wagner, G. Eggeler, Influence of Ni on martensitic phase transformations in NiTi shape memory alloys, Acta Mater. 58 (2010) 3444–3458.

[199] C. Haberland, M. Elahinia, J. Walker, H. Meier, Visions, Concepts and Strategies for Smart Nitinol Actuators and Complex Nitinol Structures Produced by Additive Manufacturing: in Proceedings of the ASME Conference on Smart Materials, Adaptive Structures and Intelligent Systems—SMASIS 2013, Snowbird, UT, USA, September 2013.

[200] M.H. Elahinia, Shape Memory Alloy Actuators: Design, Fabrication, and Experimental Evaluation, John Wiley & Sons: New York, NY, USA, 2015.

[201] S. Saedi, A.S. Turabi, M.T. Andani, C. Haberland, H. Karaca, M. Elahinia, The inflfluence of heat treatment on the thermomechanical response of Ni-rich NiTi alloys manufactured by selective laser melting, J. Alloy Compd. 677 (2016) 204–210.

[202] J. Frenzel, Z. Zhang, C. Somsen, K. Neuking, G. Eggeler, Influence of carbon on martensitic phase transformations in NiTi shape memory alloys, Acta Mater. 55 (2007) 1331–1341.

[203] G.S. Firstov, R.G. Vitchev, H. Kumar, B. Blanpain, J.V. Humbeeck, Surface oxidation of NiTi shape memory alloy, Biomater. 23 (2002) 4863–4871.

[204] C.G. Slough, A Study of the Nitinol Solid-Solid Transition by DSC, TA Instruments: New Castle, DE, USA, 2007.

[205] C. Haberland, H. Meier, J. Frenzel, On the Properties of Ni-rich NiTi Shape Memory Parts Produced by Selective Laser Melting: in Proceedings of the ASME Conference on Smart Materials, Adaptive Structures and Intelligent Systems, Stone Mountain, GA, USA, September 2012.

[206] J. Mohd-Jani, M. Leary, A. Subic, M.A. Gibson, A review of shape memory alloy research, applications and opportunities, Mater. Des. 56 (2014) 1078–1113.

[207] X. Zhou, X. Liu, D. Zhang, Z. Shen, W. Liu, Balling phenomena in selective laser melted tungsten, J. Mater. Process. Technol. 222 (2015) 33–42.

[208] D. Gu, Y. Shen, Balling phenomena in direct laser sintering of stainless steel powder: metallurgical mechanisms and control methods, Mater. Des. 30 (2009) 2903–2910.

[209] R. Li, J. Liu, Y. Shi, L. Wang, W. Jiang, Balling behavior of stainless steel and nickel powder during selective laser melting process, Int. J. Adv. Manuf. Technol. 59 (2012) 1025–1035.

[210] C. Körner, E. Attar, P. Heinl, Mesoscopic simulation of selective beam melting processes, J. Mater. Process. Technol. 211 (2011) 978–987.

[211] D. Zhang, S. Sun, D. Qiu, M.A. Gibson, M.S. Dargusch, M. Brandt, M. Qian, M. Easton, Metal alloys for fusion-based additive manufacturing, Adv. Eng. Mater. 20 (2018) 1700952.

[212] J. Walker, M.T. Andani, C. Haberland, M. Elahinia, Additive Manufacturing of Nitinol Shape Memory Alloys to Overcome Challenges in Conventional Nitinol Fabrication: in Proceedings of the ASME International Mechanical Engineering Congress and Exposition, Montreal, QC, Canada, November 2014.

[213] M.T. Andani, C. Haberland, J.M. Walker, M. Karamooz, A.S. Turabi, S. Saedi, R. Rahmanian, H. Karaca, D. Dean, M. Kadkhodaei, M. Elahinia, Achieving biocompatible stiffness in NiTi through additive manufacturing, J. Intell. Mater. Syst. Struct. 27 (2016) 2661–2671.

[214] S.M. Yusuf, N. Gao, Influence of energy density on metallurgy and properties in metal additive manufacturing, Mater. Sci. Technol. 33 (2017) 1269–1289.

[215] C.Y. Yap, C.K. Chua, Z.L. Dong, Z.H. Liu, D.Q. Zhang, L.E. Loh, S.L. Sing, Review of selective laser melting: Materials and applications, Appl. Phys. Rev. 2 (2015) 041101.

[216] R. Li, J. Liu, Y. Shi, L. Wang, W. Jiang, Balling behavior of stainless steel and nickel powder during selective laser melting process, Int. J. Adv. Manuf. Technol. 59 (2012) 1025–1035.

[217] A.E. Patterson, S.L. Messimer, P.A. Farrington, Overhanging features and the SLM/DMLS residual stresses problem: Review and future research need, Technol. 5 (2017) 15.

[218] Y. Yang, Y. Huang, W. Wu, One-Step Shaping of NiTi Biomaterial by Selective Laser Melting, Photonics Asia, International Society for Optics and Photonics, Bellingham, WA, USA, 2007.

[219] R.F. Hamilton, T.A. Palmer, B.A. Bimber, Spatial characterization of the thermal-induced phase transformation throughout as-deposited additive manufactured NiTi bulk builds, Scr. Mater. 101 (2015) 56–59.

[220] S. Li, H. Hassanin, M.M. Attallah, N.J.E. Adkins, K. Essa, The development of TiNi- based negative Poisson's ratio structure using selective laser melting, Acta Mater. 105 (2016) 75–83.

[221] Confluent, Material Data Sheet: Superelastic Nitinol Alloys, Confluent Medical Technologies: Fremont, CA, USA, 2020.

[222] P. Filip, K. Mazanec, Influence of work hardening on the reactive stress in a TiNi shape memory alloy, Mater. Sci. Eng. A A174 (1994) L41–L43.

[223] Ulbrich, Nitinol Data Sheet, Ulbrich Stainless Steels and Special Metals Inc., North Haven, CT, USA, 2020.

[224] D.E. Hodgson, R.J. Biermann, Properties and Selection: Nonferrous Alloys and Special-Purpose Materials, ASM International: Almere, Netherlands, 1990.

[225] Y. Liu, H. Xiang, Apparent modulus of elasticity of near-equiatomic NiTi, J. Alloys Comp. 270 (1998) 154–159.

[226] M.J. Mahtabi, N. Shamsaei, M.R. Mitchell, Fatigue of Nitinol: The state-of-the-art and ongoing challenges, J. Mech. Behav. Biomed. Mater. 50 (2015) 228–254.

[227] F. Nematzadeh, S.K. Sadrnezhaad, Effects of material properties on mechanical performance of Nitinol stent designed for femoral artery: Finite element analysis, Sci. Iran. 19 (2012) 1564–1571.

[228] A. Eshghinejad, Finite Element Study of a Shape Memory Alloy Bone Implant, MS Thesis, University of Toledo, Toledo, OH, USA, 2012.

[229] D.C. Lagoudas, Shape Memory Alloys: Modeling and Engineering Applications, Springer: New York, NY, USA, 2008.

[230] H. Qian, H.N. Li, G.A. Song, Constitutive Model of Shape Memory Alloys with Consideration of Martensitic Hardening Effect: in Proceedings of the 11th Aerospace Division International Conference on Engineering, Science, Construction, and Operations in Challenging Environments, Long Beach, CA, USA, March 2008.

[231] P. Theriault, P. Terriault, V. Brailovski, R. Gallo, Finite element modeling of a progressively expanding shape memory stent, J. Biomech. 39 (2006) 2837–2844.

[232] I.B. Naceur, A. Charfi, T. Bouraoui, K. Elleuch, Finite element modeling of superelastic nickel-titanium orthodontic wires, J. Biomech. 47 (2014) 3630–3638.

[233] D. Mazzaccaro, F. Berti, L. Antonini, G. Pennati, L. Petrini, F. Migliavacca, G. Nano, Biomechanical interpretation of observed fatigue fractures of peripheral Nitinol stents in the superficial femoral arteries through in silico modelling, Med. Hypotheses 142 (2020) 109771.

[234] S. Hazar, W. Zaki, Z. Moumni, G. Anlas, Modeling of steady-state crack growth in shape memory alloys using a stationary method, Int. J. Plast. 67 (2015) 26–38.

[235] X.M. Wang, Y.F. Wang, Z.Z. Lu, C.H. Deng, Z.F. Yue, An experimental study of the superelastic behavior in NiTi shape memory alloys under biaxial proportional and non-proportional cyclic loadings, Mech. Mater. 42 (2010) 365–373.

[236] F. Auricchio, G. Scalet, M. Urbano, A numerical/experimental study of Nitinol actuator springs, J. Mater. Eng. Perform. 23 (2014) 2420–2428.

[237] N. Kelly, D.J. McGrath, C.A. Sweeney, K. Kurtenbach, J.A. Grogan, S. Jockenhoevel, B.J. O'Brien, M. Bruzzi, P.E. McHugh, Comparison of computational modelling techniques for braided stent analysis, Comput. Methods Biomech. Biomed. Eng. 22 (2019) 1334–1344.

[238] M.J. Mahtabi, N. Shamsaei, Fatigue modeling for superelastic NiTi considering cyclic deformation and load ratio effects, Shape Mem. Superelast. 3 (2017) 250–263.

[239] R.N. Ghriallais, M. Bruzzi, Self-expanding stent modelling and radial force accuracy, Comput. Methods Biomech. Biomed. Eng. 17 (2014) 318–333.

[240] B. Huang, W. Pu, H. Zhang, H. Wang, G. Song, A phenomenological model for superelastic shape memory alloy helical springs, Adv. Struct. Eng. 18 (2015) 1345–1354.

[241] S. Major, M. Hubalovska, Using of finite element method and computational analysis of mechanical properties of stent-grafts, Int. J. Mech. 9 (2015) 319–322.

[242] L.C. Brinson, One dimensional constitutive behavior of shape memory alloys: Thermomechanical derivation with non-constant material functions and redefined martensite internal variable, J. Intell. Mater. Syst. Struct. 4 (1993) 229–242.

[243] A. Kumar, Comprehensive Modeling of Shape Memory Alloys for Actuation of Large-Scale Structures, Ph.D. Thesis, University of Akron, Akron, OH, USA, 2010.

[244] M. Huang, X. Gao, L.C. Brinson, Multivariant micromechanical model for SMAs, Part 2 - Polycrystal model, Int. J. Plast. 16 (2000) 1371–1390.

[245] E. Patoor, D.C. Lagoudas, P.B. Entchev, L.C. Brinson, X. Gao, Shape memory alloys. Part I: General properties and modeling of single crystals, Mech. Mater. 38 (2006) 391–429.

[246] V.I. Levitas, I.B. Ozsoy, Micromechanical modeling of stress-induced phase transformations, Part 1 - Thermodynamics and kinetics of coupled interface propagation and reorientation, Int. J. Plast. 25 (2009) 239–280.

[247] C. Dumoulin, B. Cochelin, Mechanical behavior modeling of balloon-expandable stents, J. Biomech. 33 (2000) 1461–1470.

[248] F. Etave, G. Finet, M. Boivin, J.C. Boyer, G. Rioufol, G. Thollet, Mechanical properties of coronary stents determined by using finite element analysis, J. Biomech. 34 (2001) 1065–1075.

[249] X. Gao, L. Brinson, A simplified multivariant SMA model based on invariant plane nature of martensitic transformation, J. Intell. Mater. Syst. Struct. 13 (2002) 795–810.

[250] F. Marketz, F.D. Fischer, Modelling the mechanical behavior of shape memory alloys under variant coalescence, Comput. Mater. Sci. 5 (1996) 210–226.

[251] D.G. Majo, R.J. Paterson, R.V. Curtis, R. Saidb, R.D. Wood, J. Bonet, Optimisation of the superplastic forming of a dental implant for bone augmentation using finite element simulations, Dent. Mater. 20 (2004) 409–418.

[252] A.P. Stebner, S.C. Vogel, R.D. Noebe, T.A. Sisneros, B. Clausen, D.W. Brown, Micromechanical quantification of elastic, twinning, and slip strain partitioning

exhibited by polycrystalline, monoclinic nickel–titanium during large uniaxial deformations measured via in-situ neutron diffraction, J. Mech. Phys. Solids 62 (2013) 2302–2330.

[253] M.L. Young, M.F.X. Wagner, J. Frenzel, W.W. Schmahl, G. Eggeler, Phase volume fractions and strain measurements in an ultrafine-grained NiTi shape-memory alloy during tensile loading, Acta Mater. 58 (2010) 2344–2354.

[254] L.C. Brinson, I. Schmidt, R. Lammering, Stress-induced transformation behavior of a polycrystalline NiTi shape memory alloy: Micro and micromechanical investigations via in situ optical microscopy, J. Mech. Phys. Solids 52 (2004) 1549–1571.

[255] P. Sedmák, P. Šittner, J. Pilch, C. Curfs, Instability of cyclic superelastic deformation of NiTi investigated by synchrotron x-ray diffraction, Acta Mater. 94 (2015) 257–270.

[256] S. Cai, J.E. Schaffer, C. Yu, Y. Daymond Ren, Evolution of intergranular stresses in a martensitic and an austenitic NiTi wire during loading-unloading tensile deformation metallurgical and material transactions, Metall. Mater. Trans. A 46 (2015) 2479–2490.

[257] P. Sedmák, J. Pilch, L. Heller, J. Kopeček, J. Wright, P. Sedlák, Grain-resolved analysis of localized deformation in nickel-titanium wire under tensile load, Sci. 353 (2016) 559–562.

[258] H.M. Paranjape, P.P. Paul, H. Sharma, P. Kenesei, J.S. Park, T.W. Duerig, Influences of granular constraints and surface effects on the heterogeneity of elastic, superelastic, and plastic responses of polycrystalline shape memory alloys, J. Mech. Phys. Solids 102 (2017) 46–66.

[259] J.G. Boyd, D.C. Lagoudas, A thermodynamical constitutive model for shape memory materials, Part I - The monolithic shape memory alloy, Int. J. Plast. 12 (1996) 805–842.

[260] M. Huang, L. Brinson, A multivariant model for single crystal SMA behavior, J. Mech. Phys. Solids 46 (1998) 1379–1409.

[261] J.G. Boyd, D.C. Lagoudas, Constitutive Model for Simultaneous Transformation and Reorientation in Shape Memory Materials: in Mechanics of Phase Transformation and Shape Memory Alloys, ASME Conference: Chicago, IL, USA, 1994.

[262] X. Liu, G. Liu, P. Ye, Q. Luo, Z. Chang, Investigation of mechanical behaviors and improved design of V-shaped braid stents, Proc. Inst. Mech. Eng. Part H J. Eng. Med. 236 (2022) 547–556.

[263] X. Jiang, B. Li, Finite element analysis of a superelastic shape memory alloy considering the effect of plasticity, J. Theor. Appl. Mech. 55 (2017) 1355–1368.

[264] T.W. Duerig, A.R. Pelton, K. Bhattacharya, The measurement and interpretation of transformation temperatures in nitinol, Shape Mem. Superelast. 3 (2017) 485–498.

[265] T.R.K. Dora, R. Goud, A. Sahadevan, A.H. Chand, R. Jha, P.S. De, R.S. Kottada, N. Nayan, S. Gollapudi, Investigations into sample geometry effects on the superelastic and fatigue behavior of Nitinol: Modeling and experiments, Mater. 20 (2021) 101256.

[266] L. Petrini, A. Bertini, A three-dimensional phenomenological model describing cyclic behavior of shape memory alloys, Int. J. Plast. 125 (2020) 348–373.

[267] D.J. Hartl, D.C. Lagoudas, Analysis of Simultaneous Transformation and Plastic Deformation in Shape Memory Alloys: in Proceedings of the 19th International Conference on Adaptive Structures and Technologies, Ascona, Switzerland, October, 2008.

[268] L. Gibson, M. Ashby, Cellular Solids: Structure and Properties, Cambridge University Press: Cambridge, UK, 1997.

[269] G. Helbert, L. Dieng, S. Arnab Chirani, L. Saint-Sulpice, T. Lecompte, S. Calloch, P. Pilvin, Investigation of NiTi based damper effects in bridge cables vibration response: Damping capacity and stiffness changes, Eng. Struct. 165 (2018) 184–197.

[270] A. Gullu, J.O. Danquah, S. Dilibal, Characterization of energy dissipative cushions made of Ni-Ti shape memory alloy, Smart Mater. Struct. 31 (2022) 015018.

[271] M.K. Gupta, A. Shankhdhar, A. Kumar, A. Vermon, A.K. Singh, V. Panwar, Temperature and strain rate dependent stress-strain behaviour of Nitinol, Mater. Today Proc. 43 (2020) 395–399.

[272] E. Farber, A. Orlov, A. Popovich, Effect of Lattice Structures Topology on the Properties of the TiNi Alloy: Computer Simulation: in Proceedings of the Metal 2021, 30th Anniversary International Conference on Metallurgy and Materials, Brno, Czech Republic, May 2021.

[273] S. Rajoriya, S. Mishra, Size, length, temperature and loading range effects on deformation response of NiTi SMA wire: An analytical study, Innov. Infrastruct. Solut. 7 (2022) 217.

[274] X. Zhang, L. Wei, Processing and damping capacity of NiTi foams with laminated pore architecture, J. Mech. Behav. Biomed. Mater. 96 (2019) 108–117.

[275] J. Ma, B. Franco, G. Tapia, K. Karayagiz, L. Johnson, J. Liu, R. Arróyave, I. Karaman, A. Elwany, Spatial control of functional response in 4d-printed active metallic structures, Sci. Rep. 7 (2017) 46707.

[276] S. Saedi, M.N. Shayesteh, A. Amerinatanzi, M. Elahinia, H.E. Karaca, On the effects of selective laser melting process parameters on microstructure and thermomechanical response of Ni-rich NiTi, Acta Mater. 144 (2018) 552–560.

[277] J. Walker, M. Elahinia, C. Haberland, An Investigation of Process Parameters on Selective Laser Melting of Nitinol, ASME 2013 Conference on Smart Materials, Adaptive Structures and Intelligent Systems, 2013.

[278] H. Meier, C. Haberland, J. Frenzel, Structural and Functional Properties of NiTi Shape Memory Alloys Produced by Selective Laser Melting, Innovative Developments in Virtual and Physical Prototyping – Proceedings of the 5th International Conference on Advanced Research in Virtual and Rapid Prototyping, 2012.

[279] S. Das, Physical aspects of process control in selective laser sintering of metals, Adv. Eng. Mater. 5 (2003) 701–711.

[280] A. Sola, A. Nouri, Microstructural porosity in additive manufacturing: The formation and detection of pores in metal parts fabricated by powder bed fusion, J. Adv. Manuf. Process. 1 (2019) 10021.

[281] X. Zhao, D. Gu, C. Ma, L. Xi, H. Zhang, Microstructure characteristics and its formation mechanism of selective laser melting SiC reinforced Al-based composites, Vacuum 160 (2019) 189–196.

[282] S.V. Chernyshikhin, D.G. Firsov, I.V. Shishkovsky, Selective laser melting of pre-alloyed NiTi powder: Single-track study and FE modeling with heat source calibration, Mater. 14 (2021) 7486.

[283] J.Y. Lee, S.H. Ko, D.F. Farson, C.D. Yoo, Mechanism of keyhole formation and stability in stationary laser welding, J. Phys. D: Appl. Phys. 35 (2002) 1570–1576.

[284] X. He, J.T. Norris, P.W. Fuerschbach, T. Debroy, Liquid metal expulsion during laser spot welding of 304 stainless steel, J. Phys. D: Appl. Phys. 39 (2006) 525–534.

[285] J.N. Zhu, E. Borisov, X. Liang, E. Farber, M.J.M. Hermans, V.A. Popovich, Predictive analytical modelling and experimental validation of processing maps in additive manufacturing of nitinol alloys, Addit. Manuf. 38 (2021), 101802.

[286] K.A. Mumtaz, N. Hopkinson, Selective laser melting of thin wall parts using pulse shaping, J. Mater. Process. Technol. 210 (2010) 279–287.

[287] Memry SAES Group Corporation, Introduction to Nitinol. https://www.memry.com/intro-to-nitinol/, 2017 (accessed 30 July 2021).

[288] K.M. Horvay, C.T. Schade, Development of Nitinol Alloys for Additive Manufacturing, Materials Science and Technology (MS&T18), Columbus, Ohio, USA, 2018.

[289] A. Chmielewska, B. Wysocki, J. Buhagiar, B. Michalski, B. Adamczyk-Cieślak, M. Gloc, W. Święszkowski, In situ alloying of NiTi: Influence of laser powder bed fusion (LBPF) scanning strategy on chemical composition, Mater. Today Commun. 30 (2022), 103007.

[290] S.F. Madlul, A.N. Abd, H.M. Miklif, Phase investigation of nitinol sma according to melting method, NeuroQuantology 18 (2020) 73–76.

[291] I. Müller, S. Seelecke, Thermodynamic aspects of shape memory alloys, Math. Comput. Model. 34 (2001) 1307–1355.

[292] W.B. Cross, A.H. Kariotis, F.J. Stimler, Nitinol Charaterization Study, NASA CR-1433, Ohio, USA, 1969.

[293] G. Florian, R. Gabor, C.A. Nicolae, A. Rotaru, C. Marinescu, G. Iacobescu, N. Stanica, S. Degeratu, O. Gingu, P. Rotaru, Physical and thermophysical properties of a commercial Ni–Ti shape memory alloy strip, J. Therm. Anal. Calorim. 138 (2019) 2103-2122.

[294] K. Parlinski, M. Parlinska-Wojtan, Lattice dynamics of NiTi austenite, martensite, and R phase, Phys. Rev. B 66 (2002) 064307.

[295] M. Kubenova, Processing and Martensitic Transformations of NiTi-Based Alloys, PhD Thesis, BRNO University of Technology, Czech Republic, 2014.

[296] T. Duerig, K. Bhattacharya, The influence of the R-phase on the superelastic behavior of NiTi, Shap. Mem. Superelast. 1 (2015) 153–161.

[297] T. Tamiya, D. Shindo, Y. Murakami, Y. Bando, K. Otsuka, In-situ observations of R-phase transformation in a Ti50Ni48Fe2 alloy by electron microscopy, Mater. Trans. 39 (1998) 714–723.

[298] X.B. Wang, S. Kustor, J.V. Humbeeck, A short review on the microstructure, transformation behavior and functional properties of NiTi shape memory alloys fabricated by selective laser melting, Mater. 11 (2018) 1683.

[299] K. Safaei, M. Nematollahi, P. Bayati, F. Kordizadeh, M.T. Andani, H. Abedi, B. Poorganji, M. Elahinia, On the crystallographic texture and torsional behavior of NiTi shape memory alloy processed by laser powder bed fusion: Effect of build orientation, Addit. Manuf. 59 (2022) 103184.

[300] K. Wada, Y. Liu, Shape recovery of NiTi shape memory alloy under various pre-strain and constraint conditions, Smart Mater. Struct. 14 (2005) 273–286.

[301] S. Dilibal, Investigation of nucleation and growth of detwinning mechanism in martensitic single crystal NiTi using digital image correlation, Metallogr. Microstruct. Anal. 2 (2013) 242–248.

[302] X. Gu, Y. Zhang, Y. You, X. Ju, J. Zhu, Z. Moumni, W. Zhang, Evolution of transformation characteristics of shape memory alloys during cyclic loading: transformation temperature hysteresis and residual martensite, Smart Mater. Struct. 29 (2020) 095011.

[303] Y. Liu, Z. Xie, J. Van Humbeeck, L. Delaey, Some results on the detwinning process in NiTi shape memory alloys, Scr. Mater. 41 (1999) 1273-1281.

[304] A. Saigal, M. Fonte, Solid, shape recovered "bulk" Nitinol: Part I—Tension–compression asymmetry, Mater. Sci. Eng. A 528 (2011) 5536-5550.

[305] Y. Liu, Z.L. Xie, Twinning and detwinning of ⟨0 1 1⟩ type II twin in shape memory alloy, Acta Mater. 51 (2003) 5529-5543.

[306] M. Nishida, S. Ii, K. Kitamura, T. Furukawa, A. Chiba, T. Hara, K. Hiraga, New deformation twinning mode of B19' martensite in Ti-Ni shape memory alloy, Scr. Mater. 39 (1998) 1749-1754.

[307] C.A. Biffi, J. Fiocchi, F. Valenza, P. Bassani, A. Tuissi, Selective laser melting of NiTi shape memory alloy: processability, microstructure, and superelasticity, Shap. Mem. Superelast. 6 (2020) 342–353.

[308] Y. Liu, Influence of Plasticity on Transformation Behaviour of Martensite in NiTi, IUTAM Symposium on Mechanics of Martensitic Phase Transformation in Solids. Solid Mechanics and Its Applications, Springer, Dordrecht, 2002.

[309] D.J. Hartl, D.C. Lagoudas, Simultaneous Transformation and Plastic Deformation in Shape Memory Alloys, Behavior and Mechanics of Multifunctional and Composite Materials 2008, San Diego, California, USA, 2008.

[310] Z. Shilei, Z. Kun, W. Fuwen, Microstructure and phase transition characteristics of NiTi shape memory alloy, J. Phys. Conf. Ser. 1653 (2020) 012045.

[311] G.D. Sandrock, R.F. Hehemann, The observation of surface relief during the martensitic transformation in TiNi, Metallogr. 4 (1971) 451-456.

[312] B.W. Levinger, Lattice parameters of beta titanium at room temperature, J. Metal. 5 (1953) 195 - 195.

[313] P. Jamshidi, C. Panwisawas, E. Langi, S.C. Cox, J. Feng, L. Zhao, M.M. Attallah, Development, characterisation, and modelling of processability of nitinol stents using laser powder bed fusion, J. Alloys Compd. 909 (2022) 164681.

[314] E. Farber, J.N. Zhu, A. Popovich, V. Popovich, A review of NiTi shape memory alloy as a smart material produced by additive manufacturing, Mater. Today Proc. 30 (2019) 761–767.

[315] M.C.C. Monu, E.J. Ekoi, C. Hughes, S. Kumar S., D. Brabazon, Resultant physical properties of as-built nitinol processed at specific volumetric energy densities and correlation with in-situ melt pool temperatures, J. Mater. Res. Technol. 21 (2022) 2757–2777.

[316] S. Kumar S, L. Marandi, V.K. Balla, S. Bysakh, D. Piorunek, G. Eggeler, M. Das, I. Sen, Microstructure – property correlations for additively manufactured NiTi based shape memory alloys, Mater. 8 (2019) 100456.

[317] E. Schuller, M. Bram, H.P. Buchkremer, D. Stover, Phase transformation temperatures for NiTi alloys prepared by powder metallurgical processes, Mater. Sci. Eng. A Struct. Mater. Prop. Microstruct. Process. 378 (2004) 165–169.

[318] K. Otsuka, C.M. Wayman, Shape Memory Materials, Cambridge University Press, Cambridge, UK, 1999.

[319] D. Xue, P. Balachandran, J. Hogden, J. Theiler, D. Xue, T. Lookman. Accelerated search for materials with targeted properties by adaptive design. Nat. Commun. 7 (2016) 11241.

[320] B.C. Zhang, J. Chen, C. Codder, Microstructure and transformation behavior of in-situ shape memory alloys by selective laser melting Ti-Ni mixed powder, J. Mater. Sci. Technol. 29 (2013) 863–867.

[321] S. Li, H. Hassanin, M.M. Attallah, N.J.E. Adkins, K. Essa, The development of TiNi- based negative Poisson's ratio structure using selective laser melting, Acta Mater. 105 (2016) 75–83.

[322] I. Okulov, H. Wendrock, A. Volegov, H. Attar, High strength beta titanium alloys: new design approach, Mater. Sci. Eng. A 628 (2015) 297-302.

[323] S. Kumar S, I.A. Kumar, L. Marandi, I. Sen, Assessment of small-scale deformation characteristics and stress-strain behavior of NiTi based shape memory alloy using nanoindentation, Acta Mater. 201 (2020) 303–315.

[324] S. Kumar S, A.C. Arohi, I. Sen, A Review on Micro-mechanical Testing of NiTi-Based Shape Memory Alloys, J. Indian Inst. Sci. 102 (2022) 211–235.

[325] I. Sen, S. Kumar S, Characterizing Stress-Strain Behavior of Materials through Nanoindentation, Elasticity of Materials, Intech, 2021.

[326] M.A. Obeidi, Achieving high quality nitinol parts with minimised input thermal energy by optimised pulse wave laser powder bed fusion process, Res. Mater. 14 (2022) 100279.

[327] G.M. Pharr, An improved technique for determining hardness and elastic modulus using load and displacement sensing indentation experiments, J. Mater. Res. 7 (1992) 1564–1583.

[328] J.I. Qazi, J. Rahim, O.N. Senkov, F. H. Froes, Phase transformations in the Ti-6Al-4V-H system, J. Metals 54 (2002) 68-71.

[329] M. Radovic, E. Lara-Curzio, L. Riester, Comparison of different experimental techniques for determination of elastic properties of solids, Mater. Sci. Eng. A 368 (2004) 56-70.

[330] C.J. De Araújo, N.J. Da Silva, M.M. Da Silva, C.H. Gonzalez, A comparative study of Ni-Ti and Ni-Ti-Cu shape memory alloy processed by plasma melting and injection molding, Mater. Des. 32 (2011) 4925–4930.

[331] E. Brandl, A. Schoberth, C. Leyens, Morphology, microstructure, and hardness of titanium (Ti-6Al-4V) blocks deposited by wire-feed additive layer manufacturing (ALM), Mater. Sci. Eng. A. 532 (2012) 295–307.

[332] G. Lutjering, J.C. Williams, Titanium, Second Ed., Springer, 2019.

[333] P. Nath, L. Marandi, I. Sen, Processing-microstructure-property correlation in thermo-mechanically processed Ti-6Al-4V alloys: A comparative study between conventional and novel approaches, J. Alloys Compd. 927 (2022) 167039.

Appendix A

Differences between the published paper and Chapter 2:

1. To improve readability of the thesis and avoid recurrence of information, the introduction section of Chapter 2 was accommodated in Chapter 1, sections – 1.4.2, 1.4.3, 1.4.4 and 1.10.
2. Details regarding adaptive meshing were added in section 2.2.4.
3. Details regarding the selection of porous designs and porosity levels were added in section 2.2.4.
4. Details regarding RVE requirements were added in section 2.2.4.
5. In section 2.2.5, the term "non-convergent" was changed to "insufficient-convergence."

Differences between the published paper and Chapter 3:

1. To avoid recurrence of information, the introduction section of Chapter 3 was removed.
2. Drawback of Box Behnken Design of Experiments were added in section 3.2.2.
3. Details regarding the selection of design space were added in section 3.2.2.
4. Details regarding the predicted models were amended in section 3.3.2.
5. Temperature nomenclature was added in Table 3.2.
6. Details regarding the effect of design space for end applications were added in section 3.4.

Differences between the published paper and Chapter 4:

1. To avoid recurrence of information, the introduction section of Chapter 4 was removed.
2. Drawback of Box Behnken Design of Experiments were added in section 4.2.1.

Differences between the published paper and Chapter 5:

1. To avoid recurrence of information, the introduction section of Chapter 5 was removed.